HIGH TEMPERATURE OXIDATION BEHAVIOUR OF NICKEL-BASE SUPERALLOYS

Thesis submitted in accordance with the requirements of the University of Liverpool for the degree of Doctor in Philosophy

By

Keith Arnold

September 2016

PREFACE

This dissertation is submitted for the degree of Doctor of Philosophy at the University of Liverpool. The work undertaken and described herein was carried out under the supervision of Professor Gordon J. Tatlock in the School of Engineering and Material Science, at the Centre for Materials and Structures, University of Liverpool, between October 2012 and September 2016.

The work is original except where acknowledgement and references are made to the previous work. Neither this nor any substantially similar dissertation has been or is being submitted for a degree, diploma or other qualification at any other university.

Keith Arnold

Date: 09/16

ABSTRACT

The Ni-base superalloys are a popular range of materials for study following consolidation by additive manufacturing (AM) techniques, such as selective laser melting (SLM). However, very little work has been done to assess the high temperature oxidation behaviour of Ni-base superalloys fabricated by SLM, despite the fact that this class of alloy is designed primarily for operation at temperatures >650°C.

In the present work, the isothermal oxidation behaviour of the Ni-base superalloys Alloy 718 and Alloy 625 was studied following consolidation by SLM. A third Ni-base superalloy, Haynes 230, which is doped with a small amount of the reactive element La, was also studied following SLM-consolidation. The same three alloys were studied in wrought form for comparison purposes. Also studied following consolidation by SLM were oxide dispersion strengthened (ODS) derivatives of Alloy 625 and Haynes 230, which contained a 0.5 Wt. % addition of Y_2O_3, added by mechanical alloying (MA), and developed during the project for which the present work was conducted. Comparators for the ODS variants of Alloy 625 and Haynes 230 were fabricated by spark plasma sintering (SPS). All of the alloys were oxidised in laboratory air at 900°C and the oxidation kinetics determined using thermogravimetric analysis (TGA), or from scale thickness measurements.

The work has shown that SLM-consolidated Alloy 718 oxidised slightly faster than wrought Alloy 718. SLM-consolidated Haynes 230 oxidised ~3x faster than wrought Haynes 230 alloy, but SLM-consolidated Alloy 625 oxidised ~2x slower than wrought Alloy 625. The ODS variant of Alloy 625, in SLM-consolidated and SPS-consolidated forms, oxidised ~10x more slowly than wrought Alloy 625. The SLM-consolidated ODS variant of Haynes 230 oxidised at approximately the same rate as wrought Haynes 230, but in SPS-consolidated form the ODS variant of Haynes 230 oxidised ~10x faster than wrought Haynes 230.

The improvement in the oxidation resistance of the ODS variant of Alloy 625 is attributed to the well-known reactive element effect, which occurs when alloys are appropriately doped with reactive elements. The reduction in the oxidation resistance of the SPS-consolidated ODS variant of Haynes 230 is attributed to overdoping of the alloy with reactive elements, which is known to decrease the oxidation resistance of nickel-base alloys. It is proposed that SLM-consolidation improves the oxidation resistance of the ODS variant of Haynes 230 by ‘slagging off’ reactive elements from the alloy during consolidation, but for the same reason, the oxidation resistance of Haynes 230 is reduced by SLM-consolidation.

ACKNOWLEDGMENTS

I would like to take this opportunity to thank all of the people who have involved in this work, particularly my primary supervisor Professor Gordon Tatlock for his technical advice, encouragement and support during the course of the PhD. Thank you to him for the opportunity to attend conferences in the UK and US, and OXIGEN project meetings throughout Europe. I would also like to thank my secondary supervisor, Professor Andrew Jones, for his support and encouragement.

Thank you to all of the Materials Group at Liverpool, for their friendly help and advice, and especially to Mrs. Margaret Robinshaw for her support. Thanks also to the staff at the Nanoinvestigation centre (NiCaL) at Liverpool, past and present, including Dr. Simon Romani, Dr. Karl Dawson, Dr. Tobias Heil, Dr. Kerry Abrams, Ms. Lynn Allan and Mr. Alan Tidbury. Special thanks to Dr. Karl Dawson for the provision of FIB specimens and for sessions on the STEM, and to Dr. Tobias Heil for sessions on the STEM. Also special thanks to Mr. Alan Tidbury for his support in remedying the odd equipment malfunction and breakage. Thank you also to Mr. David Atkinson for his support, particularly with regard to specimen preparation, to Dr. Thomas Boegelien, former PhD colleague, and to fellow PhD students Kiriakos Moustoukas and Mark Duffield for technical discussions, encouragement and friendship during the course of our time together.

I would also like to thank all of the members of the OXIGEN project team, on whose behalf this work was conducted, for interesting and varied technical discussions during the course of the project. Particular thanks are extended to Mr. Adriaan Spierings and Mr. Thomas Bauer, of Inspire A.G (Zürich, Switzerland), for supplying specimens of SLM-consolidated alloys, and to Dr. Christian Leinenbach and Mr. Christoph Kenel, of Empa (Dübendorf, Switzerland), for supplying the SPS-consolidated alloys. Thanks are also extended to Haynes Inc. (UK) for the supply of a sample of wrought Haynes 230 for investigation. I would also like to acknowledge

the use of the EPSRC funded National Chemical Database Service hosted by the Royal Society of Chemistry. This work was funded by European Commission within the FP7-Project OXIGEN, Grant No. NMP3-SL-2011-310279.

I would like to finish by saying thank you to my wife Angela and children Thomas and Grace, for their patience, encouragement and love during the course of the PhD.

CONTENTS

CONTRIBUTIONS ORIGINATED FROM THIS WORK

Conference posters

K.Arnold, G.J. Tatlock (2014). Oxidation of an Oxide Dispersion Strengthened (ODS) Nickel Superalloy (MA754) at 900°C. Microscopy of Oxidation 9, Nottingham (UK), April 2014.

K.Arnold, G.J. Tatlock (2014). Oxidation of an Oxide Dispersion Strengthened (ODS) Nickel-base Superalloy (MA754). University of Liverpool Postgraduate Research Day, Liverpool (UK), April 2014.

K. Arnold, G. J. Tatlock (2015). High Temperature Oxidation Behaviour of an Oxide Dispersion Strengthened (ODS) Variant of a Commercial Nickel-Base Superalloy (Alloy 625). Gordon Research Conference on High Temperature Corrosion, Colby-Sawyer College, New London, NH (USA), July 2015.

Oral conference presentations

K. Arnold, G. Tatlock (2014). Oxidation of an Oxide Dispersion Strengthened (ODS) Superalloy (MA754) at 900°C. National Student conference in Metallic Materials (2014), Sheffield (UK), June 2014

Oral presentations given at OXIGEN project meetings in Manheim (Germany, 2015), Liverpool (UK, 2015) and Berlin (Germany, 2016). Yearly oral presentations were given at the end of each academic year at the University of Liverpool.

NOMENCLATURE

AM	Additive Manufacturing
Atm.	Unit of pressure
bcc	Body Centred Cubic
bct	Body Centred Tetragonal
BF	Bright Field
BSE	Backscattered Electron
CAD	Computer Aided Design
D	Interdiffusion coefficient
DF	Dark Field
EBM	Electron Beam Melting
EBSD	Electron backscattered diffraction
EPMA	Electron Probe Micro-Analysis
EDS	Energy Dispersive Spectroscopy
fcc	Face Centred Cubic
FEG	Field Emission Gun
FIB	Focused Ion Beam
GTE	Gas Turbine Engine
ICSD	Inorganic Structure Database
HIP	Hot Isostatic Pressing
k_w	Oxidation rate constant (determined by thermogravimetric analysis)
k_p	Oxidation rate constant (determined from scale thickness measurements)
Laser	Light amplification by the stimulated emission of radiation
LCF	Low Cycle Fatigue
LMD	Laser Melting Deposition

MA	Mechanical Alloying
ODS	Oxide Dispersion Strengthened
p_{O_2}	Oxygen partial pressure
RSA	Rapid Solidified Alloys
SDD	Silicon Drift Detector
SE	Secondary Electron
SLM	Selective Laser Melting
SOFC	Solid Oxide Fuel Cell
SPS	Spark Plasma Sintering
STEM	Scanning Transmission Electron Microscope
SUTW	Super Ultra-Thin Window
TBC	Thermal Barrier Coating
TEM	Transmission Electron Microscope
TIG	Tungsten Inert Gas (welding)
TGA	Thermogravimetric Analysis
XPP	Quantitative analysis methodology for EDS data, based on ZAF
XRD	X-ray Diffraction
ZAF	Atomic number (Z), Absorption (A), Fluorescence (F) correction for EDS

CHAPTER 1

INTRODUCTION

1.1 Introduction

Additive Manufacturing (AM) technologies offer the prospect of net shape fabrication, or near net-shape fabrication, of alloys and other suitable materials, including polymers and composites. A significant amount of research effort has gone into AM during the last thirty years or more, which has led to advances in our understanding of the technologies and the properties of builds made by AM [1, 2]. This has resulted in AM moving from the research laboratory into specialist commercial manufacturing, particularly for aerospace and biomedical applications [3-8].

The oxidation behaviour of an alloy varies as a function of its composition and microstructure, so any changes in these properties are likely to impact the oxidation resistance of an alloy. It is known that the microstructure of AM alloys is significantly different to that of alloys produced conventionally [9-11]. Therefore, it is expected that AM alloys will oxidise differently to their conventional analogues. However, little work has been done to assess the high temperature oxidation behaviour of AM Ni-base superalloys despite the fact that these alloys feature heavily in AM research [12-14], and are designed primarily for operation at temperatures >650°C. In a survey of AM research papers it was found that ~10% of those relating to Ni-base superalloys referred to oxidation, and of these only three papers, produced by the same group, dealt with oxidation behaviour in any meaningful way [15-17]. It must also be noted that the database represents a biased population, as it includes the results of searches made specifically for papers relating to the oxidation behaviour of AM Ni-base superalloys. This, it is believed,

demonstrates a knowledge gap, which is a serious omission given that Ni-base alloys are designed specifically for high temperature applications. Pint makes the same point in the context of the development of high strength materials [18].

The present work was performed to support a European FP7 project (OXIGEN), which aims to use AM, specifically laser melting deposition (LMD) and selective laser melting (SLM), to build demonstrator parts for operation in a gas turbine engine (GTE) for electricity generation. One part was to be built from a Ti-aluminide by LMD, but the second part was to be built from an oxide dispersion strengthened (ODS) Ni-base superalloy using SLM. The project end users identified oxidation resistance as a critical property of the second component, which was intended for operation at a temperature of ~900°C.

ODS Ni-base superalloys exhibit excellent high temperature creep strength and oxidation resistance. During consolidation of ODS alloys, the reactive element addition, made by mechanically alloying the base alloy with reactive element oxides, reacts with Al in the alloy to form a dispersion of fine particles, typically 5-20nm in size, and which are stable at high temperatures. These inhibit the movement of dislocations at high temperatures, giving the alloy excellent high temperature creep strength properties [19-21]. In addition, reactive element additions can significantly increase the oxidation resistance of an alloy by what is known as the ‘reactive element effect’ [22, 23]. ODS alloys are no longer available commercially because they are both difficult and costly to manufacture. Therefore, in the absence of a commercial ODS alloy, an ODS variant of a commercial Ni-base superalloy was developed for the project and manufactured by SLM. Two solid solution-strengthened Ni-base superalloys, Alloy 625 and Haynes 230, were selected as base alloys for ODS development and test blocks of Alloy 625 ODS and Haynes 230 ODS were built by SLM. Blocks of Alloy 625 and Haynes 230 were also built by SLM as part of the alloy-development process. A third component was to be built for the project using Alloy 718, an age-hardenable alloy with a maximum operating

temperature of ~650°C. It was intended that the alloy would operate at a temperature of ~425°C in a gas turbine engine.

1.2 Aims and scope of the thesis

The present work aims to develop an understanding of the high temperature oxidation behaviour of SLM-consolidated nickel-base superalloys using the alloys fabricated for the OXIGEN project. Alloy 718, Alloy 625 and Haynes 230 were studied following consolidation by SLM; wrought alloys were used as comparators for this work. ODS variants of Alloy 625 and Haynes 230 were also studied following consolidation by SLM, and for comparison, following consolidation by Spark Plasma Sintering (SPS). To distinguish the ODS alloys, they are denoted Alloy 625 ODS/SLM, Alloy 625 ODS/SPS, Haynes 230 ODS/SLM and Haynes 230 ODS/SPS respectively. All of the alloys were isothermally oxidised in static laboratory air at 900°C for up to 1000 hours, and the kinetics followed by thermogravimetric analysis (TGA) and from scale thickness measurements. Optical microscopy, Scanning Electron Microscopy (SEM), X-ray Diffraction (XRD) and Scanning Transmission Electron Microscopy (STEM) were used to investigate the scales formed during oxidation and the oxidation-induced changes in the chemistry and microstructure of the alloys.

The scope of the present work is restricted to gaining an understanding of the oxidation behaviour of SLM-consolidated alloys, and how it differs from that of the same alloys consolidated by conventional means. The protocols necessary for the mechanical alloying of powders, from which the ODS alloys were consolidated, were developed by MBN Nanomaterialia S.P.A (Vascon di Carbonera (TV), Italy) and are not considered in the present work. Protocols for consolidation of the alloys by SLM were developed by Inspire AG (Zürich, Switzerland), and protocols for consolidation of the ODS alloys by SPS were developed by Empa (Dübendorf, Switzerland). These are also beyond the scope of the thesis. In addition, no attempt is made to comprehensively characterise the microstructure of the alloys e.g. the

composition and structure of the dispersoids. This was undertaken by a post-doctoral researcher at the University of Liverpool (Dr Karl Dawson).

1.3 Structure of the thesis

The thesis is set-out in 9 chapters. Chapter 1 is a brief introduction to the present work and its justification in the field of AM. Background information and a literature review pertinent to the present work are presented in Chapter 2. The techniques used to study the oxidation behaviour of the alloys are described in Chapter 3. Results obtained from experiments to determine the oxidation kinetics of the alloys are presented in Chapter 4, and the results obtained from the study of the alloys, before and after oxidation, using microscopy and XRD, are presented for Alloy 718, Alloy 625 and Haynes 230 in Chapters 5, 6 and 7 respectively. At the end of each chapter is a discussion, with conclusions. Chapter 8 is a more comprehensive discussion of the results, which aims to bring together the discussions provided in Chapters 4, 5, 6 and 7. The final conclusions are also provided in Chapter 8. Suggestions for future work are given in Chapter 9.

CHAPTER 2

BACKGROUND AND LITERATURE REVIEW

2.1 Introduction

The superalloys are introduced in section 2.2, with a brief description of the chemistry of Ni-base superalloys and strengthening mechanisms. An overview of the SLM and SPS techniques, which were used to consolidate the alloys for the study, is presented in section 2.3. Section 2.4 is a review of the base alloys studied for the present work i.e. Alloy 718, Alloy 625 and Haynes 230.

The high temperature oxidation behaviour of metals and alloys is introduced in section 2.5, which includes subsections covering the thermodynamics of oxidation, 2.5.1, the kinetics of oxidation, 2.5.2, the effect of Cr content, cold work and grain size on oxidation, 2.5.3, the reactive element effect, 2.5.4, and the oxidation of the base alloys at 900°C, 2.5.5. The literature review is summarised in section 2.6.

2.2 Superalloys

The ‘superalloys’ are based on Fe, Ni or Co, but there is no strict definition of the term. They are generally accepted as alloys suitable for high temperature applications. In ‘Superalloys II’, Sims provided the following definition: ‘A superalloy is an alloy developed for elevated temperature service, usually based on group VIIIA elements, where relatively severe mechanical stressing is encountered, and where high surface stability is frequently required’ [24].

All superalloys have a face centred cubic (fcc) structure, within which secondary strengthening phases are dispersed. The fcc structure makes the superalloys intrinsically tougher than bcc alloys. The combination of the fcc structure and

strengthening phases makes superalloys both strong and stable at high temperatures, and they can operate successfully at temperatures >0.6x their melting point [25]. Ni is the only one of the three superalloy matrix-forming elements that can maintain a fcc structure from room temperature up to its melting point (1455°C). Co and Fe both undergo phase transformations at temperatures below their melting points; in the case of Co the transformation from hcp to fcc at 417°C, and in the case of Fe the transformation is from bcc to fcc at 912°C. Co and Fe must be alloyed, usually with nickel, in order to stabilise them in the fcc structure over the gas turbine engine (GTE) temperature range [26].

Since the 1940s the development of superalloys has been inextricably linked with that of aircraft GTEs, which need high performance alloys in order to operate at very high temperatures. Therefore the work done on superalloys during the course of the last 70 years or so has mainly been focused on raising their operating temperature in order to further increase the power and fuel efficiency of GTEs [27].

2.2.1 Nickel-based superalloys

All Ni-base superalloys have an austenitic fcc matrix (γ), with additions made to improve their strength by solid-solution strengthening. Additional strengthening may be obtained from carbides, which are precipitated mainly at the grain boundaries in polycrystalline superalloys. Many Ni superalloys are also strengthened by coherent, or semi-coherent, intermetallic phases known as gamma prime (γ′) and gamma double prime (γ′′). ODS alloys, are strengthened by oxide dispersoids, which are stable at high temperatures.

The elements that may be present in Ni-base superalloys, along with their roles, are presented in Table 2.1. It should also be noted that trace level contaminants must be controlled if they are not to adversely affect the properties of the alloy e.g. S, which is reported to promote detachment of the oxide scale formed during high temperature oxidation [28].

Table 2.1: The effect of element additions on Ni-base superalloys [29]

Effect	Element
Solid-solution strengtheners	Co, Cr, Fe, Mo, W, Ta, Re
Grain-boundary refiners	B, C, Zr, Hf
Carbide form:	
MC	W, Ta, Ti, Mo, Nb, Hf
M_7C_3	Cr
$M_{23}C_6$	Cr, Mo, W
M_6C	Mo, W, Nb
Carbonitrides (MCN)	C, N
Hardening precipitates and/or intermetallics	Al, Ti, Nb
Dispersoid formers	Y, Al, O
Oxidation resistance	Al, Cr, Y, La, Ce
Improve hot corrosion resistance	La, Th
Sulphidation resistance	Cr, Co, Si
Raise solvus temperature	Co
Improve creep properties	B, Ta
Increases rupture strength	B
Retards coarsening	Re

2.2.2 Solid-solution strengthened alloys

Dislocations can move relatively easily within pure metals, which can result in plastic deformation of the metal as a result of the motion of the dislocations i.e. shear. The addition of solute atoms to a metal produces strengthening because they disrupt the movement of the dislocations, which occurs as a result of interactions between the stress fields of the solute atoms and those around the dislocations. The stress fields arise around the solute atoms because of the difference in size between them and the host atoms of the metal. This is known as elastic misfit interaction and the strengthening effect is referred to as solid-solution strengthening [30, 31]. A strong correlation exists between creep strength arising from solid-solution strengthening and the percentage difference in the size of the solvent and solute atoms, with larger solute atoms providing greater strengthening. As might be

expected the degree of creep strengthening increases with the solute concentration [25]. Modulus also plays a role in solid-solution strengthening because it is believed that extra work is required to force dislocations through the hard and soft regions of a matrix.

In nickel alloys aluminium, tungsten, molybdenum, chromium and rhenium are stronger solid-solution strengthening elements than cobalt, iron, vanadium and titanium [32]. The strengthening effects persist to ~0.6x the melting point of the alloy, above which solid solution strengthening is diffusion-dependant. Therefore, molybdenum and tungsten offer the most solid solution strengthening at high temperatures because they diffuse slowly [26].

2.2.3 Precipitation strengthened alloys

Many Ni-base superalloys are strengthened by precipitates generated in-situ using age-hardening heat treatments, which involves the precipitation of meta-stable and stable phases from homogeneous, supersaturated solid solutions. The principal intermetallic forming elements in commercial nickel superalloys are aluminium, titanium and niobium. These combine with nickel to form coherent precipitates of the type N_3X, which strengthen the alloys by disrupting dislocation movement. The major factor that contributes to strengthening by the intermetallic precipitates is order in the particles [25].

Aluminium and titanium are added to alloys to precipitate gamma prime (γ'), which has the chemical formula Ni_3Al, or $Ni_3(Al,Ti)$, but because of deviations from stoichiometry the composition is normally written $Ni_3(Al, Ti)$. Gamma prime has a primitive face centred cubic lattice, with nickel atoms occupying the face-centres and the aluminium and titanium atoms occupying the cube corners, Figure 2.1 (a). Niobium is added to alloys to precipitate gamma double prime (γ''), which is used to strengthen nickel superalloys that require high strength at relatively low temperatures (<700°C), such as turbine discs. Gamma double prime has a body centred tetragonal

(bct) lattice structure, which is approximately equivalent to two stacked γ cells, Figure 2.1 (b). It is therefore coherent with the matrix. Gamma double prime develops coherency strains of several percent, which together with the limited number of slip systems, gives rise to the high temperature strength [25]. At ~650°C gamma double prime transforms to delta phase (δ-phase), which limits the operating temperature of alloys strengthened by gamma double prime – this is because delta phase provides little strength [29]. Aluminium and titanium both partition to gamma double prime, and its composition is therefore usually written $Ni_3(Nb,Al,Ti)$.

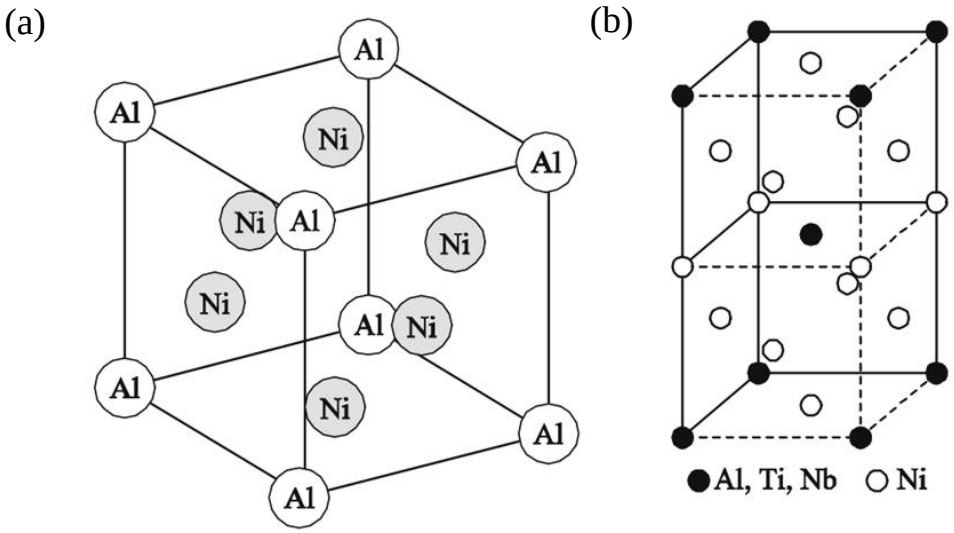

Figure 2.1: Lattice structure of the intermetallic precipitates used to strengthen Ni-base superalloys (a) gamma prime (γ′), and (b) gamma double prime (γ′′) [33]

2.2.4 ODS Alloys

The yield stress of γ′-strengthened alloys peaks at ~800°C, but thereafter falls rapidly, and beyond ~1200°C there is little resistance to plastic deformation [25]. ODS alloys are distinguished by their exceptional high temperature strength, which results from a small volume fraction of dispersoids, which are stable at very high temperatures, and strengthen the alloys by impeding the movement of dislocations within the alloys [19-21]. The strength of the alloys is dependent on the size, density

and inter-particle spacing of the dispersoids [34, 35]. It is assumed that the dispersoids present in ODS superalloys are incoherent, and therefore Orowan bowing is the only model that can be applied to the interactions that take place between dispersoids and dislocations [19, 34, 36]. However, there is a growing body of evidence that, at the smallest sizes, the dispersoids may be coherent or semi-coherent. If this theory is valid, it means that particle-cutting models may also apply for the smallest dispersoids [37, 38].

ODS alloys are consolidated from mechanically alloyed powders, which are powders that have had one or more reactive element oxides, usually yttria, forced into solution by high energy milling. During consolidation a reaction occurs between Y and O, and Al from the alloy, to form dispersoids [39, 40]. The dispersoids have compositions based on YAlO, including yttrium aluminium garnet $Y_3Al_5O_{12}$ (YAG), yttrium aluminium hexagonal $YAlO_3$ (YAH), yttrium aluminium monoclinic $Y_4Al_2O_9$ (YAM), yttrium aluminium perovskite $YAlO_3$ (YAP), yttrium aluminium pseudo-perovskite $YAlO_3$ (YAP$'$) and yttrium aluminium tetragonal $Y_3Al_5O_{12}$ (YAT) [41]. Ti may also be incorporated into the dispersoids [42]. The alloys are often recrystallised by isothermal annealing in order to achieve the desired microstructure, which may have a large grain aspect ratio (GAR) for improved creep resistance [43].

Melting of the mechanically alloyed powders during consolidation, or of the ODS alloys themselves, results in a loss of strength of the alloy due to ‘slagging-off’ of the less dense reactive element oxides [44]. This makes ODS alloys unsuitable for consolidation by melting or by conventional joining techniques such as TIG welding. Consolidation of ODS alloys is therefore usually carried-out by extrusion or by HIPping.

The nominal composition of a typical legacy ODS Ni superalloy, MA754, is shown in Table 2.2. The volume fraction of dispersoids in recrystallised MA754 has been reported to be ~1.1%, with a mean particle spacing of 94nm and the average

diameter of the dispersoids 13.6nm. The alloy also contains alumina and titanium carbonitride inclusions [19]. A bright field TEM micrograph of dispersoids and an alumina inclusion in MA754 is shown in Figure 2.2.

Table 2.2: Nominal composition of MA754 (Wt. %) [45]

Ni	Cr	Fe	Ti	Al	C	Y_2O_3
78.0	20.0	1.0	0.5	0.3	0.05	0.6

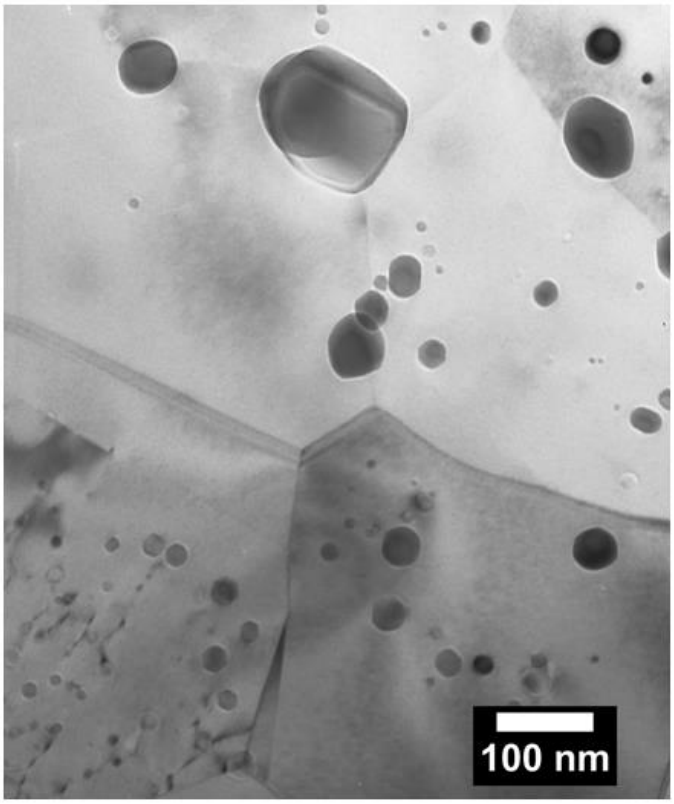

Figure 2.2: BF TEM micrograph of dispersoids, and an alumina inclusion on a triple point, in ODS Ni superalloy MA754 (from Author's collection)

The complex production route makes ODS alloys costly to produce, which when combined with the difficulties associated with joining and repair [44], means that they are no longer available commercially. Despite this a significant amount of

research effort still devoted to the ODS superalloys because of their superior properties e.g. for applications relating to nuclear power [21, 46, 47].

Mechanical Alloying

Mechanical alloying is a technique that allows an atomically-mixed solution of an alloy and a reactive element to be made that would otherwise be immiscible. The mechanical alloying process is undertaken in a high energy mill, where the alloy and reactive element powder particles are repeatedly flattened, fractured and welded until they are homogenised to a stable average size [48-50]. This produces non-equilibrium powders that are nanostructured, with grain sizes as small as 10-15nm [51]. The technique can also be used for other systems, including nanocomposites and metallic glass [52].

Mechanical alloying is typically performed for times that vary between a few hours and tens of hours. This means that mechanically alloyed powders, particularly those containing reactive elements, are prone to contamination as a consequence of the extended processing time, the small size of the particles, the large surface area of the particles and the formation of new surfaces. Contamination may be derived from the milling equipment [53, 54] and the atmosphere under which the powder is milled [55]. The use of surfactant, which is often added to prevent excessive cold welding, particularly of ductile alloys, is an additional source of carbon and oxygen contamination [56]. Contamination may be reduced by the use of high purity metals, inert milling atmospheres, short milling times and the use of balls and mills fabricated from the same composition as the powder, but in spite of these efforts contamination of the final powders remains a major problem with the process.

2.3 Consolidation techniques

In this section, the principles of consolidation by SLM and SPS are briefly covered in 2.3.1 and 2.3.2 respectively. Included in section 2.3.1 is a review of the

microstructure of SLM-consolidated ODS alloys and steels. The review was extended to steels because of a lack of papers related specifically with ODS Ni-base alloys. The microstructure of non-ODS alloys consolidated by SLM is covered in section 2.4, which describes findings reported in the open literature for Alloy 718 and Alloy 625. This review is structured this way because many more papers have been published on the subject of SLM-consolidation of non-ODS Ni-base alloys than ODS alloys and steels. There are no reports in the open literature for SLM-consolidated Haynes 230. Included in section 2.3.2 is a review of the microstructure of SPS-consolidated alloys, which is broadened to cover Fe and Co alloys as well as Ni alloys.

2.3.1 Selective Laser Melting (SLM)

Selective Laser Melting (SLM) is one of a number of additive manufacturing (AM) techniques that have appeared during the course of the past 20-30 years, which can be used to consolidated suitable materials, including alloys, into net-shape or near net-shape parts [57-59]. A schematic of a SLM system is shown in Figure 2.3. Powder is delivered to the flat-bed from a hopper, which is applied in thin layers, typically 30-100μm thick, using a wiper. A laser, under computer control, is scanned over the surface of the powder to melt it. The bed is lowered and a new layer of powder is applied over the top of the solidified part, and the laser re-scanned to melt the next layer of powder onto the part. The process is repeated until the required component is fabricated [60, 61].

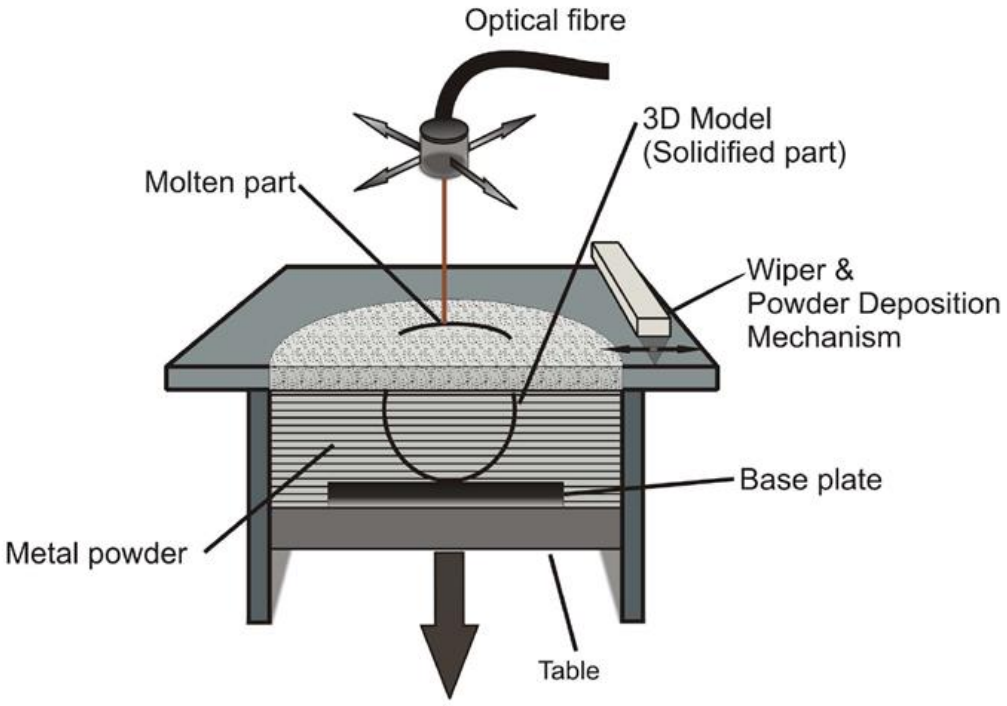

Figure 2.3: Schematic of a SLM system [61]

During SLM-consolidation heterogeneous nucleation occurs only at the start of the build process, assuming that the grains of any base plate do not just grow into the liquid. After this, all subsequent layers are formed by the freezing of molten metal with pre-existing grains present in the layer below. There are two means by which the new material may freeze, one is by the nucleation of new solid grains and the other is the growth of the pre-existing grains from the layer below. The nucleation of new grains requires an energy barrier to be overcome and this will require the liquid to under-cool significantly. In comparison there is no energy barrier to growth and so the pre-existing grains can rapidly grow into the liquid forming new solid [62, 63]. The layers deposited in SLM are thin, typically 30μm to 100μm thick, and so it is unlikely that the molten metal/gas surface of the melt pool will ever cool sufficiently for nucleation to occur before the pre-existing grains have grown through the layer. This continued growth of pre-existing grains results in columnar structures, similar to those seen in casting and welding, with the 'easy growth' <100> directions [63-65] aligning with the heat-flow direction, Figure 2.4 (a). This columnar structure refers

to the phase that grows from the liquid; if there are solid state phase transformations within the system other structures will then form within these grains, which can often lead to the formation of a cellular substructure, Figure 2.4 (b).

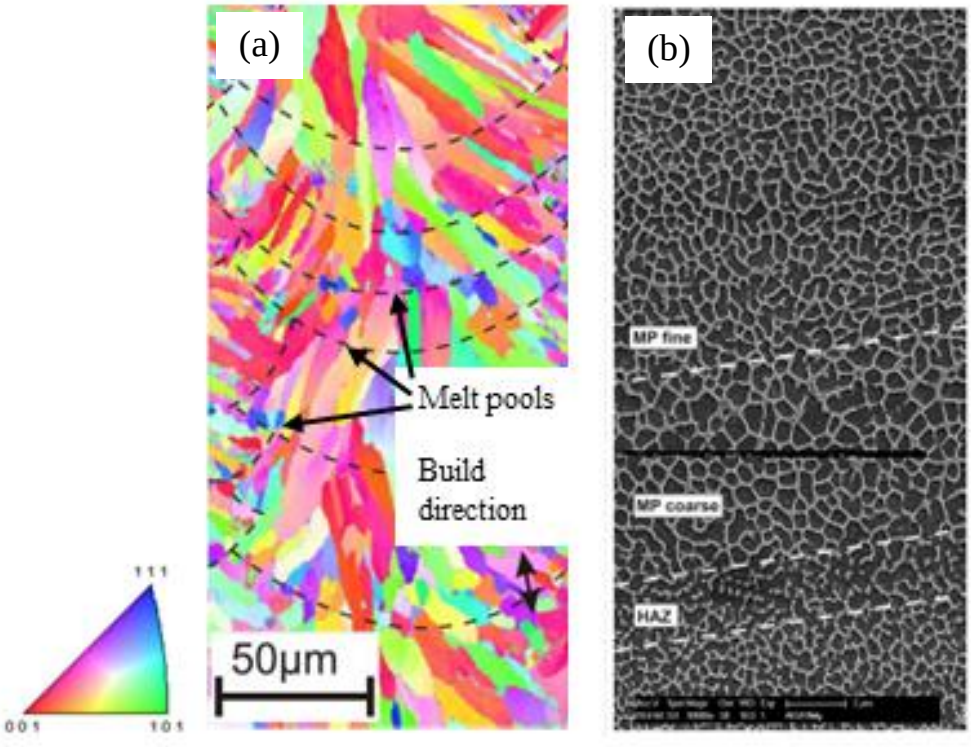

Figure 2.4: Formation of microstructure in an SLM-consolidated alloy (a) columnar grains, which transcend the melt pools and are orientated in the build direction of the alloy [65], and (b) cellular substructure [65]

Microstructure of SLM-consolidated ODS alloys

Walker et al reported that large columnar grains formed in the build direction of PM2000, a ferritic ODS alloy, and that scan speed was observed to be more important than laser power laser in retaining fine dispersoids. This was attributed to rapid solidification of the alloy [66]. Boegelein et al, using the build parameters recommended by Walker, reported that that ~25-30% of the Y present in PM2000 powder formed slag during SLM-consolidation, and additionally reported that the alloy exhibited intergranular cracking, inclusions, porosity and a poor surface finish.

Large grains were aligned with the build direction and orientated in the <001> easy growth direction [67]. Little porosity was observed in PM2000 coatings applied to superalloy IN939 by SLM [68]. The mechanical properties of PM2000 thin walls, made by SLM, were reported to be anisotropic because of the strong [001] fibre texture in the build direction. Inclusions present in the alloy were believed to be scale residues, rather than agglomerated dispersoids. Y was retained in solution in the alloy [69].

A paper by Molian, though not directly related to SLM-consolidation, is worth reporting. It was observed that TIG welded MA754, the Ni-base ODS superalloy, contained Y slag, which had floated to the surface of the weld, but laser welded MA754 was free of slag. This was attributed to a smaller weld pool arising from laser consolidation. The hot corrosion resistance of the base metal and laser weld was superior to that of the TIG weld because of the changes in composition and microstructure arising from TIG welding [44].

2.3.2 Spark Plasma Sintering (SPS)

Sintering is used to consolidate alloy powders at temperatures below their melting point, either under vacuum or under a protective atmosphere. Traditional sintering is slow because the rates of heating are low, typically <10°C min^{-1}, but in SPS heating rates of up to 1000°C min^{-1} can be obtained [70].

In SPS systems, the powder to be sintered is placed in a die, usually graphite, and heated under vacuum and uniaxial pressure by passing a pulsed DC current through it, Figure 2.5 (a). When a spark discharge appears in a gap between powder particles, or at the contact point between particles, a very high localised temperature of several thousand to tens of thousands of centigrade is generated momentarily, Figure 2.5 (b). This causes evaporation and melting of the surface of the powder particles, forming necks, which grow until the powder is fully consolidated [71]. The combination of

pressure, current and localised high temperatures increases the rate of heating and reduces the sintering time; this produces consolidation with little grain growth [72].

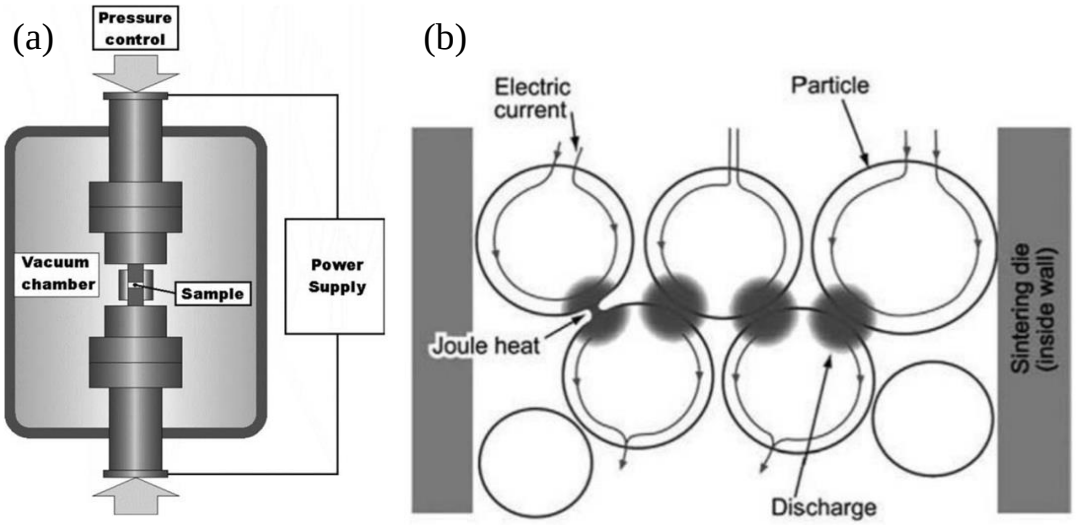

Figure 2.5: Sintering of a powder sample by SPS (a) schematic of a typical SPS system [73], (b) DC current flowing through powder particles [74]

Microstructure of SPS-consolidated ODS Alloys

Bimodal grain size distributions, comprising grains of <1µm in size and grains >1µm in size, are reported in SPS-consolidated ODS alloys [75-79]. The smaller grains are observed to contain dispersoids, which appeared to retard grain growth. This effect was also observed after a heat-treatment at 1000°C for 240 hours, but growth was observed at longer times [79]. The presence of the larger grains in the bimodal distribution has also been attributed to insufficient milling of the alloy powder with Y_2O_3, and localised melting of the alloy powder during consolidation [75]. Contamination of the SPS-consolidated alloys by C was reported as a result of the use of graphite dies or organic binder, which led to carbide formation in the contaminated alloys [75, 80]. Milling prior to consolidation reduces the grain size of SPS-consolidated alloys. Grain sizes of ~1-8µm were observed following SPS-consolidation of Y-containing alloy powders, but grain sizes of <1um were obtained following milling and SPS-consolidation of the same powders [78, 81]. This is

probably due to pinning of the alloy grains by dispersoids formed from solutionised Y during consolidation. Fine grain sizes are also reported in extruded ODS alloys, and promote selective oxidation [82]. In a study of Ni-20Cr-1.2Y_2O_3 consolidated by SPS it was reported that full densification of the alloy was achieved at temperatures >1000°C and that Cr oxides, as well as Y oxides, were present in the consolidated alloy [78]. Fast heating rates have been reported to cause porosity in alloys during consolidation by SPS [83-85].

2.4 Alloys

2.4.1 Alloy 718

Introduction

Alloy 718 is an austenitic nickel-base superalloy developed during the early 1960s [86]. The alloy can be used annealed or more usually age-hardened following a suitable heat-treatment to precipitate, by volume, up to ~21 % of the intermetallic γ´´, which provides strength [87]. Alloy 718 finds many applications, including casings and various formed sheet metal parts for aircraft and land-based gas turbine engines, and cryogenic tankage. It is also used for fasteners and instrumentation parts [88]. The nominal composition of Alloy 718 is shown in Table 2.3.

Table 2.3: Nominal composition of Alloy 718 (Wt. %) [88]

Ni	Fe	Cr	Nb	Mo	Ti	Al	Co	C	Mn
50.0-55.0	Bal.	17.0-21.0	4.75-5.50	2.80-3.30	0.65-1.15	0.20-0.80	1.00 max.	0.08 max.	0.35 max.
Si	P	S	B	Cu					
0.35 max.	0.015 max.	0.015 max.	0.006 max.	0.30 max.					

Microstructure of Alloy 718

The solidification sequence for Alloy 718 is in the order, $L \rightarrow \gamma$, which causes the inter-dendritic liquid to become enriched in Nb and C, $L \rightarrow (\gamma + NbC)$ eutectic, which occurs at ~1250-1257°C and depletes the inter-dendritic liquid of C, with termination via $L \rightarrow (\gamma + Laves)$ eutectic at ~1185-1200°C [89, 90]. The partition coefficient for Nb is ~0.5. The same solidification sequence was also reported by DuPont et al for a series of experimental Nb-containing alloys [91]. Therefore the alloy contains MC-type carbides, which have Nb(Ti)C and Ti(Nb)C compositions, and Laves phase [92]. Laves phase is a brittle phase, which has a A_2B-type composition, and typically has a composition of $(NiCrFe)_2(NbMoTi)$ [93]. It is deleterious to the strength of the alloy and is eliminated by solutionising at ~926-1010°C, which dissolves the Laves phase and precipitates grain boundary δ-phase [88]. The primary strengthening phase is the coherent bct intermetallic γ′′, which is a metastable form of Ni_3Nb. This is precipitated by age-hardening the solutionised alloy. γ′′ converts into the thermodynamically stable δ-phase at temperatures ~650°C, which limits the operating temperature of the alloy [25]. δ-phase is orthorhombic and incoherent with the γ, and therefore provides little strength to the alloy. It forms plate-like structures, usually at the grain boundaries, which are expected to lie on matrix {111} planes [87]. A small amount of δ-phase is retained in the alloy because it helps to limit grain growth, but the amount of δ-phase is carefully controlled because in addition to depleting the alloy of Nb required for γ′′ formation it can embrittle the alloy [94]. Intragranular δ-phase can be expected to form if the alloy is maintained at 900°C, the oxidation temperature for the present work, for more than ~3 hours. γ′′ can also form during the first ~10 hours of heating at 900°C before it transforms to δ-phase [87]. Alloy 718 welds, which may be considered approximately analogous to the SLM-consolidated alloy, are moderately susceptible to solidification cracking because of the large solidification temperature range of the Nb-rich eutectics, but this may be ameliorated by the use of higher C

compositions, which promotes NbC formation at the expense of Laves phase formation [91, 95, 96].

Microstructure of SLM-consolidated Alloy 718

Columnar microstructures, comprised of dendrites with a dendrite arm spacing of <1µm, form in the build direction of SLM-consolidated Alloy 718. The alloy, where reported, had a <001> texture parallel to the build direction [97-101]. Laves phase forms on the dendrite boundaries [97-100], but γ´´ was observed by one group to form in arrays orientated in the build direction of the alloy [101]. The Laves phase was dissolved by heat treatments of ~1000°C and grain boundary δ-phase precipitated [98-100, 102]. Fine carbides of <1µm in size were observed in some builds [97, 99]. The microstructure of the alloy could not be significantly modified at a temperature of 954°C, the standard annealing treatment for Alloy 718, but it could be modified at temperatures ≥1080°C [97-101].

2.4.2 Alloy 625

Introduction

Alloy 625 is an austenitic (γ) solid-solution strengthened nickel base superalloy, with excellent corrosion resistance in the aqueous environment. It was developed for steam line piping material, which required an alloy that did not age-harden, but had a high creep resistance and was easily welded and fabricated [86]. Alloy 625 is widely used for marine applications, but it is also used in nitric acid production for catalyst supports, scrubbers and stack liners [103]. The nominal composition of Alloy 625 is shown in Table 2.4.

Table 2.4: Nominal composition of Alloy 625 (Wt. %) [103]

Ni	Cr	Fe	Mo	Nb	C	Mn	Si	P	S
58.0 min.	20.0-23.0	5.0 max.	8.0-10.0	3.15-4.15	0.10 max.	0.50 max.	0.50 max.	0.015 max.	0.015 max.
Al	Ti	Co							
0.40 max.	0.40 max.	1.00 max.							

Microstructure of Alloy 625

The solidification sequence for Alloy 625 is very similar to that of Alloy 718 and is $L \rightarrow \gamma$, $L \rightarrow (\gamma + NbC)$ eutectic, which occurs at ~1231°C and $L \rightarrow (\gamma + Laves)$ eutectic, which occurs at ~1158°C. The partition coefficient for Nb is ~0.5, as it is for Alloy 718 [89]. There are two common solidification pathways for Alloy 625, which lead to the formation of NbC and NbC+Laves phase respectively, but a third pathway, which leads only to Laves phase is uncommon, but has been reported when the C concentration is <0.01Wt. % [104]. This shows that higher C contents lead to more NbC and less Laves phase, as is the case for Alloy 718. However, Alloy 625 tends to form less Laves phase than Alloy 718 because its Nb content is lower, but this beneficial effect may be off-set in some Alloy 625 compositions by Si and Mo, which tend to be higher in Alloy 625, and promote Laves phase formation [89]. Si is reported to stabilise M_6C carbides at 800°C and reach concentrations of ~12 Wt. % [105]. The MC carbides present in wrought Alloy 625 have been identified as a mixture of blocky carbides, and grain boundary MC carbides. After thermal exposure $M_{23}C_6$ carbides, M_6C carbides and Laves phase/grain boundary δ-phase can form in the alloy [104]. Because of its high chromium and molybdenum content Alloy 625 tends to retain more N than other Ni alloys, which promotes the formation of TiN inclusions that can act as initiation sites for cracks [86].

Alloy 625 welds, like Alloy 718 welds, are moderately susceptible to solidification cracking because of the large solidification temperature range of the Nb-rich eutectics. Du Pont estimated this to be as wide as ~170°C [106]. The effect can be

ameliorated by the use of higher C compositions, which promote NbC formation at the expense of Laves phase formation [91, 95, 96].

Microstructure of SLM-consolidated Alloy 625

Li et al reported columnar growth in the <001> easy growth direction of SLM-consolidated Alloy 625, and a dendrite arm spacing of ~0.5μm. The alloy was hard, because of the fine grain size and supersaturation of the strengthening elements. Carbides and precipitates were absent from the alloy because of rapid solidification, but MC-type carbides formed during subsequent heat treatment at 1000°C [107]. Amato also reported that fast cooling of Alloy 625 during SLM-consolidation appeared to restrict the nucleation and growth of precipitates [108]. Criales et al modelled the effect of build parameters on SLM-consolidated Alloy 625. The authors reported that the peak temperature, assuming a laser power of 50W and a scan speed of 130mms^{-1}, could be >2500K [109]. They also reported that the time spent above the liquidus temperature of the alloy, and the associated cooling time, which can strongly influence the microstructure of the alloy, were mainly controlled by the scan speed.

2.4.3 Haynes 230

Introduction

Haynes 230 alloy is a nickel-chromium-tungsten-molybdenum superalloy, which exhibits excellent high-temperature strength and is claimed to be thermally stable and resistant to oxidation for extended lengths of time at temperatures of up to ~1150°C [110]. The alloy is solid-solution strengthened, with W the major strengthening element. This is because slow diffusion of W in Ni promotes good creep strength [111]. A small amount of B is added to Haynes 230 to improve carbide stability by reducing the lattice mismatch between the carbides and austenite

[111]. There are no reports in the open literature relating to the consolidation of Haynes 230 by SLM.

Haynes 230 was developed for the aerospace, power generation and chemical process industries, and typical uses include combustion cans, thermocouple sheaths, high-temperature heat exchangers etc. [110]. The nominal composition of the alloy, taken from Haynes International literature, is shown in Table 2.5. It is noted that the composition does not contain B, which is often reported as present in Haynes 230 compositions.

*Table 2.5: Nominal composition of Haynes 230 alloy (Wt. %) *Maximum [110]*

Ni	Fe*	Cr	Mo	Ti*	Al	C	Si	Co*	Mn	W	La	Zr
57.0 (bal.)	3.0	22.0	2.0	0.1	0.3	0.1	0.4	5.0	0.5	14.0	0.02	0.015

Microstructure of Haynes 230

The microstructure of the solutionised alloy is comprised of fcc austenite, annealing twins and intragranular and intergranular M_6C-type carbides, which can occupy a volume fraction of ~2%. The M_6C carbides contain W and Mo and, being stable at high temperatures, help to control grain growth [110-114].

Exposure of Haynes 230 to temperatures of between 650°C and 980°C results in the precipitation $M_{23}C_6$ carbides on dislocations, grain boundaries and annealing twins [111]. Deleterious phases, such as sigma phase and mu phase, do not form in Haynes 230, even after 16000 hours of exposure to temperatures of between 649°C and 871°C [110]. However, Veverkova reported that at a temperature of 1050°C the alloy was unstable, and that Cr-rich $M_{23}C_6$ coarsened at short exposure times and formed large, pool-like structures at long exposure times [115]. Similar behaviour has been reported by Jalowicka [116]. Solidification cracking is reported in Haynes 230. Ernst reported solidification cracking in Haynes 230 welds as a result of the partitioning of Cr and W to the solidification boundaries [117] and concluded that

the mechanism was consistent with Borland's hot cracking theory [118]. Klarstrom has reported that the $M_{23}C_6$ carbides in Haynes 230 are expected to be $Cr_{21}(W,Mo)_2(C,B)_6$ [113]. The elements B, S, P, and Si are all known to promote solidification cracking by increasing the solidification temperature range in the mushy zone [119]. The presence of B in $M_{23}C_6$, as reported by Klarstrom, may be consistent with Ernst's findings. Rowe et al have also reported that B, when added to Haynes 230 base metal, can increase the susceptibility of welds to solidification cracking [95]. In addition to solidification cracking, Ernst also reported that B promoted micro-fissuring in Haynes 230 welds as a result of liquation cracking [117].

2.5 High temperature oxidation of alloys

Alloys are thermodynamically unstable with respect to oxidising atmospheres. At low temperatures the rates of reaction are so slow that the effect of the corrosion process is largely inconsequential, but at higher temperatures the rate of corrosion increases dramatically and this can result in deleterious changes in the properties of the affected alloy e.g. a loss in strength of load-bearing materials, or a breakdown of the surface. Alloys can be protected from high temperature corrosion by a thermal barrier coating (TBC), or they can have compositions designed to produce protective scales that are dense, adherent and slow-growing. This is achieved by the addition of an element, or elements, which selectively oxidise to form scales that have a low defect concentration, which limits the rate of oxidation by lattice diffusion e.g. Cr_2O_3 [120]. The vaporisation rate of the oxide should be low and the scale should also be free of pores and cracks that can promote oxidation. The scale must be adherent so that it does not fail, exposing the underlying alloy to oxidation. The elements that meet, or mainly meet, these criteria are Cr, Al and Si [121].

Aluminium and chromium are the most widely used element additions for oxidation protection, and these form alumina and chromia scales respectively. However, a minimum concentration of the element is necessary for the formation of an external

protective scale. In the case of Al this is ~15 Wt. % for a binary NiAl, but ~5 Wt. % for NiAl-10Cr. The reduction in the Al content necessary for the formation of an external Al_2O_3 scale is due to the synergistic effect Cr has on the oxidation behaviour of alumina formers, which is mainly believed to be derived from gettering [121]. Approximately 12 Wt.% chromium is required in binary NiCr alloys to form an external scale [122]. Alloys protected by Cr can only be used at temperatures of up to ~950°C because of vaporisation of oxide, particularly in the presence of water vapour [123]. Al can protect alloys up to temperatures of ~1100°C, but for operation at temperatures >1100°C refractory metals or ceramics are normally used [124].

In general, however, three distinct stages comprise the oxidation process, which in order of occurrence, are denoted 'transient', 'steady-state' and 'breakaway', Figure 2.6. 'Transient' oxidation describes the initial oxidation of the alloy, whereby the alloy oxidises according to its initial surface chemistry [121]. In the case of a highly alloyed Cr_2O_3-former, which this work will focus on, the second stage is the growth of a continuous chromia scale, which forms as a result of the diffusion of ions through the scale established during transient oxidation [122]. The final stage of the oxidation process is breakaway, when the protective scale-forming elements in the alloy can no longer replenish the scale/alloy interface, and faster growing oxides begin to form a scale [125, 126]. This is effectively the lifetime of the alloy. It should be noted that the time to breakaway is shortened by spalling of the scale during oxidation, which makes scale adherence extremely important [127, 128].

Internal oxidation is the term used to describe the process by which oxygen, which is dissolved into an alloy, reacts with a less noble component, or components, of the alloy to form oxide. The nature of the internal oxidation that develops in an alloy is dependent upon the mechanism of oxygen diffusion in the alloy. At low temperatures oxygen mainly diffuses into the alloy via grain boundaries with the result that oxide forms along the grain boundaries, but lattice diffusion becomes more important with increasing temperature and this results in homogeneous internal

oxidation. Internal oxidation at the grain boundaries of an alloy may be detrimental to its mechanical properties, but it may be beneficial in promoting scale adhesion.

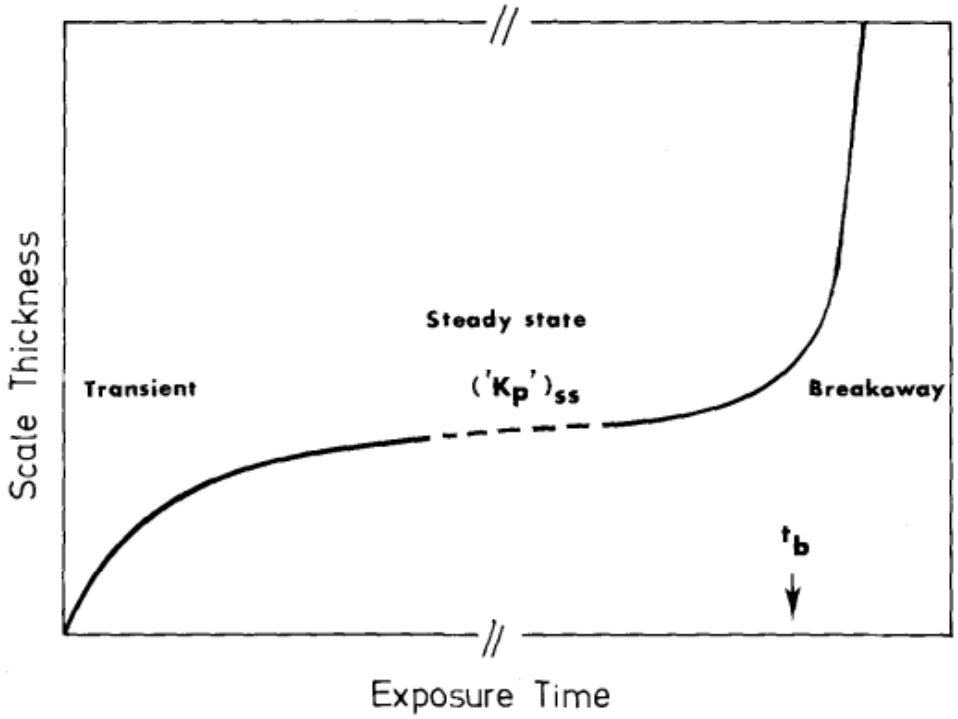

Figure 2.6: Schematic of high temperature oxidation of an alloy in air [126]

2.5.1 Thermodynamics of oxidation

The driving energy for metal/oxygen reactions is the free energy change arising from the formation of oxide. Oxide will only form if thermodynamically favoured, which occurs when the oxygen partial pressure is greater than the dissociation pressure of the oxide in equilibrium with the metal. An Ellingham/Richardson diagram is a plot of the standard free energies of formation of the oxides, $\Delta G^0 = RT \ln p_{O_2}$, per mole of oxygen, against temperature, Figure 2.7. This shows the relative thermodynamic stability of selected different metal oxides, with the most stable oxides having the largest negative values of ΔG^0. Ellingham/Richardson diagrams are used to predict whether or not a metal oxide will form at a given temperature and oxygen partial

pressure. In the case of the present work, conducted in air at 900°C, it is found from the blue lines projected on to the diagram that Cr_2O_3 and Al_2O_3, the two principal oxides of interest, form at p_{O_2} values of ~10^{-24} atm. and ~10^{-39} atm. respectively. MnO, which is also of interest in the context of the present work, but not shown in Figure 2.5, forms at a p_{O_2} value of ~10^{-27} atm. The enthalpy and entropy are approximately independent of temperature over large temperature ranges, which is why the lines are approximately straight. The lines are positive and essentially parallel because the main change in entropy arises from the elimination of one mole of oxygen. Abrupt changes occur in the lines at boiling points because of the large change in entropy. It is also worth noting that 0K represents ΔH°. The derivation of the free energy change ΔG^0 can be found in standard text books [129-131] and in review papers [132].

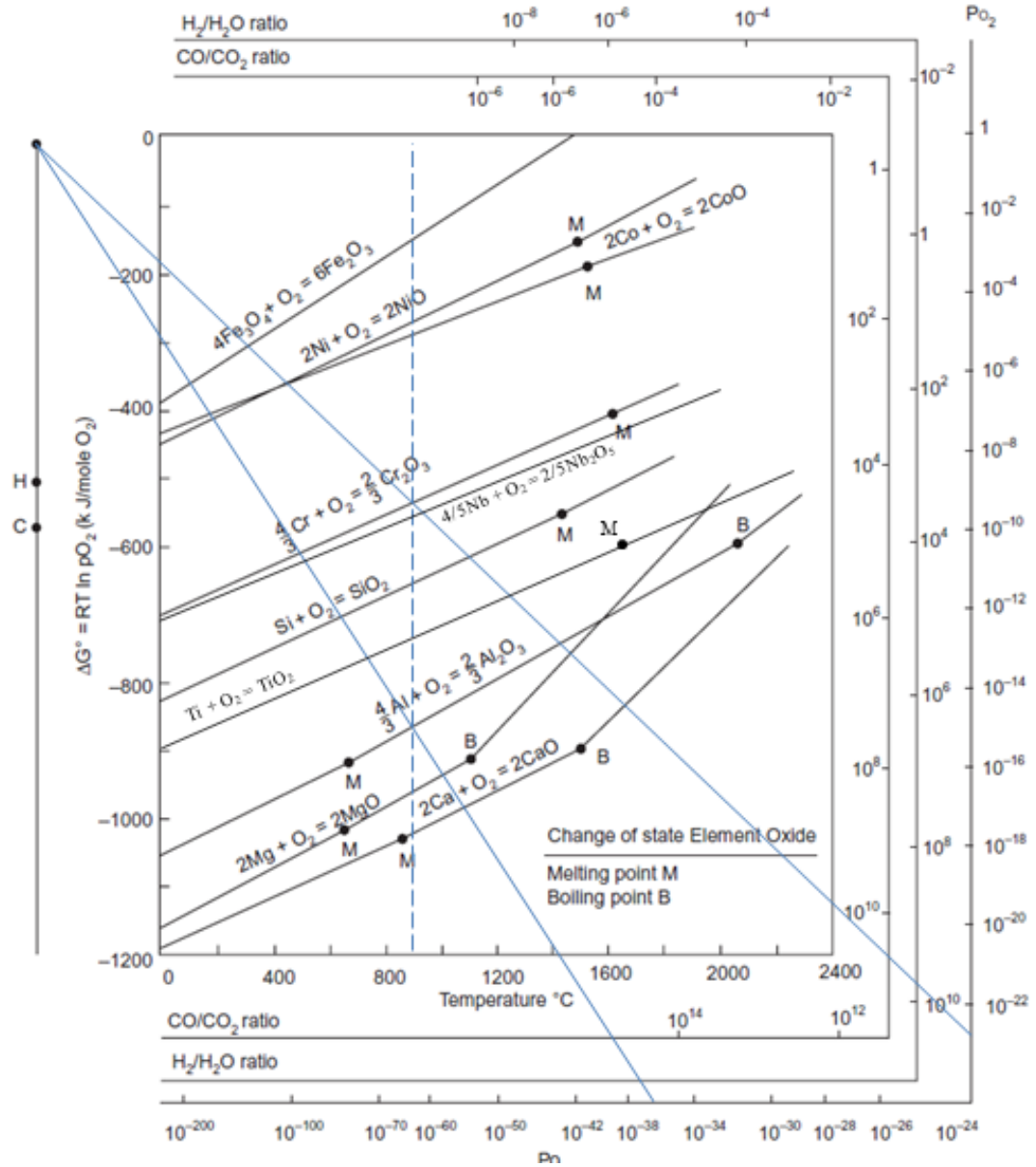

Figure 2.7: Ellingham/Richardson diagram for selected oxides (pO_2 is in atm.) adapted from [129]

2.5.2 Oxidation kinetics

Growth of the scale occurs mainly during the 'steady-state' stage of the high temperature oxidation process, and arises from solid-state diffusion of the reacting species through the scale. In most alloys the parabolic oxidation rate constant k_w, or

k_p, is much slower than the effective rate of diffusion (D_{eff}) of the scaling element in the alloy i.e. $k_w << D_{eff}$, or $k_p << D_{eff}$ where k_w is the oxidation rate constant determined from mass gain ($g^2cm^{-4}s^{-1}$), k_p is the oxidation rate constant determined from scale thickness measurements (cm^2s^{-1}) and D_{eff} (cm^2s^{-1}) is the effective diffusion rate of the scale forming element in the alloy. Therefore the rate of scaling is controlled by the rate of diffusion of the reacting species through the scale, not by the rate of diffusion of the scale-forming elements in the alloy.

Lattice Diffusion

Diffusion of electrical and ionic charges in solids occurs as a result of the presence of defects, including point defects, such as vacancies and interstitial atoms, and line defects (dislocations) and planar defects, such as grain boundaries. Under equilibrium conditions metal oxides have an exact stoichiometry at specific conditions of temperature and partial pressure; however most metal oxides have non-stoichiometric compositions and this gives rise to point defects, which can also form in metal oxides containing trace levels of contaminants. In non-stoichiometric metal oxides the defect structures occur as a consequence of a deficit or excess of oxygen or metal relative to the stoichiometric composition of the oxide. Non-stoichiometry can give rise to oxides that are O deficient, which is equivalent to the presence of O vacancies, or an excess of metal as a result of the presence of interstitial metal. These are n-type semiconductors. Non-stoichiometry can also produce oxides that have a metal deficit, which can occur when O from the gas phase enters a lattice site in the oxide, creating a metal vacancy, or excess O, which occurs as a result of the presence of interstitial O in the oxide. These are p-type semi-conductors. O interstitials are rarely found, however, and so in general n-type oxides permit anion diffusion as interstitials and cation diffusion via oxygen vacancies, but p-type oxides permit only cation diffusion via metal vacancies. If the high temperature oxidation of a metal was controlled solely by lattice diffusion then the rate of oxidation should be the same as

that of self-diffusion, but in practice the rate of oxidation it is found to be several orders of magnitude greater than self-diffusion. The reason for the anomaly is that the diffusion of ions across the growing oxide scale is controlled not only by lattice diffusion, but also by short-circuit diffusion via dislocations and grain boundaries. Lattice diffusion, tends to be dominant at high temperatures, and short-circuit diffusion at low temperatures, because the activation energy for lattice diffusion is greater than that for short-circuit diffusion [133].

Wagner Theory

The rate of oxidation at high temperatures is limited by solid-state diffusion of species through the scale. The reaction rate decreases with increasing oxide thickness because of the increase in diffusion path length. Therefore, the rate of reaction is observed to decrease with increasing oxidation time. Wagner proposed his theory to explain high temperature oxidation kinetics in 1933, which has provided a framework for all subsequent work done to understand oxidation kinetics [134]. The derivation of the parabolic rate constant can be found in standard texts on the subject [121, 135].

The theory is based on the fundamental premise that lattice diffusion of the reacting atoms, ions or electrons is rate determining and that short-circuit diffusion does not contribute to the oxidation process. Lattice diffusion is assumed to occur because of point defects, and the migrating species are deemed to be lattice and electronic defects, including vacancies, interstitial ions, electrons and electron holes. In addition, it is assumed that (i) the oxide layer must be compact and perfectly adherent; (ii) thermodynamic equilibrium exists at both boundaries; (iii) the oxide is stoichiometric; (iv) thermodynamic equilibrium exists throughout; (v) oxygen is insoluble in the metal. A schematic of the process is shown in Figure 2.8.

The mechanism of oxide scale growth is strongly dependent on the structure and mobility of the lattice defects in the oxide. For instance, the transport of oxygen

through the oxide scale can be regarded as a flux of oxygen interstitials from the gas/oxide toward the oxide/metal interface as well as a flux of oxygen vacancies in the opposite direction. The transport of metal occurs as an outward flux of metal interstitials or as an inward flux of metal vacancies. If oxygen ions are the mobile species, they diffuse through the oxide scale to form the new oxide at the oxide/metal interface. In the case of metal ions diffusing outwards the oxide formation occurs at the oxide/gas interface.

Oxidation under diffusion control follows on from the establishment of a continuous layer of scale, and under these conditions the growth rate of the scale is found to decrease as the scale thickness increases. This gives rise to a parabolic relationship, which can be expressed in terms of mass gain arising from the uptake of oxygen, using Equation 1, or scale thickness, using Equation 2.

$$\left(\frac{m}{a}\right)^2 = k_w t \qquad \text{Equation 1}$$

Where $\frac{m}{a}$ is the mass gain per unit area (gcm^{-2}), k_w is the oxidation rate constant ($g^2cm^{-4}s^{-1}$) and t is time (s), or

$$x^2 = k_p t \qquad \text{Equation 2}$$

Where x is the scale thickness, in cm, k_p is the oxidation rate constant (cm^2s^{-1}) and t is time (s).

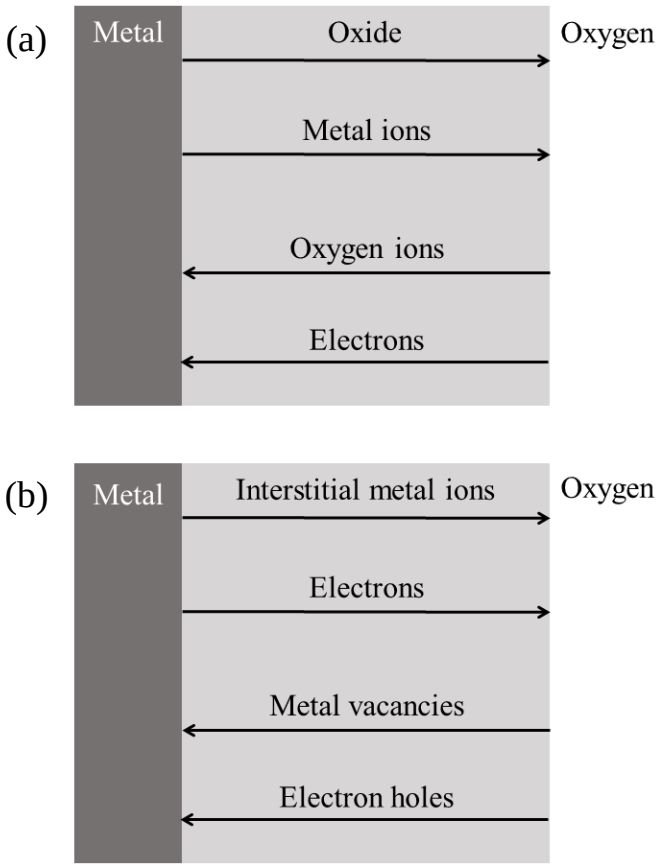

Figure 2.8: Schematic showing for Wagner theory (a) transport through a growing scale by lattice diffusion, and (b) transport through a growing scale in terms of lattice and electronic defects (adapted from [136])

Short-Circuit Diffusion

Short-circuit diffusion describes diffusion that takes place along line and surface defects in the growing oxide scale, which include grain boundaries and dislocations [137]. It tends to dominate at low temperatures, typically <1000°C, because of the difference in activation energy of the two diffusion mechanisms, and because at low temperatures the grain size of oxide scales tend to be smaller than those which form at high temperatures. In metals short-circuit diffusion is ~10^4-10^6 times greater than lattice diffusion, but it has an activation energy of ~0.5-0.7x that of lattice diffusion [133]. Effective diffusion in a polycrystalline material combines lattice diffusion and short-circuit diffusion [138]. This can be written:

$$D_{eff} = D_L + \frac{2\delta D_{gb}}{g}$$ Equation 3

Where D_{eff} is the effective diffusion in the oxide scale, D_L is the lattice diffusion component, δ is the grain boundary width, D_{gb} is the grain boundary diffusion component and g is the grain size of the oxide scale

Equation 3 clearly shows that the effective diffusion in the oxide scale, D_{eff} , is, assuming that lattice diffusion, grain boundary diffusion and the grain boundary width remain constant, inversely proportional to the grain size of the scale. However, at temperatures >1000°C the contribution made by grain boundary diffusion to the overall diffusion rate in the scale can be small, even though $D_{gb} > D_L$.

2.5.3 Effect of Cr content, cold work and grain size on oxidation

Effect of Cr content in a Ni-base alloy

In the case of dilute alloys, which typically contain <10 Wt. % Cr, a scale consisting of an outer layer of NiO and an inner porous layer of Cr_2O_3 is usually formed. Cr is selectively oxidised during the oxidation of Ni-Cr alloys that contain 15-20 Wt. % Cr, which results in the formation of a continuous layer of Cr_2O_3. The establishment of a protective Cr_2O_3 layer is therefore dependent upon the Cr content of the alloy, and the rate of diffusion of Cr in the alloy. Once a protective scale is established the alloy oxidises as a result of solid-state diffusion processes. An oxidation rate minimum occurs at a concentration of ~20 Wt. % Cr, Figure 2.9. The increase in oxidation rate at a low Cr content is due to doping by Cr of the Ni oxide scale that forms on the very dilute alloy; the increase in oxidation rate at Cr concentrations >20 Wt. % may be due, at least in part, to the outward diffusion of Cr interstitials, which is expected to increase with increasing Cr activity at the scale/alloy interface. It may

also be related to the effect of doping of the scale by Ni. Additions of Mn to Cr forming alloys can result in the formation of $MnCr_2O_4$-type spinel.

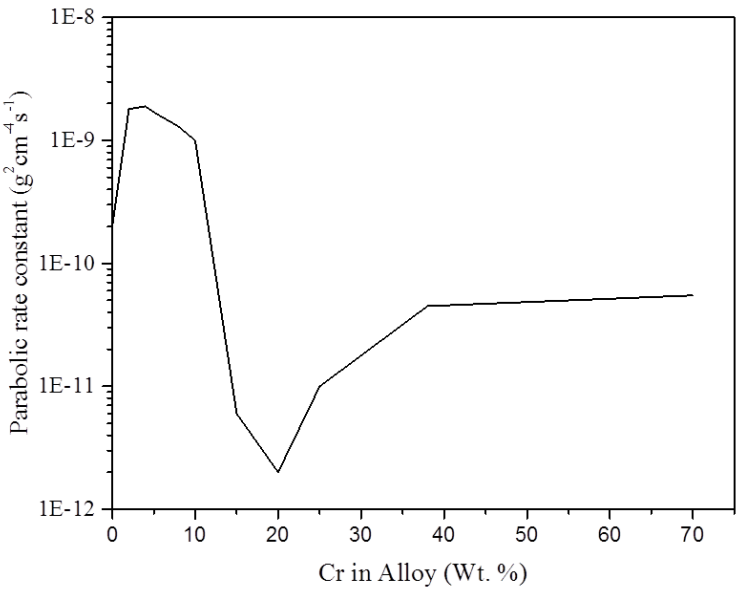

Figure 2.9: Variation of parabolic oxidation rate constant of Ni-Cr alloys oxidised at 1000°C in 1 atm. oxygen (adapted from [139])

Effect of cold work and grain size on oxidation

Transient oxidation occurs when O is adsorbed onto the surface of the alloy where it reacts to form an oxide scale that contains every active component of the alloy surface [121]. If grain boundary diffusion is rapid enough Cr can establish a continuous Cr_2O_3 scale over the grain boundaries, preventing the growth of NiO. At the same time, over the grain interiors, a Cr_2O_3 scale cannot be established quickly enough because of slower lattice diffusion, and NiO growth dominates because Ni has faster oxidation kinetics. Eventually lateral growth of Cr_2O_3 from the grain boundaries results in full coverage of the surface by Cr_2O_3, which prevents the growth of NiO. Some of the NiO reacts with Cr_2O_3 to form $NiCr_2O_4$, and together with the unreacted NiO, this is pushed up toward the surface of the scale [140]. In nickel-base superalloys the mechanism is the same, though it is complicated by the presence of additional elements [141]. The nature of the transient oxidation can vary

with alloy composition and microstructure [140, 142]. Cold work damage and fine grain sizes improve selective oxidation, so that transient oxidation, as described above, can largely be suppressed and a continuous layer of slow-growing, protective Cr_2O_3 scale established on the surface of the alloy during the early stages of oxidation [143-145]. In the case of cold work damage, the effect is due to recovery and recrystallisation, which leads to the formation of small alloy grains at the surface of the alloy and an increase in the rate of diffusion of Cr into the scale. Rapid establishment of a protective chromia layer can lead to a reduction in the overall oxidation rate of the alloy [127] and increase the lifetime of an alloy [138]. However, in the case of metals and dilute alloys, cold working can actually increase the oxidation rate by promoting the formation of non-protective oxides [139, 146].

During the oxidation of an alloy the solute concentration at the scale/alloy interface initially changes with time. In the case of thick samples, which can be considered as having a semi-infinite geometry, an equilibrium concentration is attained at the scale/alloy interface, which is a function of the rate of incorporation of the solute into the scale and the rate of arrival of the solute at the scale/alloy interface [147, 148]. Assuming parabolic growth of the scale with time t, and no recession of the interface during oxidation, the concentration of the solute C at a given distance x from the scale/interface is given by:

$$\frac{C - C_i}{C_B - C_i} = erf\left(\frac{x}{2D_t^{1/2}}\right) \qquad \text{Equation 4}$$

Where C_B is the initial bulk concentration (Wt. %), C_i is the interfacial concentration (Wt. %), C is the Cr concentration (Wt. %) at distance x (m) from the scale/alloy interface, and D is the interdiffusion coefficient (m^2s^{-1})

This model can be used to determine Cr interdiffusion coefficients, using SEM/EDS or EPMA profiles of sectioned alloy couples [149, 150], or oxidised alloys [151]. Examples of Cr interdiffusion coefficients are provided in Table 2.6.

Table 2.6: Chromium interdiffusion coefficients (D) estimated from fitting of Cr depth profiles

Alloy	Chromium interdiffusion coefficients (m^2s^{-1})			
	Dayananda [149]	Campbell [150]	Chyrkin [151]	
Alloy 718	1.2-1.7E-14 (1100°C)	1.58E-14 (1150°C)	-	-
Alloy 625	-	-	7.29E-16 (1000°C)	2.5E-16 (900°C)

2.5.4 The reactive element effect

In 1937 Griffiths and Pfeil obtained a patent in which it is claimed that the lifetime of heat-resistant alloys can be improved by the addition of small amounts of reactive elements, including Y and Sc, to alloy melts. The mechanism for the improvement in alloy lifetime was not understood at the time, and it was speculated in the patent that it could be due to de-oxidation, de-sulphurisation, the production of compounds by reaction of the alloy with the reactive elements, or by changes to the properties of the scale [152]. A second patent, obtained in 1945 by Pfeil, extends the original patent to include gas-permeable reactive element coatings, and attributes the improvement in oxidation behaviour to changes in the microstructure of the oxide scale [153]. This behaviour, which is known as the rare earth effect, or reactive element effect, has been extensively studied in the years since it was first patented. This has led to a vast number of research papers being published, but despite all of the effort, the mechanisms underpinning the reactive element effect are still not fully understood. However, it is now universally accepted that reactive element additions improve

scale adhesion and reduce the rate of oxidation. Improved scale adhesion has, at various times, been attributed to increased scale plasticity [154], the formation of oxide pegs at the scale/alloy interface [155], changes in growth stress [156], the formation of a graded seal by a layer of reactive element at the scale/alloy interface [157], vacancy sinks [158] and sulphur-gettering [28]. The reduction in oxidation kinetics has been attributed to a switch from anion to cation dominated scale growth, which has been attributed to the blocking of anion diffusion by reactive elements segregated to oxide grain boundaries [159], the poisoned interface model [160], which proposes that anions are blocked at the scale/alloy interface, and in ODS alloys, the promotion of selective oxidation [161].

The latest thinking is that sulphur-gettering is most probably responsible for the improvement in scale adhesion, and that reduced oxidation kinetics is the result of the blocking of anion diffusion as a result of grain boundary segregation. The most complete explanation for the reactive element effect is probably the dynamic segregation theory, which was proposed by Pint [23]. Comprehensive reviews of the subject were written by Whittle and Stringer in 1980 [22], and by Pint in 2003 [162]. The subject of the reactive element effect in alumina formers has recently been reviewed by Naumenko, Pint and Quadakkers [163].

Sulphur-gettering

Ikeda et al identified that sulphur promoted the spalling of Al_2O_3 scale from alloys, but that this could be suppressed by the addition of reactive elements, either by direct addition or by the formation of Y_2O_3 dispersions in the alloy. It was proposed that the mechanism involved trapping of S as sulphide, which otherwise weakens the scale/alloy interface [28]. These findings were confirmed by other workers, including Smeggil et al, and Lees, and have also been shown to be operative in Cr_2O_3-forming alloys [164-166]. Hydrogen annealing experiments have also shown that the adhesion of oxide scales is improved by lowering the sulphur content of alloys [167, 168].

Kinetics

The reduction in the rate of oxidation of alloys that contain reactive elements is now considered most likely to be mainly due to a switch from a scale growth mechanism dominated by cation diffusion, to a scale growth mechanism dominated by anion diffusion [23, 163]. It is believed that reactive elements diffuse into the scale, where they segregate to the grain boundaries and block the outward diffusion of cations, but allow the inward diffusion of anions. The presence of reactive elements on the grain boundaries of oxide scales has been widely reported [169-171].

Over-doping

It is reported that alloys containing too high a concentration of reactive element exhibit poor oxidation behaviour [172]. The effect has mainly been reported in alumina formers, but chromia-formers are also affected. Klower observed that doping with up to 0.18 Wt. % mischmetal increased the rate of oxidation of Fe-Al10-Cr2 and Fe-Al15Cr2 alloys by more than an order of magnitude, causing spalling of the scale and extensive internal oxidation of Al, Figure 2.10. It was also observed that the deleterious effects increased with increasing Al content [173]. In a second paper, Klower reported that over-doping leads to high oxidation rates and severe alumina internal oxidation, and concluded that the propensity for over-doping is related to the composition of the reactive element, its concentration and the concentration of aluminium [174]. Pint reported that 0.2 Wt. % additions of Yb, Ce, Hf and Sc caused overdoping in FeCrAl, and stated that La and Zr are also prone to producing over-doped alloys [175, 176]. Chevalier et al, in a study of the oxidation behaviour of Nd_2O_3-coated and Sm_2O_3-coated stainless steel, found that over-doping produced severe internal oxidation [177], and in a review paper speculated that over-doping was probably attributable to an increase in the oxygen diffusion rate as a consequence of oxygen vacancies in reactive element oxides [178]. Pint observed that over-doped ODS β-NiAl alloy oxidised more quickly, and formed a more convoluted scale than the base alloy. This scale morphology was thought to be the

result of a synergistic effect between an excess of reactive element and the dispersoids, and resulted in interfacial void formation. A 1.0 Wt. % addition of La_2O_3 to the alloy produced very large weight losses due to spalling [179].

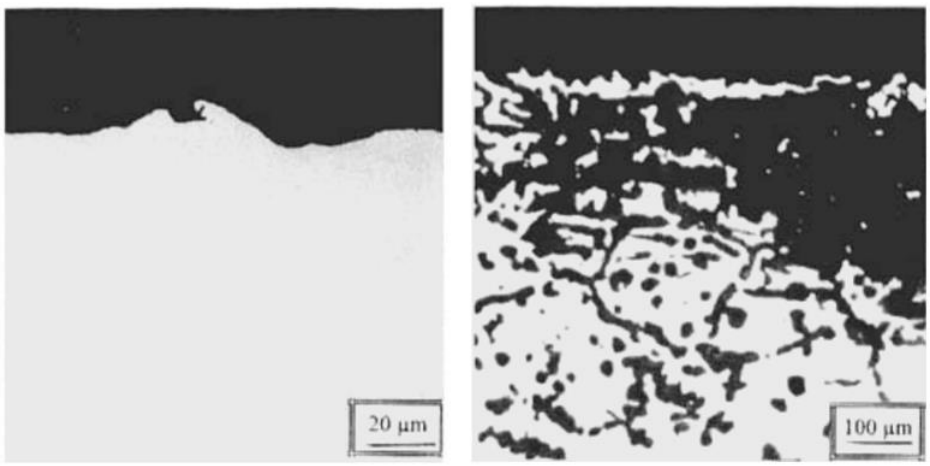

Figure 2.10: Fe-Al-Cr alloys following 1008 hours of cyclic oxidation in air at 1100°C (a) Fe-Al10-Cr2, and (b) Fe-Al15-Cr2+0.18 Wt. % mischmetal [173]

2.5.5 Oxidation of base alloys at 900°C

Alloy 718

It is reported that the wrought alloy forms a Cr-rich scale during high temperature oxidation [180, 181]. Dissolution of δ-phase occurs in the oxidation affected zone of the alloy, which reforms as a discrete layer at the scale/alloy interface. It was suggested by Delaunay et al that this may contribute to the oxidation resistance of the alloy [181]. Alumina forms as internal oxide at the grain boundaries of the alloy, as a result of the inward diffusion of oxygen [145].

Jia and Gu reported that the oxidation SLM-consolidated Alloy 718 was similar to that of the wrought alloy in terms of scale composition, morphology and internal oxidation [15]. In a second paper the same authors propose that scale formed initially over the grain boundaries of the alloy as a result of fast grain boundary transport

[16]. The authors report that spallation was a problem for alloys consolidated at a laser energy input of 70Jmm^{-3}, but that good oxidation behaviour was observed at laser energy input values of 110 and 130Jmm^{-3}.

Isothermal oxidation rate constants have been determined for wrought Alloy 718 and SLM-consolidated Alloy 718 oxidised in air at 900°C [180-182]. These are presented in Table 2.7 with the experimental conditions used to obtain them. The results indicate that the oxidation rate constant of wrought Alloy 718 is ~5.0E-12–1.0E-13 $g^2cm^{-4}s^{-1}$, whereas the oxidation rate constant obtained by Jia and Gu for SLM-consolidated Alloy 718 is 2.1E-11 $g^2cm^{-4}s^{-1}$ – 4.45E-12 $g^2cm^{-4}s^{-1}$. However, Jia and Gu reported spalling problems with their specimens, oxidised using an interrupted method, which means that oxidation of alloy exposed by spalling may have occurred during their experiments, resulting in high oxidation rates.

Table 2.7: Parabolic oxidation rate constants determined for Alloy 718 in air at 900°C ($g^2cm^{-4}s^{-1}$) or (cm^2s^{-1})

	England and Virkar [180]	Greene and Finfrock [182]	Delaunay [181]	Jia and Gu [15]
Temperature (°C)	900	900	900	900
Environment	Air	Air	Air	Air
Oxidation time (hours)	<10000	1000	<48	100 hours
Data collection	Interrupted	Discontinuous	Discontinuous	Interrupted
Specimen size	113µm thick foil	3mm diameter rods	30x20x1mm	2x2mm
Surface finish	Undisclosed	Undisclosed	1µm	1000 grit finish
Grain size	Undisclosed	Undisclosed	Undisclosed	Undisclosed
Oxidation rate constant ($g^2cm^{-4}s^{-1}$)	1.06E-13	2.67E-12 - 6.29E-12	1.50E-13 cm^2s^{-1}	2.1E-11 - 4.4E-12

Alloy 625

The oxidation behaviour of Alloy 625 is essentially the same as that of Alloy 718, as discussed in section 2.7.1. The alloy is a chromia-former [180, 183, 184], but $Mn_xCr_{3-x}O_4$ spinel is sometimes identified in the scale formed on alloy that contains an appreciable Mn content [180, 183]. Dissolution of the δ-phase occurs in the alloy immediately below the scale, which reforms as a discrete layer at the scale/alloy interface [105, 183]. This remains unoxidised because the dissociation pressure of NbO is higher than that of Cr_2O_3 in equilibrium with the δ-phase [105]. Particles of δ-phase may be locally incorporated into the scale [105]. Internal oxides form at the grain boundaries of the alloy, as a result of the inward diffusion of oxygen. These have been identified as alumina [105].

Several workers have reported isothermal oxidation rate constant values for wrought Alloy 625 oxidised in air at 900°C. These are produced in Table 2.8, along with the experimental conditions used [180, 184-186]. The results are in good agreement, despite the differences in experimental procedure, with the exception being the value reported by Buscail, which is ~5-10x slower than the others. England noted that significant spalling of the scale formed on Alloy 625 occurred at oxidation times >1200 hours at 800°C [180]. Taken as whole, the results of the experiments indicate that the oxidation rate constant of wrought Alloy 625, oxidised in air at 900°C, is ~1-2E-13 $g^2cm^{-4}s^{-1}$.

Alloy 625, consolidated by laser metal deposition (LMD), was oxidised in air at 800°C by Hong et al [17]. The alloy formed a chromia scale and a parabolic oxidation rate constant of 5.55E-11 $g^2cm^{-4}s^{-1}$ was obtained for the alloy in an experiment lasting 100 hours, which, not accounting for the temperature difference, is ~20-40x faster than that reported by most workers. The TGA data presented by the authors shows that rapid oxidation took place within the first 10 hours of the experiment, giving the plot of unit mass gain ($mgcm^{-2}$) against time (h) a non-parabolic appearance.

Table 2.8: Parabolic oxidation rate constants determined for Alloy 625 in air at 900°C ($g^2cm^{-4}s^{-1}$)

	England [180]	Chyrkin [186]	Kumar [185]	Buscail [184]
Temperature (°C)	900	900	900	900
Environment	Air	Air	Air	Dry Air
Oxidation time (hours)	<'Several thousand'	1000	2.5	48 + 15 mins ramping time in Ar
Data collection	Discontinuous	Discontinuous	Continuous	Continuous
Specimen size	113µm thick foil	20x10mm 0.3-1.0mm	10x10x1mm	$5cm^2$ area 1.6mm thick
Surface finish	Undisclosed	1200 grit	Electropolished	800 grit
Grain size	Undisclosed	Undisclosed	Undisclosed	Undisclosed
Oxidation rate constant ($g^2cm^{-4}s^{-1}$)	1.54E-12	2.5E-12	3.9E-12 (estimated from Arrhenius relationship)	3.2E-13

Effect of Reactive Element Additions on the High Temperature Oxidation Behaviour of Alloy 625

Several papers have been published showing that the oxidation behaviour of Alloy 625 can be improved by applying a thin coating of CeO_2 or Y_2O_3 to the alloy prior to oxidation. This improvement in oxidation behaviour is attributed to the reactive element effect [187, 188].

A Ni ODS alloy, having a base composition similar to that of Alloy 625, has also been studied [189]. The alloy, whose exact composition was Ni-20Cr-20Fe-5Nb-$1Y_2O_3$, was made by mechanically alloying Y with elemental powders and oxidised in air at 1000°C following consolidation by SPS. The new ODS alloy was found to oxidise more slowly than the alloy on which it was based, and more slowly than

Alloy 718 and the legacy Ni ODS superalloy PM1000, Figure 2.11. The authors did not calculate oxidation rate constants from their results, but from their data, which are presented in Figure 2.11, oxidation rate constant values of 2.0E-13 $g^2cm^{-4}s^{-1}$, 6.27E-12 $g^2cm^{-4}s^{-1}$ and 1.60E-12$g^2cm^{-4}s^{-1}$ are estimated for as-consolidated Ni-20Cr-20Fe-5Nb-1Y_2O_3, as-consolidated Ni-20Cr-20Fe-5Nb and PM1000 respectively. This shows that the oxidation rate of the new ODS alloy was ~30x slower than the alloy on which it was based, which illustrates the benefits of reactive element additions. It is interesting that the oxidation rate of the new ODS alloy was also ~8x slower than that of the legacy ODS alloy, which contains ~0.5 Wt. % Y_2O_3. It may have been expected that a 1.0 Wt. % addition of Y_2O_3 to the alloy would have caused it to be overdoped, as discussed in section 2.6.2, resulting in fast oxidation kinetics, but this was clearly not the case and indicates that the base alloy may be tolerant of reactive element additions.

Several papers comment on the effect of reactive element additions made to Nb-containing steels; these include a report that Ce and Nb additions act synergistically to improve the oxidation behaviour of TIG welded 316L stainless steel oxidised in air for 240 hours at 700°C [190], and that scale adhesion improves following Y additions to 20Cr25Ni0.7Nb austenitic stainless steel [191].

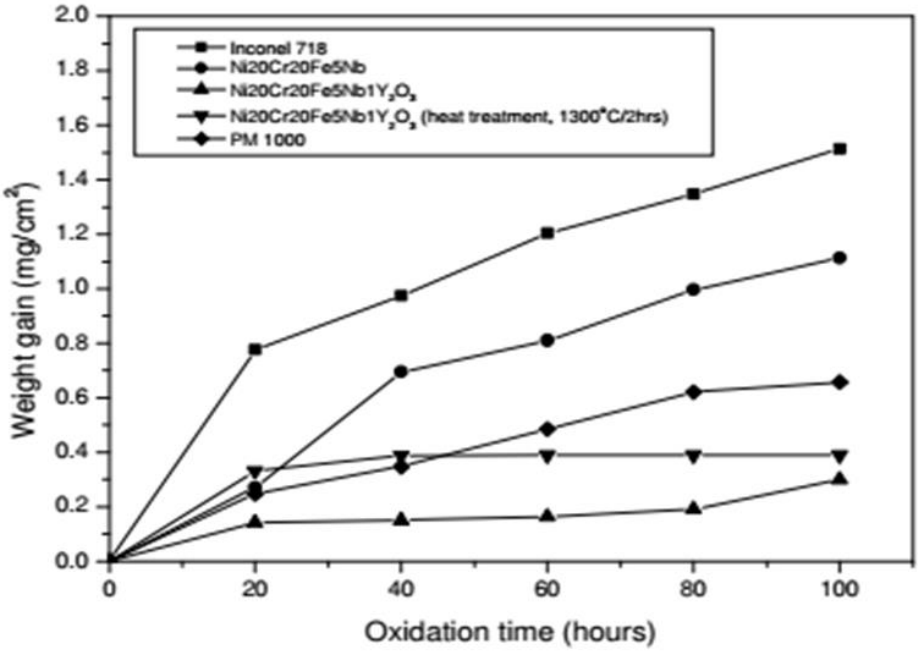

Figure 2.11: Graph of mass gain/surface ($mgcm^{-2}$) area against oxidation time (hours) for oxidation of Ni-20Cr-20Fe-5Nb-1Y_2O_3 ODS alloy and comparators at 1000°C [189]

Haynes 230

Haynes 230 forms a duplex scale comprising chromia at the scale/alloy interface, and manganese chromate spinel at the scale/gas interface [116, 180, 192-198]. It is claimed that the manganese chromate spinel is protective during oxidation of the alloy [111], and limits Cr losses due to volatilisation [199]. However, at 900°C, Mn increased the oxidation rate of dilute and highly alloyed steels [200]. Haynes 230 contains ~0.02 Wt. % La, which improves the scale adhesion and oxidation resistance during cyclic oxidation testing [95].

Presented in Table 2.9, with the experimental conditions, are isothermal oxidation rate constant values determined by several groups for Haynes 230. England and Virkar oxidised thin foils of Haynes 230 in air at a range of temperatures between 800-1100°C and obtained a single parabolic oxidation rate constant for each

temperature [180]. Cr_2O_3 and $Mn_xCr_{3-x}O_4$ were detected by XRD in the scale formed on the oxidised coupons. It was observed that oxidation was controlled by diffusion through the scale rather than in the alloy, and that the slower oxidisation rate of Haynes 230, compared to Alloy 718 and Alloy 625, may be due to the formation of a mixed $Cr_2O_3/Mn_xCr_{3-x}O_4$ scale on Haynes 230.

Kim et al found that the alloy oxidised parabolically at all oxidation times up to 1000 hours, but that it oxidised more slowly at oxidation times >200 hours [194]. The high initial oxidation rate was attributed to rapid formation of $MnCr_2O_4$ in the scale during the early stages of oxidation, which slowed at longer oxidation times because of exhaustion of Mn in the alloy, leaving the scale to grow more slowly by the growth of Cr_2O_3. The results reported by Kim et al were later reported, with some new results, in a paper written by Jang et al [195]. In this paper the oxidation rate of Haynes 230 in air is reported to slow after 160 hours of oxidation and is attributed to the late formation of a protective layer of $MnCr_2O_4$ at the scale to gas interface, rather than because of exhaustion of the Mn reservoir. The authors also report that the alloy oxidised more slowly, with a single parabolic function, in impure He than in air. This was attributed to the rapid formation of a protective layer of $MnCr_2O_4$ at the scale to gas interface. However, a pro rata oxidation rate constant of 9.6E-14 $g^2cm^{-4}s^{-1}$ is calculated from the two oxidation rate constants provided by the authors for 1000 hours of oxidation in air, which is comparable, or slower, than that presented by the authors for 1000 hours of oxidation in the impure He atmosphere. This would suggest that the $MnCr_2O_4$ spinel layer that forms on the alloy in air at oxidation times >160 hours is more protective than that which forms rapidly in an impure He atmosphere.

Jian et al oxidised Haynes 230 in air at temperatures between 650°C and 850°C, for oxidation times of up to 500 hours [196]. The authors found that the alloy oxidised more quickly at oxidation times >200 hours, which was attributed to enhanced manganese chromate growth as a result of fast diffusion of Mn through the chromia scale at extended oxidation times. This finding is in direct contradiction of the results

presented by Kim et al, and Jang et al [194, 195], albeit with the caveat that the oxidation temperature was a little lower. The oxidation rate constant values determined by Olivares [197] and Tung [198] were obtained from short duration experiments with continuous data collection. Significant oxidation of the specimens may have occurred during ramping to the required temperature prior to the start of the experiments, which means that these data may have been expected to yield low oxidation rate constant values. The oxidation rate constant value provided by Olivares was in fact the largest of those shown in Table 2.9, with that provided by Tung being among the largest.

The overall impression gained from the assessment of Haynes 230 oxidation rate constant values available in the open literature is of a confused situation, with groups reporting contradictory results and interpretations. The role of spinel appears uncertain. $Mn_xCr_{3-x}O_4$ spinel is known to reduce volatilisation of Cr at high temperatures [201-203], thus reducing the oxidation rate, but this would only apply at temperatures above which the vaporisation of the chromia scale is significant. Cr losses due to vaporisation are reported to occur in Haynes 230 at 1100°C [204]. However, Young has stated that chromium losses can be significant at >900°C at an oxygen partial pressure of 1 atm. [120]. Mn can have an adverse effect on Cr formers at 900°C because it is more thermodynamically stable and has a higher diffusivity in Cr_2O_3 [205]. Marasco and Young showed that the rate of oxidation of austenitic stainless steel was increased by the addition of 2 Wt. % Mn, which resulted in initial slow growth of Cr_2O_3 followed by faster growth of $MnCr_2O_4$ at the scale/gas interface at longer oxidation times [200]. The role played by Mn is not defined in the Haynes 230 patent [206], but in a prior art patent it is stated that Mn is added to a Ni base alloy in order to improve its oxidation resistance by forming a spinel layer [207]. It is further stated that the Mn addition should be <1.5 Wt. % because larger additions impede the high temperature workability of the alloy. It is claimed in the Haynes 230 patent that the superior high temperature oxidation behaviour and strength of the alloy is due to an unknown mechanism achieved by the control of the elements Cr, Mo and W to produce a microstructure combining optimal proportions

of carbide formers and Cr, Mo and W in solid solution. This is stated to be achieved when the ratio $\frac{Cr}{Mo+0.5W}$ is in the range 2.05-2.65, preferably 2.2-2.6, where Cr, Mo and W are the element concentrations in Wt. %.

The Haynes 230 patent does not discuss the role of La, nor does any of the research papers studied for the literature review. This may be understandable in a patent, but it is surely a significant omission from research papers given the importance of the reactive element effect. However, the patent for Haynes 230 does state that La should be in present in the alloy between 'trace' level and 0.05 Wt. %, with the preferred range 0.005-0.05 Wt. %. A typical La concentration in the alloy is stated to be 0.02 Wt. %. The patent also states that Al may be present in the alloy, at a concentration <0.50 Wt. %, in order to 'control' the La. Careful melting procedures are recommended for the alloy, which may imply problems with La retention. The examination of a second prior art patent [208] shows that La additions give rise to a dramatic improvement in the oxidation resistance of a Co-base alloy in static and dynamic tests when used in the concentration range <0.005-0.01 Wt. %, but only in the presence of Al, which must be in the range 0.02-0.5 Wt. %. The cause of the improvement in oxidation behaviour arising from the synergistic effect of La and Al additions is not discussed in the patent. La concentrations in the range <0.005-0.01 Wt. % gave the same results in the oxidation tests. The patent further shows that, at concentrations >0.018%, La causes a dramatic increase in cracking of the alloy. The fact that the upper limit for La is ~0.05 Wt. % in Haynes 230, as opposed to 0.018 Wt. % for the Co-base alloy, suggests that cracking arising from La additions may be less of a problem in Ni-base alloys.

Table 2.9: Parabolic oxidation rate constants determined for Haynes 230 in air at 850°C and 900°C ($g^2cm^{-4}s^{-1}$)

	England [180]	Kim [194]	Jian [196]	Olivares [197]	Tung [198]
Temperature (°C)	900	900	850	900	900
Environment	Air	Air	Air	Dry Air	Air
Oxidation time (hours)	<10000	1000	<500	10 (+3 hours ramping)	6
Data collection	Interrupted	Discontinuous	Discontinuous	Continuous	Continuous
Specimen size	113µm thick foil	1mm thick	25x25x1mm	5mmx2.25mm diameter cylinder	10x15x1mm
Surface finish	Undisclosed	Undisclosed	Undisclosed	Undisclosed	600 grit
Grain size	Undisclosed	Undisclosed	Undisclosed	Undisclosed	Undisclosed
Oxidation rate constant ($g^2cm^{-4}s^{-1}$)	1.06E-13	3.83E-13 (<200 hours) 0.43E-13 (>200 hours)	0.67E-13 (<200 hours) 1.89E-13 (>200 hours)	5.56E-13	3.84E-13 (<0.3 hours) 1.67E-13 (>0.3 hours)
Pro rata oxidation rate constant ($g^2cm^{-4}s^{-1}$)	1.06E-13	1.10E-13	1.51E-13	5.56E-13	1.67E-13

Effect of Reactive Element Additions on the High Temperature Oxidation Behaviour of Haynes 230

There are no reports in the open literature of an ODS variant of Haynes 230, and only one report could be found dealing with the effect of reactive element additions on Haynes 230. In this work a thin CeO_2 coating improved the spalling resistance of Haynes 230 when subjected to discontinuous testing at 800°C in air+3%H_2O [187].

2.6 Summary of literature review

The literature review has shown that SLM-consolidated alloys have a dendritic/cellular microstructure, with large columnar grains orientated in the build direction of the alloy. SPS-consolidated alloys usually have fine grain microstructures as a result of relatively fast cooling, and often bimodal grain structures as a result of pinning of the alloy grains by dispersoids. Fast cooling during SLM-consolidation limits segregation and the formation of carbide inclusions.

The literature review has shown that the base alloys oxidise in the order Alloy 718>Alloy 625>Haynes 230. The superior oxidation resistance of Haynes 230 may be due to the addition of La, which reduces the rate of oxidation as a result of the reactive element effect, though this is not discussed in the literature. A layer of $Mn_xCr_{3-x}O_4$ spinel forms on the alloy at the scale/gas interface, which, at higher temperatures, is reported to reduce Cr losses arising from volatilisation of the oxide. It is claimed in the Haynes 230 patent that the superior properties of the alloy, including its oxidation resistance, are due to the $\frac{Cr}{Mo+0.5W}$ ratio, but the mechanism is unknown. Alloy 718 and Alloy 625 have similar compositions, and oxidise to form a chromia scale with a layer of δ-phase at the scale/alloy interface. It is not clear why Alloy 718 oxidises faster than Alloy 625, but this does not appear to have been studied. Significant variations are observed in the results obtained from experiments to determine the oxidation kinetics of alloys, which are probably attributable to differences in methodology. A whole number of variables, including, but not restricted to, surface finish, grain size, sample size, shape, continuous/discontinuous measuring etc., contribute to the differences in measured oxidation rates, and make comparisons difficult. Small grain alloys and cold-worked alloys exhibit better selective oxidation as a consequence of faster transport of Cr to the surface of the alloy via the grain boundaries. Alloys that contain reactive elements, including ODS alloys, oxidise more slowly than alloys that do not contain

reactive elements and exhibit improved scale adhesion. This is known as the reactive element effect. The mechanisms by which the reactive element effect occurs are not clear, but they appear to be related to a change in the scale growth mechanism, possibly arising from the segregation of reactive elements to the grain boundaries of the scale, and the gettering of sulphur, that would otherwise interfere with the adhesion of the scale/alloy interface. It is therefore expected that the ODS variants of the alloys will oxidise more slowly than the base alloys.

The effect of SLM-consolidation on the oxidation behaviour of Ni-base superalloys is largely unknown, with only a few papers published on the subject in the open literature. The authors of these papers claim that the oxidation resistance of SLM-consolidated alloys is as good as that of the same alloys made conventionally.

CHAPTER 3

EXPERIMENTAL

3.1 Introduction

The materials, analytical techniques and specimen preparation methods used in the present study are described in sections 3.2, 3.3 and 3.4 respectively.

3.2 Materials

Alloy 718, Alloy 625 and Haynes 230 were studied in SLM-consolidated and wrought forms. Alloy 625 ODS and Haynes 230 ODS were studied following consolidation by SLM and by SPS. The compositions of the gas atomised powders, from which the base alloys were consolidated by SLM, the mechanically alloyed powders, from which the ODS alloys were consolidated by SLM and SPS, and the wrought alloys, are shown in Table 3.1 (analyses provided by suppliers). The gas atomised powders were obtained from LPW Technology Ltd (Runcorn, UK). The mechanically alloyed powders were provided by MBN Nanomaterialia S.P.A (Vascon di Carbonera (TV), Italy). The powders were produced by milling nano-yttria into the same gas atomised powders of Alloy 625 and Haynes 230 used to consolidate the base alloy blocks by SLM. The details of the milling process are proprietary.

Table 3.1: Composition of powders and alloys studied for present work (Wt. %)

	Gas atomised powder			Mechanically alloyed powder		Wrought alloy		
Element	Alloy 718	Alloy 625	Haynes 230	Alloy 625	Haynes 230	Alloy 718	Alloy 625	Haynes 230
Ni	52.4	Bal.	Bal.	Bal.	Bal.	53.79	60.08	Bal.
Fe	Bal.	3.60	1.53	3.42	1.45	17.95	4.68	1.53
Cr	19.00	20.83	21.88	19.79	20.79	18.05	22.02	22.12
Nb(Ta)	4.98	3.64	-	3.46	-	5.24	3.44	-
Mo	3.06	9.10	1.92	8.65	1.82	2.90	8.84	1.20
Ti	0.86	0.02	<0.01	0.02	<0.01	1.00	0.20	<0.01
Al	0.52	0.04	0.39	0.04	0.37	0.48	0.19	0.26
S	0.05	0.006	0.001	0.006	0.001	0.0004	0.001	<0.002
C	0.05	0.02	0.10	0.02	0.10	0.026	0.035	0.11
Si	0.05	0.10	0.48	0.10	0.46	0.07	0.201	0.40
Co	0.03	<0.01	0.13	<0.01	0.12	0.23	0.04	0.18
Cu	0.03	0.08	<0.1	0.08	<0.10	0.05	0.08	0.07
O	0.011	0.0132	-	0.0132	-	<0.0005	0.0132	-
P	0.01	<0.001	0.005	<0.001	0.005	0.09	0.006	0.005
Mn	0.01	<0.01	0.68	<0.01	0.65	-	0.20	0.50
Mg	<0.01	-	-	-	-	0.001	-	-
Ca	<0.01	-	-	-	-	<0.001	-	-
N	0.0083	0.0094	-	0.0094	-	0.0053	0.0094	-
B	0.005	-	<0.001	-	<0.001	0.004	-	0.002
Se	<0.003	-	-	-	-	<0.00005	-	-
W	-	-	14.06	-	13.36	0.03	-	14.63
La	-	-	0.01	-	0.01	-	-	0.016
Y_2O_3	-	-	-	0.50	0.50	-	-	-

3.2.1 Alloys consolidated by SLM

Alloy 718, Alloy 625, Haynes 230, Alloy 625 ODS and Haynes 230 ODS were all received in the form of SLM-consolidated blocks, which were built by Inspire AG (Zürich, Switzerland) using a ConceptLaser machine type M2, with a fibre laser having a wavelength of 1071nm. Building was performed using a cross-hatching strategy, which helps to reduce anisotropy in the x and y planes of the build [65]. The build parameters, which were optimised for the attainment of maximum density, are shown in Table 3.2. The conventional alloys were received as blocks of ~10.0x10.0x10.0mm in size. The blocks were annealed prior to oxidation using the schedules shown in Table 3.3. The ODS alloys were received as blocks of

~8.0x8.0x8.0mm in size and these were oxidised as-received because of their small size.

Table 3.2: Build parameters used for the consolidation of gas atomised powders and mechanically alloyed powders by SLM

Power (W)	Scan speed (mms^{-1})	Layer thickness (µm)	Hatch distance (µm)
200	900.0	30.0	30.0

Table 3.3: Schedules used to anneal SLM-consolidated blocks of Alloy 718, Alloy 625 and Haynes 230 prior to oxidation experiments

Alloy	AMS Reference	Temperature (°C)	Time (minutes)	Quench
718	5662	954	30	Air
625	5666	1038	45	Air
Haynes 230	5891	1200	45	Water

3.2.2 Alloys consolidated by SPS

The MA powders were consolidated into blocks by Empa (Dübendorf, Switzerland) on a HP D 10 commercial instrument (FCT Systeme GmbH, Germany), in cylindrical graphite dies lined with graphite sheets. Sintering was performed at a pressure of ~50 MPa under vacuum in pulsed current mode with 12 pulses of 3 ms, followed by a waiting time of 6 ms with zero current. The schedule used to consolidate the blocks is shown in Figure 3.1. The alloys, which are denoted Alloy 625 ODS/SPS and Haynes 230 ODS/SPS, were oxidised in the as-built condition.

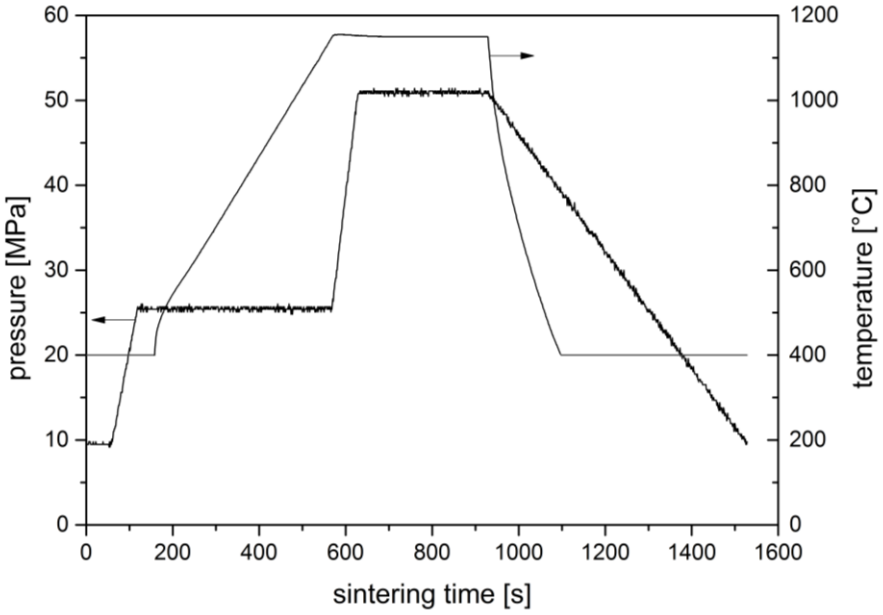

Figure 3.1: Consolidation of the mechanically alloyed powders by spark plasma sintering, showing pressure (MPa) and temperature (°C) against sintering time (s)

3.2.3 Wrought alloys

Alloy 718 and Alloy 625 were procured from a commercial supplier in the UK. Haynes 230 alloy was obtained directly from Haynes International, Inc. (Manchester, UK). The form of the alloys is shown in Table 3.4; the annealing schedules used to anneal the alloys prior to receipt are shown in Table 3.5.

Table 3.4: Wrought alloys obtained for this study

Alloy	Condition	Form	Sample dimensions in mm (length x diameter)	Grain Size (μm)
718	Annealed	Round bar	1000x16	~30
625	Annealed	Round bar	150x32	~10
Haynes 230	Annealed	Round bar	150x16	~45-65

Table 3.5: Annealing schedules for wrought alloys

Alloy	Temperature (°C)	Time (minutes)	Quench
718	980	60	Water
625	926	60	Water
Haynes 230	1230	30	Water

3.3 Analytical techniques

In this section the techniques used to study the various alloys are described. These are thermogravimetric analysis, optical microscopy, hardness measurements, SEM, XRD and STEM.

3.3.1 Thermogravimetric analysis (TGA)

TGA is used to follow the kinetics governing the high temperature oxidation of metals and alloys, preferably using continuously-recorded TGA experiments [121, 209]. This option was not available for the project, so it was decided that individual specimens should be used for each oxidation time. This methodology is used by many researchers [121]. The specimens were isothermally oxidised in laboratory air for up to 1000 hours at a temperature of 900°C, for times of 10, 25, 50, 75, 100, 215 and 1000 hours.

Calibration of 60cm long thermocouple and tube furnace

A 120cm long tube furnace (Elite Thermal Systems Ltd, UK) was selected as being suitable for the oxidation experiments, and the central region of the furnace calibrated over the temperature range 450-950°C using a 60cm long K-type thermocouple (RS Components, UK) and a digital thermometer (Comark, UK). Prior to the calibration of the tube furnace, the thermocouple was itself calibrated over the

same temperature range using a 30cm long K-type thermocouple (RS Components, UK) and a muffle furnace (Elite Thermal Systems Ltd, UK).

Calibration of 60cm long thermocouple

The results of the calibration can be seen in Figure 3.2 (a), which shows that at high temperatures (>600°C) the 60cm long thermocouple produced temperature readings higher than those of obtained from the 30cm long thermocouple and the muffle furnace. Given that the temperature readings obtained from the 30cm long thermocouple and the muffle furnace were in good agreement over the entire temperature range, it was assumed that the readings from the 60cm long thermocouple were erroneous at temperatures >600°C and that it was over-reading the temperature by ~10°C at 900°C (~1% error). The temperature stability of the thermocouples was approximately ±5°C.

Calibration of tube furnace

The results of the calibration of the tube furnace are presented in Figure 3.2 (b), in the form of a plot of the temperature of the tube furnace obtained using the 60cm thermocouple and corrected for the over-reading of the thermocouple, against the set temperature of the tube furnace. The plot shows that the tube furnace was ~18°C too hot at a furnace setting of 900°C (~2% error), and therefore it was necessary to set the tube furnace to a temperature of ~882°C to achieve the required temperature of 900±5°C. This was confirmed by taking additional readings with the tube furnace set to 882°C.

It was intended that the alloys would be oxidised within ~50mm of the centre of the tube furnace in modified alumina crucibles on an alumina boat of 100mm length. Therefore, the calibrated thermocouple was used to measure the temperature of the tube furnace, set to 882°C, at positions ~50mm either side of its centre. Both positions were found to measure 895±5°C. The work done to calibrate the tube

furnace showed that the coupons would be oxidised at a temperature that ranged between 890°C and 905°C. This represents a maximum deviation of ~1% from the target temperature of 900°C, with a temperature range of <2% of the target temperature.

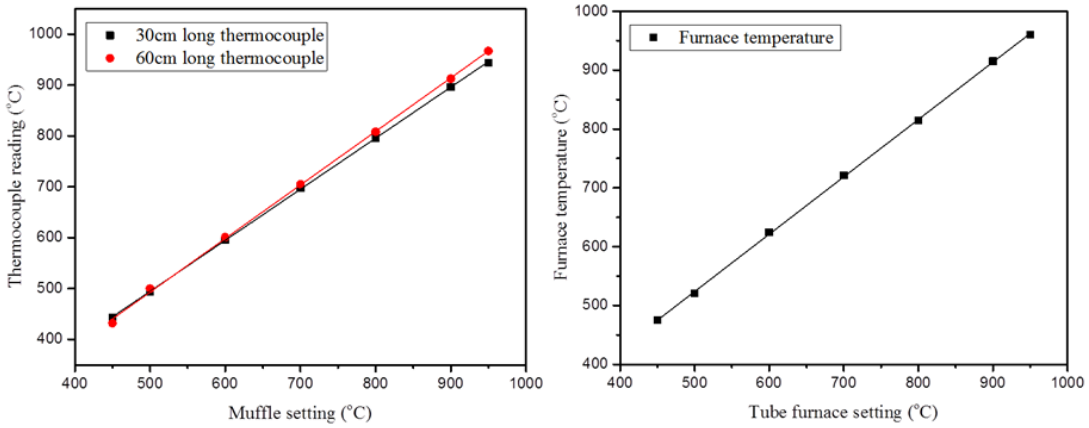

a b

Figure 3.2: Calibration of tube furnace prior to oxidation experiments (a) Plots of temperature reading obtained using 60cm thermocouple and 30cm thermocouple (°C) against the temperature of the muffle furnace (°C), (b) Plot of tube furnace temperature measured using corrected 60cm thermocouple (°C) against the set temperature (°C)

Preparation of crucibles for oxidation experiments

The intention was to oxidise small coupons of alloy in modified alumina crucibles (with loose fitting lids) in the tube furnace. Crucibles were to be used because they allow any oxide spalled from the coupons to be collected (and weighed) and because they also allow the coupons to be suspended from a short length of ceramic rod (thus ensuring that all of their surfaces are equally exposed to the oxidising atmosphere). Numerous researchers have used crucibles in this way, including Pint [210].

Crucibles and lids (x2), and a short length of 1.0mm diameter alumina rod, were obtained from Almath (Oxford, UK) and Goodfellows (Huntingdon, UK)

respectively. The crucibles and lids were very ‘dusty’ when received, so each crucible ‘set’, comprising a crucible, lid and short length of alumina rod, was ultrasonically cleaned in distilled water followed by absolute ethanol. This procedure removed a significant amount of ‘white’ dust from the crucible ‘sets’, presumably alumina, as evidenced by a significant residue left behind following ultrasonic cleaning. At all times the crucible ‘sets’ were handled using nitrile gloves to prevent their contamination by salts and grease. Each crucible ‘set’ was heated at 900°C for approximately 200 hours before use in order to stabilise their mass.

Oxidation of alloy coupons

Each coupon and its crucible ‘set’ was weighed five times in a clean room environment using a 5-place digital balance (Metler Toledo XS205). This was done before and after oxidation. A stable, chemically inert standard block of alloy MA754, of similar mass to each crucible ‘set’ i.e. ~13g mass, was weighed 5 times at the beginning and end of each weighing session in order to monitor the performance of the balance.

Two coupons of alloy were oxidised at a time in their crucible ‘sets’, which increased the rate at which the oxidation behaviour of the alloys could be studied. A single coupon of each alloy was oxidised for 10, 25, 50, 75, 100, 215 and 1000 hours in laboratory air at 900°C.

The crucibles were pushed straight into the tube furnace so that there was not time for any ‘warm-up’ to occur. Similarly, on removal from the furnace, the crucibles were brought straight out of the tube furnace and placed in a desiccator. The coupons and their crucible ‘sets’ were weighed after 1 hour of cooling in the desiccator.

Between oxidation experiments, the crucible ‘sets’ were rinsed with distilled water, followed by absolute ethanol and heated in the tube furnace for between 12 and 24 hours at 900°C. Following their removal from the furnace they were allowed to cool

for 1 hour in a desiccator before weighing. As previously stated, the coupons and crucible ‘sets’ were always handled using nitrile gloves to prevent their becoming contaminated by salts and grease.

Long term stability of the crucible ‘sets’

A graph of cumulative mass change of the crucible ‘sets’ (g) against furnace residence time (h) can be seen in Figure 3.3. Both crucible ‘sets’ lost mass up to approximately 2500 hours, particularly between 1500 and 2500 hours. By reference to the standard block of alloy it can be seen that the mass loss was real, rather than being due to a ‘step-change’ in the performance of the balance. Beyond approximately 3000 hours the crucible ‘sets’ were quite stable. Some instability in the balance, particularly at approximately 3500 hours, was observed (this instability does appear to be reflected in the crucible results).

Fortunately, the significant mass drops that affected both crucible ‘sets’ occurred between TGA experiments, rather than during an experiment. The smaller changes that occurred during the experiments did not seriously affect the results because the crucibles were weighed carefully before and after each experiment. However, these results do suggest that, if mass changes are to be determined by difference, then the crucible ‘sets’ should be heated for a significant length of time prior to their use (in this case >3000 hours at 900°C). The instability of crucibles at high temperatures has been reported before, and is attributed to the volatilisation of residual species that can remain in sintered components following firing of the ‘green’ parts.

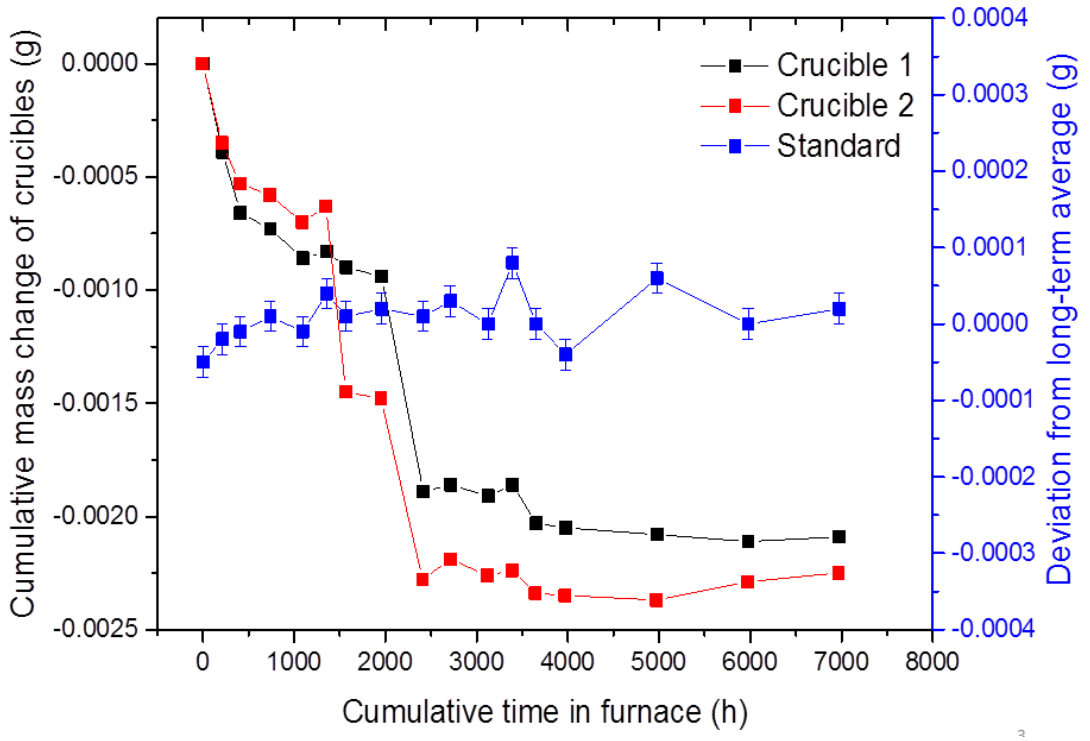

Figure 3.3: Cumulative change in mass of crucibles (g) against furnace residence time (h). The blue line is a plot of the deviation from the long-term average mass of a standard block weighed at the same time as the crucibles (the standard deviation shown for each point is the long-term standard deviation of the block)

3.3.2 Optical microscopy

A Metalloplan optical microscope (Leitz, Germany) and epi-axial reflected light illumination was used to study sections of the bulk alloys and oxidised coupons of the alloys. Micrographs were recorded using an Infinity 2 digital camera (Luminera, Canada) interfaced to a PC (Dell, USA) equipped with Infinity Analyse software (Luminera, Canada). Objective lenses ranging from x8 to x64 in magnification were used to study the specimens. A ruled glass graticule, 1mm in 100µm divisions, was photographed using each objective lens and the micrographs used to calibrate the magnification of each lens using Image J [211].

3.3.3 Hardness measurements

Vickers hardness measurements were obtained for this research using a Matsuzawa Seiko micro-hardness tester (model DMH-2), using a 500g load and a dwell time of 15 seconds. The diagonals were measured using the integrated binoculars and the hardness values calculated using the on-board computer. Prior to the measurement of the alloys the hardness tester was calibrated using a 220HV test block, which gave an arithmetic mean of 225±10HV0.5 from 10 measurements. Multiple measurements were made because the Vickers method can be prone to errors arising from inaccurate measuring of the indent diagonals. All of the indents were made so that they separated from their nearest neighbours by at least 3x the length of the indent diagonals, as stipulated by ASTM E384 [212]. This is done to so that the hardness of the positions tested is not affected by pre-existing indents.

3.3.4 Scanning Electron Microscopy (SEM)

A SEM is an instrument used to study solid materials by illumination them with a beam of electrons. It combines high spatial resolution imaging, potentially <2nm in a modern SEM, with great depth of focus, which is due to the short wavelength of the primary electrons and the small diameter of the electron beam. A suitably equipped SEM can also be used for elemental chemical analysis using energy dispersive spectroscopy (EDS).

Most of the specimens were examined using a 7100F Field Emission Gun (FEG) SEM (JEOL, Japan). Compositional depth profiles were obtained from the cross-sections of the oxidised alloys using a 6610 SEM (JEOL, Japan). Both SEM instruments are equipped with an INCA microanalysis suite (Oxford Instruments, UK) that comprises an X-act Silicon Drift Device (SDD) detector, Super Ultra-Thin Window (SUTW) and associated electronics and software. The 7001F is a thermal FEG SEM with a nominal resolution of 2nm. Most of the results were obtained at an accelerating voltage of 20kV, but accelerating voltages of between 5kV and 30kV

were also used when appropriate. Spot sizes were selected to give beam currents in the range 0.5 to 1nA. The specimens were examined at a working distance of 10mm, which is the analytical working distance of the microscope. The accelerating voltage, spot size and processing time were varied to maintain a dead-time of 25-35%, while ensuring that the over-voltage was sufficient to excite all peaks of interest. Spectra were collected using a livetime of either 50 seconds or 100 seconds. The instrument was operated overnight in an automated mode to collect maps using a 'site-lock' function to correct for specimen drift. Linescans were acquired for several hours. In both cases this was done to improve the signal to noise. The quantification of spectra was carried-out the INCA software.

The 6610 is a SEM that uses a thermionic gun as the electron source. The SEM was used to obtain compositional depth profiles from the cross-sections of the alloys. The specimens were presented normal to the electron beam in a top surface reference holder at the analytical working distance of the SEM (10mm). The SEM was operated at 20kV, with the same spot size and processing time used for each specimen, configured to produce a dead-time of ~25-35%. A livetime of 100 seconds was used to acquire the spectra, which gives a minimum detection limit of ~0.1%. A series of points were collected automatically by the INCA software, starting at the scale/alloy interface and ending beyond the oxidation-affected zone in the alloy. The spectra were quantified using a variant of ZAF [213, 214].

3.3.5 X-ray Diffraction (XRD)

XRD is a well-established, non-destructive technique that is routinely used to investigate crystalline materials. The technique is based on Bragg's Law [215]. A Miniflex X-ray diffractometer (Rigaku, Japan) equipped with a Cu source was used to determine the phases present in the alloys and the oxide scales. The beam was filtered using Ni, to reduce the CuKβ component, giving a beam comprised mainly of $CuK\alpha_1$ and $CuK\alpha_2$ radiation. The nominal wavelength of the filtered beam is 0.154nm. Diffraction patterns were obtained over the 2θ angular range of 10 to 80°,

at a collection rate of 0.2° min^{-1}. The data was smoothed using Rigaku software and the diffractograms plotted using Origin software. Identification of the phases present in the diffractograms was conducted using the ICSD data base [216].

3.3.6 Scanning Transmission Electron Microscopy (STEM)

A scanning transmission electron microscope (STEM) is similar to a conventional scanning electron microscope (SEM) because it scans a focused beam of electrons on to specimens held under vacuum [217]. However, a STEM is used to examine electron-transparent specimens using an accelerating voltage of 200-300kV, whereas a SEM is used to study bulk specimens and using an accelerating voltage of <30kV. Spatial resolution is typically a few angstroms in a STEM, instead of a few nanometres in a SEM, because of the shorter wavelength of the electrons.

The study of electron-transparent lamellae in a STEM makes it similar to a transmission electron microscope, but whereas a STEM uses a convergent electron beam to interrogate the specimen a TEM uses a parallel electron beam. The principal components of an aberration-corrected STEM are a field emission gun, a set of condensing lenses, an aberration-corrector, an objective lens and electron detectors. Electrons generated by the field-emission gun are formed into a beam using a set of condenser lenses, and this is corrected using an aberration corrector. The beam is focused on to the specimen by an objective lens and the resulting electron beam/specimen interactions produce transmitted and scattered electron that are used for imaging. A scan generator synchronises and controls the scanning of the beam and the monitor, so that an image of the specimen can be formed from the electrons.

Complementary BF and ADF images are obtained simultaneously from a STEM. A BF detector collects transmitted electrons, so that holes in a specimen appear ‘bright’, and an ADF detector collects electrons that have been scattered by the specimen, so that holes in a specimen appear ‘dark’. The ADF detector can also be tuned for the collection of electrons scattered thorough larger angles, which gives

rise to images optimised for Z-contrast. This mode of imaging is referred to as High Angle ADF (HAADF) imaging.

A 2100F TEM (JEOL, Japan) was used in STEM mode to examine the lamellae prepared by FIB. The instrument operates at 200kV, giving a wavelength of 7nm and a best, nominal resolution, of ~2A.

3.4 Specimen preparation

Preparation of coupons for TGA

The coupons were prepared from sections of the SLM-consolidated blocks, which were cut slightly over-size and parallel to the build direction, Figure 3.4. Coupons of wrought Alloy 718 and wrought Haynes 230 were prepared from sections cut perpendicular to the extrusion direction of the parent rods, but the coupons of Alloy 625 were prepared from sections cut parallel to the extrusion direction of the parent rod. All of the wrought alloys had an equiaxed grain size, so their oxidation behaviour should be isotropic. The SPS-consolidated alloys were cut parallel to the direction in which they were compressed during sintering. An abrasive-wheel cut-off saw was used to cut all of the sections (ATM Brillant 220).

All of the specimens were ground sequentially using P180, P320 and P600 SiC-impregnated papers to form coupons of 11.0±1.0x11.0±1.0x1.1±0.1mm in size. Specimens of wrought Alloy 718 were also studied following sequential grinding using P180, P320, P600, P1200, P2500 and P4000 SiC papers. The corners of each coupon were rounded, to reduce the likelihood of enhanced oxidation in the corners. A hole of 1.5mm diameter was drilled in the coupons using a WC bit so that they could be suspended in the crucibles during the oxidation experiments. Drilling of the coupons was performed under mineral oil for cooling and lubrication. The drilled coupons were washed using liquid soap and water, and rinsed using acetone. All six surfaces of each coupon were photographed at a low magnification, ~x2, using

reflected light and a stereo optical microscope (Wild (Leica), Germany). The main scale of a Vernier caliper, comprising 1mm divisions, was used as a scale for the micrographs, which allowed the surface area of the coupons to be calculated using Image J. This method of determining the surface area of the coupons was believed to be more accurate than measuring the length, width and thickness using a Vernier caliper, as is sometimes reported [218].

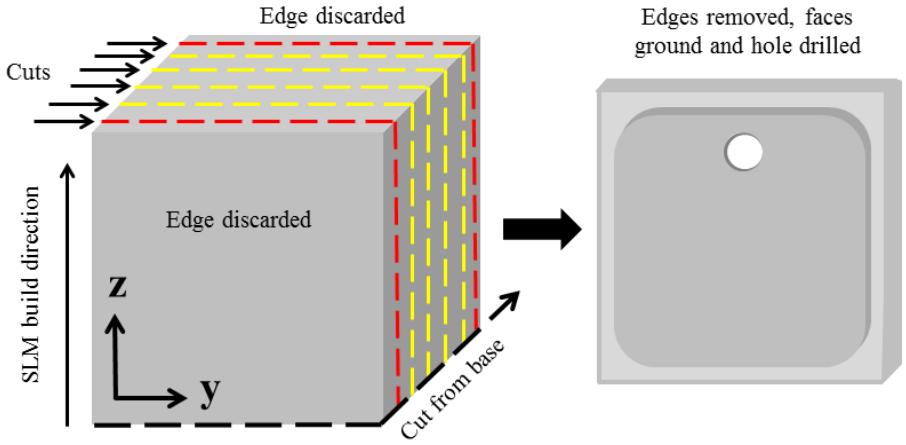

Figure 3.4: Preparation of coupons from SLM-consolidated blocks for thermogravimetric analysis

Specimens for Optical microscopy and SEM

Specimens for optical microscopy and SEM were cut from the parent alloys using an abrasive-wheel cut-off saw and mounted in conductive acrylic resin. In accordance with standard metallographic procedures the mounted specimens were ground using SiC-impregnated papers (P180 to P4000) and polished using 1µm polycrystalline diamond, 0.25µm polycrystalline diamond and an aqueous suspension of colloidal silica (40nm). Some specimens were polished using 1µm and 0.5µm alumina instead of 1µm and 0.25µm polycrystalline diamond.

To prevent rounding of the edges during preparation, the oxidised coupons of the alloys were Ni-plated [219] using an electrolyte proposed by Brown and Knapp,

which produces a ‘hard’ coating of 350-500HV [220]. The composition of the electrolyte is, in Wt. %, 18% $NiSO_4.6H_2O$, 2.5% NH_4Cl and 3.0% H_3BO_3. The balance is made-up using distilled H_2O. In order to make the oxidised specimens sufficiently conductive for electroplating they were mounted on a 15mm diameter copper disc of ~200µm thickness using conductive silver dag. After air drying, each coupon was coated with a thin layer of Au (~40nm) using an Edwards S150 sputter coater (Edwards Ltd., UK). Electroplating was performed in a plastic housing, with the anode (a 60mm by 5mm rod of Ni) suspended ~25mm above the cathode (the specimen). The entire housing was immersed in the electrolyte, which was maintained at a temperature of 50±5°C and agitated by a magnetic stirrer. Plating was carried-out for ~1 hour at 4V DC, with a current density of ≤5nA cm^{-2}. Under these deposition conditions a Ni layer of ~10µm thickness was obtained. Sometimes a porous, non-adherent Ni layer was obtained when the plating solution was near-exhausted, and it was necessary to change electrolyte once this was observed to occur. Following Ni-plating the specimens were mounted and ground and polished using standard metallographic procedures, using P180 SiC-impregnated papers to 40nm colloidal silica. It should be noted that the coupons prepared for TGA were too large for electroplating, so small specimens of ~5x5mm in size were used instead. These specimens were not drilled, but otherwise were prepared in the same way as the coupons for TGA.

Etching of wrought alloys for Optical microscopy

The wrought alloys were ground and polished using standard metallographic procedures to a 1µm diamond finish and etched at room temperatures in an electrolyte comprised of a 90/10 v/v mixture of 1M HCl and 0.1M oxalic acid. The voltage used was 4 volts DC. This method is based on one used by Haynes Inc. for etching Haynes 230 [110], and was preferred to the use of standard etchants because it produced more consistent results.

Lamellae for study using STEM

Lamellae were produced from the oxide scale presents on 625 ODS and Haynes 230 ODS for examination in the STEM. A dual beam FIB is an instrument that, in essence, adds a liquid metal ion gun, usually Ga, to an SEM. The instrument can be used for imaging, using either the electron gun or the ion gun, but its principal usefulness stems from the ability of the operator to operate both guns in conjunction to produce electron-transparent lamellae for TEM/STEM, or for making site-specific cross-sections of materials e.g. the sectioning of small features in a matrix, such as inclusions. Lamellae were prepared by FIB from oxidised coupons of Alloy 625 ODS/SLM, Alloy 625 ODS/SPS, Haynes 230 ODS/SLM and Haynes 230 ODS/SPS. The lamellae were prepared using a Helios 600i dual beam FIB (FEI, USA), which is equipped with gas injectors and micromanipulators for the lift-out and transportation of lamellae. It is also equipped with the EDAX team analysis suite, which includes detectors for EDS and EBSD.

The lamellae were prepared using a lift-out procedure similar to that described by Tomus [221] and Gianuzzi [222]. A strap of Pt or C (~10x10x1µm) was first deposited over the site of interest to protect the oxide from damage, before two trenches were milled parallel to the long axis of the strap (one either side). During trenching and the early stages of milling the Ga ion beam was operated at an acceleration voltage of 30kV and a beam current of between 20 and 65nA; this was done to achieve fast removal of the oxide and its underlying alloy. The lamellae were released from the bulk alloy by making J-cut incisions. Once free the lamellae were thinned to ~100nm (using 30kV ion beam and beam currents of between 80pA and 2.5nA). The lamellae were tilted ±2° to the ion beam during this step. A final polishing step was made at an accelerating voltage of between 2 and 8kV, which is done to remove any remaining surface damage and deposits [223]. After the final polishing steps had been completed the lamellae were moved (using the micromanipulator) to Cu support grids, to which they were attached using Pt. On

removal from the FIB each lamella was transferred to a membrane box; these were stored in a desiccator prior to examination.

CHAPTER 4

Oxidation Kinetics

4.1 Introduction

The aim of the experiments was to determine the oxidation kinetics for each variant of the alloys. Oxidation was performed in laboratory air at 900°C for exposure times of up to 1000 hours, using multiple coupons of each variant so that the results were genuinely isothermal. The oxidation kinetics were determined using either TGA or from measurements of scale thickness made in a SEM, or both.

All of the SLM-consolidated alloys were prepared from sections cut parallel to the build direction of the alloy. The wrought alloy coupons were prepared from sections cut perpendicular to the extrusion direction, or in the case of Alloy 625, parallel to the extrusion direction. The coupons of SPS-consolidated alloy were prepared from sections cut parallel to the direction in which the blocks were compressed during consolidation. All of the coupons were tested following preparation to a P600 grit finish; Alloy 718 was additionally tested following preparation to a P4000 grit finish. SLM-consolidated Alloy 718, Alloy 625 and Haynes 230 were oxidised following heat-treatment according to the schedules provided in Chapter 3. The wrought alloys were oxidised in the as-received annealed condition. SLM-consolidated and SPS-consolidated Alloy 625 ODS and Haynes 230 ODS were oxidised in the as-consolidated condition.

Sections of the alloys, prepared to a 40nm colloidal silica finish, were examined prior to oxidation using optical microscopy to identify the presence of defects, or other microstructural features, that might affect the oxidation kinetics of the alloys. The SLM-consolidated specimens were orientated as shown in Figure 3.4. In the case of the wrought alloys, the term transverse is used to describe sections cut

perpendicular to the extrusion direction, while longitudinal is used to describe sections cut parallel to the extrusion direction. The results are presented in section 4.2, Examination of the alloys prior to oxidation, and section 4.3, Determination of oxidation kinetics. The results are discussed in section 4.4, and a chapter summary is provided in section 4.5.

4.2 Examination of alloys prior to oxidation

The SLM-consolidated variants of Alloy 718, Alloy 625 and Haynes 230 were examined un-etched, using optical microscopy, following heat-treatment, Figure 4.1. The coupons contained small numbers of angular voids, orientated perpendicular to the build direction, which were visible in the silica-polished specimens but not in the coupons prepared for oxidation. This could be due to the roughness of the ground coupons, or perhaps because of smearing of the ductile alloys. Voids are often reported in SLM-consolidated alloys, and are usually attributed to gas bubbles or incomplete consolidation of the gas atomised powder [224]. However, the appearance of the voids, in all three alloys, is more consistent with un-melted regions between layers of the build rather than gas bubbles. All of the SLM-consolidated alloys appeared to be essentially free of inclusions.

The wrought alloys had an equiaxed grain structure, with grain sizes consistent with those provided by the suppliers, Figure 4.2. Grain boundary δ-phase, which is expected to form in Alloy 718 and Alloy 625 [92], was evident in Alloy 718, but not in Alloy 625. Differential etching of the grains occurred in Alloy 718, which is presumably a grain orientation effect. Alloy 718 and Alloy 625 contained inclusions aligned with the extrusion direction of the alloy, which have been identified as MC-type carbides based on Nb, Ti and C [92]. The carbides were ~1-20µm in size and were typically larger, but less numerous, in Alloy 718. Haynes 230 contained a large number of twins and a very large number of intergranular and intragranular inclusions of ~1-15µm in size, which have been identified as tungsten-rich M_6C type carbides [114].

Alloy 625 ODS/SLM and Haynes 230 ODS/SLM contained cracks, inclusions and voids, with Alloy 625 ODS/SLM particularly badly affected, Figure 4.3. The inclusions and voids were thought to be due to ‘slagging-off’ of Y present in the mechanically alloyed powders. The same effect has been observed in blocks of a SLM-consolidated ferritic ODS alloy [68], and in a TIG welded Ni-base ODS alloy [44]. The cracks appear to be solidification cracks, which have been reported to occur in alloys that contain Nb, such as Alloy 625, due to the wide solidification temperature range of Nb-containing alloys [96, 106]. Solidification cracking, reported in Haynes 230 welds, has been attributed to B [117]. The SPS-consolidated alloys contained large numbers of pores, with Alloy 625 ODS/SPS mainly affected, Figure 4.4.

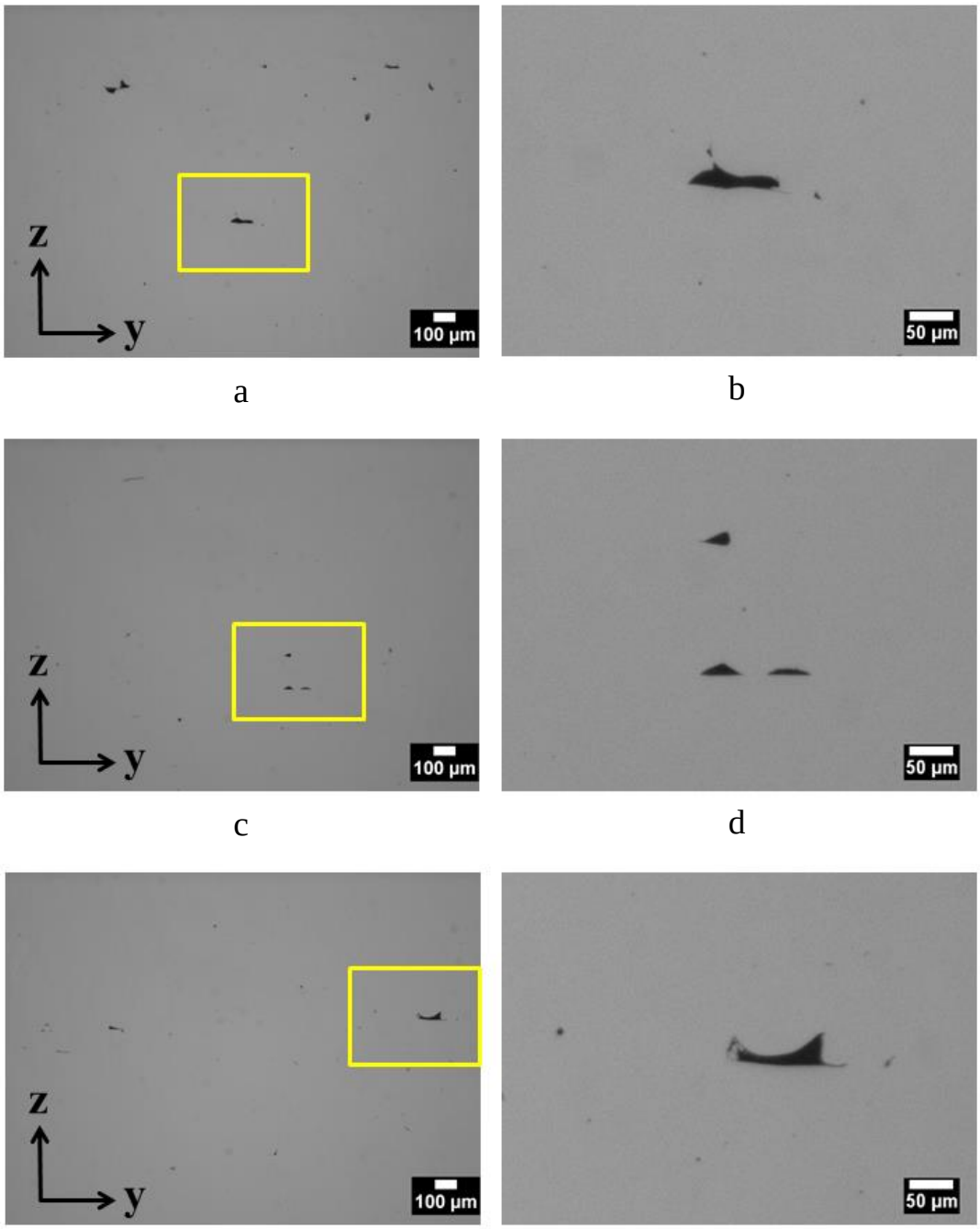

Figure 4.1: Optical micrographs of voids present in longitudinal sections of the SLM-consolidated alloys (a), (b) Alloy 718, (c), (d) Alloy 625, and (e), (f) Haynes 230

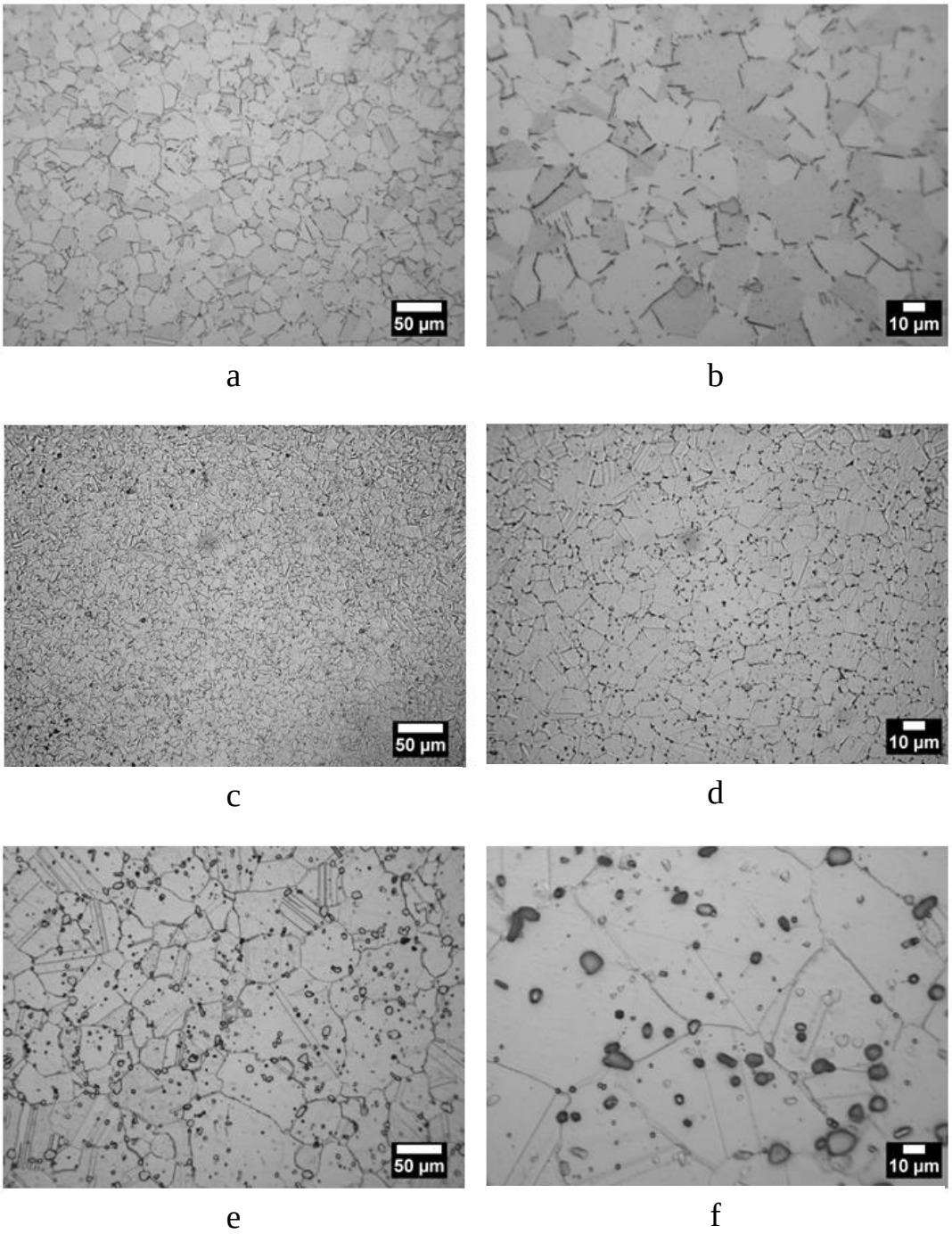

Figure 4.2: Optical micrographs of the wrought alloys following etching (a), (b) Transverse section of Alloy 718, (c), (d) Longitudinal section of Alloy 625, and (e), (f) Transverse section of Haynes 230

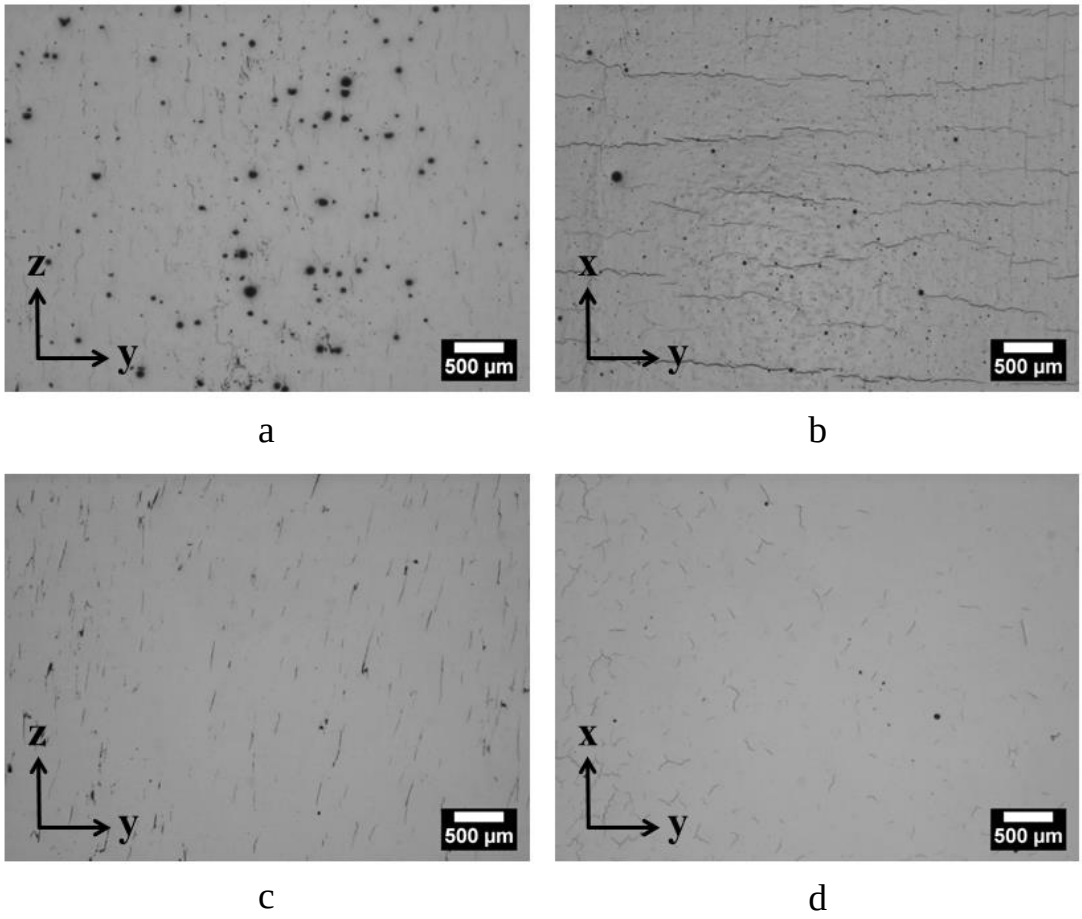

Figure 4.3: Optical micrographs of SLM-consolidated ODS alloys (a) Longitudinal section of Alloy 625 ODS/SLM, (b) Transverse section of Alloy 625 ODS/SLM, (c) Longitudinal section of Haynes 230 ODS/SLM, and (d) Transverse section of Haynes 230 ODS/SLM

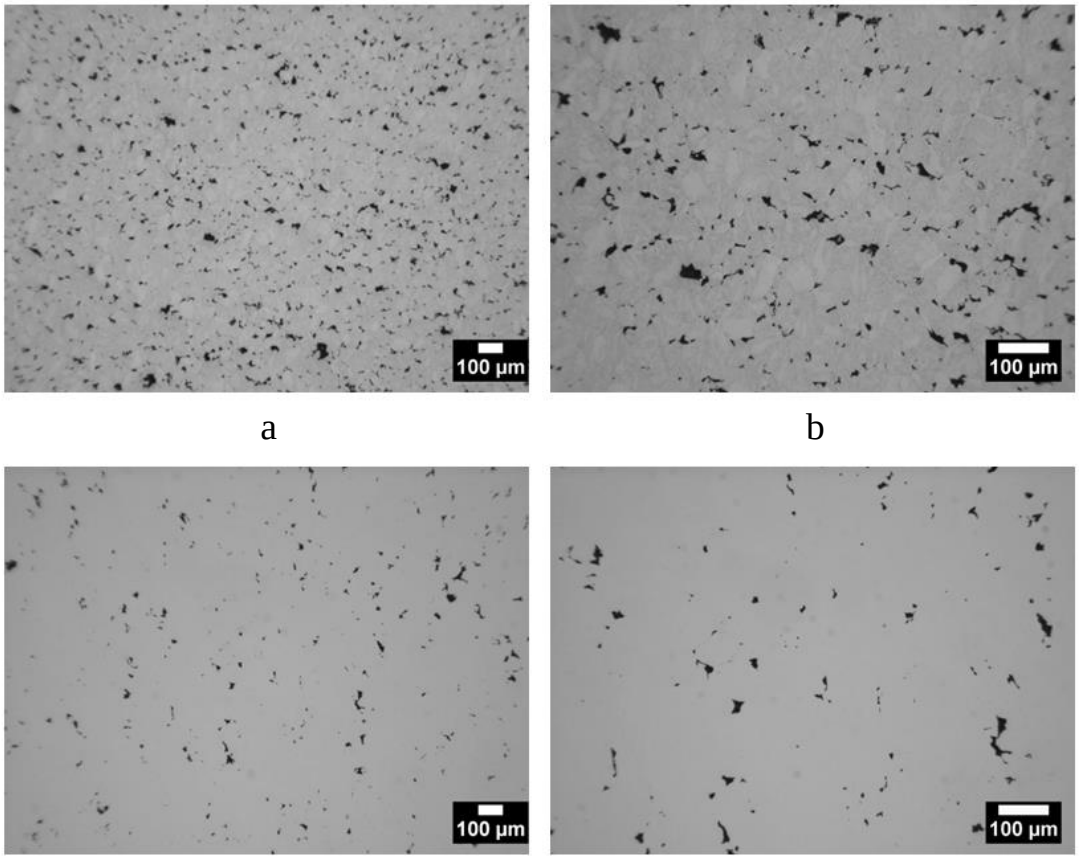

Figure 4.4: Optical micrographs of porosity in SPS-consolidated ODS alloys (a), (b) Alloy 625 ODS, (c), (d) Haynes 230 ODS

4.3 Determination of oxidation kinetics

TGA results were obtained for coupons oxidised for 10, 25, 50, 75, 100, 215 and 1000 hours. Scale thickness measurements were obtained following 25, 215 and 1000 hours of oxidation. The two data sets were used to determine the oxidation kinetics of Alloy 718, Alloy 625 and Haynes 230 in SLM-consolidated and wrought forms, and Alloy 625 ODS and Haynes 230 ODS in SPS-consolidated form. The oxidation kinetics of SLM-consolidated Alloy 625 ODS and SLM-consolidated Haynes 230 ODS were determined only from scale thickness measurements, again following 25, 215 and 1000 hours of oxidation, because the blocks received for study

were too small for TGA specimens to be obtained. It should also be noted that TGA data was not obtained for Alloy 625 ODS/SPS following 10 hours and 25 hours of oxidation because the mass gains for this alloy were so low, even at long oxidation times.

Graphs of mass change/surface area (gcm^{-2}) against time (s), and scale thickness (cm) against time (s), are shown in Figures 4.5-4.7. Log-log plots of the data obtained from Alloy 718 and Alloy 625 indicated that they oxidised according to parabolic kinetics, and so the data are fitted using the appropriate Wagner equation i.e. Equation 1 for the TGA data, and Equation 2 for the scale thickness data.

SLM-consolidated Alloy 718 oxidised slightly faster than wrought Alloy 718, which essentially oxidised at a rate independent of its surface finish, Figure 4.5. The data obtained for Alloy 625, Figure 4.6, shows that the different variants of the alloy oxidised in the order Wrought>SLM>ODS/SPS≈Hf-ODS/SPS>ODS/SLM. It will be noted that the ranking includes data for an additional Alloy 625 variant, consolidated by SPS from mechanically alloyed powder made with an addition of 0.5 Wt.% HfO_2 and 0.5 Wt.% Y_2O_3 to the gas atomised powder - this alloy was made because Hf is reported to improve dispersoid refinement, rather than because of its effect on oxidation [225]. All of the Haynes 230 alloys, with the exception of the ODS/SPS alloy, oxidised according to parabolic kinetics in the order SLM>Wrought>ODS/SLM, Figure 4.7. Haynes 230 ODS/SPS oxidised much faster than the other variants of the alloy, but while the scale thickness data could be fitted using a single parabolic equation, the TGA data could only be fitted using a single parabolic equation for the time period 10-215 hours, producing a clear discrepancy, after 1000 hours of oxidation, between the actual unit mass gain and the projected unit mass gain. It should be noted that there was no evidence of spalling having occurred during the oxidation of Haynes 230 ODS/SPS, or any of the alloys.

Graphs of mass gain/surface area (gcm^{-2}) against the $time^{1/2}$ ($s^{1/2}$), and oxide thickness (cm) against $time^{1/2}$ ($s^{1/2}$) are shown for the alloys in Figures 4.8-4.10. The

parabolic oxidation rate constants obtained from the graphs are presented Table 4.1, along with $\frac{k_{w_{Variant}}}{k_{w_{Wrought}}}$ and $\frac{k_{p_{Variant}}}{k_{p_{Wrought}}}$ ratios, which are used to rank the alloys. Also included in Table 4.1 is a parabolic oxidation rate constant determined for MA754, which was obtained using the methodology used to obtain the results from Alloy 718, Alloy 625 and Haynes 230.

Two oxidation rate constants were obtained for Haynes 230 ODS/SPS; the first by fitting the data using two parabolic rate constants i.e. one for 10-215 hours of oxidation, and a second for 215-1000 hours. The pro rata parabolic oxidation rate constant was 5.24E-13 $g^2cm^{-4}s^{-1}$, which represents the slowest oxidation rate for the data, as it assumes that the transition from fast to slow oxidation kinetics occurred at 215 hours, when it could have occurred much later. The second parabolic oxidation rate constant was obtained by assuming that the oxidation proceeded at a single parabolic rate to the intersection of the dashed lines shown in Figure 4.10. A pro rata parabolic oxidation rate constant calculated from this time, when oxidation is assumed to have stopped completely, is 9.50E-13 $g^2cm^{-4}s^{-1}$. This represents the upper limit for the rate of oxidation. Therefore, it would appear that the parabolic oxidation rate for Haynes 230 ODS/SPS probably ranged somewhere between the two limiting values of 5.24E-13$g^2cm^{-4}s^{-1}$ and 9.5E-13$g^2cm^{-4}s^{-1}$.

It should be noted that plots of mass grain/surface area (gcm^{-2}) against time$^{1/2}$ ($s^{1/2}$) represent steady state growth; the finite thickness of the scales at t=0 is likely to be due to transient oxidation. The coupons were oxidised within ~1 hour of weighing, and a measureable mass change due the formation of oxide prior to oxidation is highly unlikely.

Table 4.1: Parabolic oxidation rate constants k_w ($g^2cm^{-4}s^{-1}$) and k_p (cm^2s^{-1}) obtained for the alloys following isothermal oxidation in laboratory air at 900°C

Alloy	TGA		Scale Thickness	
	k_w ($g^2cm^{-4}s^{-1}$)	$\frac{k_{w_{Variant}}}{k_{w_{Wrought}}}$	k_p (cm^2s^{-1})	$\frac{k_{p_{Variant}}}{k_{p_{Wrought}}}$
718 SLM	4.75E-13	1.338	2.89E-13	1.214
Wrought Alloy 718 (P600)	3.55E-13	1.000	2.38E-13	1.000
Wrought Alloy 718 (P4000)	3.56E-13	1.003	2.29E-13	0.962
625 SLM	7.34E-14	0.230	8.16E-14	0.453
625 ODS/SLM	-	-	1.29E-15	0.007
Wrought Alloy 625	3.19E-13	1.000	1.80E-13	1.000
625 ODS/SPS	8.73E-15	0.027	1.37E-14	0.076
625 Hf-ODS/SPS	7.43E-15	0.023	-	-
Haynes 230 SLM	1.72E-13	3.23	1.34E-13	2.579
Haynes 230 ODS/SLM	-	-	3.92E-14	0.756
Wrought Haynes 230	5.32E-14	1.000	5.18E-14	1.000
Haynes 230 ODS/SPS	5.24E-13-9.50E-13	9.8-17.86	5.36E-13	10.34
MA754	2.19E-14	-	-	-

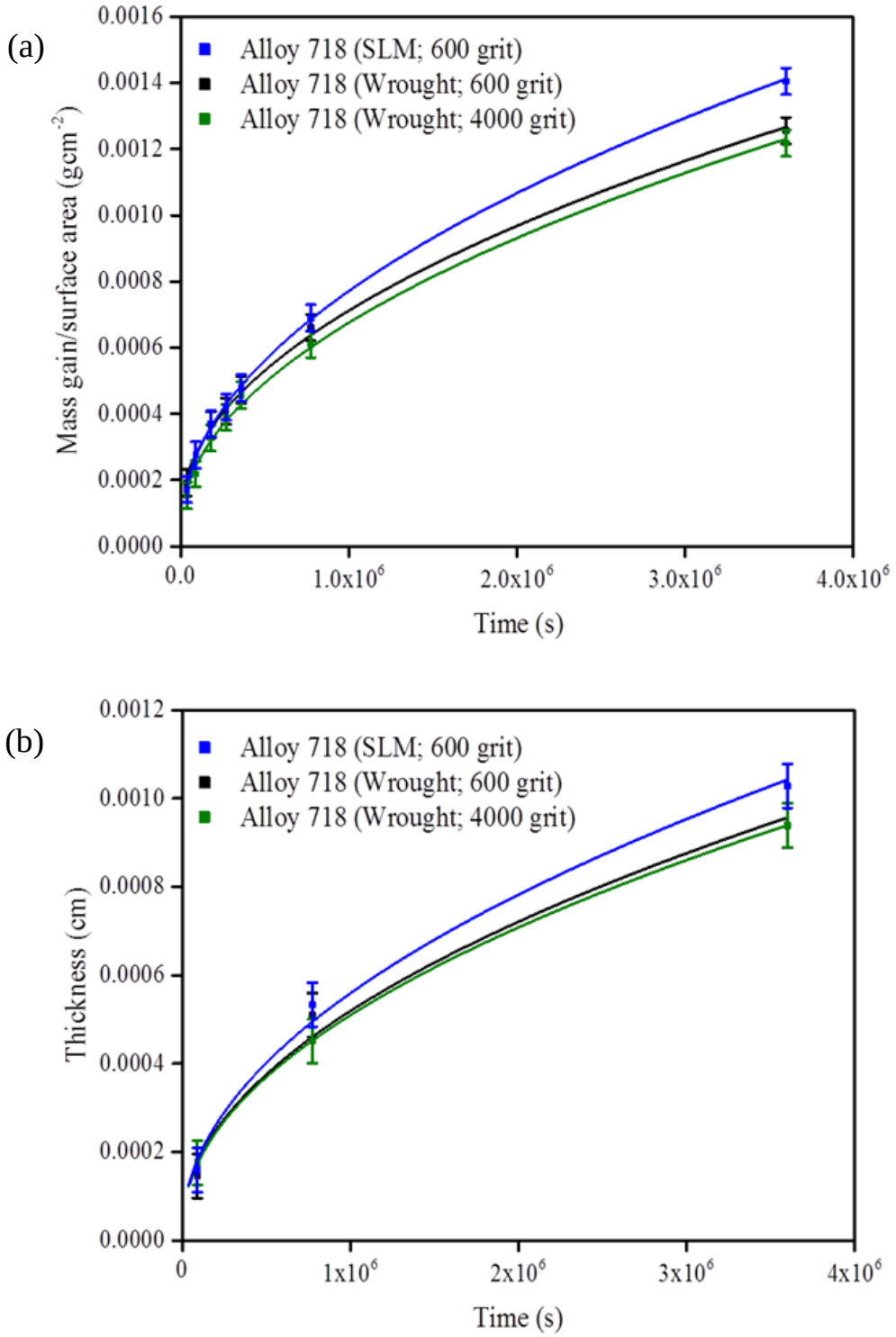

Figure 4.5: Isothermal oxidation of Alloy 718 in laboratory air at 900°C (a) Mass gain/surface area (gcm^{-2}) against Time (s), and (b) Scale thickness (cm) against Time (s)

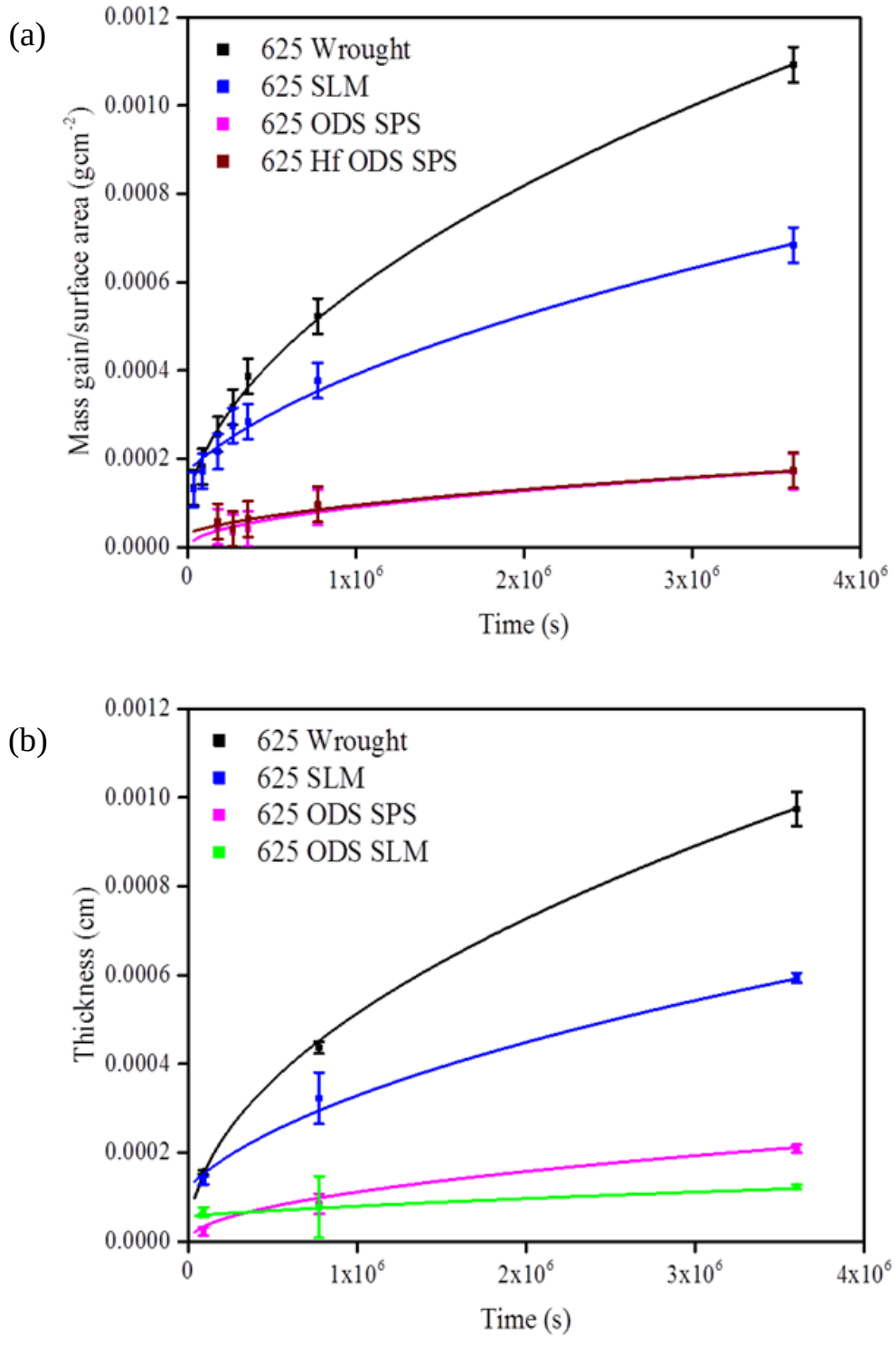

Figure 4.6: Isothermal oxidation of Alloy 625 in laboratory air at 900°C (a) Mass gain/surface area (gcm^{-2}) against Time (s), and (b) Scale thickness (cm) against Time (s)

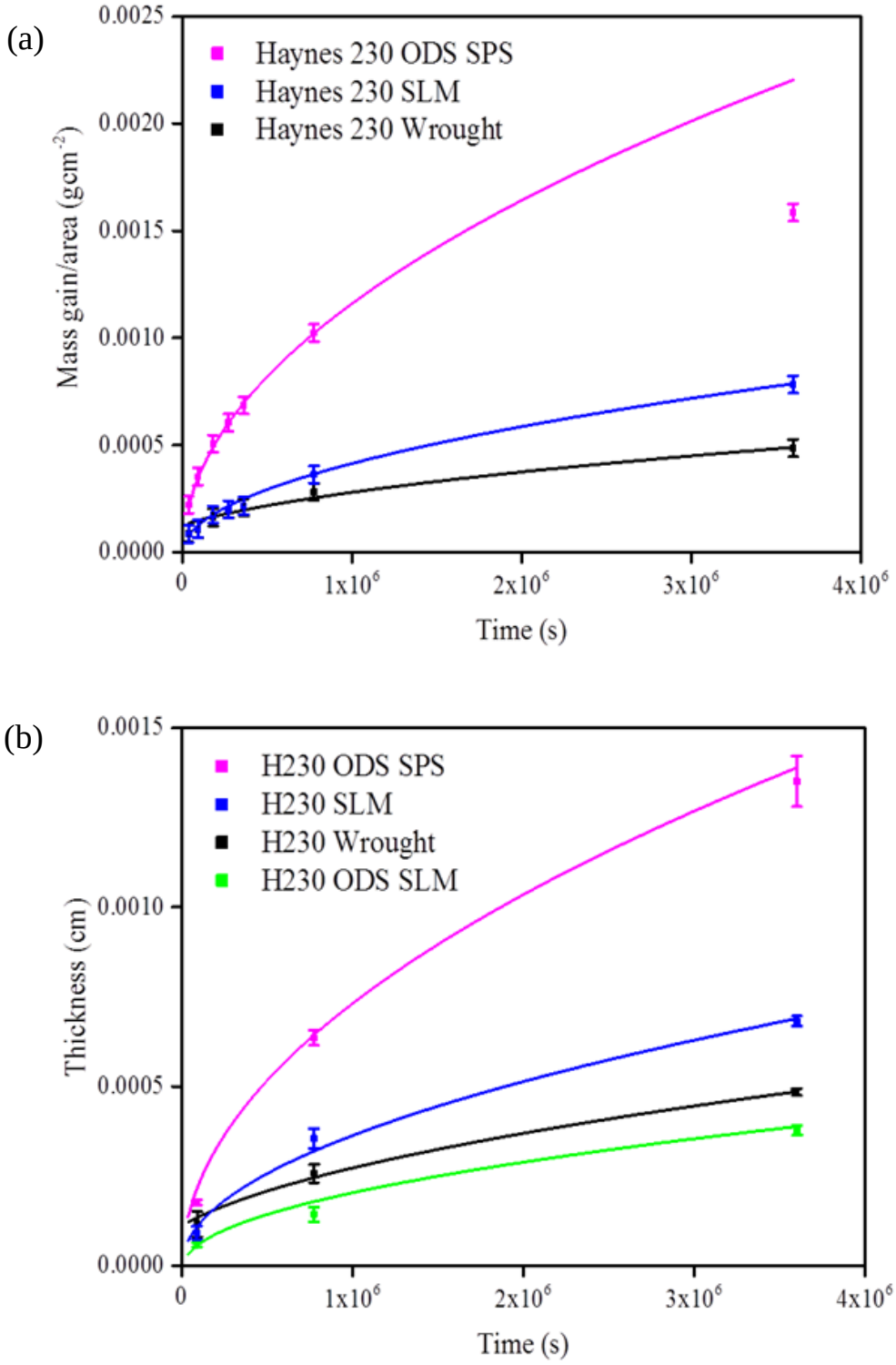

Figure 4.7: Isothermal oxidation of Haynes 230 in laboratory air at 900°C (a) Mass gain/surface area (gcm^{-2}) against Time (s), and (b) Scale thickness (cm) against Time (s)

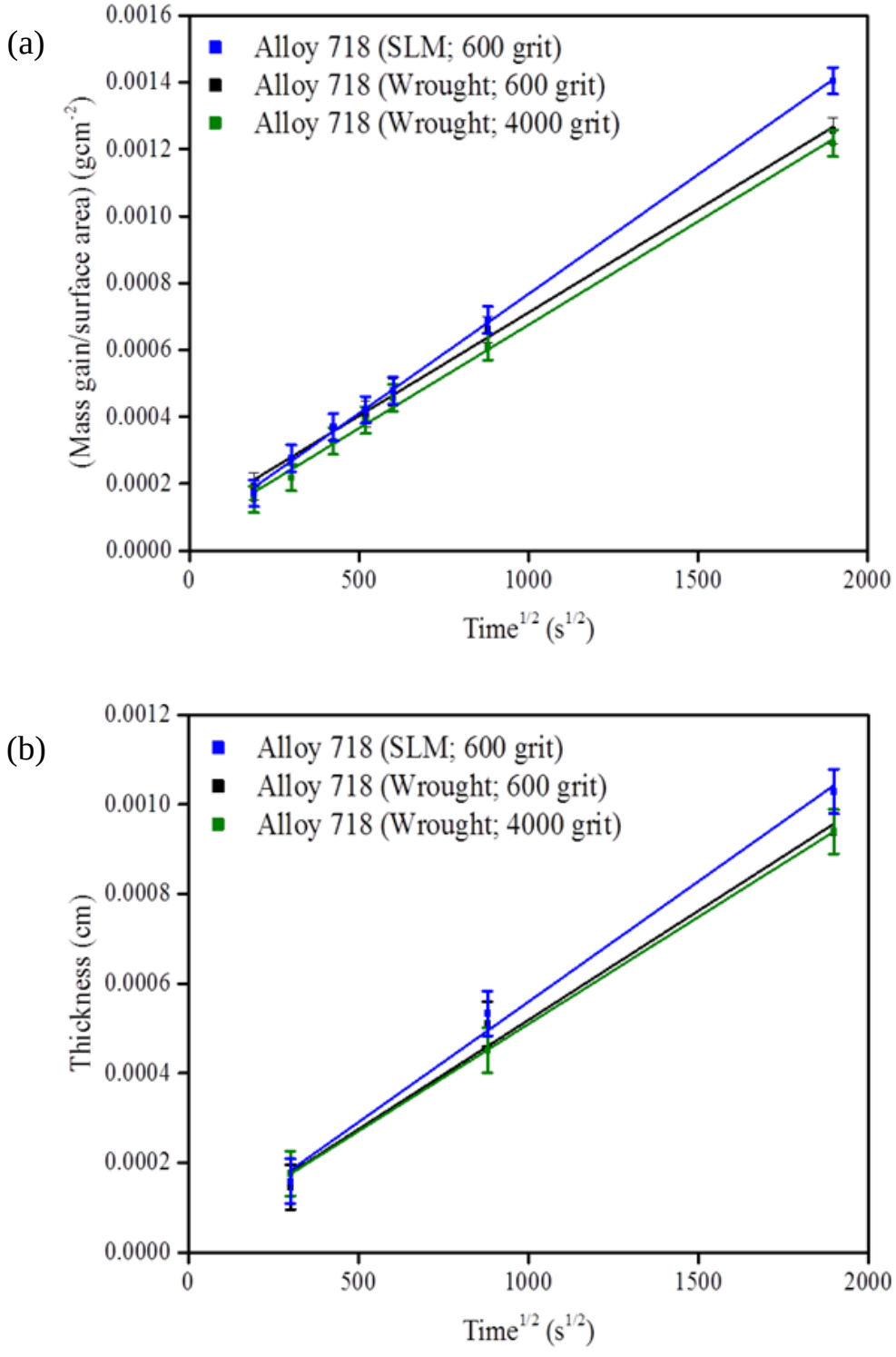

Figure 4.8: Isothermal oxidation of Alloy 718 in laboratory air at 900°C (a) Mass gain/surface area (gcm^{-2}) against $Time^{1/2}$ ($s^{1/2}$), and (b) Scale thickness (cm) against $Time^{1/2}$ ($s^{1/2}$)

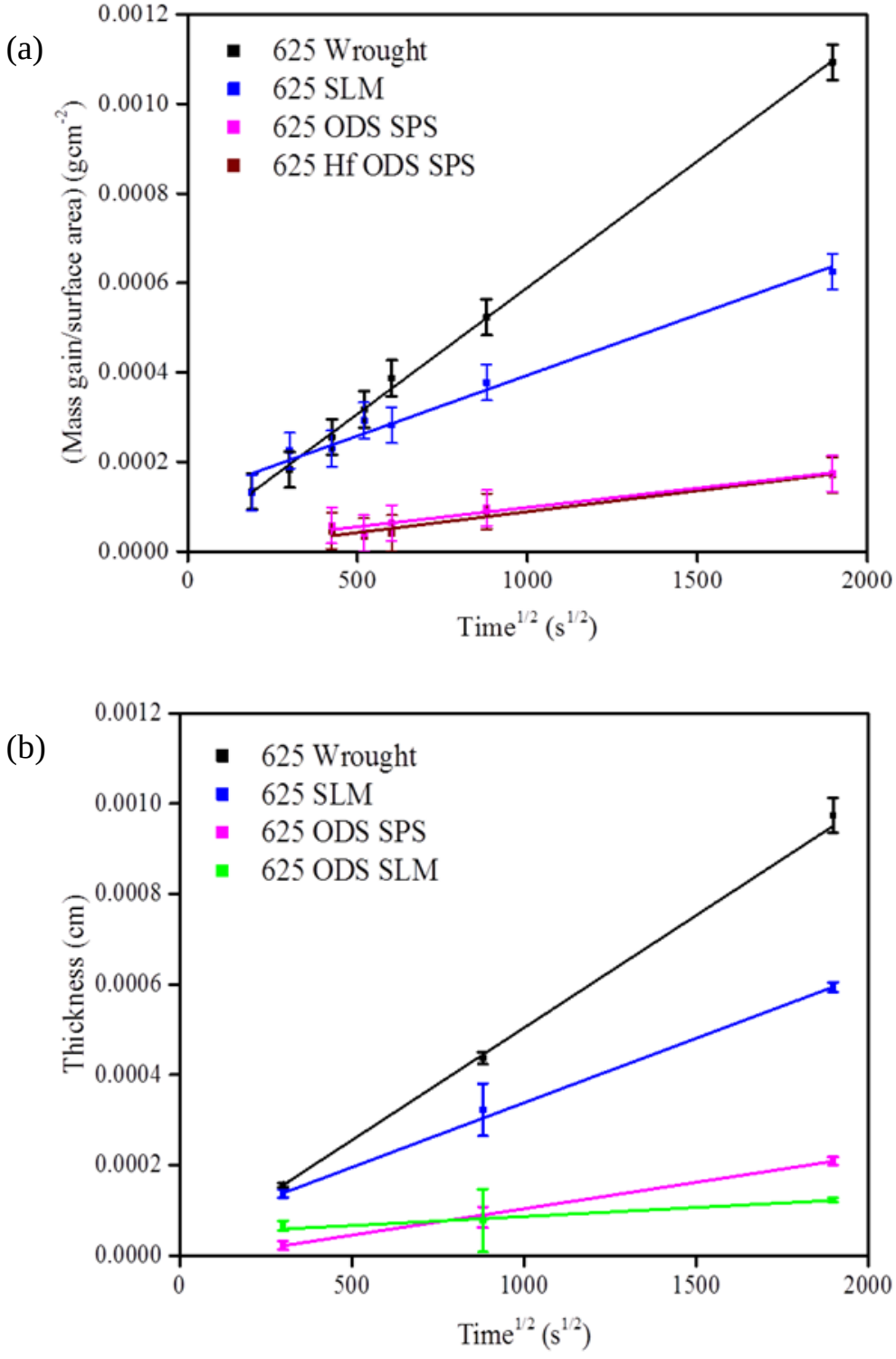

Figure 4.9: Isothermal oxidation of Alloy 625 in laboratory air at 900°C (a) Mass gain/surface area (gcm^{-2}) against $Time^{1/2}$ ($s^{1/2}$), and (b) Scale thickness (cm) against $Time^{1/2}$ ($s^{1/2}$)

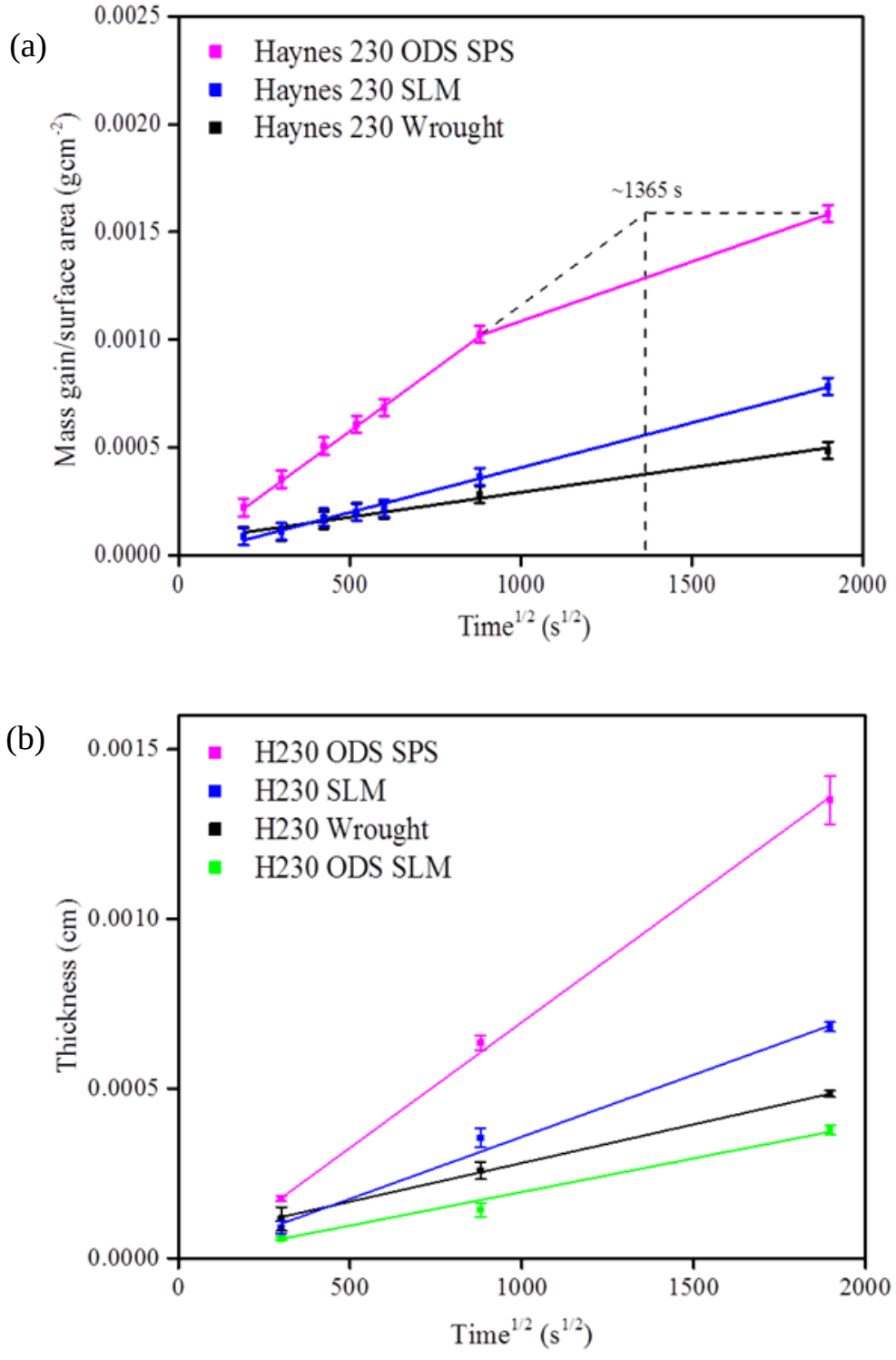

Figure 4.10: Isothermal oxidation of Haynes 230 in laboratory air at 900°C (a) Mass gain/surface area (gcm^{-2}) against Time$^{1/2}$ ($s^{1/2}$), and (b) Scale thickness (cm) against Time$^{1/2}$ ($s^{1/2}$)

4.4 Discussion

Examination of the SLM-consolidated alloys, Alloy 718, Alloy 625 and Haynes 230, showed that they were crack-free and largely free of voids. On the other hand, SLM-consolidated Alloy 625 ODS and SLM-consolidated Haynes 230 ODS were both cracked and contained slag particles and voids, which has been reported during SLM-consolidation of the ferritic ODS alloy PM2000 [66, 67]. The presence of cracks in the specimens has the potential to affect the oxidation results, but because scale thickness measurements were used to determine oxidation rate constants for these alloys, which were taken from positions distant from the cracks, it is considered that the results are valid. Both of the SPS-consolidated alloys were porous, which could result in the parabolic oxidation rate constants being over-estimated by TGA because the true surface area of the coupons is larger than the measured surface area. However, this is not really an issue for Alloy 625 ODS because the oxidation rate is so low, nor is it an issue for Haynes 230 ODS because the oxidation rate is so fast. Alloy 625 ODS, in SLM-consolidated form, contained more defects than SLM-consolidated Haynes 230 ODS. This may be due to solidification cracking, which is known to be an issue for Nb-containing alloys [96, 106]. However, as cracking was only observed in the ODS variant of the alloy, it must be related to the presence of the dispersoids, presumably making the alloy more rigid, or be due to contamination picked-up during MA. SLM-consolidated Haynes 230 ODS was also cracked, but SLM-consolidated Haynes 230 was not, which again implies that either the dispersoids or possibly contamination introduced during MA were responsible for the cracking. The absence of cracking in Alloy 625 ODS/SPS and Haynes 230 ODS/SPS indicates that the effect is probably due to a combination of stresses arising from fast cooling of the SLM-consolidated blocks, and the presence of dispersoids or contamination in the alloys. The porosity evident in the ODS/SPS specimens, again worse for Alloy 625 ODS/SPS than for Haynes 230 ODS/SPS, may be related to the fast heating rate used to consolidate the specimens i.e. ~150Kmin^{-1}. Fast heating rates have been reported to cause porosity in alloys during consolidation by SPS [83-85].

Formal tests were not made to assess the reproducibility of the methodology used, but the rate constants k_w and k_p, obtained for P600 and P4000 grit finished coupons of wrought Alloy 718, differed by <1% and <5% respectively. This gives some confidence in the robustness of the methodology employed. Unfortunately, there was not time within the project to run Repeatability and Reproducibility (R&R) studies, which means that the kinetics results can only be assessed by reference to the literature. This is extremely difficult because the results are so dependent on the methodology used to obtain them. However, comparisons show that the parabolic rate constants obtained for the wrought alloys in the present work are generally slower than those reported in the literature [180-182, 185, 194, 196]. On the other hand, the parabolic oxidation rate constant determined for MA754, obtained using the same methodology used for the alloys studied for the present work, is in very good agreement with that reported by Pint and Wright [210]. Irrespective of possible differences between the results obtained for the present work and those reported in the literature, the comparisons made between the various alloys studied in this work are valid because the alloys were tested under the same experimental conditions.

The wrought alloys oxidised in the order Alloy 718>Alloy 625>>Haynes 230, which is an agreement with typical literature results. The SLM-consolidated variants of the same alloys oxidised in the order Alloy 718>Haynes 230>Alloy 625. The change in order, with respect to the wrought alloys, is surprising and occurs because SLM-consolidated Haynes 230 oxidises ~3x faster than the wrought alloy, while SLM-consolidated Alloy 625 oxidises at a rate ~0.2-0.5x that of the wrought alloy. The ODS alloys oxidised in the order Haynes 230 ODS/SPS>>Haynes 230 ODS/SLM>MA754>Alloy 625 ODS/SPS>>Alloy 625 ODS/SLM, which clearly shows that Alloy 625 ODS has, based on its high temperature oxidation behaviour, potential as a high temperature alloy. The improvement in the oxidation resistance of Alloy 625, arising from the addition of Y_2O_3, is consistent with the reactive element effect, and is very similar to that obtained for an ODS alloy having the composition Ni-20Cr-20Fe-5Nb-1Y_2O_3 [189]. It is possible that Nb, present in Haynes 230 ODS

and Ni-20Cr-20Fe-5Nb-1Y_2O_3, but absent from the commercial comparator alloys PM1000 and MA754, may contribute to the oxidation resistance of ODS alloys, but additional work is needed to verify this. The results also show that there are major problems with Haynes 230 ODS in SPS-consolidated form, and even in SLM-consolidated form, the alloy oxidised only slightly better than the wrought alloy on which it is based. The improvement obtained by SLM-consolidation of Haynes 230 ODS may be related to the 'slagging off' of reactive elements, as observed in the optical micrographs. This suggests that the alloy was overdoped, which is known to produce fast rates of oxidation, or that the alloy was contaminated during SPS-consolidation. It is known that C contamination can occur during SPS-consolidation [75, 226], but it is difficult to predict the likely effect of any C contamination on the oxidation resistance of the alloy.

The TGA data obtained for Haynes 230 ODS/SPS could not be fitted according to a single parabolic oxidation rate constant, but the scale thickness data could. However, it was also found that that the TGA data could be fitted using a paralinear equation of the type used to describe kinetics for the simultaneous oxidation of chromium and vaporisation of chromia [227, 228]. This is of the form:

$$\frac{m}{a} = \left(k_w t\right)^{0.5} - k_l t \qquad \text{Equation 5}$$

Where m, a, t and k_w have their usual meanings, and k_l is a linear rate constant in units of $gcm^{-2}s^{-1}$

The data fitted using Equation 5 is shown in Figure 4.11. It is worth noting that paralinear equations are usually used to describe the formation of a compact scale at the scale/alloy interface during oxidation, which grows under diffusion control, and a porous non-protective scale that grows at a linear rate at the scale/gas interface [229, 230]. However, the TGA data for Haynes 230 ODS could not be fitted using this

particular model, in which k_w and k_l are additive. The value obtained for the parabolic rate constant k_w, corresponding to scale growth, determined using Equation 5, was 5.20E-13 $g^2cm^{-4}s^{-1}$. This is essentially the same as the smaller of the two limiting values determined using two parabolic equations. The linear rate k_l, which corresponding to chromia loss, was determined to be 2.57E-10 $gcm^{-2}s^{-1}$. It was thought that Cr losses due to evaporation would be small at 900°C, but Young has stated that chromium losses can be significant at >900°C at an oxygen partial pressure of 1 atm. via the reaction $Cr_2O_3(s) + ½\ O_2(g) = 2CrO_3(g)$ [120]. Berthod has calculated Cr losses from a Ni-30Cr alloy at 1000°C to be ~0.9E-10 $gcm^{-2}s^{-1}$ [231], and Gindorf reported Cr losses of 4.05E-10 $gcm^{-2}s^{-1}$ for a Cr-5Al-1Y_2O_3 ODS alloy at 950°C [232]. Therefore, it may be possible that chromia vaporisation is a valid explanation for the TGA result. However, this result is at odds with (i) the scale thickness results, which are consistent with parabolic growth for the full duration of the experiment, (ii) the absence of similar results for any of the other alloys, which were oxidised under the same conditions, and (iii) the presence of a spinel layer at the scale/gas interface, which is known to reduce the vaporisation of chromia. Therefore, it seems unlikely that vaporisation of the scale was the cause of the non-parabolic TGA data, but it cannot be ruled out.

It must also be considered that the anomalous TGA result could be due to experimental error, and that one or more of the coupons was weighed incorrectly. However, it is difficult to envisage how all 6 coupons oxidised for 10-215 hours of oxidation, and consistent with a single parabolic oxidation rate constant, could have been weighed incorrectly. This leaves the final data point, obtained after 1000 hours of oxidation, as suspect. This coupon was re-weighed, but was found to have been weighed correctly. It is possible that the coupon was weighed incorrectly prior to oxidation, but it is unlikely because the difference between the expected mass gain following 1000 hours of oxidation, assuming parabolic growth at the rate determined between 10 and 215 hours of oxidation, and the actual mass gain is so large, at

~0.0005gcm^{-2}. Because the coupon had a surface area of ~2cm^2, the weighing error would be ~0.001g. An examination of the graph produced for the long term thermal stability of the crucible 'sets', Figure 3.4, shows that the maximum deviation of the standard block from the long term average, which encompasses many measurements, was 0.0002g i.e. ~5x smaller than the supposed weighing error. It is therefore difficult to see how the discrepancy could be due to a problem with the balance, or human error. It should also be noted that the coupon was weighed 5 times prior to oxidation, as were all of the coupons. There was insufficient alloy to repeat the experiment. The most convincing explanation for the discrepancy between the TGA and scale thickness data is mass gain arising from a source other than the scale at oxidation times <215 hours, which slowed or stopped between 215 hours and 1000 hours of oxidation i.e. the scale measured following 215 hours of oxidation is too thin, rather than the unit mass gain at 1000 hours is too low. This is apparent because of the rough equivalence of the unit mass gain and scale thickness data, for all of the alloys, and can be seen for the Haynes 230 variants in Figures 4.7 and 4.10. It is noted that the only data points at variance with this 1:1 approximation are the TGA and scale thickness data points for Haynes 230 ODS/SPS following 215 hours of oxidation. The scale thickness results were checked and found to be correct. This subject will be revisited in Chapter 7.

Alloy 625 ODS/SPS was processed in the same way as Haynes 230 ODS/SPS, and had the same reactive element addition of 0.5 Wt. %, but had excellent oxidation resistance properties. There was a near 40 fold improvement in the oxidation resistance of Alloy 625 ODS, based on k_w, compared to wrought Alloy 625. It is also noted that Alloy 625 Hf-ODS/SPS had a total reactive element addition of ~1.0 Wt. %, which is very high by modern day standards and would, it might be thought, make the alloy susceptible to over-doping. Pint, in his paper describing the 'dynamic segregation theory', consciously ignored the results obtained from alloys containing reactive element additions >0.5 at. % on the grounds that they were probably overdoped [23]. The very small mass gains obtained for Alloy 625 ODS/SPS and

Alloy 625 Hf-ODS/SPS indicate that the scales grew at a very slow rate, or that spalling of the scales had occurred. Spalling of the scale was not observed to occur during the oxidation of Alloy 625 ODS/SPS, or Alloy 625 Hf-ODS/SPS, which indicates that the base alloy is very tolerant of reactive element additions. The results obtained from Alloy 625 ODS appear to show the SLM-consolidated variant to be more oxidation resistant than the SPS-consolidated variant, which may be inferred as an above optimal reactive element addition to the MA powder, with the excess being reduced by slag formation during consolidation. The fact that Alloy 625 Hf-ODS oxidised at essentially the same rate as Alloy 625 ODS/SPS, despite containing twice as much reactive element, may also be consistent with the reactive element addition in Alloy 625 ODS being above optimal. It should also be noted that the oxidation rate of Alloy 625 ODS/SLM was determined from scale thickness measurements, which is a less reliable method than using TGA data because scale thickness measurements are obtained over a very small length of scale.

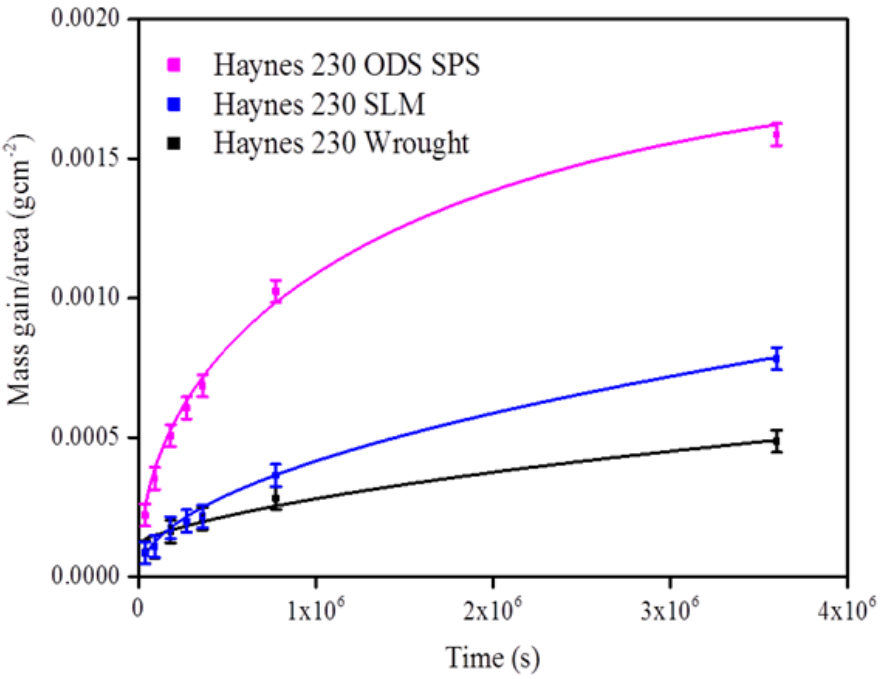

Figure 4.11: Isothermal oxidation of Haynes 230 in laboratory air at 900°C - Mass gain/surface area (gcm^{-2}) against Time (s) showing paralinear fit for Haynes 230 ODS/SPS

4.5 Chapter summary

Isothermal oxidation rate constants were determined for SLM-consolidated and wrought variants of Alloy 718, Alloy 625 and Haynes 230, and ODS variants of Alloy 625 and Haynes 230 following their consolidation by SLM and SPS. The oxidation experiments were conducted in laboratory air at 900°C for exposure times of up to 1000 hours, and the rate constants determined using TGA and, or from, scale thickness measurements obtained in a SEM.

All of the alloys, except for Haynes 230 ODS/SPS, oxidised according to parabolic oxidation kinetics. The scale thickness data for Haynes 230 ODS/SPS was fitted using a parabolic equation, but the TGA data could only be fitted using two parabolic equations, or a paralinear equation corresponding the simultaneous growth and vaporisation of chromia. However, it is felt that this mechanism is unlikely to be operative, and the most likely reason for the discrepancy is mass gain arising from a source other than scale formation. This occurred at a parabolic rate during the first 215 hours of oxidation, but thereafter slowed or stopped. It is thought unlikely that the discrepancy is related to an experimental error.

The wrought alloys oxidised in the order Alloy 718>Alloy 625>>Haynes 230, but the SLM-consolidated variants of the same alloys oxidised in the order Alloy 718>Haynes 230>Alloy 625. This was due to a significant improvement in the oxidation resistance of SLM-consolidated Alloy 625, but a significant degradation in the oxidation resistance of SLM-consolidated Haynes 230. The oxidation resistance of Alloy 718 was ~20% worse in the SLM-consolidated form than in the wrought form.

The ODS alloys oxidised in the order Haynes 230 ODS/SPS>>Haynes 230 ODS/SLM>MA754>Alloy 625 ODS/SPS>>Alloy 625 ODS/SLM. These results show that there is a problem with Haynes 230 ODS/SPS, possibly as a result of overdoping of the MA powder from which the alloy was consolidated. The effect

may have been ameliorated in the SLM-consolidated alloy by ‘slagging off’ of excess reactive elements during consolidation. Based on its oxidation behaviour, Alloy 625 ODS has potential as a high temperature alloy showing a near 40 fold improvement in oxidation resistance with respect to the wrought alloy.

CHAPTER 5

ALLOY 718

5.1 Introduction

SLM-consolidated Alloy 718 and Wrought Alloy 718 were characterised following high temperature isothermal oxidation at 900°C for durations of up to 1000 hours. Results obtained from the characterisation of the alloy prior to oxidation are presented in section 5.2, and includes subsections 5.2.1, SLM-consolidated Alloy 718, and 5.2.2, Wrought Alloy 718. The results obtained from the characterisation of the oxidised alloy are presented in section 5.3, and includes subsections 5.3.1, XRD analysis, 5.3.2, Initial examination of oxidised alloy, 5.3.3, Detailed examination of scale morphology, 5.3.4, Internal oxide at scale/alloy interface, 5.3.5, Oxidation-induced changes in alloy, 5.3.6, Oxidation of carbides in wrought alloy, and 5.3.7, Effect of surface preparation on oxidation. The results are discussed in section 5.4, and a chapter summary is provided in 5.5.

5.2 Characterisation of Alloy

5.2.1 SLM-consolidated Alloy 718

The alloy had a columnar grain structure orientated parallel to the build direction, which had grown through multiple layers of the build, Figure 5.1 (a). The grain structure was comprised of dendrites/cells and the inter-dendritic/cell spacing was ~1µm, Figure 5.1 (b). The high average atomic number phase present on the dendrite/cell boundaries was rich in Nb and is likely to be Laves phase, which has been identified by others as present in SLM-consolidated Alloy 718 [97-100]. Laves phase has a nominal composition (Ni, Cr, $Fe)_2$ (Nb, Mo, Ti) [93]. The alloy was

heat-treated at 954°C for 30 minutes, followed by air cooling. This appeared to modify, but did not destroy, the underlying columnar microstructure of the alloy, Figure 5.1 (c). This observation is consistent with the work of Liu et al, who found that the microstructure of SLM-consolidated Alloy 718 could only be modified at temperatures >1100°C [233]. The Laves phase was replaced during heat-treatment by a Nb-rich acicular phase, Figure 5.1 (d). This is consistent with the dissolution of Laves phase and the precipitation of δ-phase, which is expected to occur during solutionising of Alloy 718 [88].

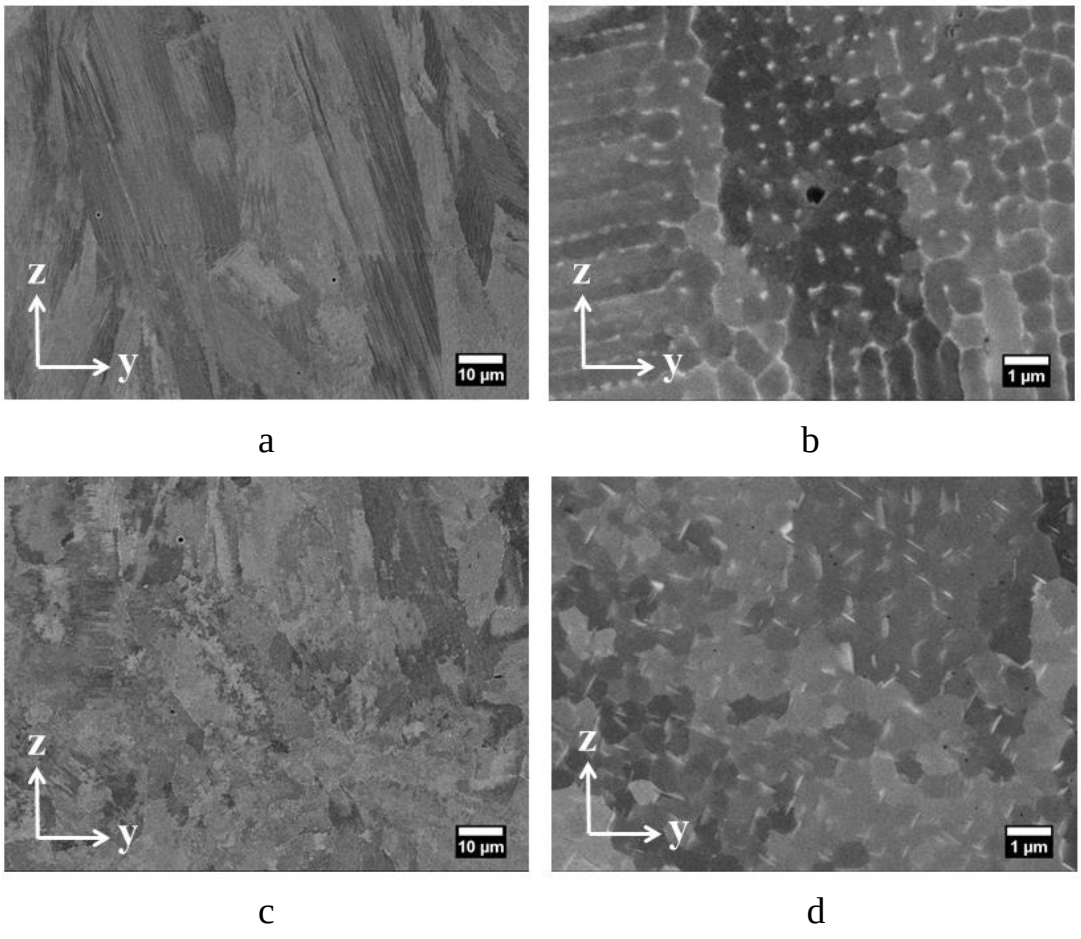

Figure 5.1: BSE micrographs of longitudinal section of SLM-consolidated Alloy 718 (a), (b) before heat-treatment, and (c), (d) after heat-treatment

5.2.2 Wrought Alloy 718

The alloy contained numerous inclusions of ~1-10μm in size, which occupied a mean volume fraction of ~0.2 %, and were orientated in the extrusion direction of the alloy, Figure 5.2 (a). These have been identified by other workers as MC-type carbides, which have (Nb,Ti)C and (Ti,Nb)C compositions [93]. A phase rich in Ni, Nb and Ti was present on many of the grain boundaries, which is probably δ-phase, Figure 5.2 (b). The alloy had an equiaxed grain structure with a grain size of ~30μm.

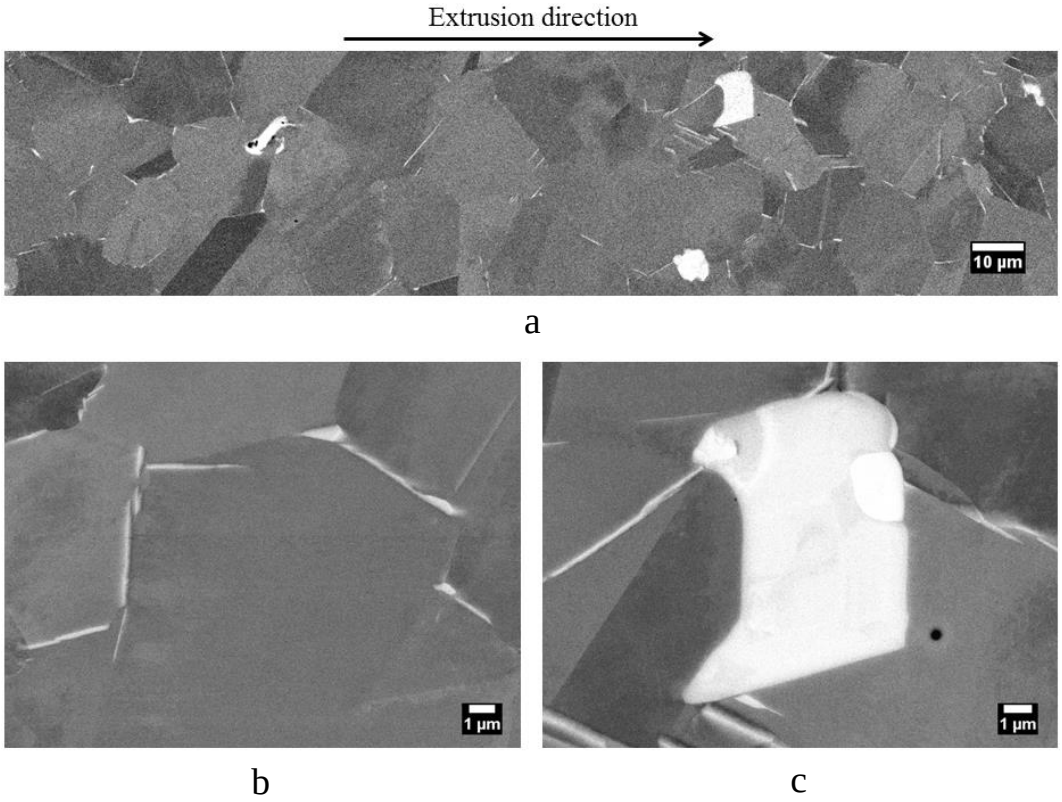

Figure 5.2: BSE micrographs of transverse section of wrought Alloy 718 (a) grain-boundary δ-phase and carbides, (b) detail of δ-phase, and (c) detail of Nb(Ti)C carbide reveals segregation

5.3 Characterisation of oxidised alloy

5.3.1 XRD Analysis

Diffractograms obtained from the SLM-consolidated alloy and the wrought alloy, following 25, 215 and 1000 hours of oxidation, are presented in Figure 5.3. Both variants of the alloy formed a scale mainly comprised of Cr_2O_3. TiO_2 was also detected, as was the intermetallic δ-phase, Ni_3Nb, which is reported to form during oxidation as a discrete layer at the scale/alloy interface [181]. It has been reported that the texture of SLM-consolidated Ni-base superalloys, including Alloy 718, is <100> in the build direction [234, 235].

5.3.2 Initial examination of oxidised alloy

Ridges grew in the scale that formed on the SLM-consolidated alloy, which thickened and coalesced with increasing oxidation time, Figures 5.4 (a) and 5.4 (b). The ridges persisted to 1000 hours of oxidation and their presence shows that Cr diffusion was faster via the grain boundaries of the alloy than the dendrite/cell boundaries. It also shows that diffusion, either of Cr or O, or both, was faster through the scale formed over the grain boundaries of the alloy. Ridges also formed in the scale on the P600 grit finish wrought alloy, but these were less evident and did not persist for as long as those formed on the SLM-consolidated alloy, Figures 5.4 (c) and 5.4 (d). A large population of oxidised inclusions littered the oxidised surfaces of the wrought alloy, but these were absent from the oxidised surfaces of the SLM-consolidated alloy, consistent with the observations made using optical microscopy and reported in Chapter 4.

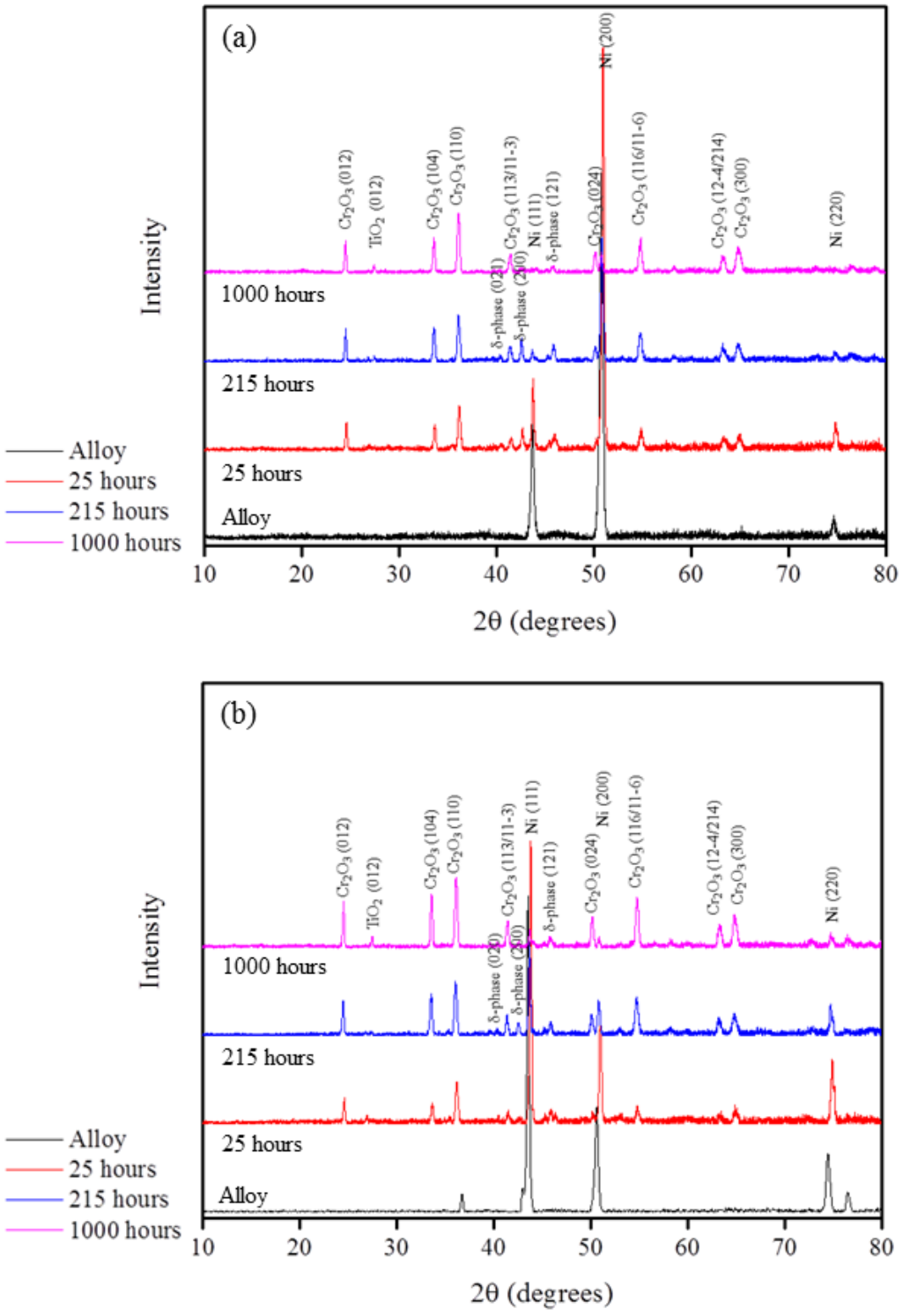

Figure 5.3: Diffractograms obtained from SLM-consolidated Alloy 718 following isothermal oxidation in laboratory air at 900°C (a) SLM-consolidated, and (b) Wrought (P600 grit finish)

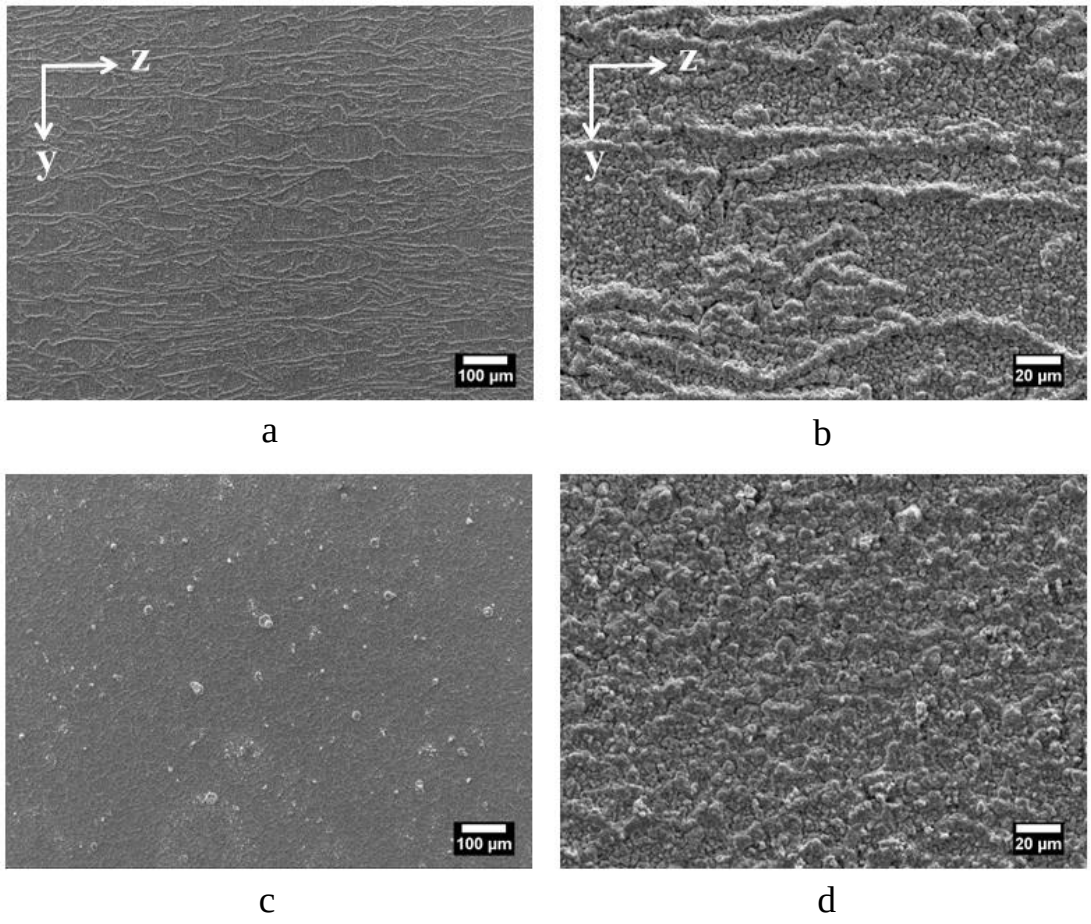

Figure 5.4: SE micrographs of ridges in scale on Alloy 718 following isothermal oxidation in laboratory air at 900°C (a) Alloy 718 SLM oxidised for 215 hours, (b) Alloy 718 SLM oxidised for 1000 hours, (c) Wrought alloy oxidised for 215 hours (P600 grit finish), and (d) Wrought alloy oxidised for 1000 hours (P600 grit finish)

A relatively thick scale formed on the surface of the alloy during oxidation, Figures 5.5 and 5.6. During the early stages of oxidation, the δ-phase present in the SLM-consolidated alloy coarsened on the grain boundaries of the alloy and became blocky in shape. In the wrought alloy, intragranular δ-phase formed. Dissolution of the δ-phase occurred in both variants of the alloy, which started within the first 25 hours of oxidation, resulting, after 1000 hours of oxidation, in a δ-phase-depleted zone of ~20µm. Concomitant with depletion of δ-phase in the oxidation-affected zone of the alloy was the formation of a layer of δ-phase at the scale/alloy interface. This was

initially semi-continuous and <1µm thick, but grew to a continuous layer of ~5µm thickness after 1000 hours of oxidation. Particles of δ-phase were incorporated into the scale, probably by inward growth of the scale or due to deformation of the scale at the scale/alloy interface in order to maintain contact with the alloy, Figure 5.7. A layer of small grains formed at the surface of the alloy during the early stages of oxidation, as a result of recovery and recrystallisation of cold work damage caused during preparation of the coupons prior to oxidation. These acted as pathways for the ingress of O, as a result of which internal oxide particles precipitated on them. Deep oxide fissures formed at the grain boundaries of the wrought alloy, which reached a depth of ~15µm after 1000 hours of oxidation. This is comparable to the depth of the zone depleted of δ-phase. In the SLM-consolidated alloy, the internal oxide formed a network of intergranular and intragranular oxide. Also present in the SLM-consolidated alloy, but absent from the wrought alloy, was a dispersion of spheroidal oxide particles, of 100-200nm in size. These were present in the alloy to a depth of ~60µm.

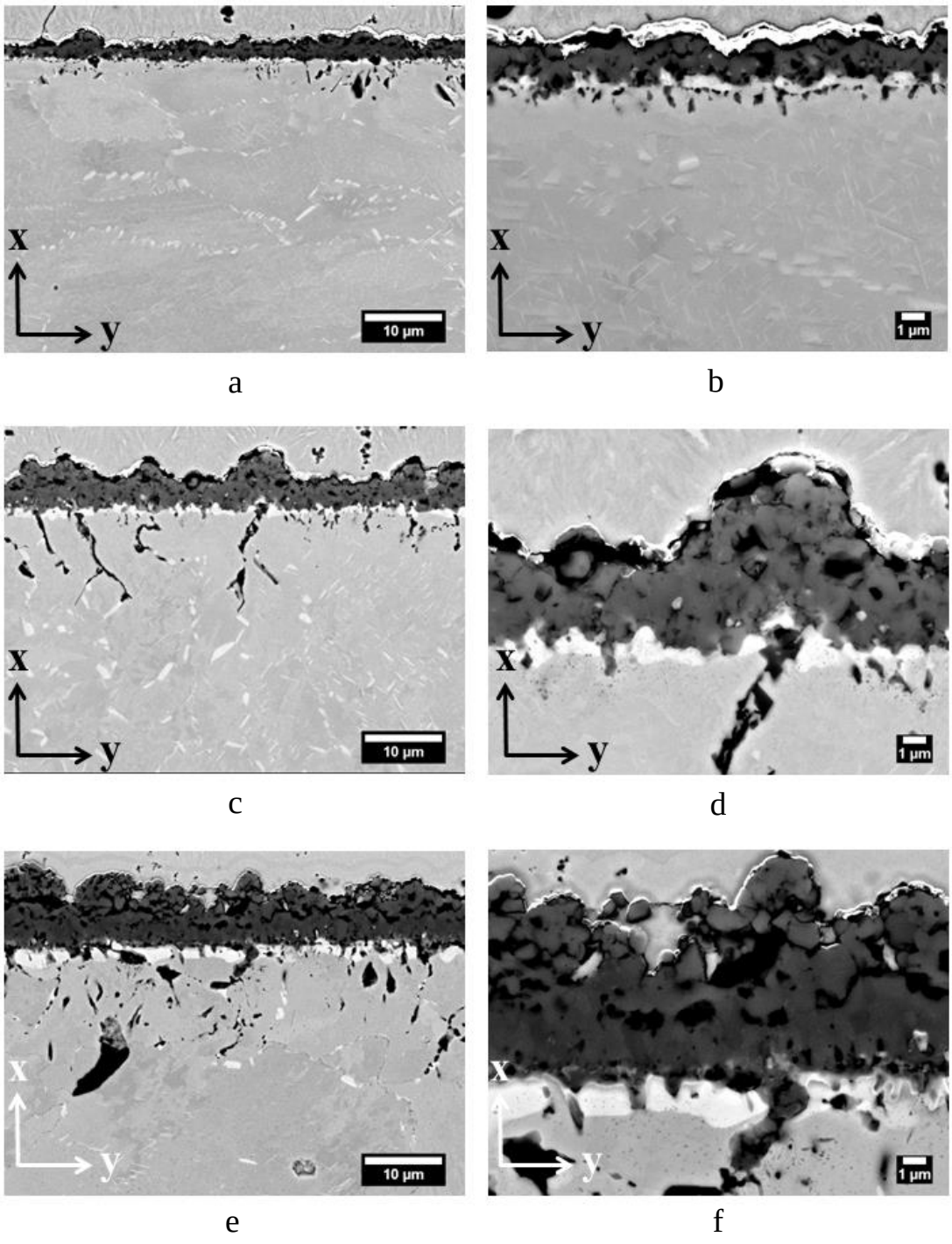

Figure 5.5: BSE micrographs of cross-sections of SLM-consolidated Alloy 718 following isothermal oxidation in laboratory air at 900°C (a), (b) 25 hours, (c), (d) 215 hours and (e), (f) 1000 hours

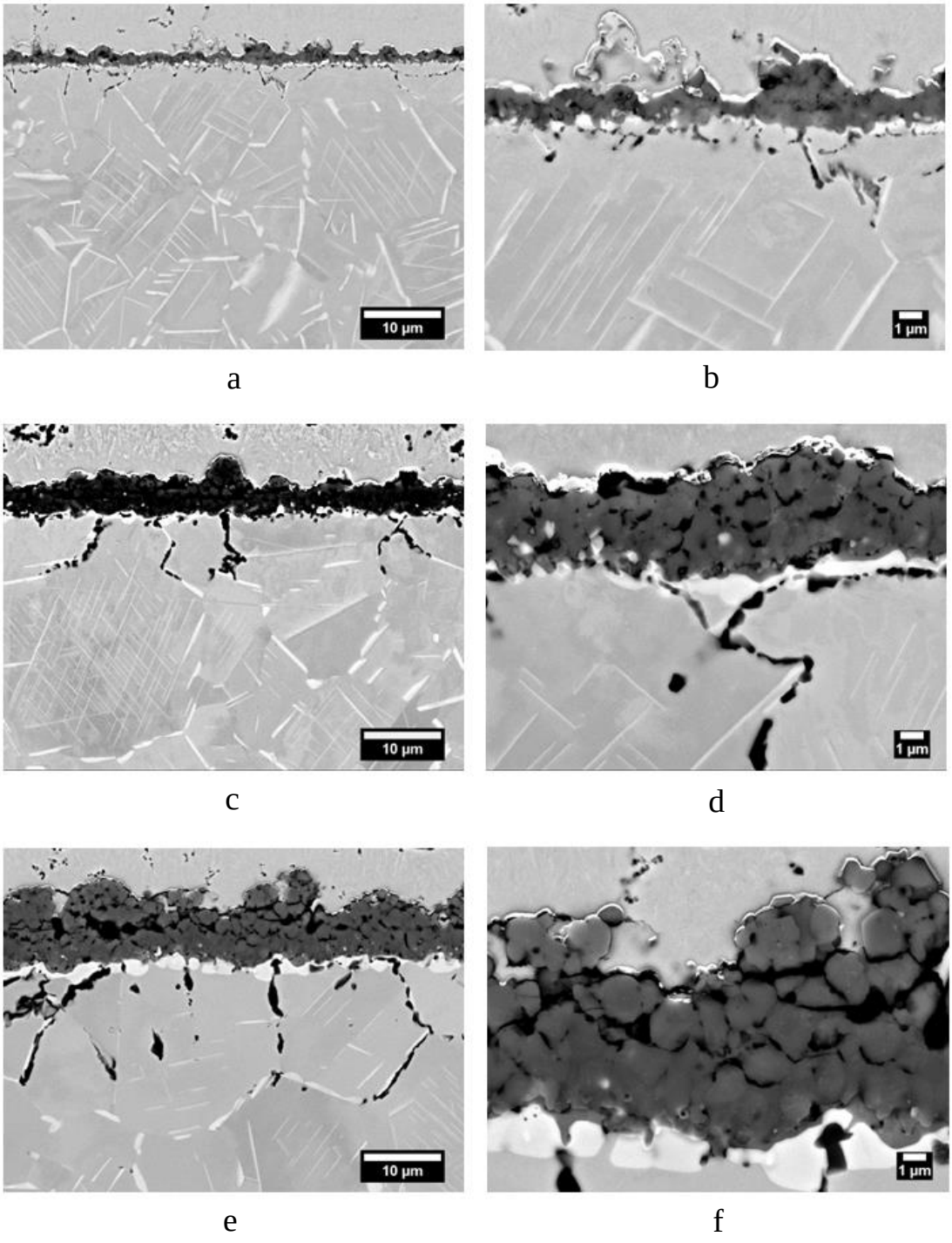

Figure 5.6: BSE micrographs of cross-sections of wrought Alloy 718 (P600 grit finish) following isothermal oxidation in laboratory air at 900°C (a), (b) 25 hours, (c), (d) 215 and (e), (f) 1000 hours

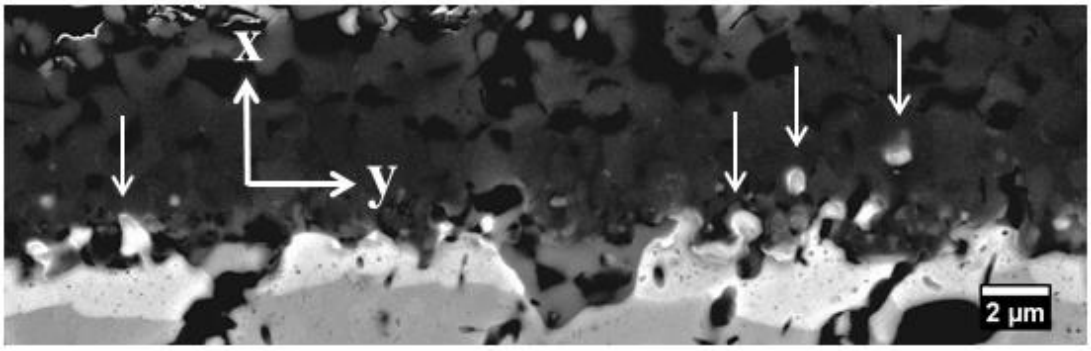

Figure 5.7: BSE micrograph of discrete particles of δ-phase (arrowed) in the process of being incorporated into the scale formed on SLM-consolidated Alloy 718 following 215 hours of isothermal oxidation in laboratory air at 900°C

Element maps, obtained from cross-sections of the SLM-consolidated alloy and the wrought alloy following 215 hours of oxidation, are presented in Figures 5.8 and 5.9 respectively. Cr is depleted at the surface of the alloy, as a result of scale-formation, but Fe is enriched to the same depth. The presence of Nb-rich δ-phase at the scale/alloy interface is evidenced in both maps.

Al-rich internal oxide is more extensive in the SLM-consolidated alloy than in the wrought alloy. Ti-rich internal oxide is also present to a greater depth in the SLM-consolidated alloy, but is more strongly concentrated in the wrought alloy at the scale/alloy interface and at the scale/gas interface, particularly where the scale is thickest. Ti is depleted in the alloy below where it is concentrated at the scale/alloy interface or at the scale/gas interface. In the SLM-consolidated alloy, Ti is concentrated on the grain boundaries below the Ti-depleted zone, possibly as a result of oxidation deep within the alloy – evidence of this is also present in the form of spherical oxide precipitates, rich in Al and O, but too small to be observed in the Al and O maps, which were present in the SLM-consolidated alloy to a depth of ~60µm.

Image analysis was used to determine the area fraction of internal oxide in the mapped region of the SLM-consolidated alloy – this was equivalent to a layer 3.3µm thick, of which 1.7µm was rich in Al and O, and 1.6µm rich in Ti and O. At a second position the total internal oxide was estimated to be equivalent to a layer 0.8µm thick, which is ~0.25x that of the first position and indicates how inhomogeneous oxidation can be. The internal oxide in the wrought alloy was estimated, by the same method, to be equivalent to a layer 0.3µm thick, of which 0.1µm was Al-rich oxide and 0.2µm Ti-rich oxide. These results show that the SLM-consolidated alloy contained more internal oxide; there was essentially an equivalence of Al-rich and Ti-rich internal oxides in the two variants of the alloy.

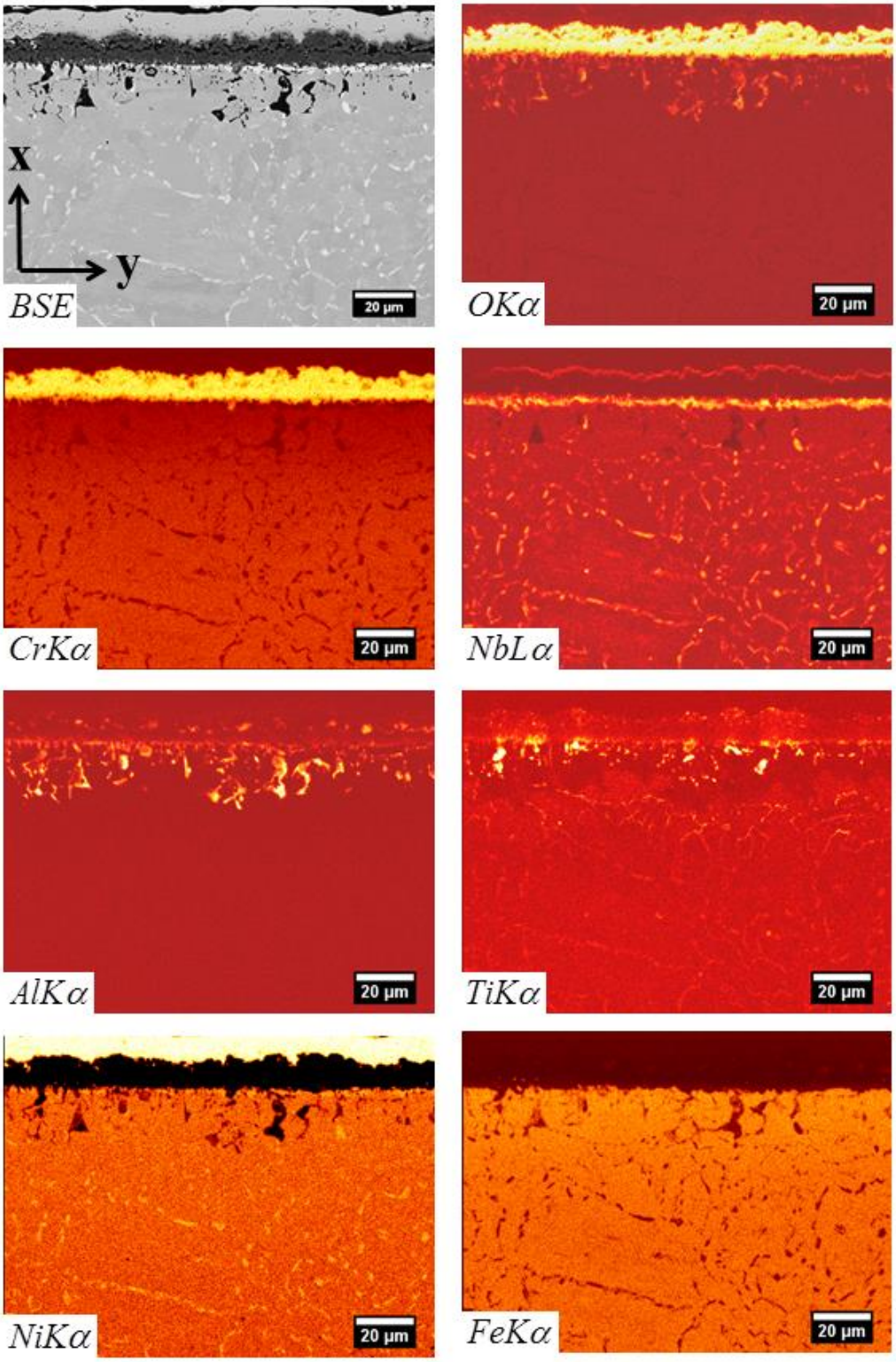

Figure 5.8: Element maps obtained from a cross-section of SLM-consolidated Alloy 718 following 215 hours of isothermal oxidation in laboratory air at 900°C

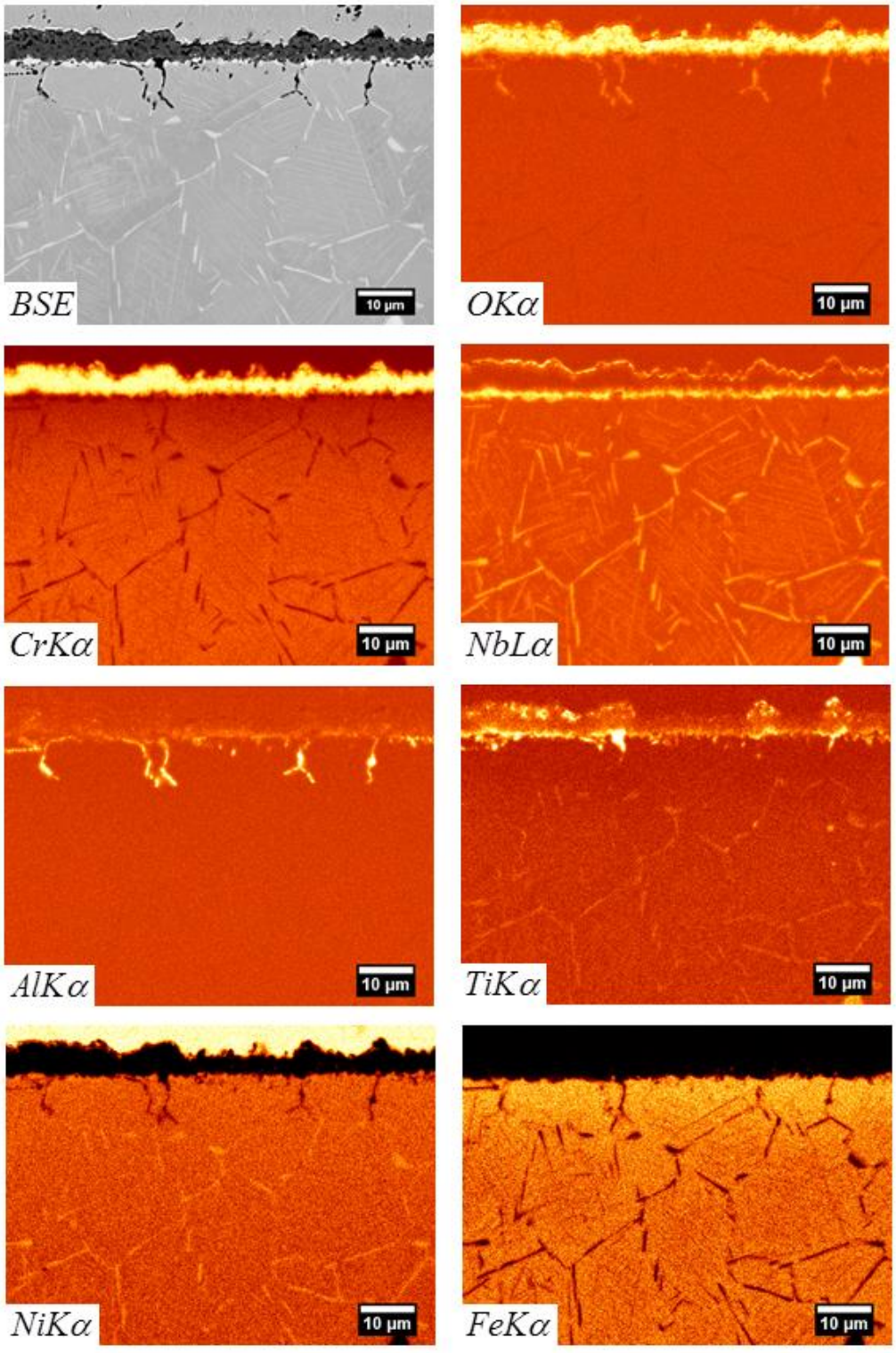

Figure 5.9: Element maps obtained from a cross-section of wrought Alloy 718 (P600 grit finish) following 215 hours of isothermal oxidation in laboratory air at 900°C

5.3.3 Detailed examination of scale morphology

The scale formed on both variants of the alloy was, after 1000 hours of oxidation, comprised of blocky oxide grains, Figure 5.10. In cross-section, Figures 5.11 and 5.12, the scale formed on the SLM-consolidated alloy was, after 25 hours of oxidation, comprised of small columnar grains whereas the scale formed on the wrought alloy was comprised of slightly larger and more blocky grains. The scale had grown more thickly over the grain boundaries of the alloy after 1000 hours of oxidation, particularly on the SLM-consolidated alloy. The oxide grains in both scales were ~1μm in size, but were possibly slightly smaller and more columnar in the scale formed on the SLM-consolidated alloy. Layers of smaller grains were present at the scale/alloy interface and at the scale/gas interface, an effect more noticeable on the SLM-consolidated alloy. These observations may be consistent with nucleation of the oxide grains at the interfaces, and competitive growth in the bulk scale. The ratio of nucleation to growth appeared larger for the SLM-consolidated alloy, which may be related to a greater flux of Cr through the SLM-consolidated alloy, possibly as result of enhanced transport in the grain boundaries and dendritic/cellular substructure. Grain orientation, which is different for the two variants of the alloy, can also affect oxidation rates [236]. Voids of ~100-200nm in size were present on the grain boundaries of the scale formed on the SLM-consolidated and the wrought alloy. The voids were concentrated in the thick scale above the grain boundaries of the SLM-consolidated alloy and often multiple voids were present on a single grain boundary, with triple points favoured sites. Intergranular cracks were also evident in the scales. Voids and cracks can form in oxide scales as a result of mechanical damage arising from sample preparation, but in the case of the SLM-consolidated alloy the same voids and intergranular cracks were observed in a cross-section prepared by FIB. It is likely, therefore, that the voids and cracks present in the scale on the SLM-consolidated alloy formed during oxidation. It is possible that this is also the case for the wrought alloy. It has been reported that interconnected voids and cracks may increase the gas permeability of a scale and therefore the oxidation kinetics of the underlying alloy [137, 237].

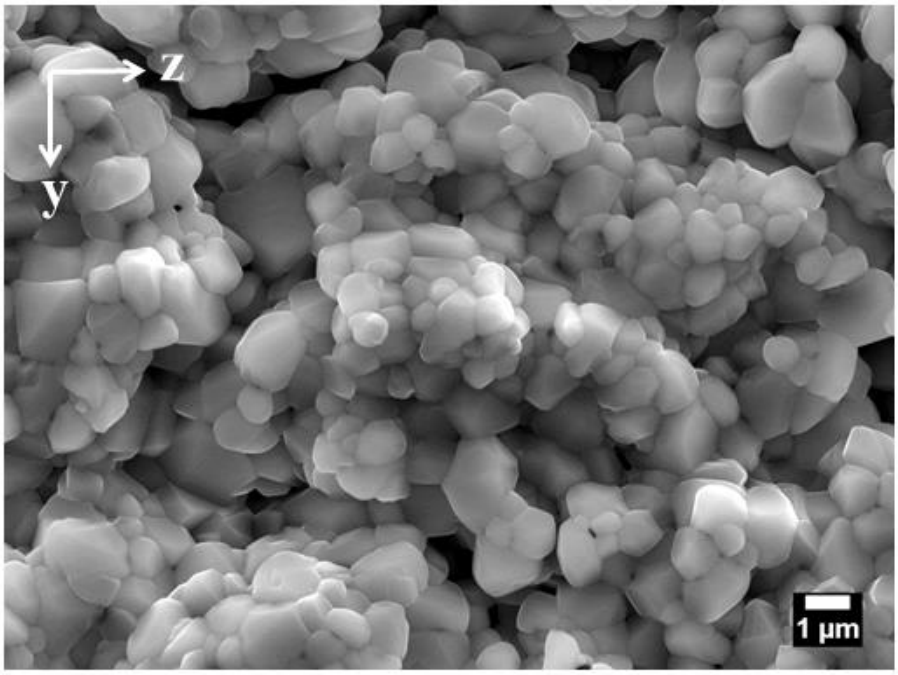

a

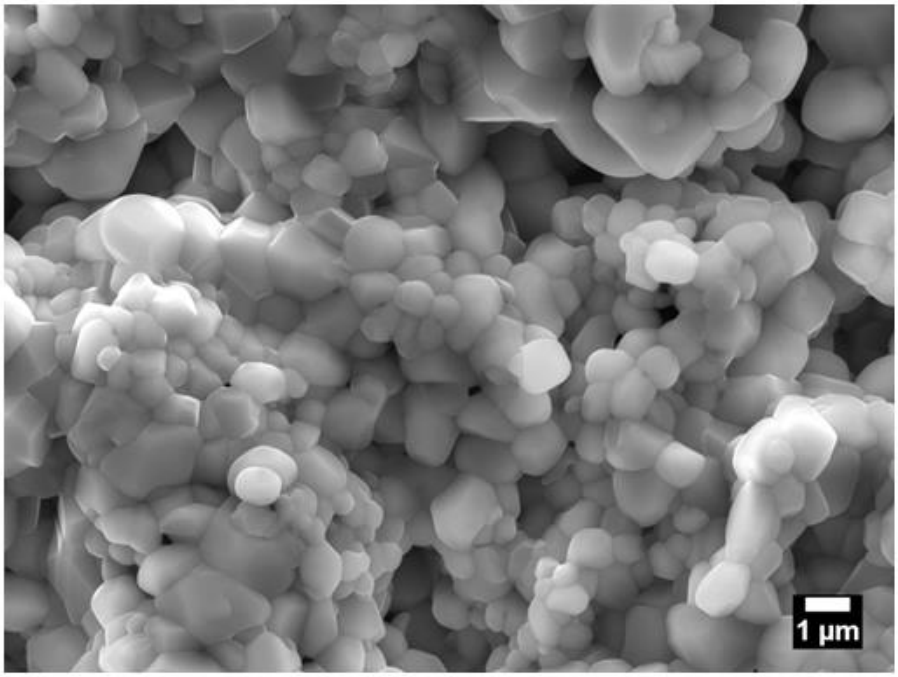

b

Figure 5.10: SE micrographs of scale on Alloy 718 following 1000 hours of isothermal oxidation in laboratory air at 900°C (a) SLM-consolidated, (b) Wrought (P600 grit finish)

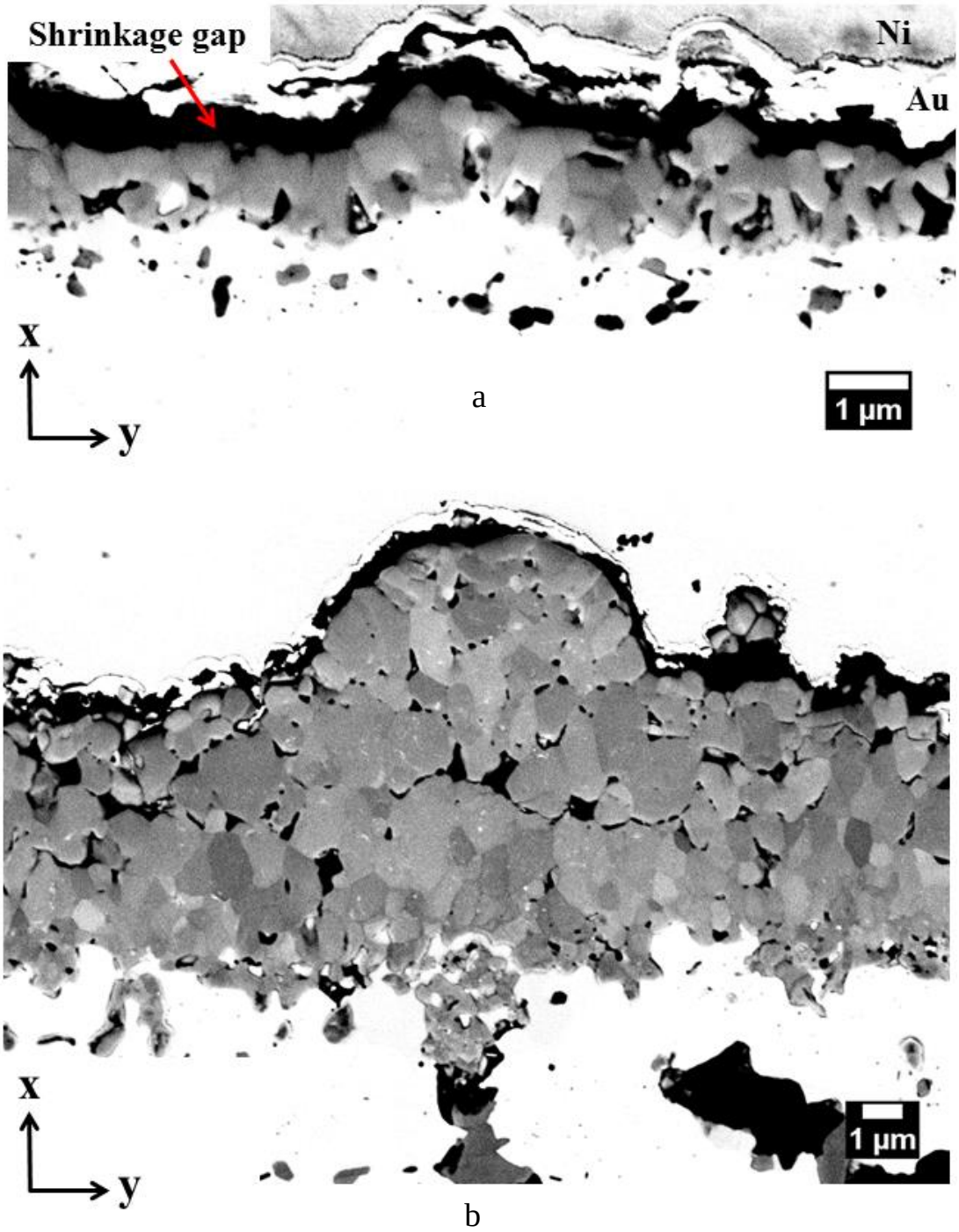

Figure 5.11: Low voltage channelling contrast micrographs of the scale formed on SLM-consolidated Alloy 718 following isothermal oxidation in laboratory air at 900°C (a) 25 hours, and (b) 1000 hours

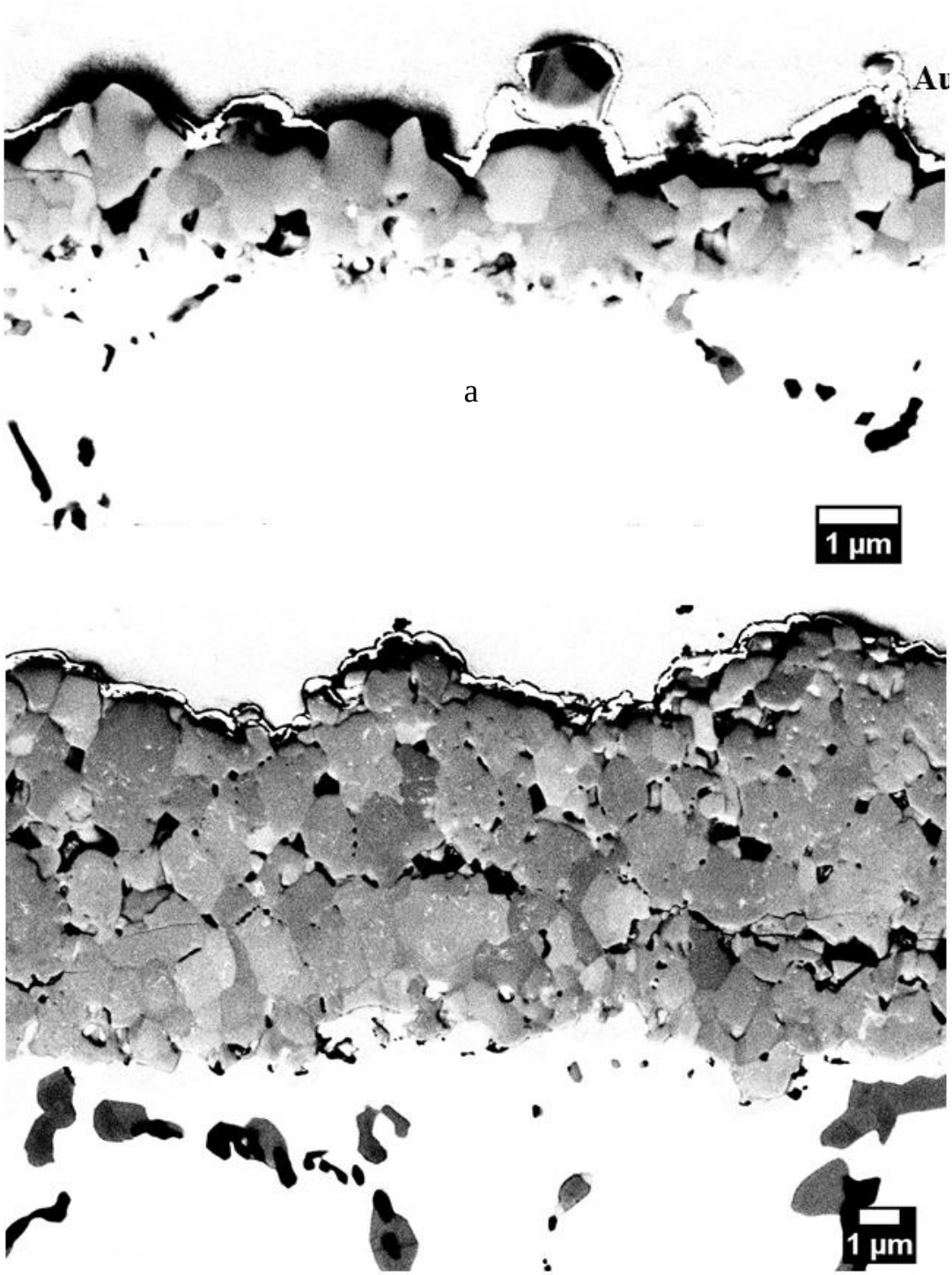

a

b

Figure 5.12: Low voltage channelling contrast micrographs of the scale formed on wrought Alloy 718 following isothermal oxidation in laboratory air at 900°C (a) 25 hours, and (b) 1000 hours

5.3.4 Internal oxide present at the scale/alloy interface

A layer of Ti-rich internal oxide was present in both variants of the alloy at the scale/alloy interface. After 1000 hours of oxidation, a semi-continuous layer of Ti-rich internal oxide had formed in the SLM-consolidated alloy, but a continuous layer of Ti-rich internal oxide had formed in the wrought alloy, Figures 5.13 and 5.14. This is consistent with the element maps shown in section 5.3.2, which showed more Ti-rich internal oxide at the scale/alloy interface of the wrought alloy. This is consistent with the Ti contents, which were 1.00 Wt. % in the wrought alloy and 0.86 Wt. % in the gas atomised powder from which the SLM-consolidated alloy was built.

A series of EDS spectra were collected from the wrought alloy in the SEM using the electron beam focused to a spot. An accelerating voltage of 8kV was used in order to minimise the specimen interaction volume. The analysed positions are indicated by the yellow arrows in Figure 5.14 (b). The internal oxide contained Ti, Cr, Nb and O, but no Ni, as seen in the spectrum denoted ‘position 1’. A spectrum acquired from the δ-phase, ‘position 2’ contains Ni and Nb. The absence of Ni from the spectrum acquired from the internal oxide shows that Nb was present in the internal oxide, and was not detected as a result of sampling of the adjacent δ-phase or alloy.

The stoichiometry of the internal oxide and δ-phase was estimated, using semi-quantitative ZAF procedures, to be ~$Ti_{1.3}Cr_{0.5}Nb_{2.1}O_{6.1}$ and ~Ni_4Nb respectively; the latter, which it is believed to be Ni_3Nb, is probably erroneous because Ni was quantified using NiLα rather than NiKα. The results of this work show that the internal oxide is Ti-rich and contains Nb, and possibly Cr, though this may have been detected as a result of sampling of the base of the chromia scale. The same results were obtained from the SLM-consolidated alloy.

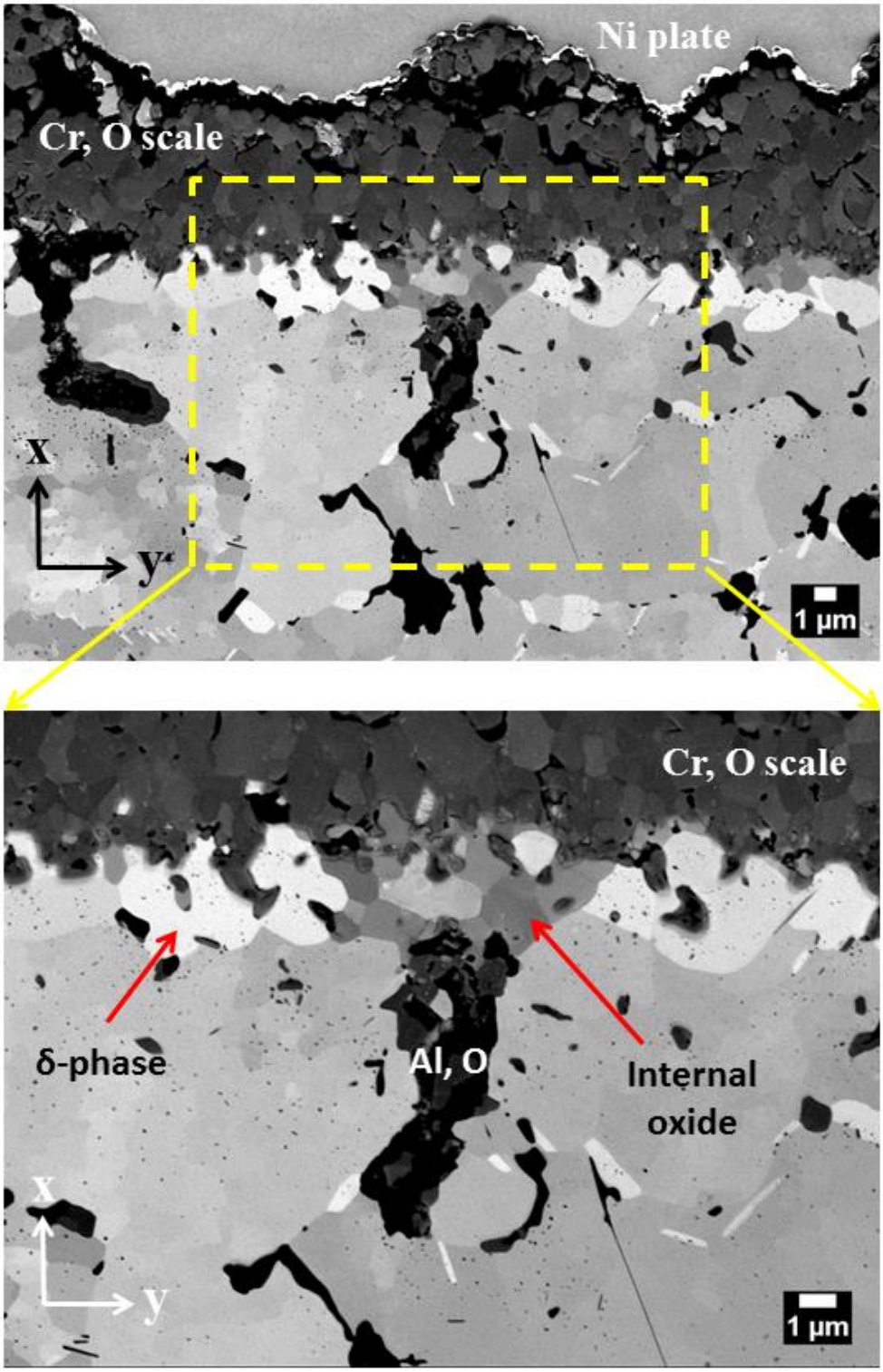

Figure 5.13: Channelling contrast micrographs of internal oxide and layer of δ-phase formed at the scale/alloy interface of SLM-consolidated Alloy 718 following 1000 hours of isothermal oxidation in laboratory air at 900°C

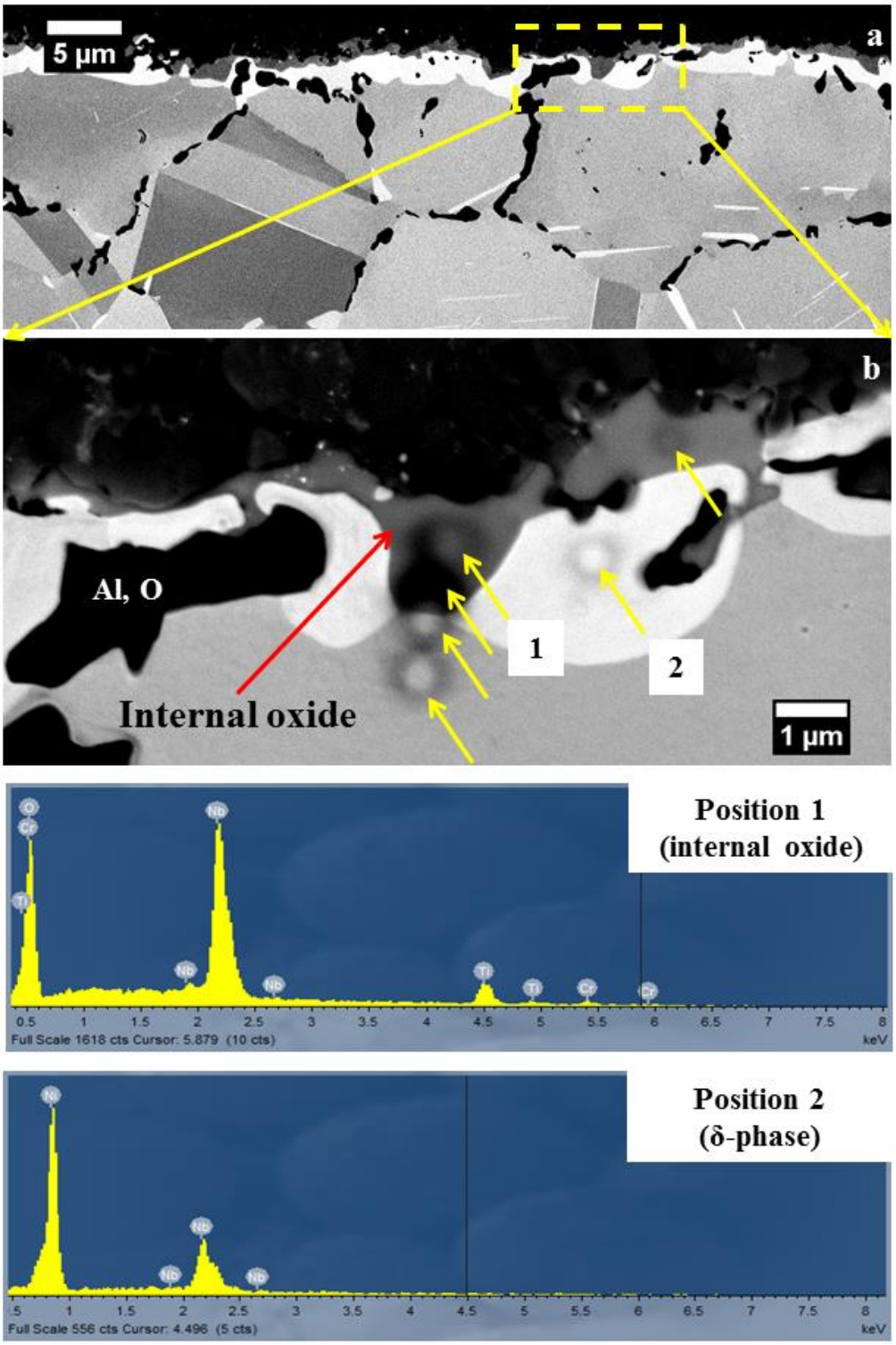

Figure 5.14: Channelling contrast micrographs and EDS spectra from internal oxide and layer of δ-phase formed at the scale/alloy interface of wrought Alloy 718 (P600 grit finish) following 1000 hours of isothermal oxidation in laboratory air at 900°C

5.3.5 Oxidation-induced changes in alloy

Analysis of Bulk Alloy

The composition of the two variants of the alloy was determined from multiple spectra acquired from the centre of cross-sections of the coupons oxidised for 1000 hours. Analysis was performed in the SEM using EDS. This was done in order to establish a terminal composition for the depth profiles, and to confirm that the analyses obtained for the present work were consistent with those provided by the suppliers. The results are provided in Table 5.1, along with the supplier analyses for the gas atomised powder and wrought alloy. The spectra were quantified using ZAF procedures and were normalised to 100%; the results are quoted to the first place of decimals and the minimum detection limit is ~0.1 Wt. %.

The analysis obtained from the SLM-consolidated alloy is in reasonable agreement that of the gas atomised powder from which it was fabricated, though the Nb is low. This may be because the EDS spectra were acquired from the matrix between δ-phase and carbides using the electron beam focused to a spot, whereas the analyses provided by the suppliers were determined using XRF, which is usually a bulk analysis technique. The analysis obtained from the wrought alloy is in good agreement with that provided by the supplier.

Table 5.1: Mean composition and standard deviation of bulk Alloy 718 determined for this work by SEM/EDS (Wt. %). Supplier analyses were obtained by XRF

Alloy	Ni	Fe	Cr	Nb	Mo	Ti	Al
SLM-consolidated (this work)	49.3 ±0.5	21.0 ±0.5	21.6 ±0.5	3.5 ±0.5	3.0 ±0.7	0.7 ±0.1	0.5 ±0.1
Gas atomised powder (supplier)	52.4	19.18	19.0	4.98	3.06	0.86	0.52
Wrought alloy (this work)	51.9 ±0.8	18.0 ±0.6	18.6 ±0.7	5.5 ±0.8	3.7 ±0.3	1.1 ±0.1	0.5 ±0.1
Wrought alloy (supplier)	53.79	17.95	18.05	5.24*	2.90	1.0	0.26

** Includes Ta*

Depth Profiles

Depth profiles obtained from the alloy following 1000 hours of oxidation are presented in Figure 5.15. Cr is depleted to a depth of ~50µm, but Fe is enriched to the same depth. Nb-enrichment is evidence of a layer of δ-phase at the scale/alloy interface, which forms a result of dissolution of the δ-phase in the alloy. This occurred to a depth of ~40µm in the SLM-consolidated alloy, and ~50-60µm in the wrought alloy. δ-phase is indicated in the profiles by upward 'spikes' in the Nb concentration; the presence of such 'spikes', indicated by red arrows in the depth profiles, shows that the δ-phase had not fully dissolved in the δ-phase-depleted zone of the wrought alloy during oxidation. Ti and Al, which are depleted in both variants of the alloy, were more strongly depleted in the SLM-consolidated alloy. Ti enrichment in the SLM-consolidated alloy, which occurs at a depth of ~20µm, is consistent with the internal oxide evident in the Ti map, Figure 5.8.

Interdiffusion coefficient

The Cr interdiffusion coefficient (D) was estimated for the SLM-consolidated alloy and the wrought alloy. This was done by fitting the Cr depth profiles using Equation 4, Figure 5.16. The model data was fitted to the experimental data by applying small changes to the interdiffusion coefficient, with the quality of fit judged by eye. The estimated values of D are presented in Table 5.2, which shows that $D^{SLM} \approx 2D^{Wrought}$. Also shown in Table 5.2 are values of D taken for reference from the literature.

Faster Cr diffusion in the SLM-consolidated alloy suggests that the boundaries of the dendrites/cells contribute strongly to diffusion in the alloy; however the morphology of the scale formed on the SLM-consolidated alloy indicates much faster growth, and therefore Cr transport, via the grain boundaries of the alloy. The results presented in section 5.3.2, which show that internal oxides form at greater depths in the SLM-consolidated alloy also indicates faster diffusion in this variant of the alloy.

Table 5.2: Chromium interdiffusion coefficients (D) estimated from fitting of the Cr depth profiles

	Chromium interdiffusion coefficients (m^2s^{-1})				
	This work	Dayananda [149]	Campbell [150]	Chyrkin [151]	Chyrkin [151]
Alloy 718 SLM	1.5E-16 (900°C)	-	-	-	-
Alloy 718 Wrought	0.8E-16 (900°C)	1.2-1.7E-14 (1100°C)	1.58E-14 (1150°C)	-	-
Alloy 625	-	-	-	7.29E-16 (1000°C)	2.5E-16 (900°C)

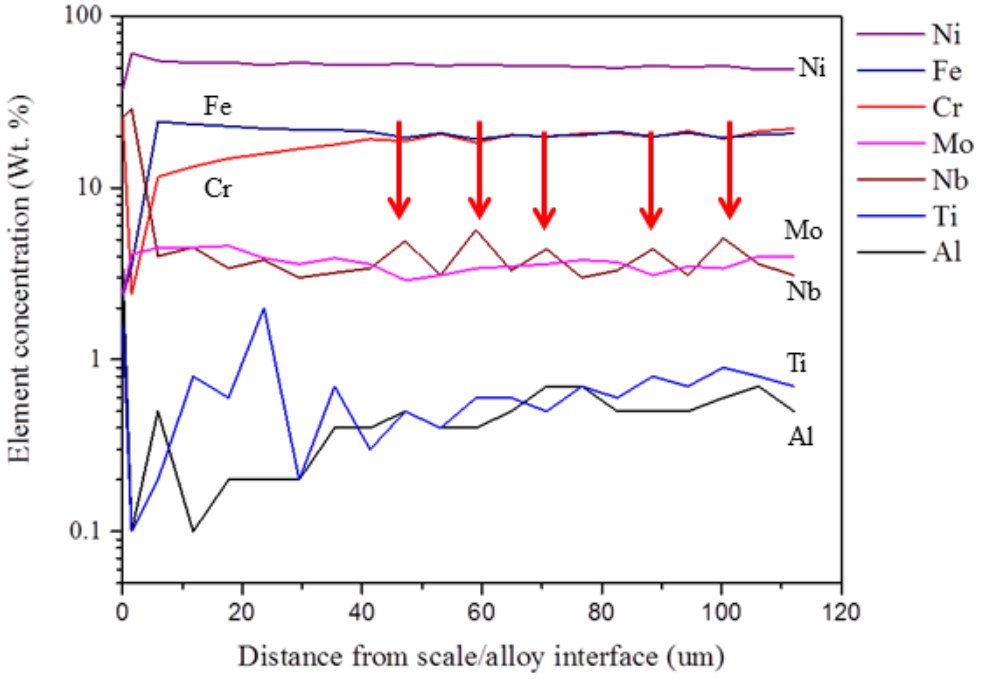

a

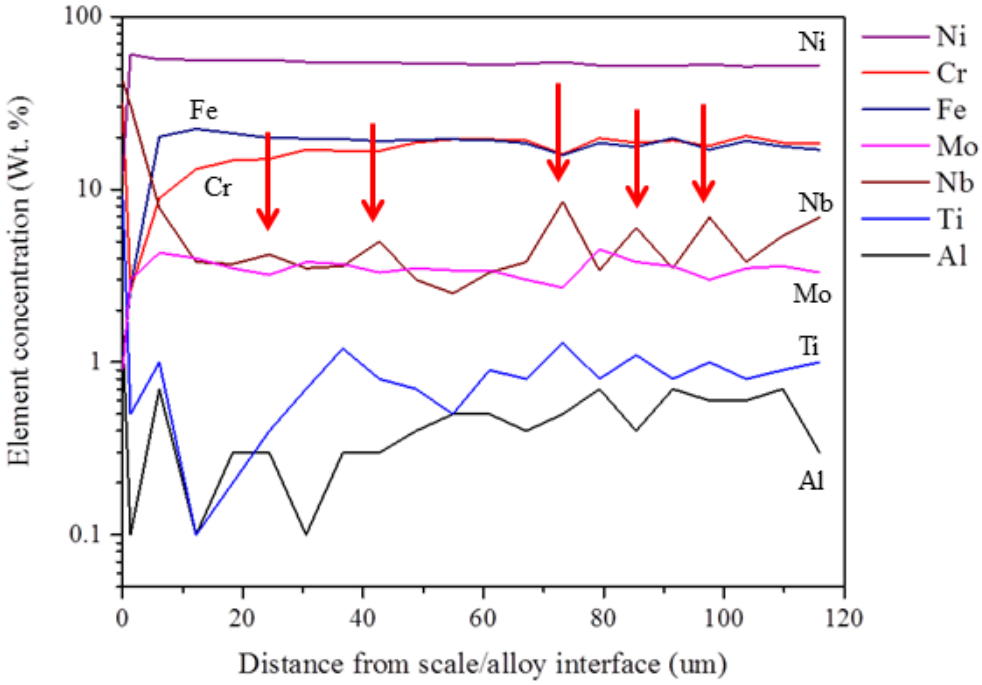

b

Figure 5.15: Compositional depth profiles obtained from cross-sections of Alloy 718 following 1000 hours of isothermal oxidation at 900°C (a) SLM-consolidated alloy, and (b) Wrought alloy (P600 grit finish)

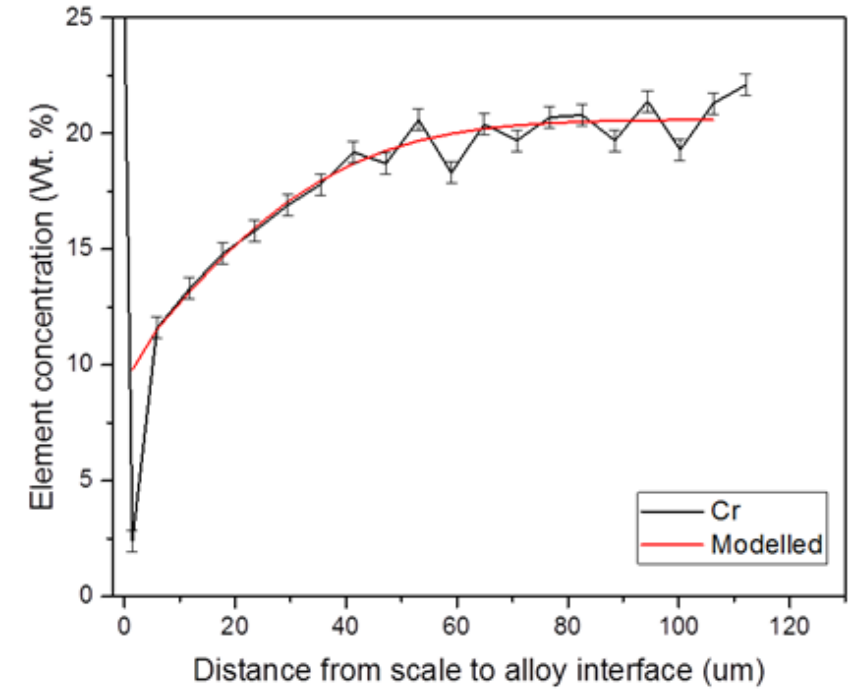

a

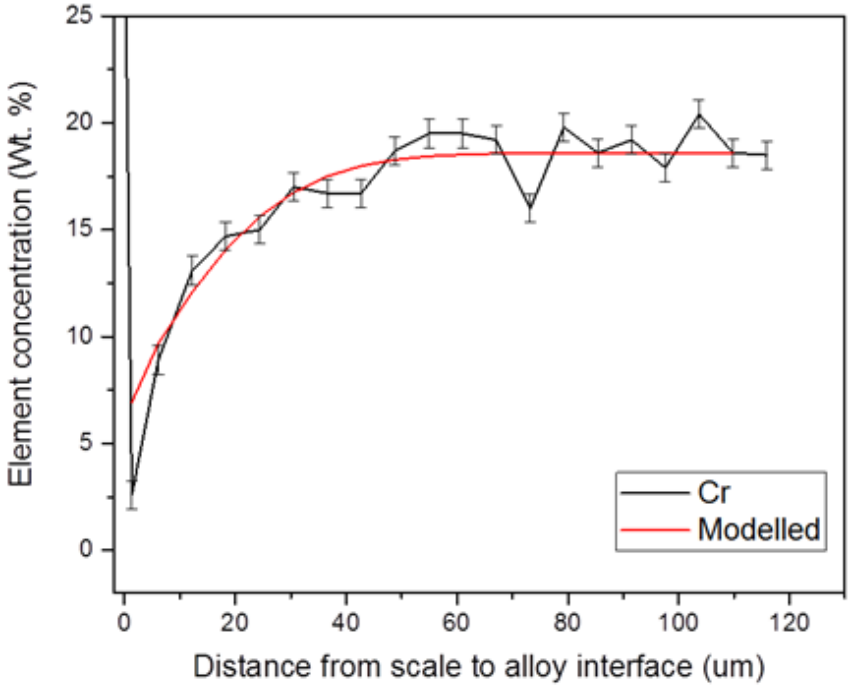

b

Figure 5.16: Modelled plots of Cr concentration (Wt. %) against distance from scale/alloy interface (µm) following 1000 hours of isothermal oxidation in laboratory air at 900°C (a) SLM-consolidated Alloy 718, and (b) wrought Alloy 718

5.3.6 Oxidation of carbides in wrought alloy

The oxidised surfaces of the wrought alloy were littered with oxidised inclusions of ~5-10µm in size, Figure 5.17 (a). The inclusions were almost certainly oxidised MC-type carbides and were rich in the elements Nb, Ti and O. The carbides were mainly present in the alloy as members of long stringers, which were orientated parallel to the extrusion direction of the parent alloy, Figure 5.17 (b).

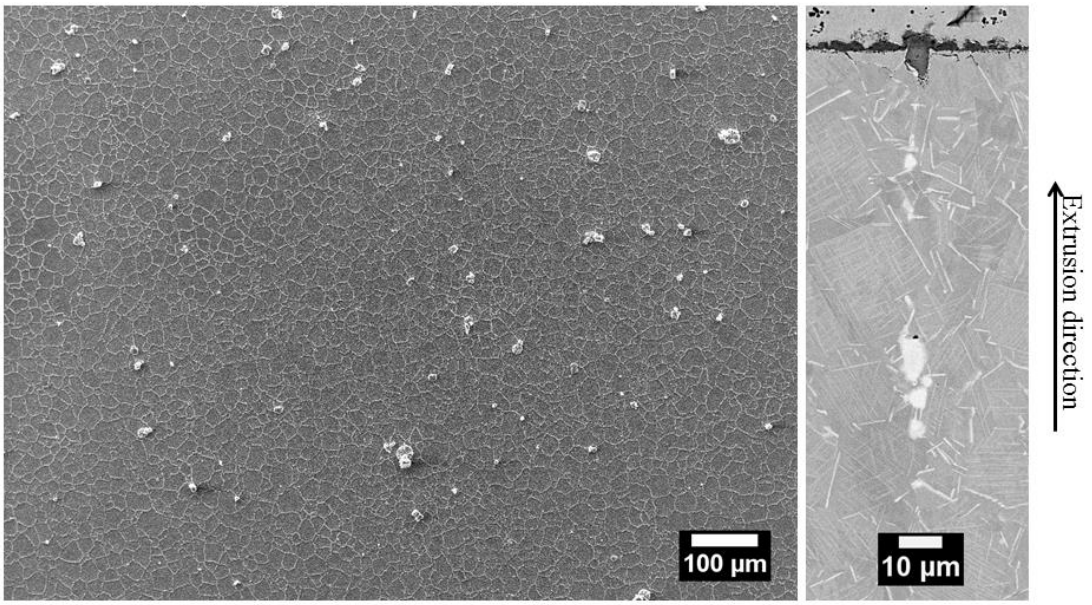

Figure 5.17: Wrought Alloy 718 following 25 hours of isothermal oxidation in laboratory air at 900°C (P4000 grit finish) (a) SE micrograph of carbides on oxidised surface, and (b) BSE micrograph of oxidised carbide that is part of a stringer

Many of the oxidised carbides had grown out of the plane of the surface of the alloy during its oxidation, Figure 5.18. Others remained essentially in the plane of the surface. Outward growth of carbides was also observed by Connolley, who concluded that it was carbides exposed at the surface of the alloy prior to oxidation that grew outwards [238]. Litz et al observed the same outward growth of oxidised

carbides, but ascribed the behaviour to the blocky morphology of some carbides [239].

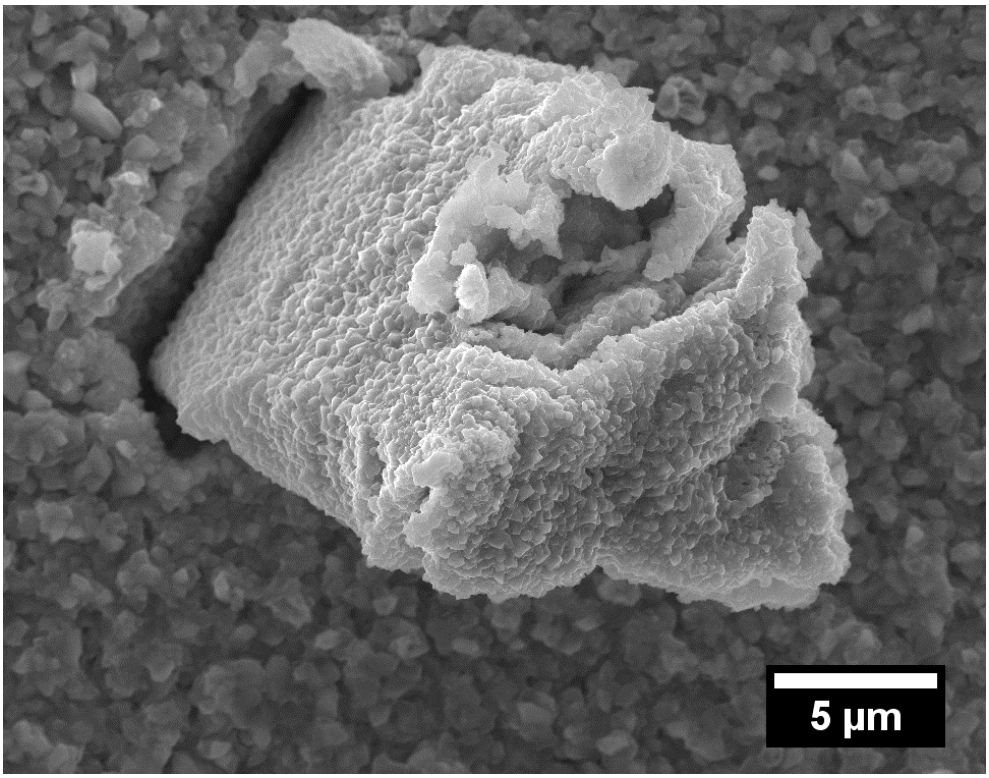

Figure 5.18: SE micrograph of (Nb,Ti)C carbide in wrought Alloy 718 after 10 hours of isothermal oxidation in laboratory air at 900°C (P600 grit finish)

A BSE micrograph of an oxidised carbide present in the P4000 grit finish wrought alloy, following 215 hours of oxidation, is shown in Figure 5.19. The carbide was of a relatively low average atomic number with respect to the alloy, and had grown ~10µm above the plane of the surface of the alloy during oxidation, where it appeared porous. Plastic deformation of the alloy had occurred adjacent to the inclusion, as reported by Connolley [240].

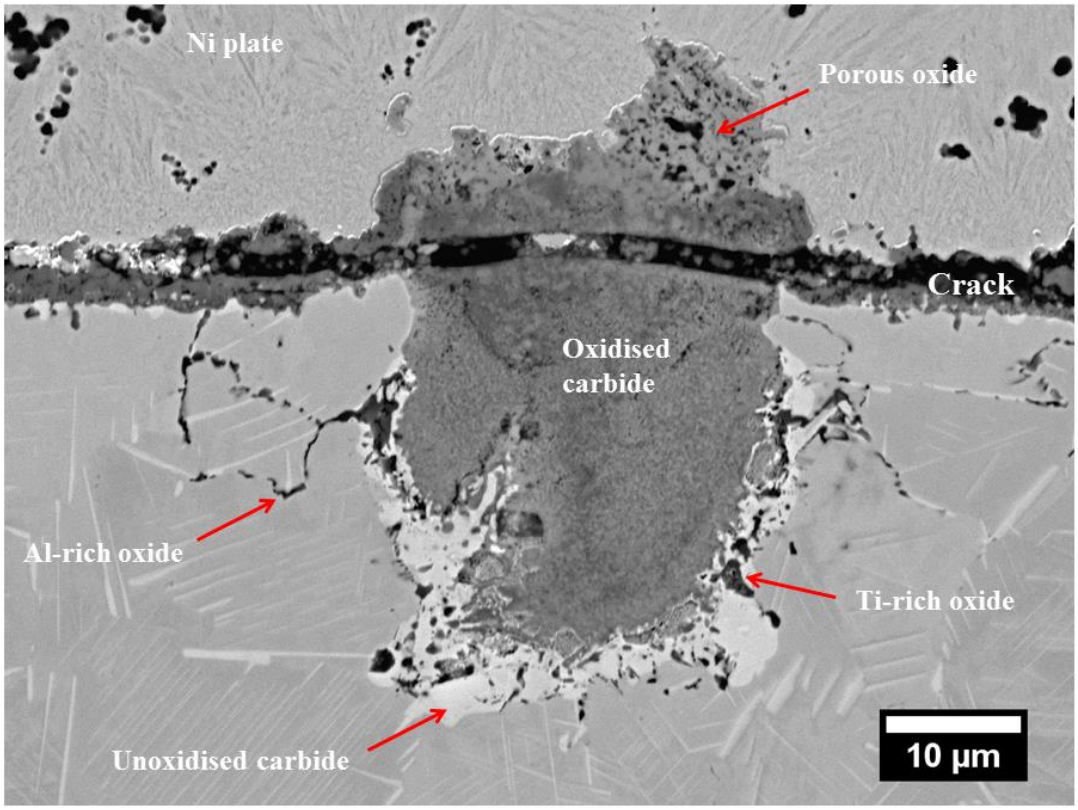

Figure 5.19: BSE micrograph of (Nb,Ti)C carbide in wrought Alloy 718 after 215 hours of isothermal oxidation in laboratory air at 900°C (P4000 grit finish)

Element maps obtained from the oxidised carbide shown in Figure 5.19 are presented in Figure 5.20. These show that a distinct layer of Cr-rich oxide is present in the oxidised carbide, which appears to be a continuation of the scale that covers the oxidised alloy. The elements Fe, Cr, Nb and O are dominant above the crack in the carbide, but below the crack a 'V-shape' concentration profile is evident, with the elements Cr and O concentrated on its inside and Nb and Ti concentrated around it. A layer rich in Nb surrounds the oxidised carbide, which is believed to be unoxidised carbide rather than precipitated δ-phase. This is assumed because there is no dissolution of δ-phase in the alloy adjacent to the Nb-rich phase, nor is there evidence of a Cr-depleted zone in the alloy adjacent to the base of the carbide thought necessary for δ-phase dissolution. The carbide appears fully oxidised to a depth of ~10µm from the scale/alloy interface. Precipitation of Al-rich oxide and Ti-rich oxide occurred within the unoxidised carbide, and Al-rich oxide precipitated in

the alloy adjacent to the unoxidised carbide. Al and Ti are readily oxidised c.f. Figure 2.7, but elsewhere in the alloy they are not found as oxides, at least to this extent, at this depth i.e. ~20μm from the scale/alloy interface. This means that the oxygen activity at the base of the inclusion and in the alloy adjacent to the base of the inclusion is probably higher than that in the alloy distant from inclusions i.e. it is probable that the oxidised carbides act as a conduit for the transport of O into the alloy. It has also been reported that, during high temperature oxidation experiments conducted in air, N derived from the atmosphere can react with Ti in alloys to form inclusions. Cruchley and Evans reported the formation of TiN on grain boundaries of the Ni-base alloy RR1000 following 100 hours of oxidation in air at 900°C [241] and Perez-Gonzalez et al reported the formation of acicular TiN in the Ni-base alloy Haynes 282 during its oxidation in air at 1000°C [242]. Therefore it is possible that Ti nitrides formed alongside Ti oxides during the course of the present oxidation experiments, but it was not possible to confirm this because NKα is overlapped by TiLα in EDS spectra.

At positions adjacent to the carbides the scale was, at oxidation times of 25 hours, often comprised of a compact layer at the scale/alloy interface and a porous layer at the scale/gas interface, Figures 5.21(a) and 5.21(b). The effect was also observed more generally within the scale, Figure 5.21(c), but was not observed in the scale formed on the SLM-consolidated alloy, Figure 5.21(d), nor was it observed on coupons of the wrought alloy oxidised for >25 hours, which suggests that the porous scale is consumed by the growth of dense scale at longer oxidation times, and that the porous scale does not form at oxidation times ≥215 hours. Analysis indicated that the scale, both compact and porous, was Cr-rich oxide, though Nb was sometimes detected in the scale adjacent to the oxidised inclusions.

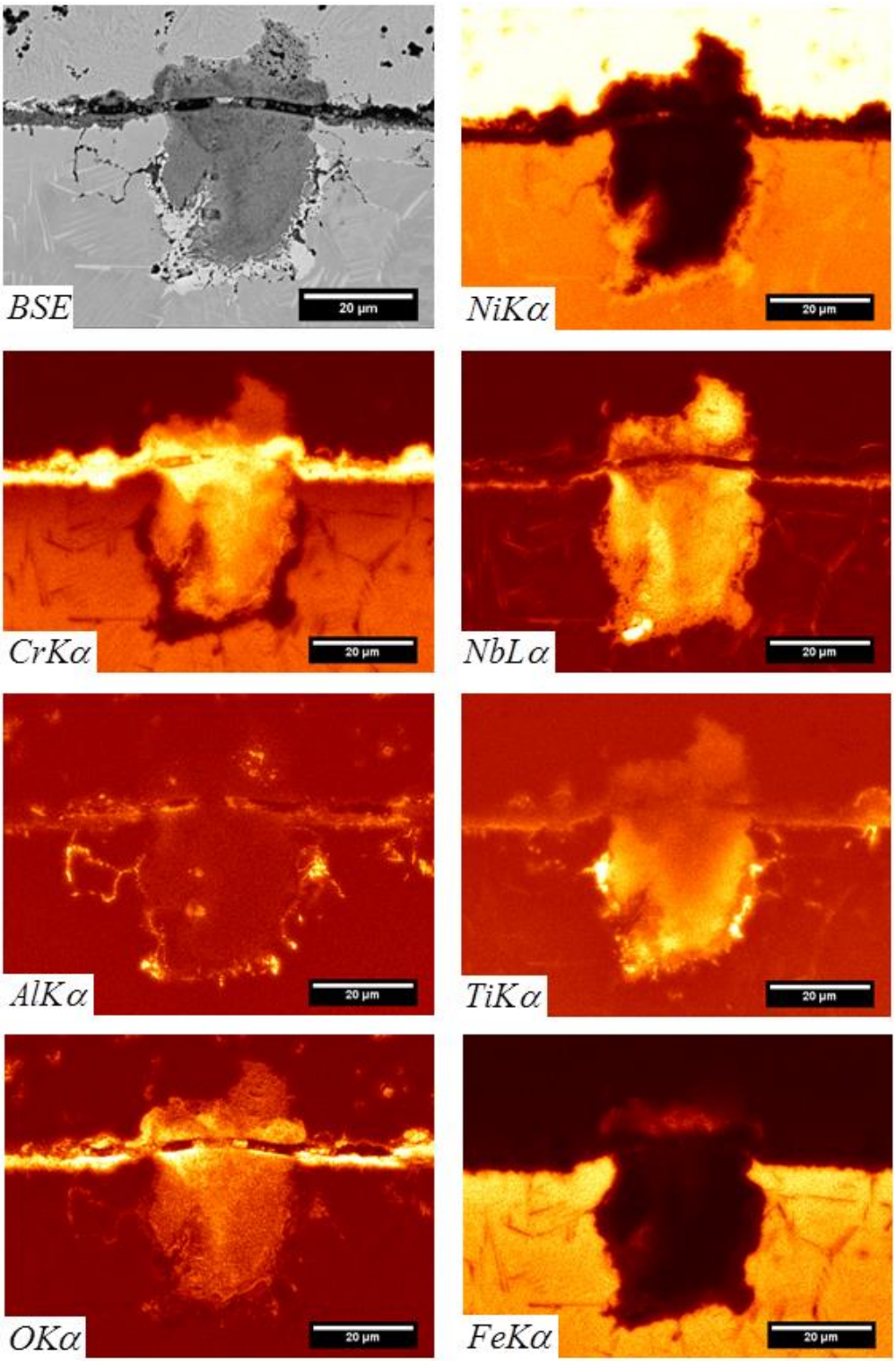

Figure 5.20: Element maps obtained from an oxidised carbide in wrought Alloy 718 (P4000 grit finish) after 215 hours of isothermal oxidation in laboratory air at 900°C

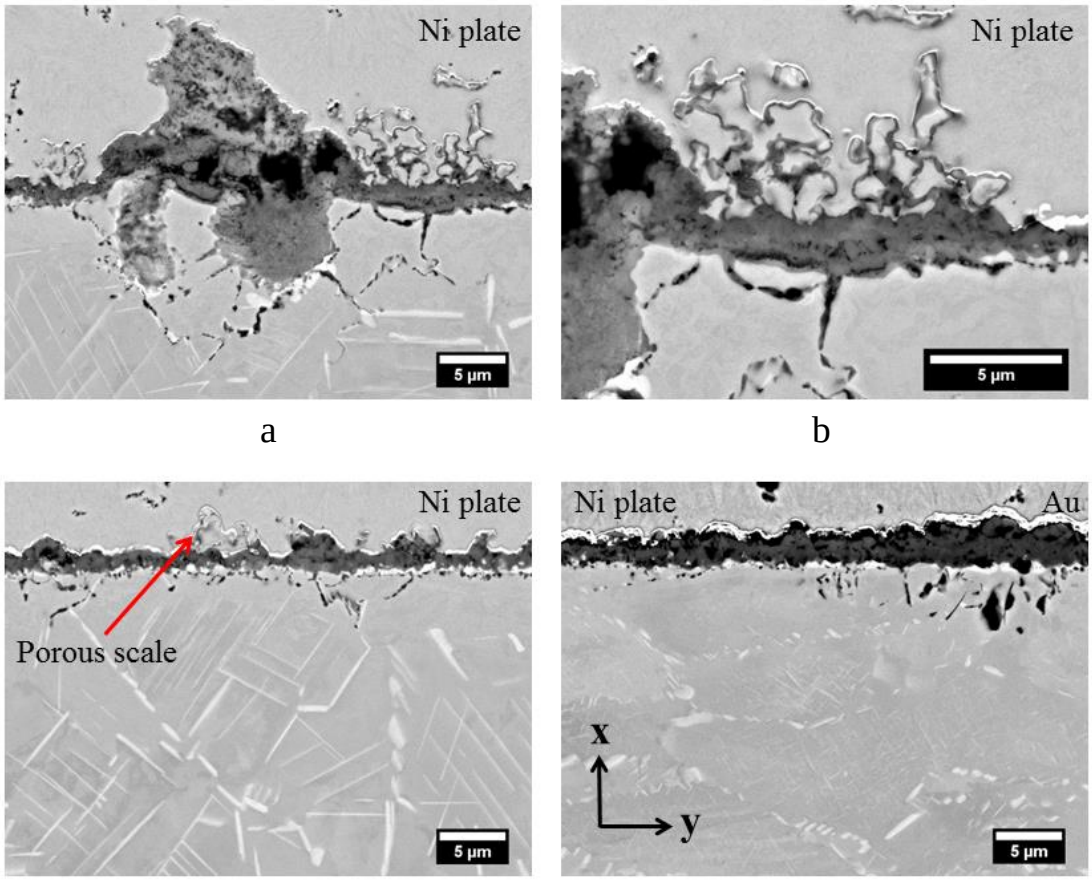

Figure 5.21: BSE micrographs of cross-sections of Alloy 718 following 25 hours of isothermal oxidation in laboratory air at 900°C (a), (b) porous scale adjacent to an oxidised (Nb,Ti)C carbide in wrought alloy (P600 grit finish), (c) porous scale in compact scale on wrought alloy (P600 grit finish), and (d) compact scale on SLM-consolidated alloy

5.3.7 Effect of surface finish on oxidation

Ridges formed on the surface of the wrought alloy coupons, which corresponded to the grain boundaries of the alloy, and were more evident on the coupons prepared to a P4000 grit finish, Figure 5.22. This may arise because intragranular oxidation is faster for the specimens ground to a P600 grit finish, reducing the delineation between intragranular scale and intergranular scale. This may be caused by

additional cold work damage introduced during preparation of the coupons for oxidation - P600 grade SiC paper has an average grit diameter of ~26µm, as opposed to ~5µm for P4000 grit paper [243]. In order to investigate the effect of surface finish on the oxidation of wrought Alloy 718, specimens of the alloy, which had been ground and polished to a 40nm silica finish, were oxidised in laboratory air at 900°C for durations of ~1-4 hours. Specimens of the legacy Ni-base ODS superalloy MA754, prepared in the same way, were oxidised for comparison. Alloy 718 formed a thin Cr-rich scale, with ridges developing where δ-phase was present on the grain boundaries of the alloy, Figure 5.23 (a). Enhanced scale growth over the grain boundaries of the alloy may be promoted by the formation of Nb-rich oxides, which are known to form porous, non-protective scales [136], but not all grain boundaries appear to have δ-phase on them, whereas all of the grain boundaries on the P4000 grit finish coupons oxidised faster than the grain interiors. There was evidence that some grains, indicated by the dashed red lines, oxidised faster than others, presumably an effect of grain orientation. MA754 formed a thick Ni-rich scale, with thin Cr-rich scale present only over the grain boundaries of the alloy where diffusion is expected to be most rapid, Figure 5.23 (b). A diffractogram obtained from silica-polished MA754 shows that the Ni-rich scale and the Cr-rich scale are NiO and Cr_2O_3 respectively, Figure 5.23 (c). The scales formed on specimens of P600 grit finish MA754, P4000 grit finish MA754 and silica-polished Alloy 718 were too thin to be detected by XRD. These results show that Alloy 718 forms a Cr-rich scale irrespective of whether it is ground to a P600 grit finish or silica-polished, whereas MA754 can be switched from a Cr_2O_3-former to a NiO-former by the elimination of cold work damage.

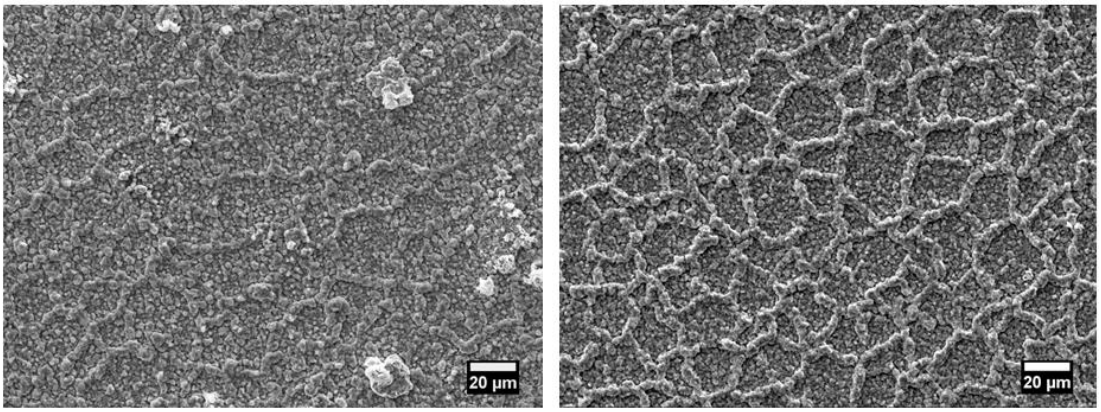

a b

Figure 5.22: SE micrographs of ridges in scale on wrought Alloy 718 following 215 hours of isothermal oxidation in laboratory air at 900°C (a) P600 grit finish (b) P4000 grit finish

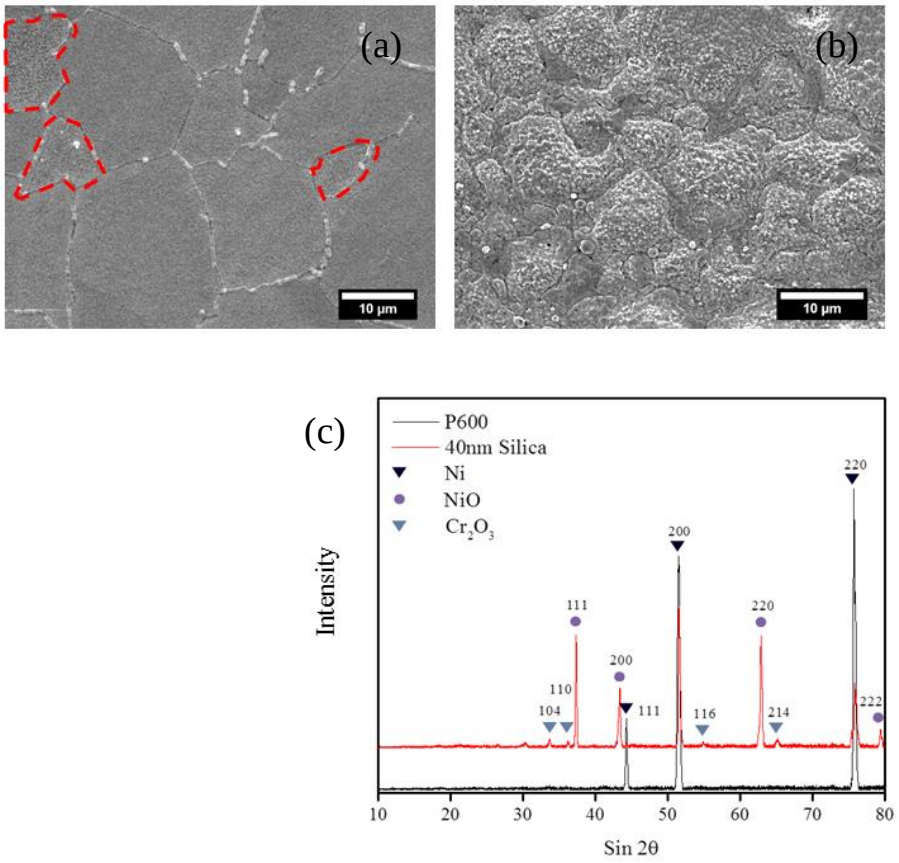

Figure 5.23: Silica-polished alloys after oxidation in air at 900°C (a) SE micrograph of Alloy 718, (b) SE micrograph of MA754, and (c) Diffractograms obtained from P600 grit finish MA754 (black) and silica finish MA754 (red)

5.4 Discussion

The SLM-consolidated alloy had a columnar grain structure, with a submicron dendritic/cellular substructure. A Nb-rich phase, probably Laves, was segregated to dendrite/cell boundaries of the as-consolidated alloy, but this was replaced by δ-phase during heat-treatment at 954°C. This is consistent with the literature review for SLM-consolidated Alloy 718 [97-101].

SLM-consolidated Alloy 718 oxidised slightly faster than the wrought alloy, which appears to be due to a slightly smaller oxide grain size in the scale formed on the SLM-consolidated alloy. This is expected to increase short-circuit diffusion of Cr and O through the growing scale. The smaller grain size may be attributable to faster nucleation of the oxide grains, which in turn may be due to faster Cr diffusion in the alloy as a result of its dendritic/cellular substructure, or the orientation of the grains at the surface of the alloy, which were mainly (200) for the SLM-consolidated alloy and (111) for the wrought alloy, or the rate of grain boundary diffusion in the alloy. It is known that high angle grain boundaries in alloys provide fast diffusion paths [244], and that certain crystallographic orientations of Ni oxidise more rapidly than others due to faster ion transport [236]. The presence of ridges in the scale formed over the grain boundaries of the SLM-consolidated alloy indicates that grain boundary diffusion is the dominant Cr transport mechanism in the SLM-consolidated alloy.

The chromium interdiffusion coefficient (D) was determined to be $D^{SLM} \approx 2D^{Wrought}$ which may be due to faster grain boundary diffusion in the SLM-consolidated alloy, or faster diffusion via the dendritic/cellular substructure of the SLM-consolidated alloy, or probably a combination of the two. As discussed above, grain boundary diffusion is dominant in the SLM-consolidated alloy, and it is therefore likely that grain boundary diffusion is much faster in the SLM-consolidated alloy than it is in the wrought alloy. High-angle grain boundaries have been

identified as present in SLM-consolidated ferritic ODS steel [245] and in SLM-consolidated Alloy 718 [246].

Both the SLM-consolidated alloy and the wrought alloy formed a layer of δ-phase at the scale/alloy interface, as a result of oxidation-induced dissolution of δ-phase in the alloy. This has been reported for wrought Alloy 718 [181]. Chyrkin has proposed that, in Alloy 625, dissolution of δ-phase occurs because its chemical potential is lower in the Cr-depleted region of the alloy, and that a layer of δ-phase forms at the scale/alloy interface because it becomes saturated in the region of lowest chemical potential [105]. In the present work, undercutting of the layer of δ-phase resulted in particles of δ-phase being incorporated into the scale, consistent with Chyrkin's observations re Alloy 625 [105]. Ti-rich internal oxide was identified in the SLM-consolidated alloy and wrought alloy, which was located the chromia scale and the layer of δ-phase at the scale/alloy interface. The internal oxide was present as a semi-continuous layer in the SLM-consolidated alloy and as a continuous layer in the wrought alloy, probably because of the higher Ti content of the wrought alloy. The internal oxide is rich in Ti, Nb, O and, possibly, Cr. A semi-quantitative EDS analysis of the internal oxide indicated that the stoichiometry was ~$Ti_{1.3}Cr_{0.5}Nb_{2.1}O_{6.1}$. Zakrzewska et al [247] and Ruiz et al [248] have shown the solubility limit of Nb in TiO_2 to be ~6-7 Atom %, and that beyond the solubility limit $TiNb_2O_7$ is precipitated. Zakrzewska et al also found the solubility of Cr in TiO_2 to be >3.5 Atom % [247]. It is therefore proposed that the internal oxide present at the scale/alloy interface of the examined specimens is not TiO_2, as may have been expected, but a mixture of TiO_2, doped with Nb, and possibly Cr, and $TiNb_2O_7$. This occurs because Nb from the δ-phase is dissolved into the TiO_2 until it becomes saturated and $TiNb_2O_7$ precipitates. Likely confirmation of this observation is found in paper by Al-hatab et al, who identified $TiNb_2O_7$ in XRD patterns obtained from Alloy 718 following cyclic oxidation experiments conducted at temperatures between 750°C and 950°C [249]. The authors suggested that the δ-phase layer at the scale/alloy interface contained Nb, Ti and Al oxides. It is noted that the alloy they studied contained 0.9 Wt. % Ti, and so, like the SLM-

consolidated alloy studied for the present work, which contained 0.86 Wt. % Ti, may have been expected to produce a semi-continuous layer of $TiNb_2O_7$ at the interface between the scale and the δ-phase.

The wrought alloy contained a large number MC-type carbides of ~1-10μm in size, consistent with Nb(Ti)C and Ti(Nb)CN carbides. These have been reported by others as present in Alloy 718 [93]. The SLM-consolidated alloy contained very few carbides, despite the higher C content of the SLM-consolidated alloy. C is known to promote NbC formation, at the expense of Laves phase [91, 95, 96], while high levels of Fe and Si promote Laves phase at the expense of MC-type carbides [91]. The absence of carbides from the SLM-consolidated alloy may be due to rapid cooling of the alloy during consolidation, which has been reported in Alloy 625 [107, 108]. The effect has also been observed in Rapid Solidified Alloys (RSA), which have cooling rates analogous to that observed for SLM-consolidation i.e. $\sim 10^4$-$10^6 Ks^{-1}$ [250, 251]. A lack of NbC carbides in the SLM-consolidated alloy may improve its mechanical strength, as reported by Jackman et al, who found the fracture toughness of Alloy 718 was improved by reducing C from 0.027 Wt. % to 0.008 Wt. %. This was attributed to the elimination of carbide stringers [252]. Connolley has shown that oxidised Nb(Ti)C carbides can initiate failure during high temperature LCF testing of Alloy 718 [240]. Litz et al reported that cracks can form in the Cr_2O_3 scale on the Ni-base alloys IN939 and IN 738LC as a result of shear strain arising from the upward movement of carbides during oxidation, as a result of the volume increase, and that this can lead to internal oxidation in the alloy because of the ingress of aggressive components via the cracks [239]. In the present work the composition of oxidised carbides was elucidated, and shown to comprise a porous mixture of Nb-rich and Cr-rich oxides. The porosity may be due to the evolution of CO_2, as a result of decomposition of the carbide, but Nb_2O_5, which is reported to be the principal decomposition product [253], may be likely and is reported to form a porous and non-protective scale [136]. It is also possible that the alloy locally goes into ‘breakaway’ in the vicinity of oxidised carbides, evidenced by the presence of Fe in the scale. Litz et al reported that internal oxidation occurred as a result of

ingress via the cracked scale, but the present work appears to show that the oxidised carbides act as a conduit for oxygen ingress into the alloy, leading to localised, but deep internal oxidation. The scale adjacent to the oxidised carbides is often found to wrinkle and spall, leading to oxidation of the exposed alloy and reforming of the scale. Nb may be incorporated into the reformed scale. It is proposed that spalling occurs because of compressive stresses generated locally within the scale parallel to the scale/alloy interface, as a consequence of the increase in volume of the carbides. Litz et al proposed that oxidation of carbides should be continuous because of exposure of underlying carbides to the advancing oxidation front, but in the present work the effect disappeared after 25 hours of oxidation. This is probably because the oxygen partial pressure is insufficient to oxidise carbides under the chromia scale. The effects of carbide oxidation probably disappear after 25 hours of oxidation because the spalled scale is replaced by more compact scale, and being fully oxidised, the carbides do not any cause additional spalling. It is noted that the wrinkled, spalled scale was absent from the inclusion-free SLM-consolidated alloy. Atkinson has observed that stress generation in Cr_2O_3 scales causes wrinkling, buckling and cracking [137]; Rhines and Wolf proposed that the poor scale morphology was due to counter-current diffusion, which causes compressive stresses to form in scales as a result of the formation of new oxide on the grain boundaries perpendicular to the scale/alloy interface [254]. A very similar effect to that observed in the present work was reported by Caplan and Sproule following their work on the oxidation behaviour of electropolished Cr at 890-1200°C [255], and electropolished Fe26Cr alloy at 980-1200°C [256]. They found that wrinkled, polycrystalline scales formed on the alloys at short oxidation times, which readily spalled as a result of compressive stresses arising from oxide formation within the scale, Figure 5.24. This is consistent with the proposal that spalling of the scale was caused by large compressive stresses, which given the observed propensity for spalling of the scale at positions adjacent to oxidised carbides, suggests that the carbides are the source of the compressive stresses.

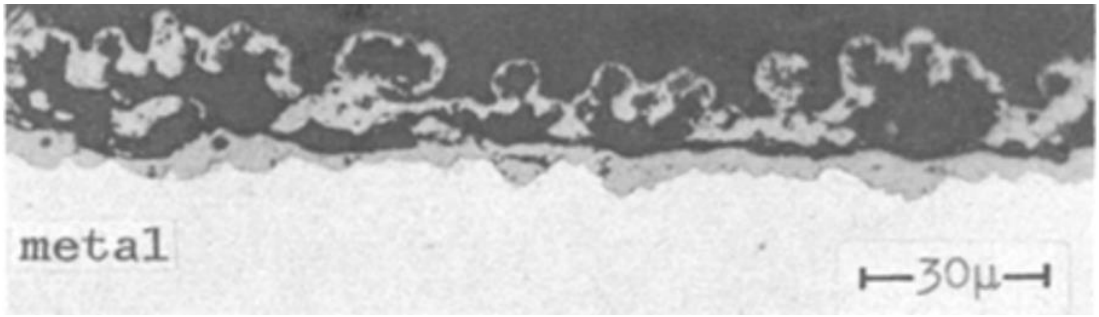

Figure 5.24: Wrinkled, detached $(Cr,Fe)_2O_3$ scale on electropolished Fe26Cr alloy following 0.6 hours oxidation in 1 atm. O_2 at 1200°C [256]

The oxidation behaviour of wrought Alloy 718 was studied following silica polishing, using the ODS Ni-alloy MA754 as a reference. In oxidation experiments of <4 hours, in air, at 900°C, Alloy 718 was observed to form a thin Cr-rich scale, but MA754 a thick NiO scale. However, when ground using P600 or P4000 SiC grit papers both MA754 and Alloy 718 formed a thin Cr-rich scale. The difference in the oxidation behaviour of the two alloys may be explained by reference to oxide maps prepared for Fe-Cr-Ni and Ni-Cr-Al alloys, albeit at 1000°C, Figure 5.25. Alloy 718, which can be considered to have a composition that approximates to Fe-20Cr-20Ni-60, falls easily within the Cr_2O_3 phase field of Figures 5.25 (a) and 5.25 (b) and forms a Cr_2O_3 scale irrespective of whether it is silica-polished, or ground using P4000 or P600 SiC grit. On the other hand, MA754, which is essentially a Ni-80Cr-20 alloy, falls on the boundary between a Cr_2O_3 former and a NiO former in Figure 5.25 (b). This means that a certain level of cold-work damage is needed to switch MA754 from a NiO former to a Cr_2O_3 former. In longer tests it might be expected that the NiO formed during the early stages of the oxidation of silica-polished MA754 would transform to $NiCr_2O_4$ spinel, as reported by Douglass for Ni-80Cr-20 [257].

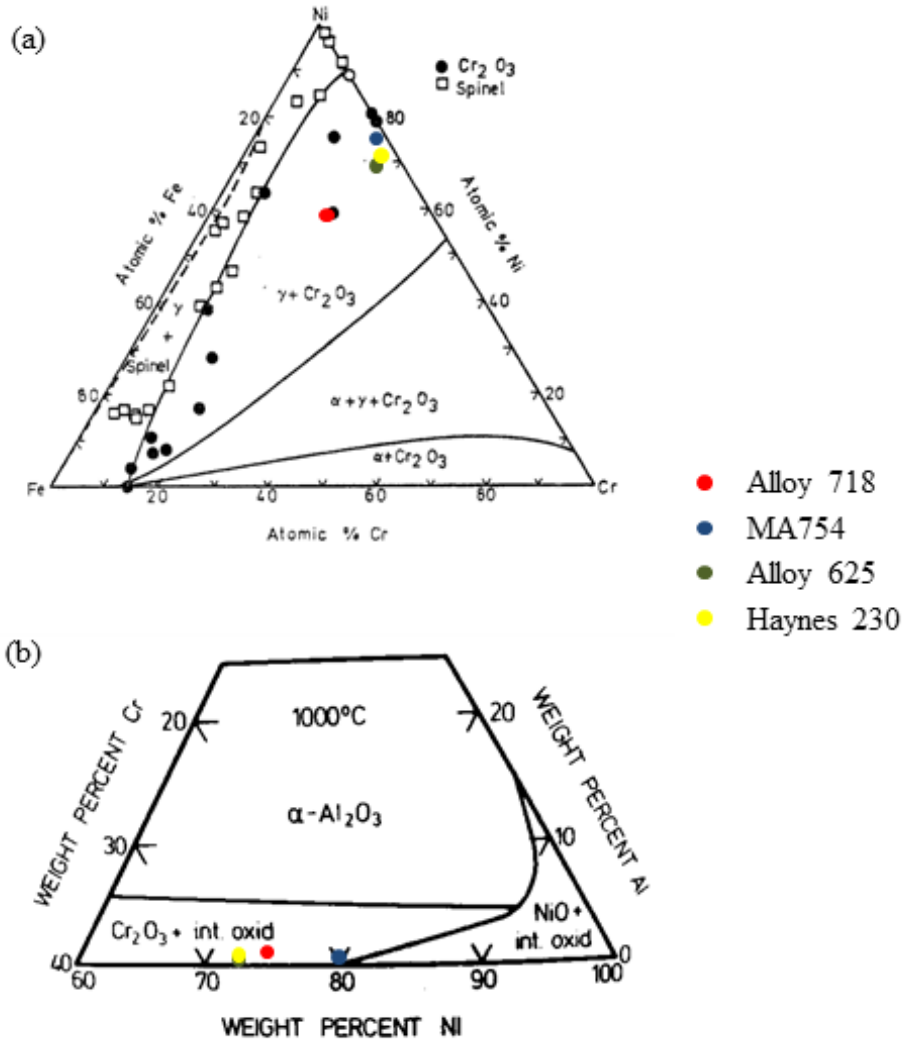

Figure 5.25: Oxide maps determined at 1000°C for Fe-Cr-Ni [258]and Ni-Cr-Al [135], with delineations marked for the formation of oxide scales and internal oxide. The composition of each alloy studied for the present work is plotted on the maps.

5.5 Chapter summary

The oxidation behaviour of SLM-consolidated specimens of Alloy 718 was assessed, using the wrought alloy as a control. Both the SLM-consolidated alloy and the wrought alloy formed a chromia scale, but the scale grew more rapidly on the SLM-consolidated alloy than it did on the wrought alloy. This is in accordance with the oxidation rate constant data presented in Chapter 4. Faster growth of the scale on the

SLM-consolidated alloy appears to result from a slightly smaller grain size and therefore greater short-circuit diffusion. The smaller grain size of the oxide scale may be due to faster nucleation of the oxide grains in the scale, arising from faster Cr transport in the SLM-consolidated alloy. Ridges formed in the scale on the SLM-consolidated alloy indicate that grain boundary transport is significantly faster than transport via the dendritic/cellular substructure of the grains. Cr interdiffusion coefficients were determined for the SLM-consolidated and wrought alloy, which showed that $D^{SLM} \approx 2D^{Wrought}$. This is attributed to faster grain boundary transport in the SLM-consolidated alloy, and probably faster transport via the dendritic/cellular substructure.

A layer of δ-phase was precipitated at the scale/alloy interface of the alloy, SLM-consolidated and wrought, as a result of dissolution of δ-phase in the oxidation affected zone of the alloy, and was undercut by the scale releasing particles of δ-phase into the scale. Formed between the scale and the layer of δ-phase was a layer of internal oxide that was rich in Ti, O, Nb and possibly Cr, and is thought to be a mixture of TiO_2, doped with Nb, and possibly Cr, and $TiNb_2O_7$, rather than TiO_2 as was expected. $TiNb_2O_7$ is precipitated as a result of the dissolution of Nb by TiO_2 internal oxide until the solubility limit is exceeded. These findings clarify the results reported by Al-hatab et al, who identified $TiNb_2O_7$ in XRD patterns obtained from oxidised Alloy 718, which they attributed to Nb and Ti oxides in the layer of δ-phase present at the scale/alloy interface.

The wrought alloy contained a large number of Nb(Ti)C carbides that were absent from the SLM-consolidated alloy. These have been identified, by others, as deleterious to the strength of the alloy. In the present work, at short oxidation times, the carbides underwent a volume increase as a result of oxidation, causing the protective chromia scale adjacent to them wrinkle and spall. This may be due to compressive stresses imparted to the scale during volume expansion of the carbides.

CHAPTER 6

ALLOY 625

6.1 Introduction

SLM-consolidated Alloy 625 and SLM-consolidated Alloy 625 ODS were studied following high temperature isothermal oxidation at 900°C for durations of up to 1000 hours. Wrought Alloy 625 and SPS-consolidated Alloy 625 ODS were also studied as comparators. The results are reported in 6.2, Characterisation of alloys, which includes subsections 6.2.1, SLM-consolidated Alloy 625, 6.2.2, Wrought Alloy 625, 6.2.3, Alloy 625 ODS/SLM, and 6.2.4, Alloy 625 ODS/SPS. The results obtained from the study of the oxidised alloys are reported in section 6.3, Characterisation of oxidised alloys, and includes subsections 6.3.1, XRD analysis, 6.3.2, Alloy 625, 6.3.3, Alloy 625 ODS, and 6.3.4, Oxidation-induced changes in alloys. The results are discussed in 6.4, and a chapter summary provided in 6.5.

6.2 Characterisation of alloys

6.2.1 SLM-consolidated Alloy 625

The as-consolidated alloy had a columnar microstructure orientated parallel to the build direction, Figure 6.1 (a). The alloy had a dendritic/cellular substructure, with an inter-dendritic spacing of ~1µm, Figure 6.1 (b). A phase rich in Nb, possibly Laves phase, was present on the dendrite/cell boundaries of the alloy. The microstructure of the alloy was not modified during heat-treatment at 1038°C, but most of the Nb-rich phase was solutionised leaving particles, probably δ-phase, mainly on the triple-points of the dendrite/cell boundaries, Figures 6.1 (c) and (d).

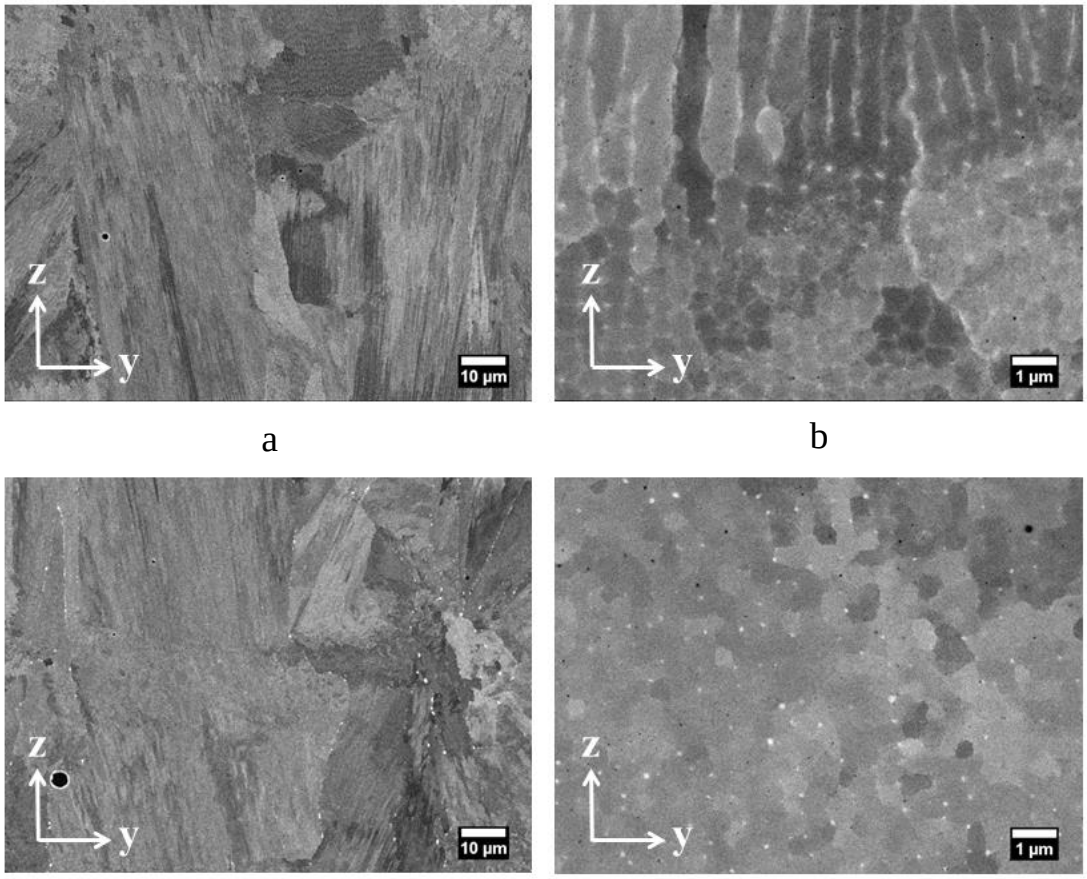

Figure 6.1: BSE micrographs of longitudinal sections of SLM-consolidated Alloy 625 (a), (b) as-consolidated, and (c), (d) after heat treatment

6.2.2 Wrought Alloy 625

The alloy contained long stringers of inclusions, identified as having Nb-rich and Ti-rich compositions, consistent with (Nb,Ti)C and (Ti,Nb)N. The carbides were orientated in the extrusion direction of the alloy, Figure 6.2 (a). The alloy had an equiaxed grain structure with a grain size of ~10µm, Figures 6.2 (b). Numerous twins were evident in the alloy and some of the grain boundaries were decorated by a phase rich in Ni, Nb and Mo, and 6.2 (c). This phase has been identified by others as δ-phase [93].

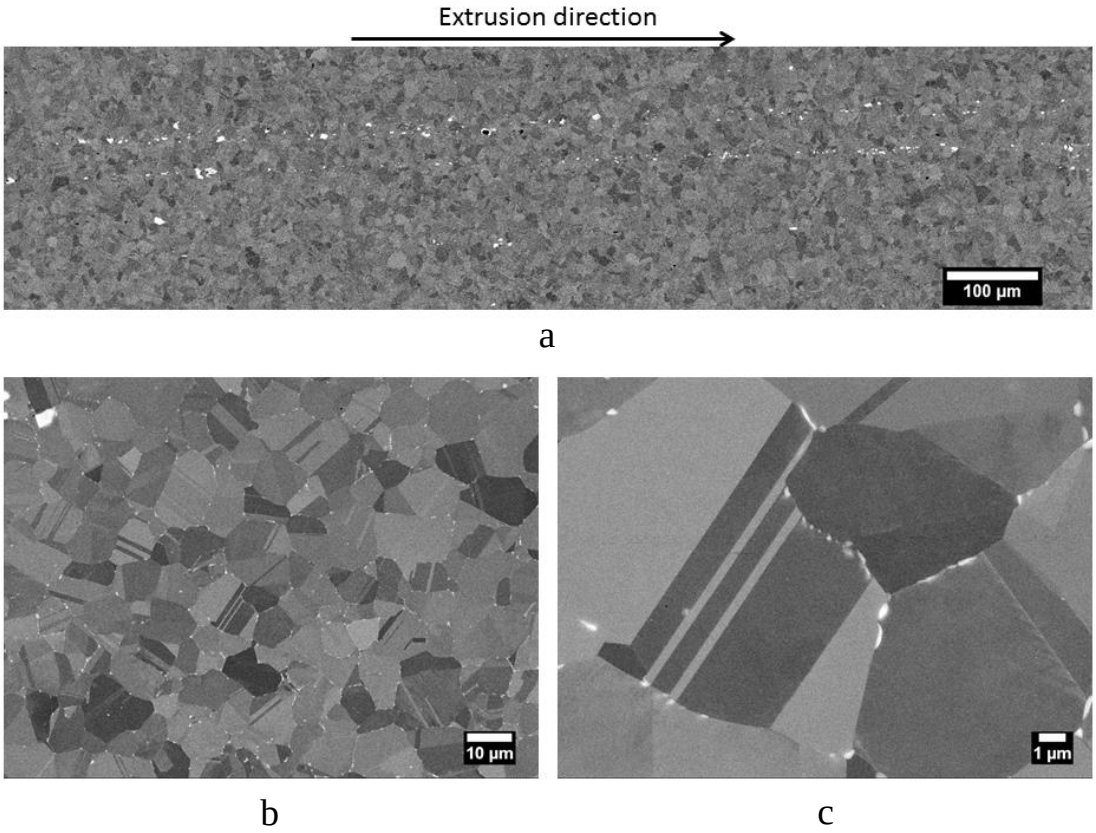

Figure 6.2: BSE micrographs of a longitudinal section of wrought Alloy 625 showing (a) stringers of MC-type carbides orientated parallel to the extrusion direction of the alloy, (b) equiaxed grain structure, (c) δ-phase on grain boundaries

6.2.3 Alloy 625 ODS/SLM

The microstructure was comprised of columnar grains orientated in the build direction of the alloy, with a dendritic/cellular substructure, Figures 6.3 (a). A phase rich in Nb was present on the boundaries of the dendrites/cells, possibly Laves phase or a film of Nb-rich carbide, and the inter-dendritic spacing was ~1µm. The inclusions present in the alloy were mainly oxides rich in Mo and Si, and Y-rich oxides, thought to have formed during consolidation, and Cr-rich oxides thought to have formed mainly during mechanical alloying as a result of O-entrainment. Pores were also evident in the alloy, as were cracks.

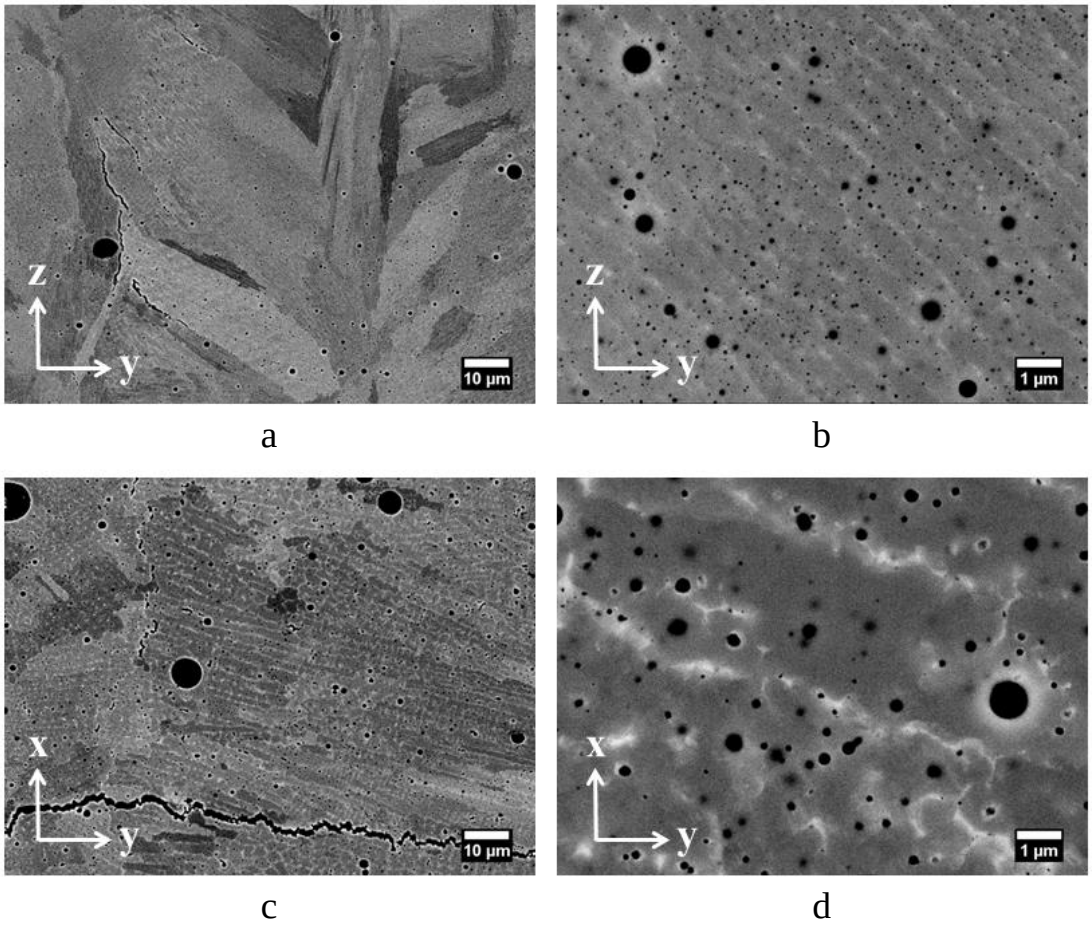

Figure 6.3: BSE micrographs Alloy 625 ODS/SLM (a), (b) longitudinal section, and (c), (d) transverse section

6.2.4 Alloy 625 ODS/SPS

The alloy was mainly comprised of grains of ~1µm in size, with a smaller volume of grains of ~0.2µm in size, Figure 6.4 (a). The small grain regions were populated by particles of <0.2µm in size, which appeared to be a mixture of Cr-rich oxides and possibly Nb-rich carbides. The inhomogeneous grain size of the alloy may be consistent with Zener pinning of the small grains by the particles. The alloy was free of the large cracks and slag that characterised the SLM-consolidated alloy.

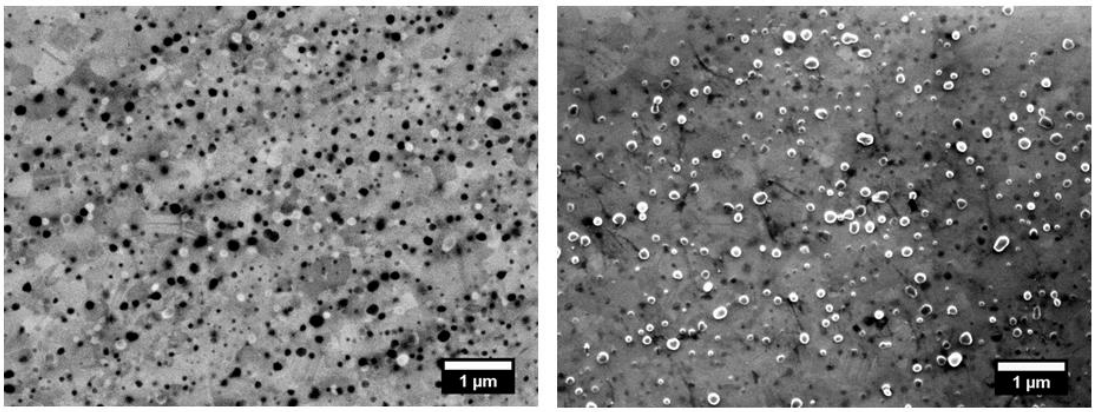

a b

Figure 6.4: Micrographs of Alloy 625 ODS/SPS (a) BSE micrograph of large grain and small grain regions showing Cr-rich oxide inclusions (black) in the small grain regions of the alloy, and (b) SE micrograph reveals a second population of inclusions, possibly Nb-rich carbides, in the small grain regions of the alloy

6.3 Characterisation of oxidised alloys

All of the XRD results are presented in section 6.3.1. The results of the initial examination are presented in section 6.3.2 for Alloy 625 SLM and wrought Alloy 625, and for Alloy 625 ODS/SLM and Alloy 625 ODS/SPS in section 6.3.3. The results obtained from a more detailed examination of the changes arising in the alloys immediately under the scales are presented in section 6.3.4.

6.3.1 XRD analysis

Diffractograms obtained from the oxidised coupons showed that a chromia scale formed on all four variants of the alloy during oxidation, which appeared thicker on Alloy 625 SLM and wrought Alloy 625 than on Alloy 625 ODS/SLM and Alloy 625 ODS/SPS, Figures 6.5 and 6.6. Detected in each oxidised variant of the alloy was the intermetallic δ-phase. A very small peak, corresponding to manganese chromate spinel, was detected in the diffractogram obtained from the wrought alloy, but not any of the other variants of the alloy.

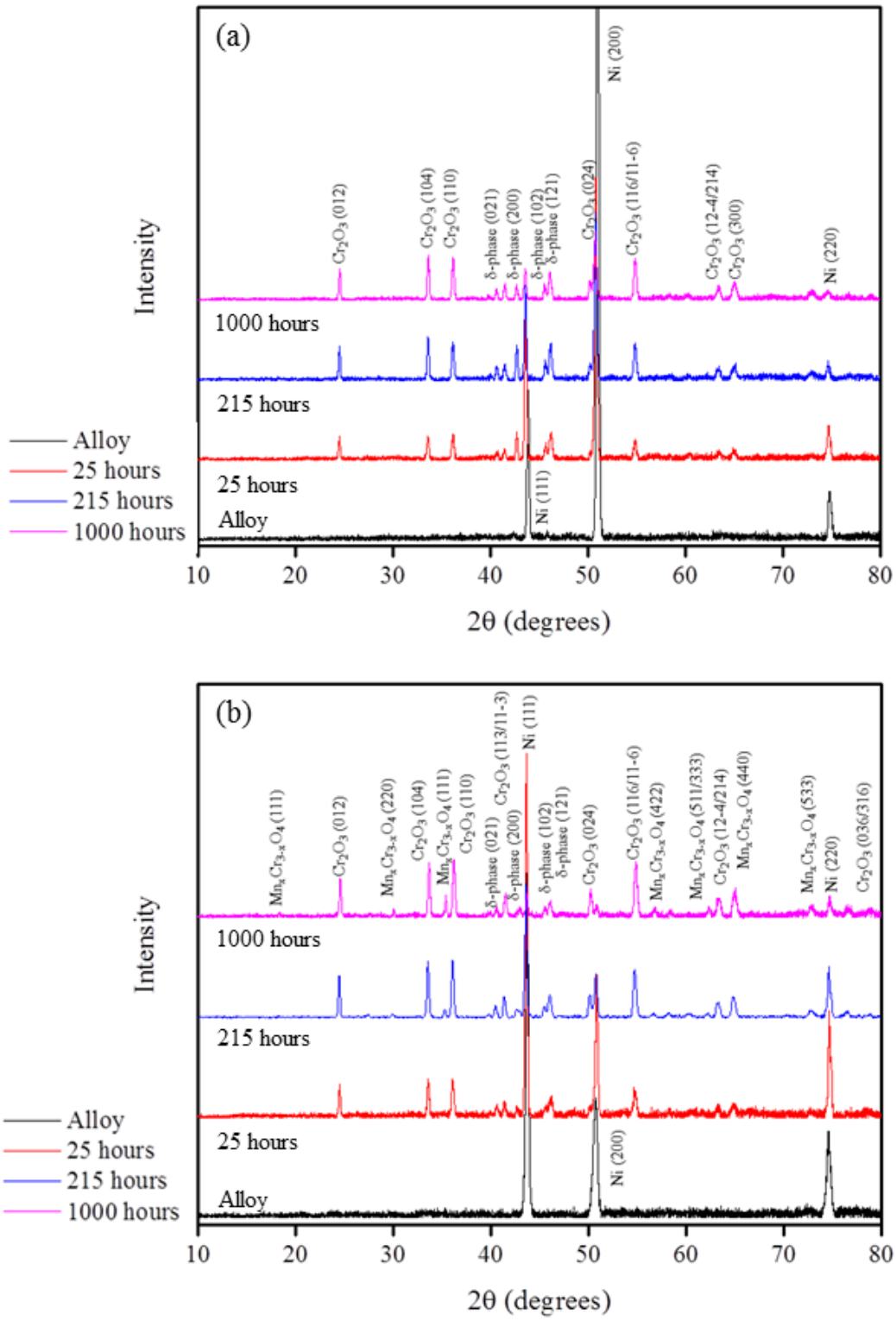

Figure 6.5: Diffractograms obtained from Alloy 625 following isothermal oxidation in laboratory air at 900°C (a) Alloy 625 SLM, (b) Wrought Alloy 625

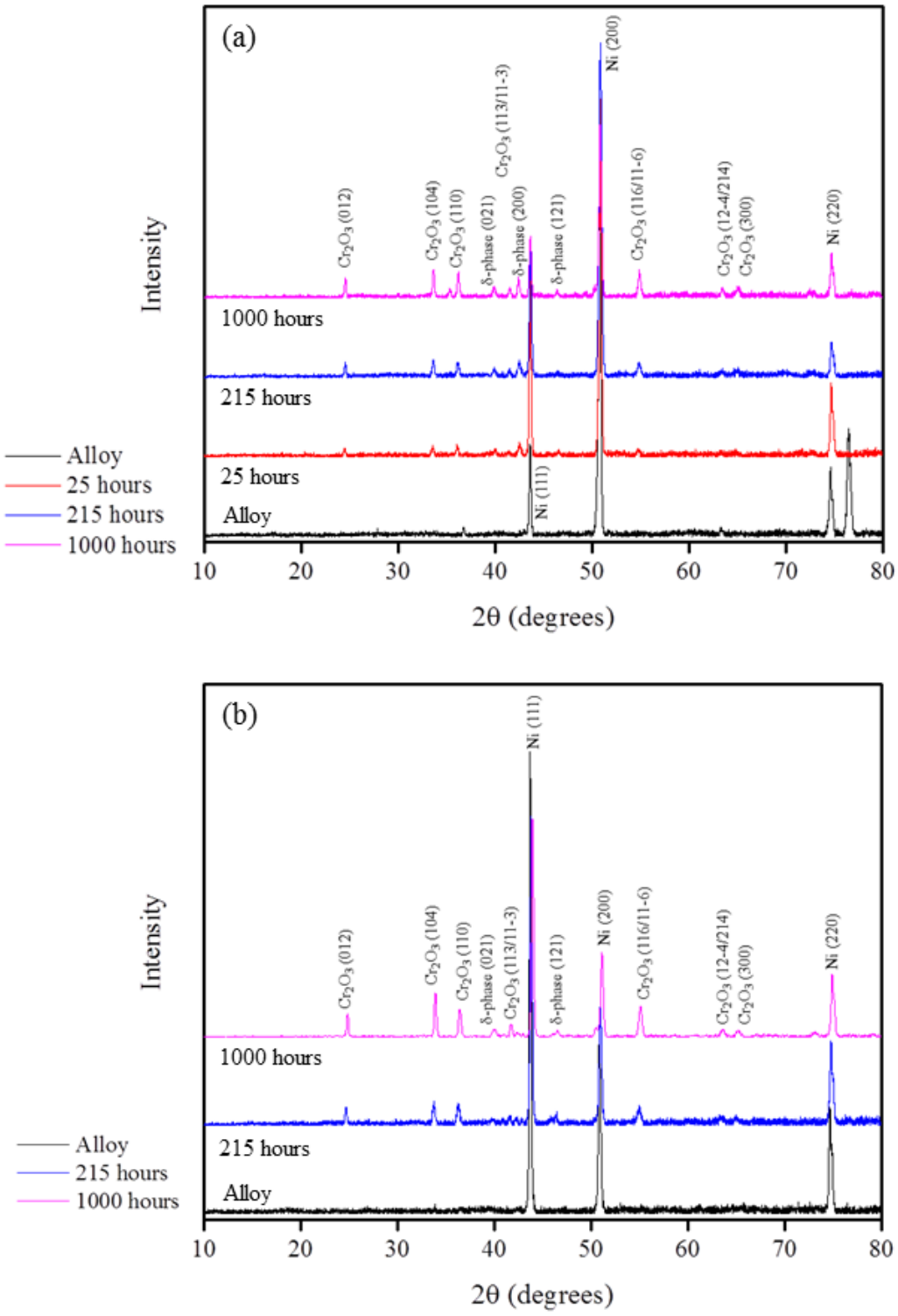

Figure 6.6: Diffractograms obtained from Alloy 625 ODS following isothermal oxidation in laboratory air at 900°C (a) Alloy 625 ODS/SLM, (b) Alloy 625 ODS/SPS

6.3.2 Alloy 625

Initial Examination by Microscopy

The oxidised surfaces of the SLM-consolidated alloy were, at low magnifications, featureless, but long stringers of oxidised inclusions, believed to be Nb(Ti)C carbides, were readily apparent in the scale that formed on the oxidised coupons of the wrought alloy, Figure 6.7.

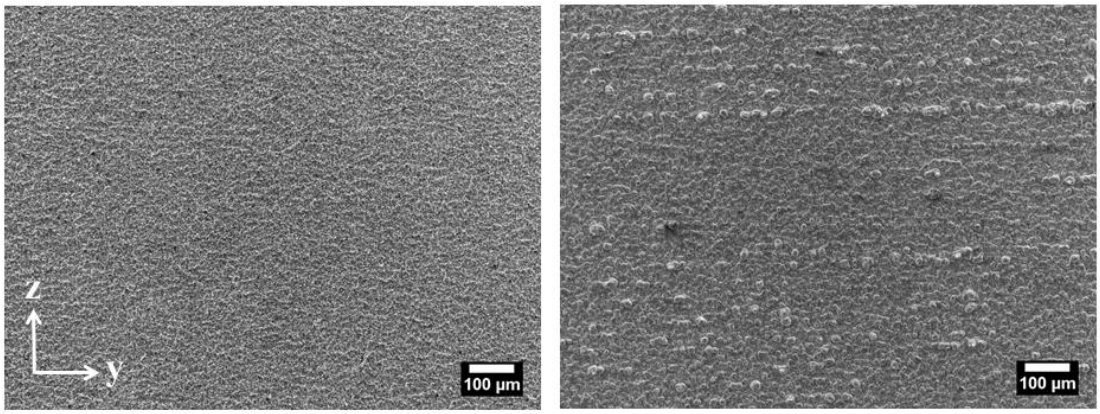

a b

Figure 6.7: SE micrographs Alloy 625 following 1000 hours of isothermal oxidation in laboratory air at 900°C (a) SLM-consolidated, (b) Wrought

The scale formed on the SLM-consolidated alloy was significantly thinner, but more wrinkled, than that which formed on the wrought alloy, Figures 6.8 and 6.9. A layer of δ-phase formed at the scale/alloy interface, as a result of oxidation-induced depletion of the δ-phase present in the bulk alloy. The depth of the depleted zone increased from ~10µm after 25 hours of oxidation to 50µm after 1000 hours of oxidation. Incorporation of δ-phase particles into the scale resulted from inward growth or deformation of the scale at the scale/alloy interface. Internal oxide particles, of <100nm in size, precipitated in the SLM-consolidated alloy during the first 25 hours of oxidation, which persisted to 1000 hours, but did not obviously grow in size or increase in number. At all oxidation times the alloy remained free of large internal oxides. The wrought alloy also developed small internal oxide particles

within the first 25 hours of oxidation, initially at the boundaries of small grains formed at the scale/alloy interface as a result of recovery and recrystallisation, but later as deep oxide fissures at the grain boundaries of the alloy. The SLM-consolidated alloy formed significantly less internal oxide than the wrought alloy because the Al and Ti content of the gas atomised powder, from which the SLM-consolidated alloy was consolidated, was much lower i.e. 0.04 Wt.% and 0.02 Wt.% respectively, as opposed to 0.19 Wt.% and 0.20 Wt.% respectively for the wrought alloy. The dendritic/cellular microstructure of the SLM-consolidated alloy was maintained to 25 hours of oxidation, but grain growth occurred at oxidation times >25 hours. However, even after at 215 and 1000 hours of oxidation, a layer of fine grains, ~5-10µm deep, was often preserved at the scale/alloy interface. Grain growth occurred beyond this zone as a result of dissolution of the grain boundary δ-phase. Facetted voids of ~1µm in size, possibly Kirkendall voids, were present in the SLM-consolidated alloy at all oxidation times, Figure 6.10. The voids were mainly concentrated in the upper 10µm of the alloy, possibly because vacancy condensation is enhanced where there is a high density of dendrite/cell boundaries in the alloy. The voids have an orientation relationship with the alloy, but this was not investigated.

Element maps, obtained following 215 hours of oxidation, are shown for the SLM-consolidated alloy and the wrought alloy in Figures 6.11 and 6.12 respectively. The surface of the alloy was depleted in Cr, but enriched in Ni and Fe (Fe map not shown for wrought alloy). In the SLM-consolidated alloy, a semi-continuous layer, ~1µm thick, of Nb-rich δ-phase is present at the scale/alloy interface but depleted in the alloy to a depth of ~20µm. Al and Ti were not detected. The wrought alloy contained a blocky phase, rich in Nb and Mo, but of variable composition, and ~1-5µm in size. This appeared to be more resistant to dissolution than the δ-phase present in the SLM-consolidated alloy, but precipitated in the form of large grains at the scale/alloy interface. Al-rich oxide formed on the grain boundaries of the alloy.

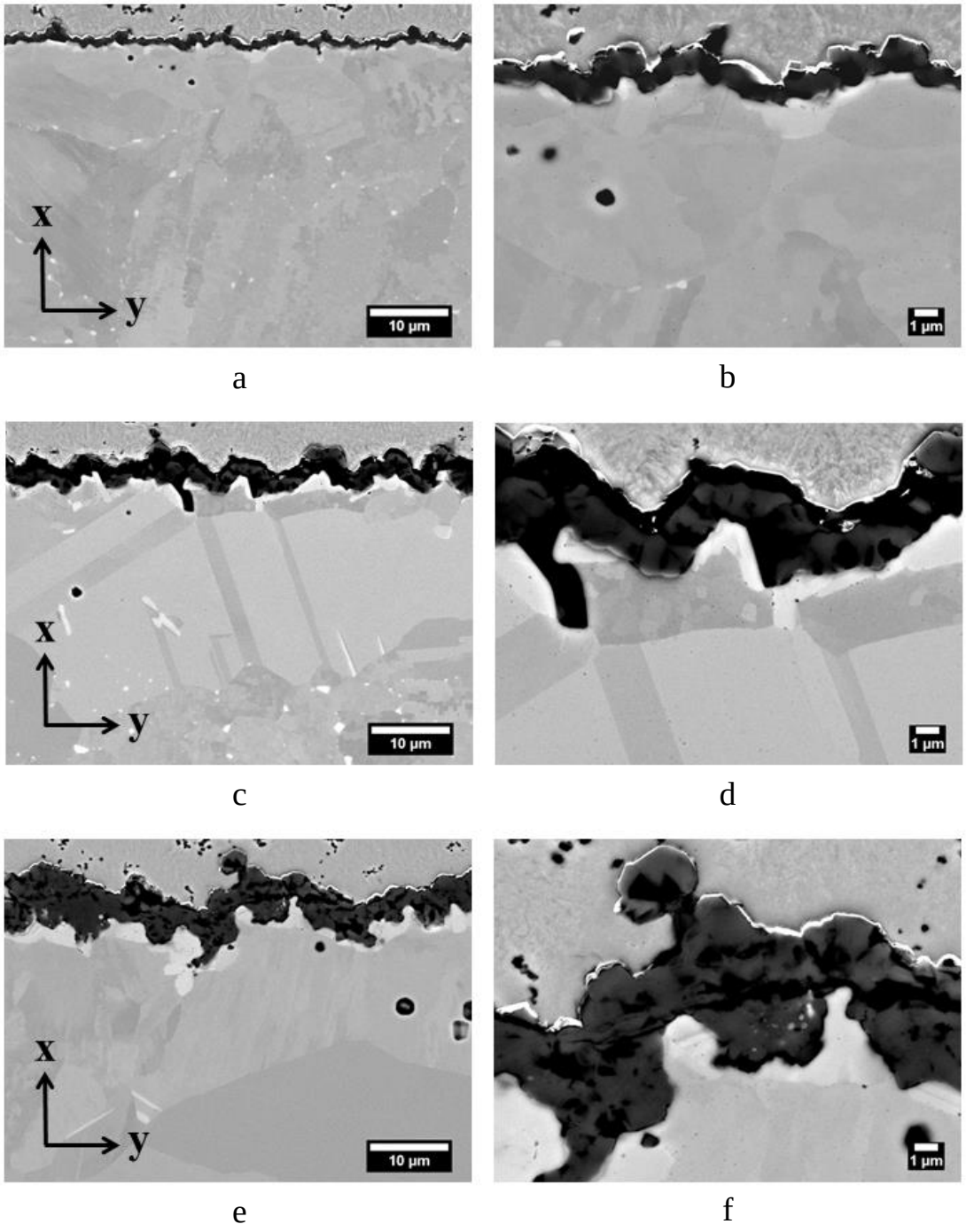

Figure 6.8: BSE micrographs of cross-sections of SLM-consolidated Alloy 625 following isothermal oxidation in laboratory air at 900°C (a), (b) 25 hours, (c), (d) 215 hours and (e), (f) 1000 hours

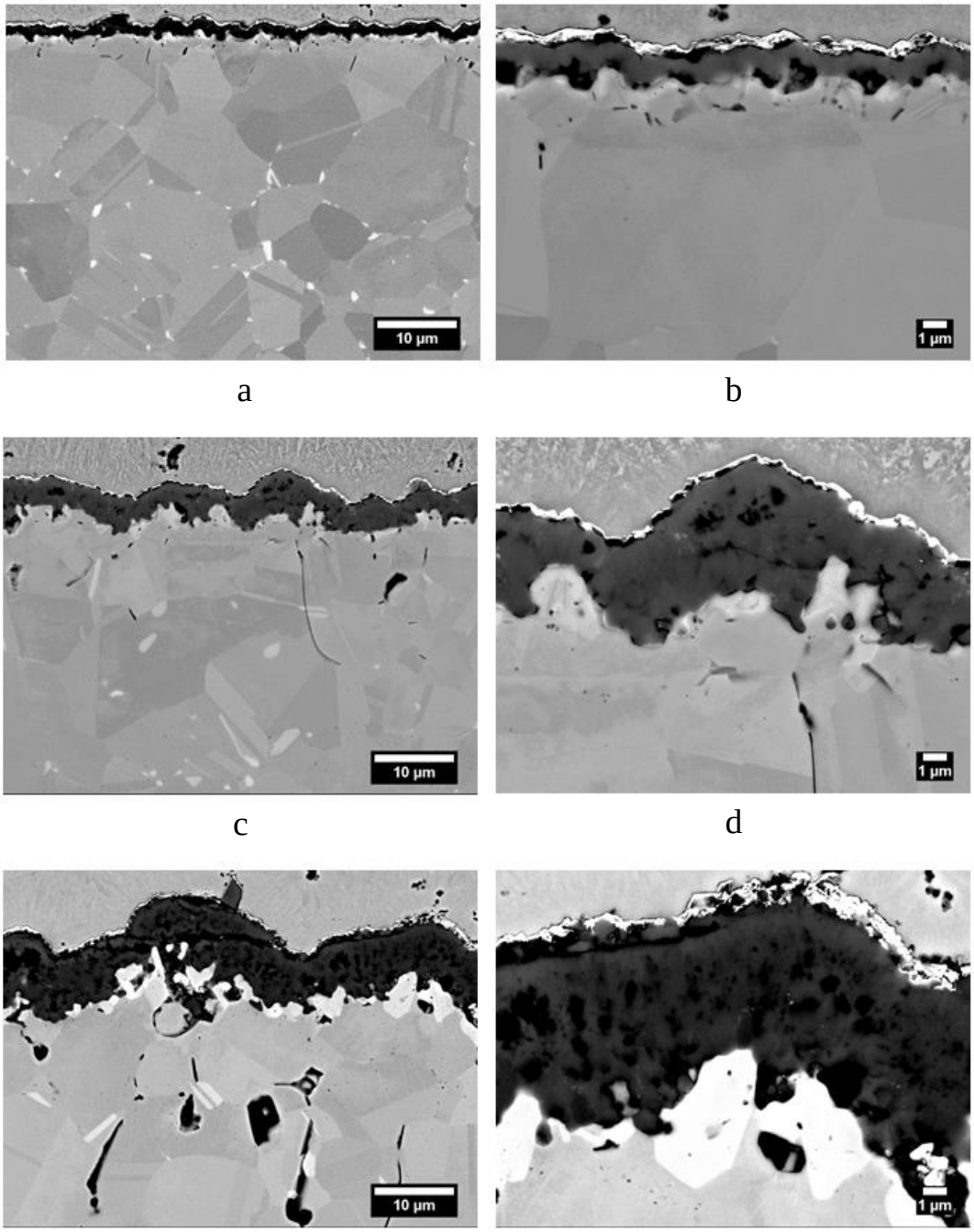

Figure 6.9: BSE micrographs of cross-sections of wrought Alloy 625 following isothermal oxidation in laboratory air at 900°C (a), (b) 25 hours, (c), (d) 215 hours and (e), (f) 1000 hours

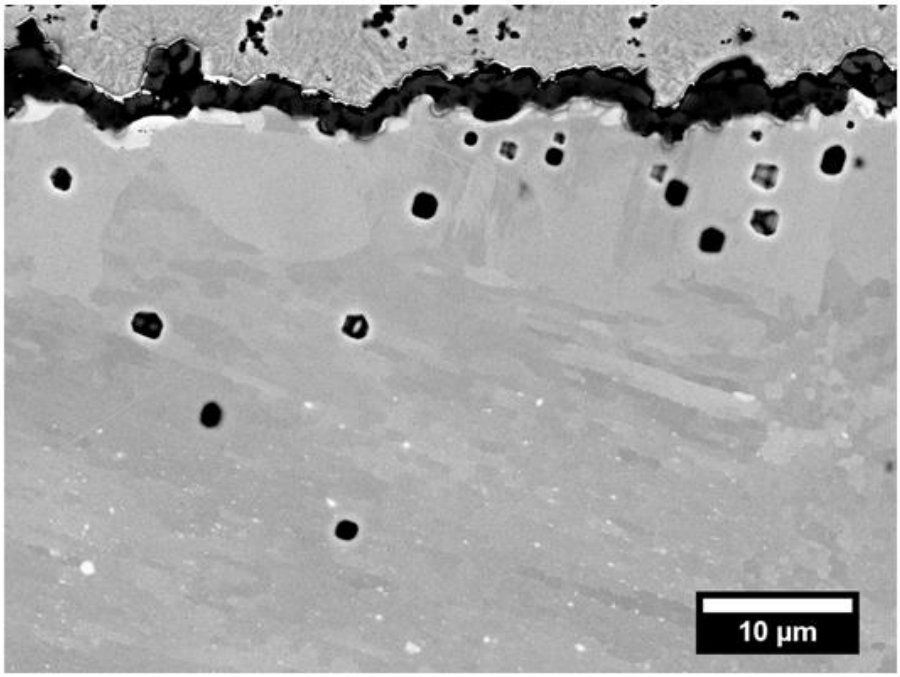

a

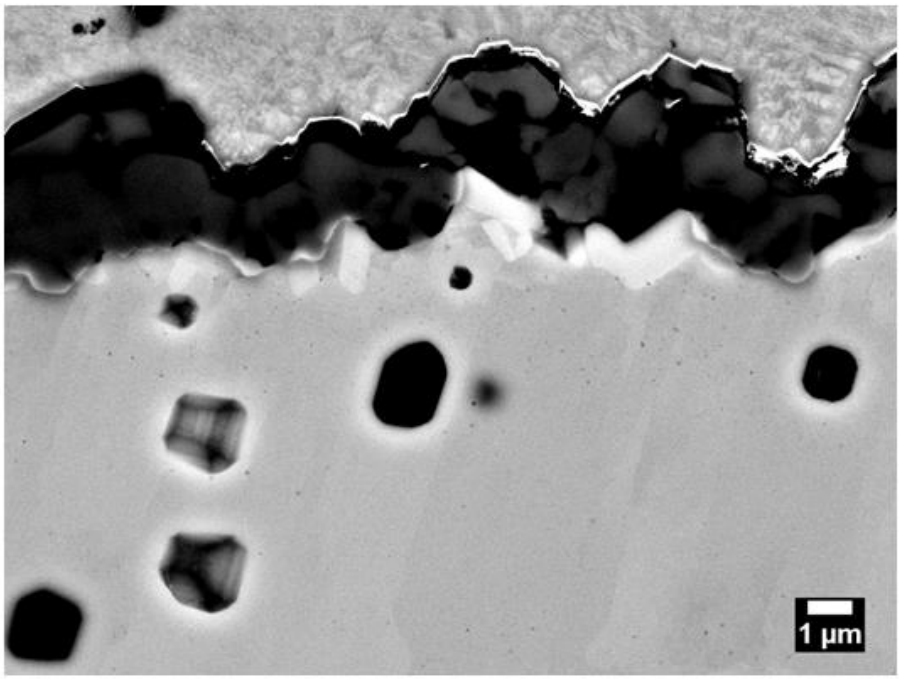

b

Figure 6.10: Voids in cross-section of SLM-consolidated Alloy 625 following 215 hours of isothermal oxidation in laboratory air at 900°C (a) low magnification, and (b) detail

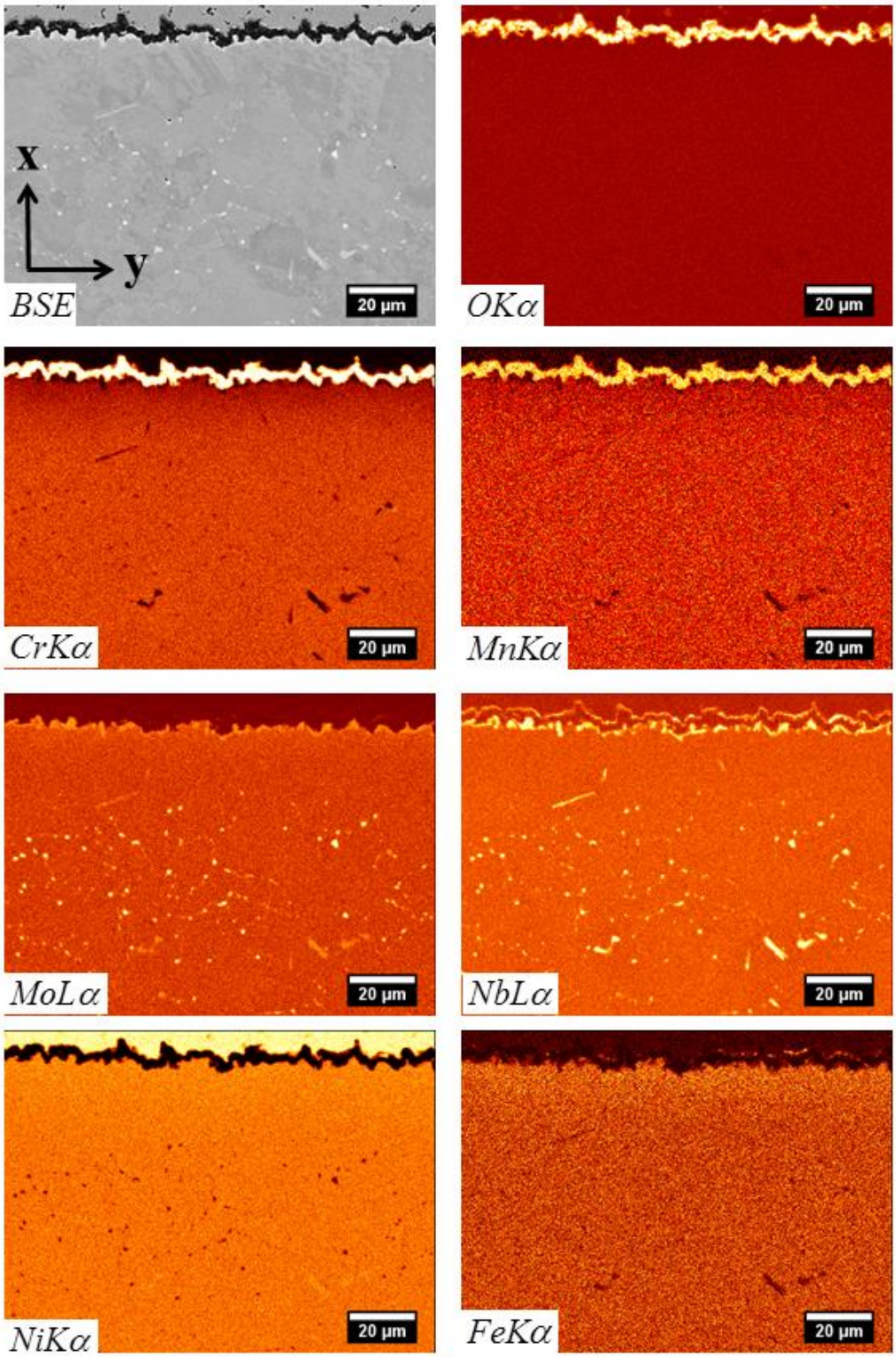

Figure 6.11: Element maps obtained from a cross-section of SLM-consolidated Alloy 625 following 215 hours of isothermal oxidation in laboratory air at 900°C

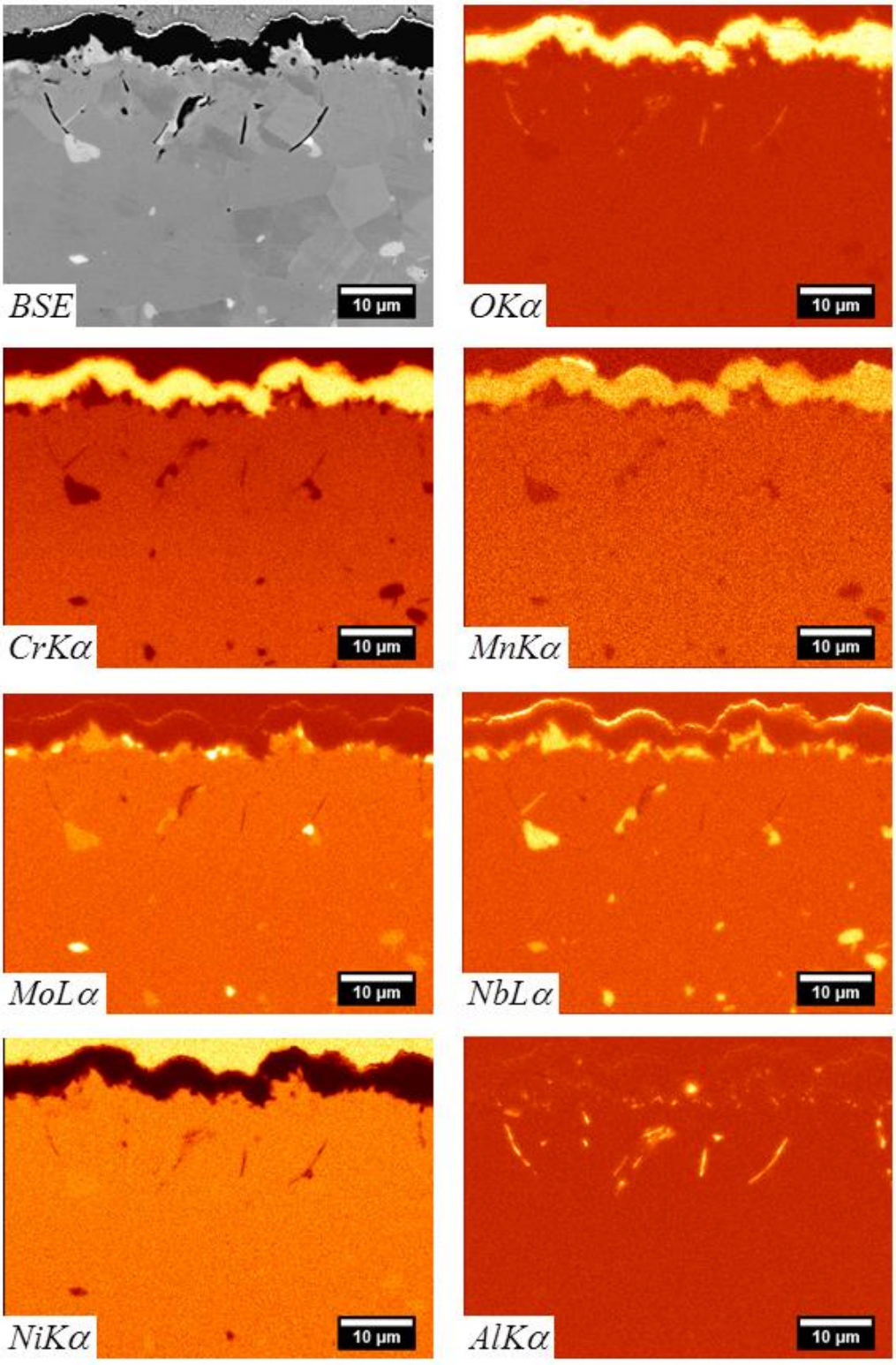

Figure 6.12: Element maps obtained from a cross-section of wrought Alloy 625 following 215 hours of isothermal oxidation in laboratory air at 900°C

Detailed Examination of Scale Morphology

The scale present on the SLM-consolidated alloy was, after 1000 hours of oxidation, comprised of facetted grains that ranged in size from ~0.5-2µm, whereas the scale formed on the wrought alloy was, after the same oxidation time, comprised of a relatively small number of 2-5µm grains covered by many submicron grains, Figure 6.13.

The oxide grains in the scale on the SLM-consolidated alloy increased in size from ~0.5µm after 25 hours of oxidation, to ~1µm in size after 1000 hours of oxidation, Figure 6.14. 'Knots' of ~3-4µm diameter, and comprised of equiaxed and columnar grains of ~0.1-0.5µm in size, formed in the scale at the longer oxidation time, Figure 6.14(b). The 'knots' were present in the scale at intervals of 20-50µm and developed where the scale appeared to have grown inwardly, or deformed to maintain contact with the alloy, to undercut the layer of δ-phase present at the scale/alloy interface, releasing particles of δ-phase of ~20-50nm in size into the scale, Figure 6.15. The particles of δ-phase were often present on the grain boundaries in the fine scale 'knots', including triple points. The fine grain 'knots' only appeared where δ-phase was incorporated into the scale, possibly due to the grains in the 'knots' being pinned by particles of δ-phase, or possibly due to enhanced nucleation of the oxide grains by the particles of δ-phase.

The microstructure of the scale formed on the wrought alloy is shown in Figures 6.16 and 6.17. The scale formed on the wrought alloy was, after 25 hours of oxidation, thicker than that which formed on the SLM-consolidated alloy, but comprised of smaller grains, which were typically ~0.2µm in size. Small voids formed at the scale/alloy interface and localised detachment of the scale occurred above them. By 1000 hours of oxidation the scale had formed a duplex grain structure, which was comprised of columnar grains of ~1µm in size at the scale/alloy interface, and equiaxed grains of ~0.2µm in size at the scale/gas interface. The alloy had plastically deformed, consistent with large tensile stresses perpendicular to the

scale/alloy interface. The columnar structure of the basal oxide grains may be due to creep. The wrinkled appearance of the scale is consistent with counter-current diffusion, which is believed to generate compressive stresses as a result of grain growth on the boundaries of the oxide grains [254-256]. δ-phase was incorporated into the basal region of the scale, but there was no clear correlation between oxide grain size and the distribution of δ-phase particles in the scale, as was observed for the SLM-consolidated alloy. Isolated patches of $Mn_xCr_{3-x}O_4$ spinel were present on the wrought alloy at the scale/gas interface, but the SLM-consolidated alloy did not form spinel because it had a much lower Mn content i.e. <0.01 Wt. % Mn in the SLM-consolidated alloy, as opposed to 0.2 Wt. % Mn in the wrought alloy.

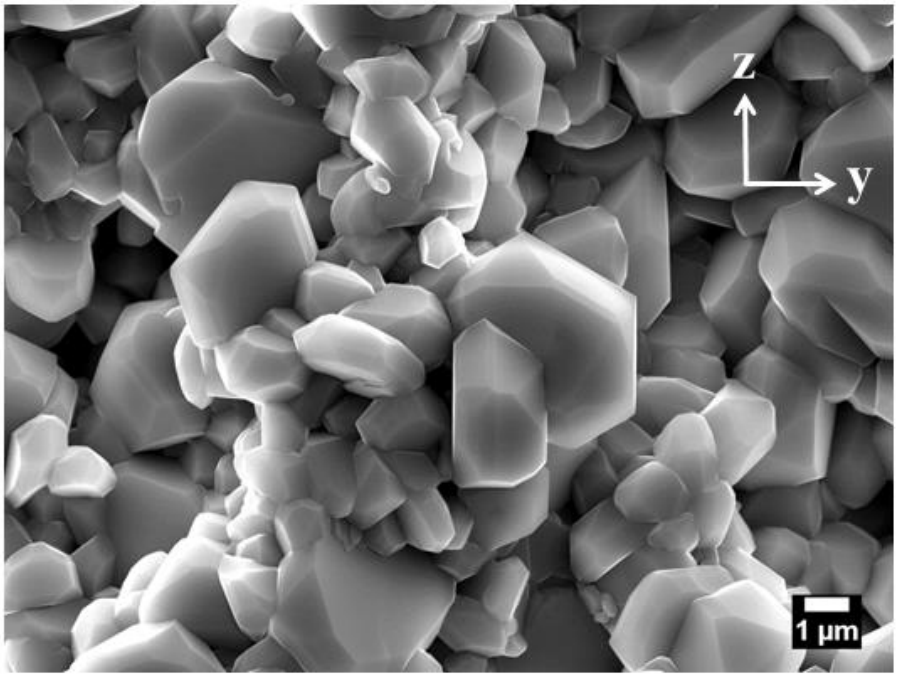

a

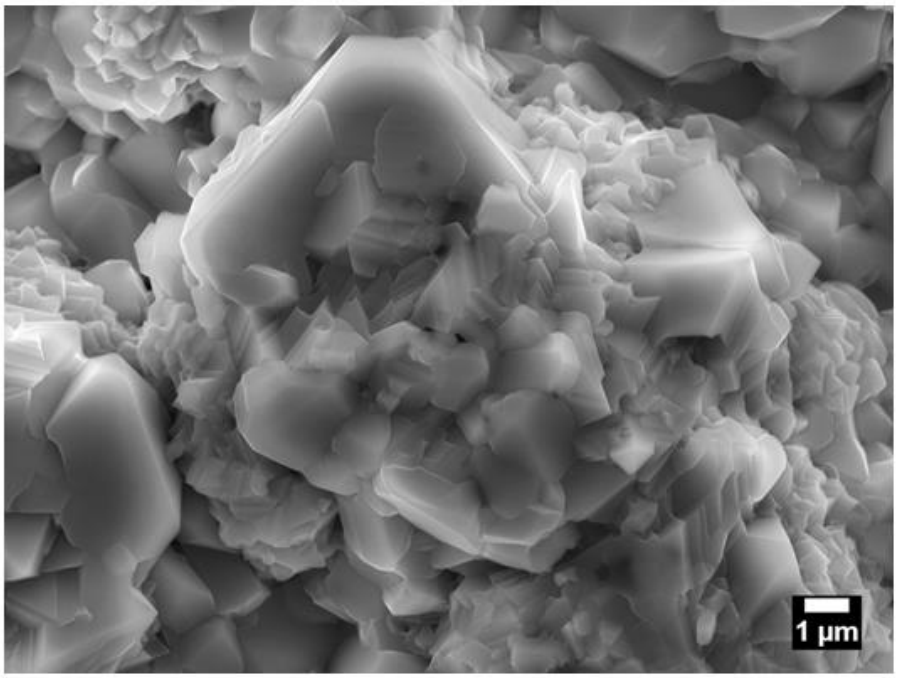

b

Figure 6.13: SE micrographs of Alloy 625 following isothermal oxidation in laboratory air at 900°C for 1000 hours (a) SLM-consolidated, (b) Wrought

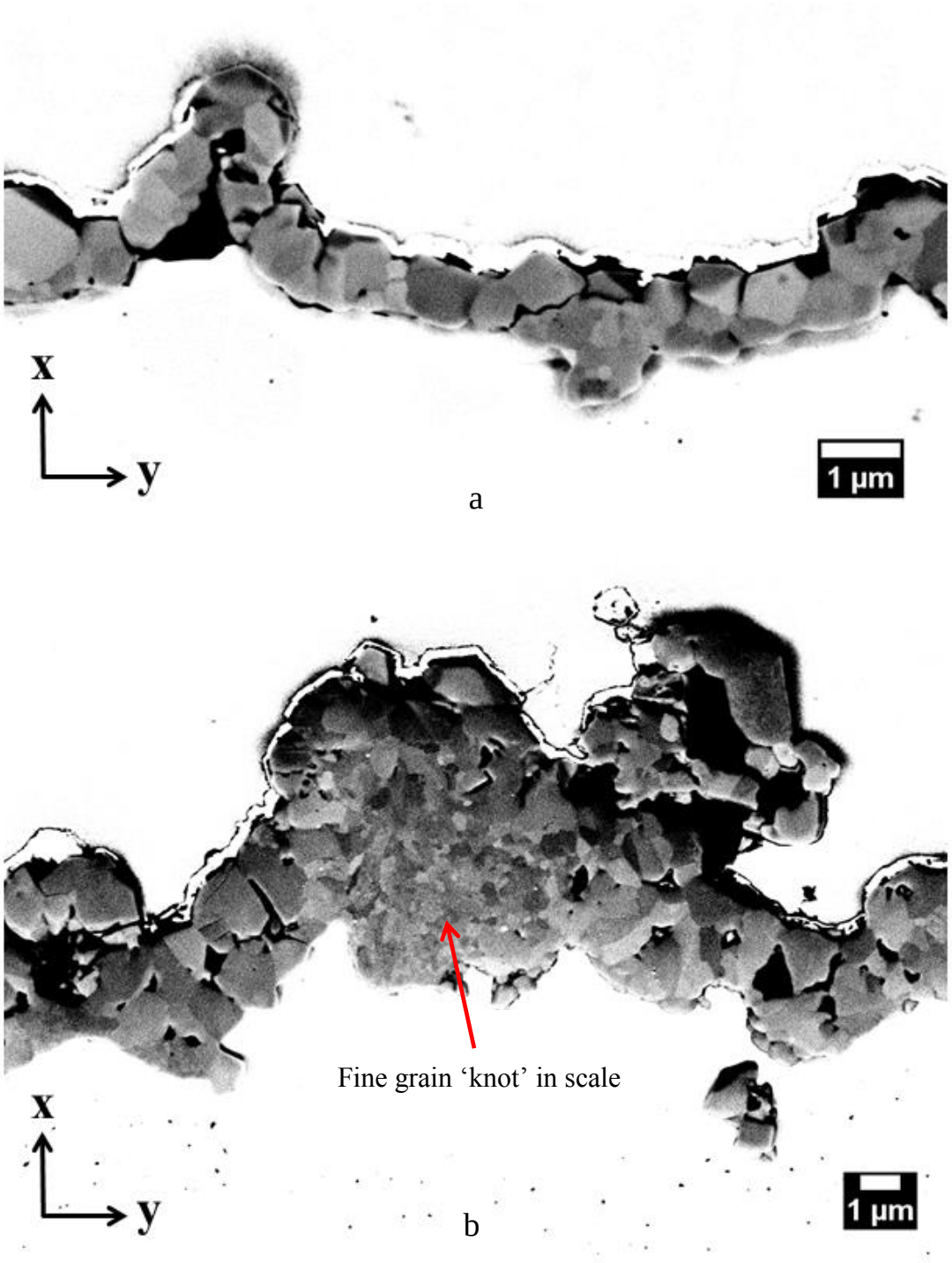

Figure 6.14: Low voltage channelling contrast micrographs of the scale formed on SLM-consolidated Alloy 625 following isothermal oxidation in laboratory air at 900°C (a) 10 hours, and (b) 1000 hours

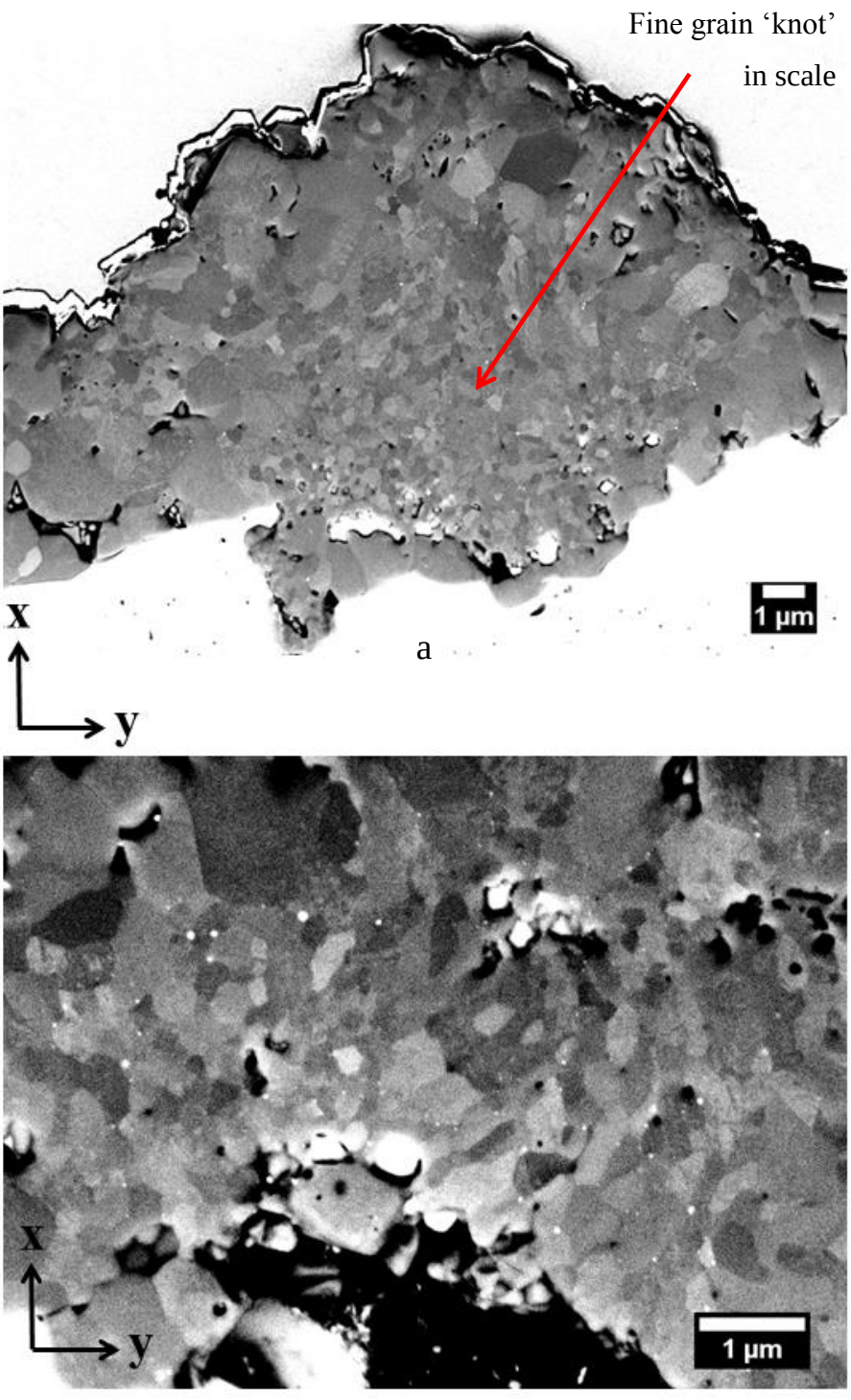

Figure 6.15: Low voltage channelling contrast micrographs of the scale formed on SLM-consolidated Alloy 625 following 1000 hours of isothermal oxidation in laboratory air at 900°C (a) low magnification, and (b) detail of a fine grain 'knot'

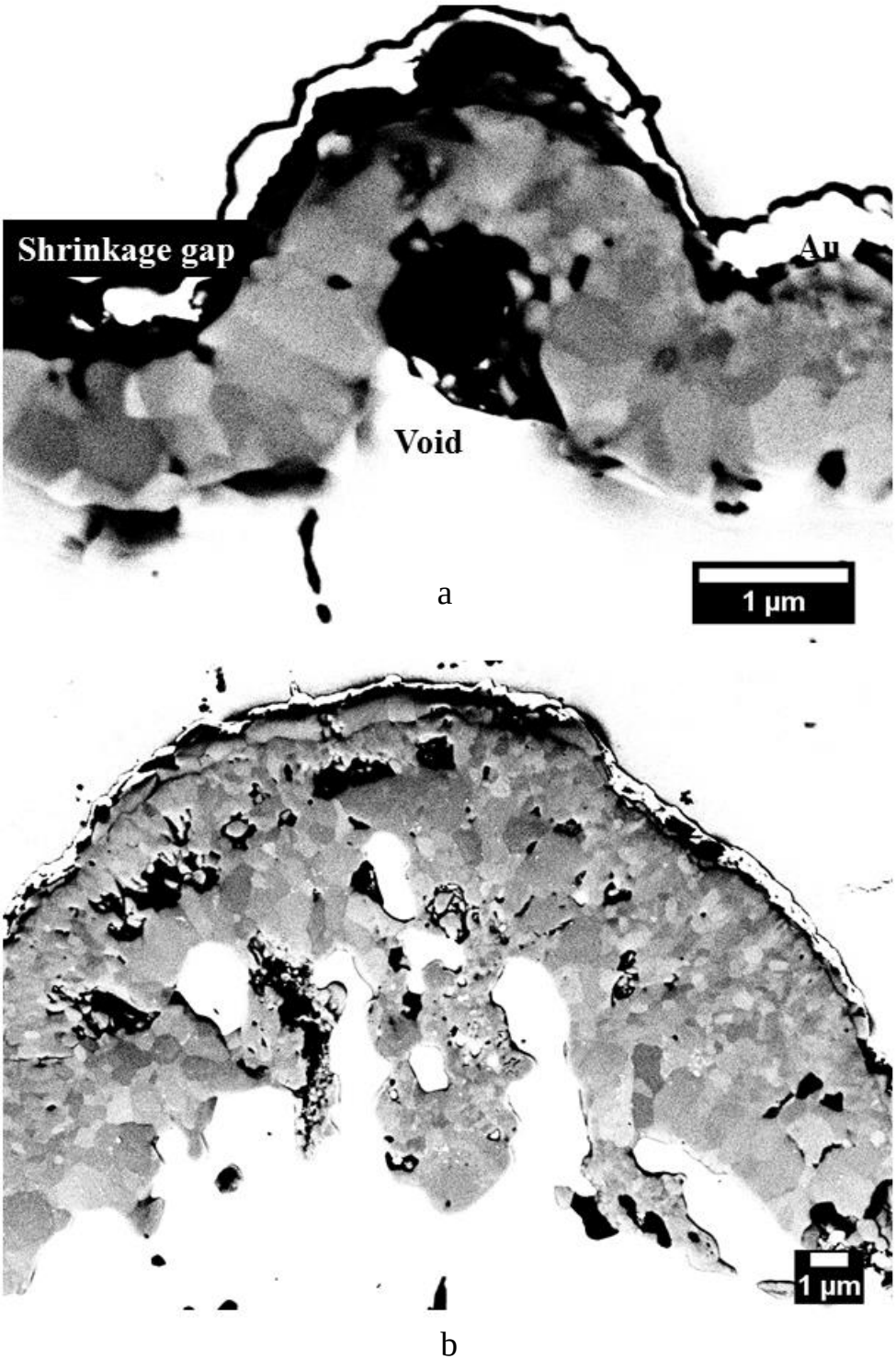

Figure 6.16: Low voltage channelling contrast micrographs of the scale formed on wrought Alloy 625 following isothermal oxidation in laboratory air at 900°C (a) 25 hours, and (b) 1000 hours

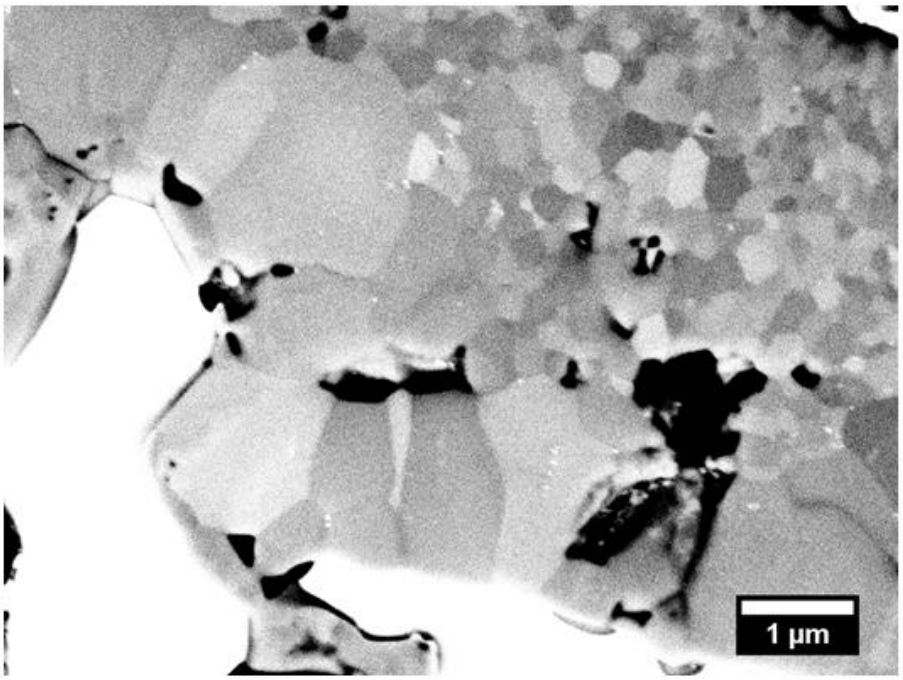

a

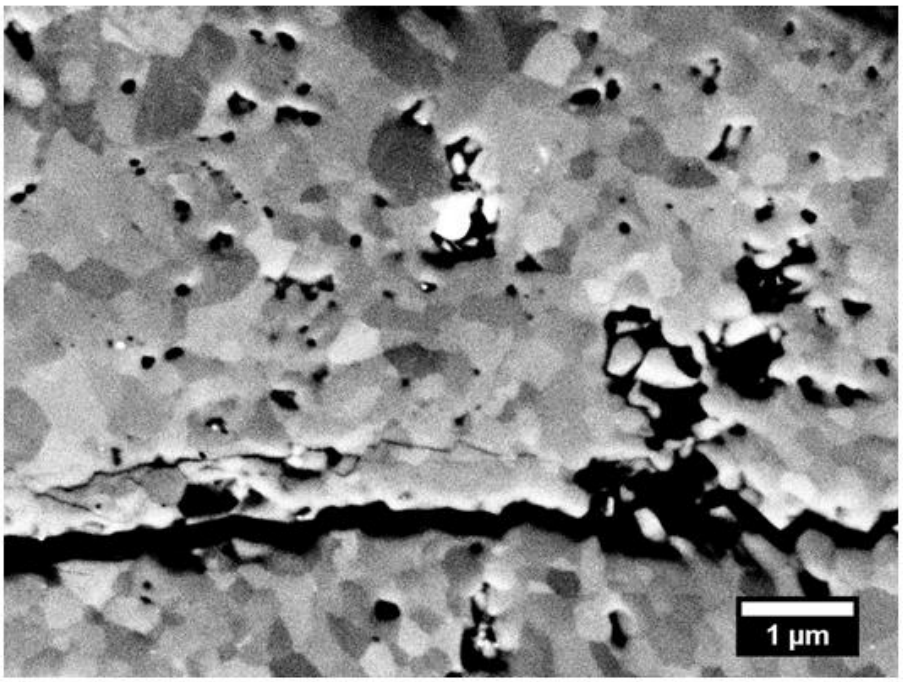

b

Figure 6.17: Low voltage channelling contrast micrographs of the scale formed on wrought Alloy 625 following 1000 hours of isothermal oxidation in laboratory air at 900°C (a) scale/alloy interface, and (b) within fine grain scale

6.3.3 Alloy 625 ODS

Initial Examination by Microscopy

The scale formed on Alloy 625 ODS/SLM was initially comprised of smooth, thin regions that formed a distinct pattern of interconnected and approximately circular patches in a scale that was otherwise relatively thick and rough, Figure 6.18 (a). Most of the circular patches had at their centre a particle rich in Y, but these were no longer evident after 1000 hours of oxidation. The ratio of thick, rough scale to thin, smooth scale increased with oxidation time until the pattern evident at short oxidation times was replaced by a surface of relatively uniform average atomic number. After 1000 hours of oxidation, nodules of ~10-20µm in diameter appeared in the scale, which were comprised of large, smooth Cr_2O_3 grains and small faceted $Mn_xCr_{3-x}O_4$ grains, Figure 6.18 (b). It was not clear if the nodules had developed where the scale was initially thin or thick.

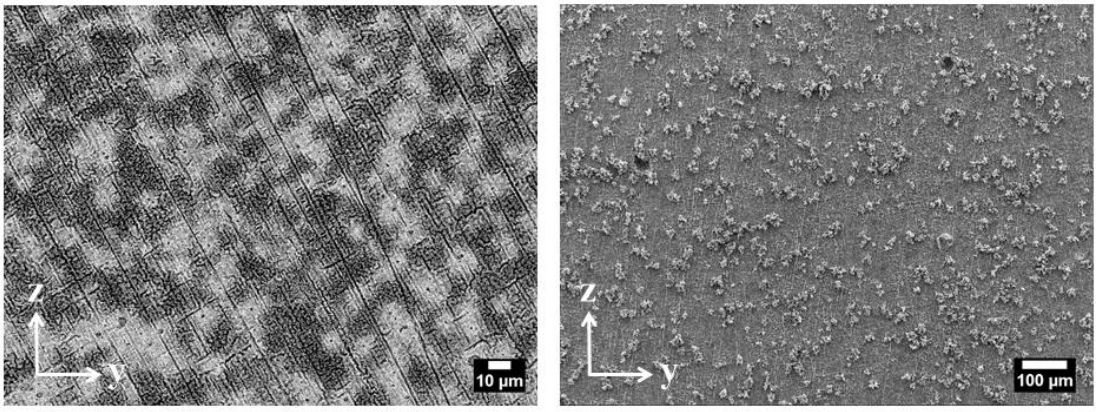

a b

Figure 6.18: Scale formed on Alloy 625 ODS/SLM following isothermal oxidation in laboratory air at 900°C (a) 25 hours (BSE), (b) 1000 hours (SE)

The scale that developed on Alloy 625 ODS/SPS was generally very thin, except where submicron particles locally formed into slightly thicker patches, Figure 6.19

(a). A small number of facetted Cr particles of ~5µm size formed in the scale after 1000 hours of oxidation, but the scale remained thin, Figure 6.19 (b).

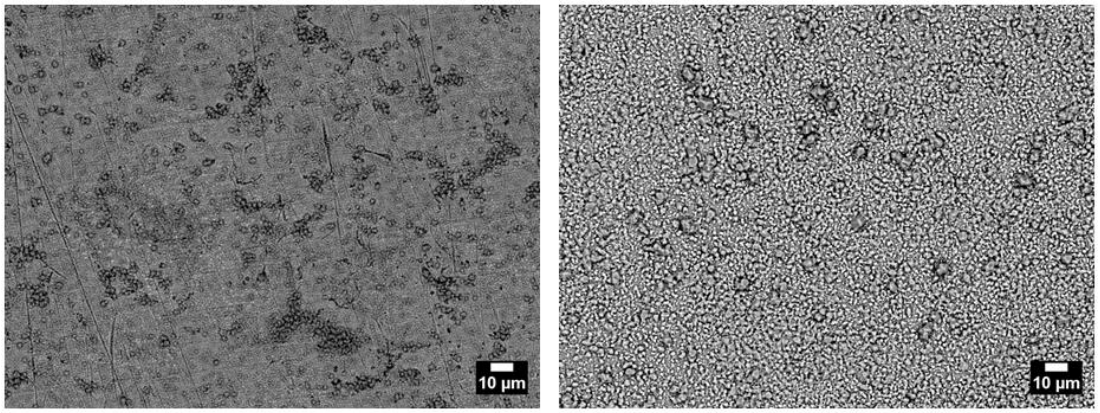

a b

Figure 6.19: BSE micrographs of scale formed on Alloy 625 ODS/SPS following isothermal oxidation in laboratory air at 900°C (a) 50 hours, (b) 1000 hours

Examination of the scales in cross-section revealed that they were dense and free of porosity, and attained a maximum thickness of ~1-2µm during oxidation, Figures 6.20 and 6.21. The scale formed on the SLM-consolidated alloy was generally thinner, but more irregular in thickness, than that which formed on the SPS-consolidated alloy. The parent alloys were not annealed prior to oxidation, so the Nb-rich phase was still present in the coupons prepared for oxidation. If the phase were Laves phase it would have been solutionised and δ-phase precipitated during oxidation testing, but this did not occur and the phase remained present in the bulk alloy for the full duration of the oxidation experiments. It is also noticeable that a layer of δ-phase did not form at the scale/alloy interface, as it did in SLM-consolidated Alloy 625 and wrought Alloy 625. This suggests that the Nb-rich phase is not Laves phase, but possibly Nb-rich carbide. The alloy did not form internal oxides, which is explained by the low Al and Ti content of the gas atomised powder from which the alloy was consolidated; 0.04 Wt. % and 0.02 Wt. % respectively. The original microstructure of the alloy was preserved during oxidation, with no obvious grain growth evident. This is probably due to pinning of the grains by

dispersoids. Numerous voids formed in Alloy 625 ODS/SLM, but not in Alloy 625 ODS/SPS. The voids were ~1µm in size and developed between 25 hours and 215 hours of oxidation in a zone ~20µm deep from the scale/alloy interface. These were probably Kirkendall voids.

Element maps obtained from sections of Alloy 625 ODS/SLM and Alloy 625 ODS/SPS are presented in Figures 6.22 and 6.23 respectively. These were obtained from coupons oxidised for 215 hours. The SLM-consolidated alloy contained voids and Y-rich inclusions. The Nb/Mo-rich phase, probably carbide, is depleted to a depth of ~5µm from the scale/alloy interface. A phase rich in Nb and Mo is observed at the scale/alloy interface, but it is not continuous, unlike the phase that formed in SLM-consolidated Alloy 625 and wrought Alloy 625. It should be noted that continuous layer on the scale in Nb map is Au, which was applied to make the coupon conductive for Ni-plating and overlaps Nb in EDS spectra.

The SPS-consolidated alloy is free of the voids and inclusions that characterise the SLM-consolidated alloy. Swathes of particles rich in Nb and Mo are present in the alloy, but Y, which appears to be present in the alloy, is not observed when the spectra used to construct the map are scrutinised, and is observed because of an overlap with Mo - the map is shown to illustrate the fact that particulate Y is not present in the alloy, unlike in the SLM-consolidated alloy. There is no evidence of dissolution of the Nb/Mo-rich phase or the development of a layer of δ-phase at the scale/alloy interface. The continuous layer on the surface of the Cr in the Nb map is Au, which had to be applied thickly to this specimen because of issues with Ni-plating.

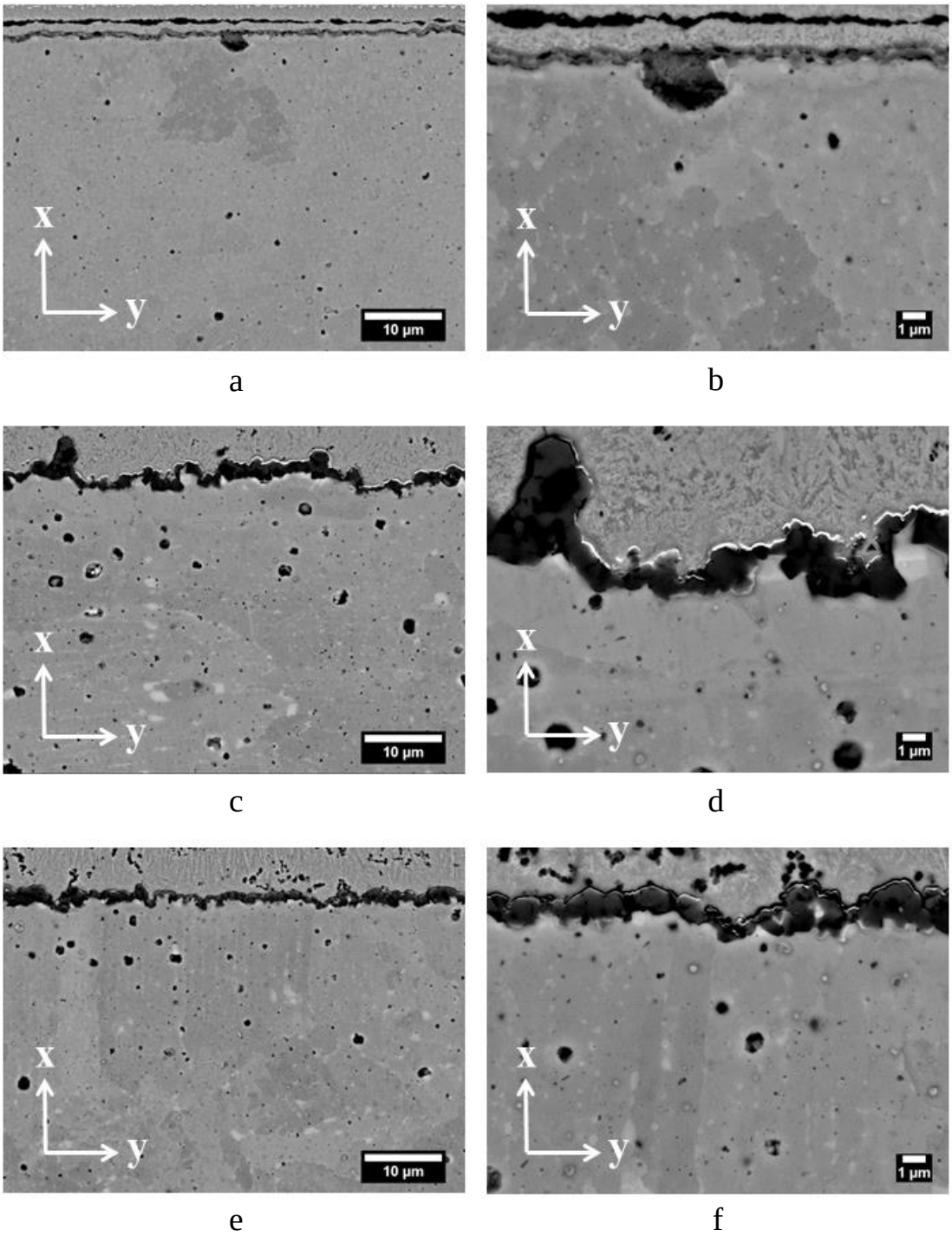

Figure 6.20: BSE micrographs of cross-sections of Alloy 625 ODS/SLM following isothermal oxidation in laboratory air at 900°C (a), (b) 25 hours, (c), (d) 215 hours and (e), (f) 1000 hours

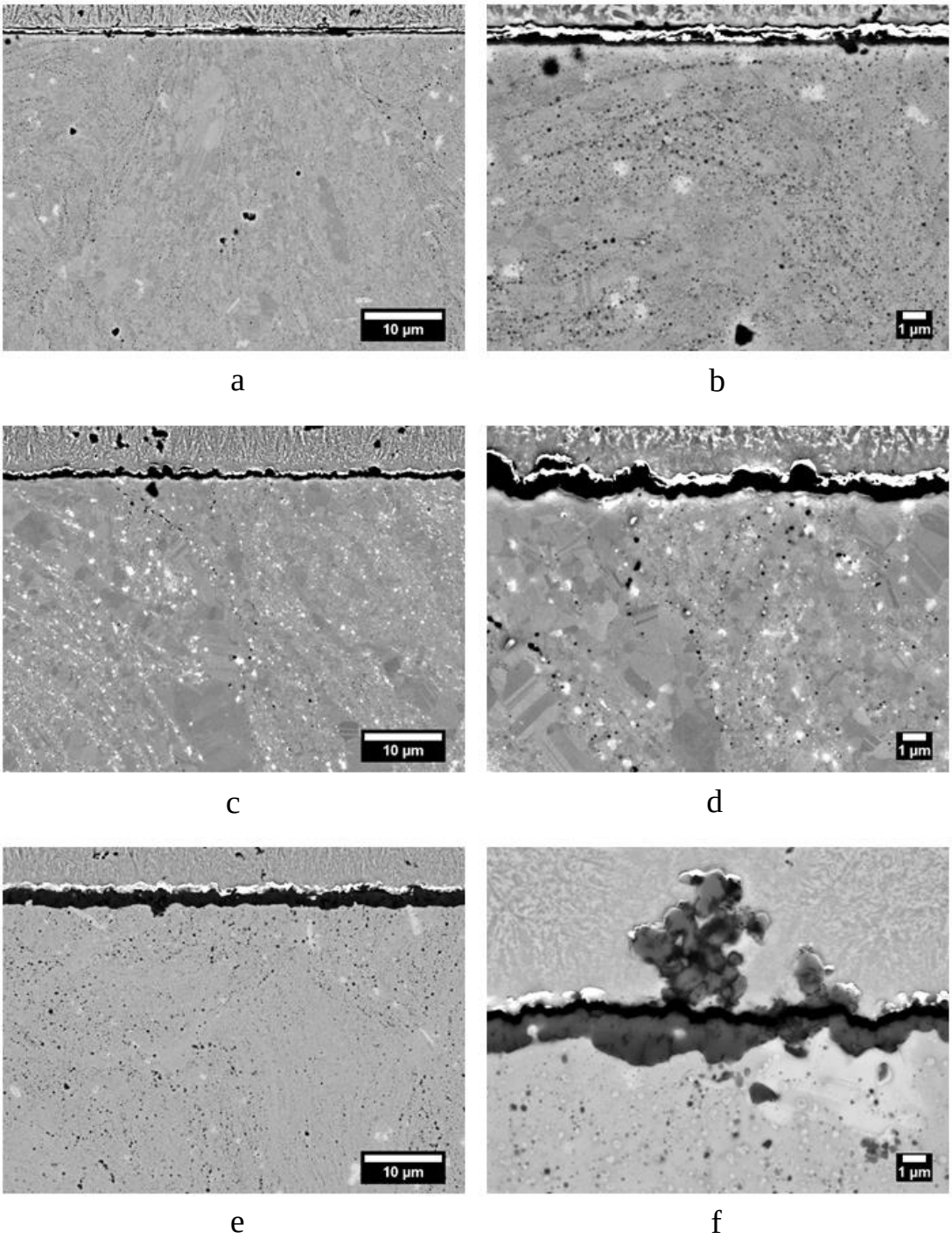

Figure 6.21: BSE micrographs of cross-sections of Alloy 625 ODS/SPS following isothermal oxidation in laboratory air at 900°C (a), (b) 25 hours, (c), (d) 215 hours and (e), (f) 1000 hours

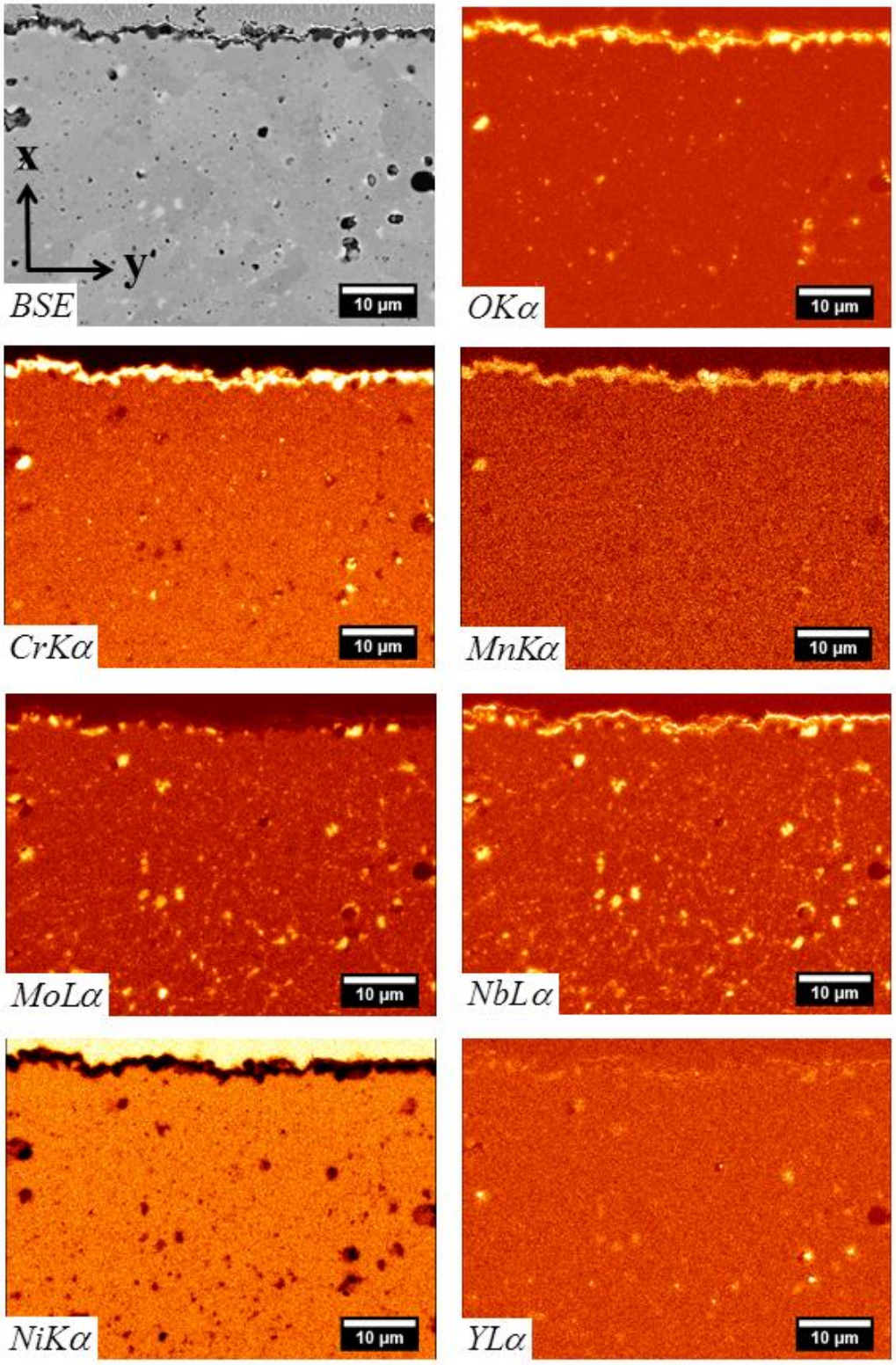

Figure 6.22: Element maps obtained from a cross-section of Alloy 625 ODS/SLM following 215 hours of isothermal oxidation in laboratory air at 900°C

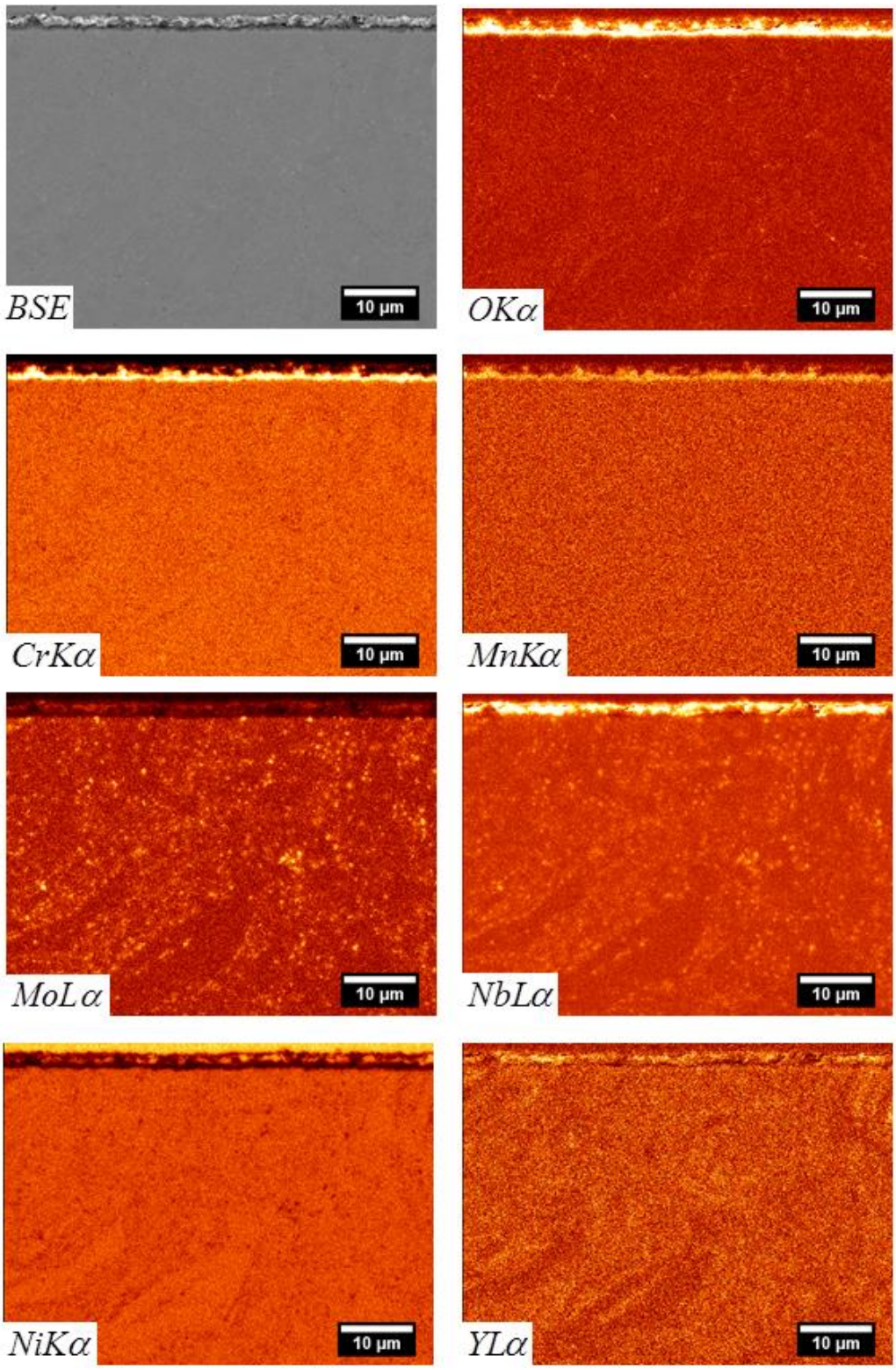

Figure 6.23: Element maps obtained from a cross-section of Alloy 625 ODS/SPS following 215 hours of isothermal oxidation in laboratory air at 900°C

Detailed Examination of Scale Morphology

The scale formed on the SLM-consolidated alloy had a relatively uniform grain size of ~0.5µm, whereas the scale formed on the SPS-consolidated alloy was mainly comprised of grains of <0.5µm in size, with a smaller number of facetted grains of 1-2µm also present, Figure 6.24.

Cross-sections of the scales were prepared by FIB from scales formed after 215 hours of oxidation. These were examined in a STEM. Micrographs of the scales are shown for Alloy 625 ODS/SLM in Figure 6.25, and for Alloy 625 ODS/SPS in Figure 6.26. The scale formed on the SLM-consolidated alloy was ~200-500nm thick and comprised of a single layer of chromia grains, Figures 6.25 (a) and 6.25 (b). Present within the chromia scale was a band of particles, ~20nm wide and comprising a thin inner layer and a thick outer layer, which ran parallel to the scale/alloy interface. A position within the thick layer, like that indicated by the yellow box on Figure 6.25 (b), can be seen in Figures 6.25 (c) and 6.25 (d), which show it to be comprised of particles of <5nm in size. Analysis of the larger particles indicated that they were rich in Nb and O. The scale on the SPS-consolidated alloy was typically ~200nm thick, but with grains of ~1µm thick also present, Figure 6.26 (a-c). This is consistent with the SEM image, Figure 6.24 (b). At one position, adjacent to the scale/alloy interface, Y-rich particles and grain boundary rich in Y were observed, Figure 6.26(d). However, this was rare and was only of 2 or 3 positions where Y could be located, despite numerous attempts. A band of particles rich in Nb and O was visible in the scale at a position approximately equidistant from the scale/gas and scale/alloy interfaces, Figures 6.26 (a-c). The band had numerous voids associated with it, Figure 6.26 (e-f).

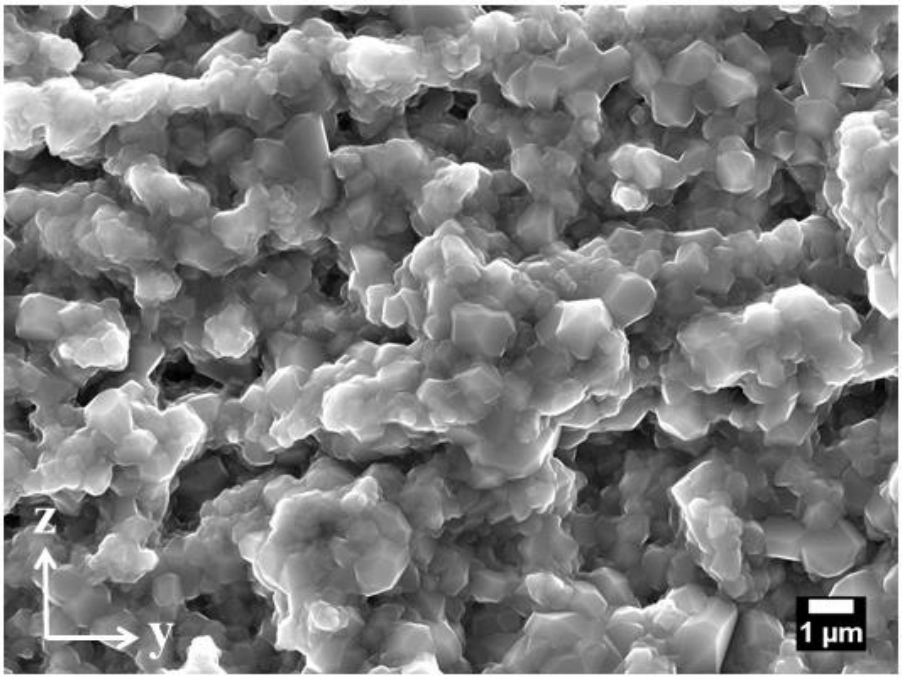

a

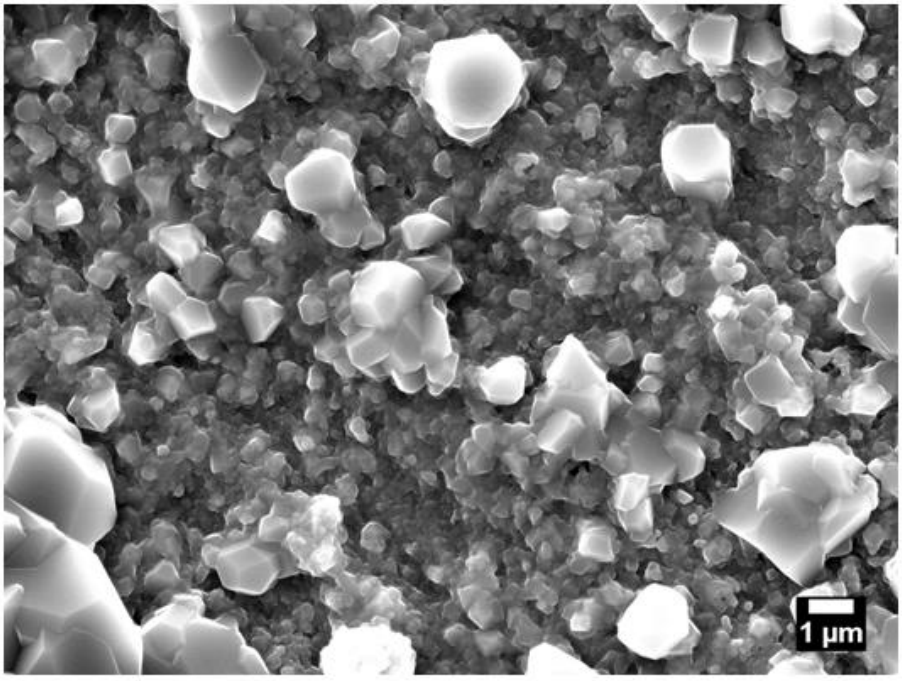

b

Figure 6.24: SE micrographs of Alloy 625 ODS following 215 hours of isothermal oxidation in laboratory air at 900°C (a) SLM-consolidated, (b) SPS-consolidated

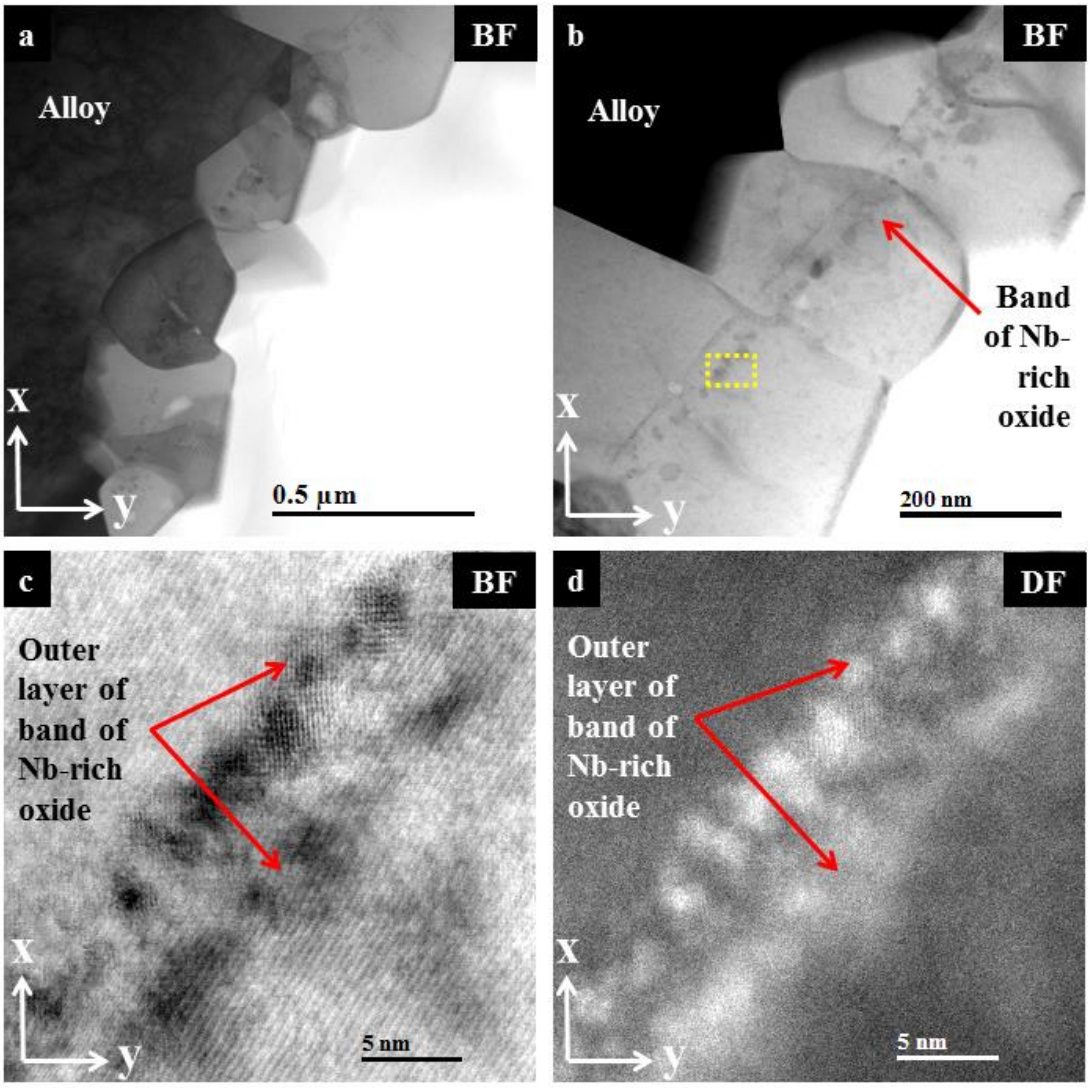

Figure 6.25: FIB cross-section of scale on Alloy 625 ODS/SLM following 215 hours of isothermal oxidation in laboratory air at 900°C

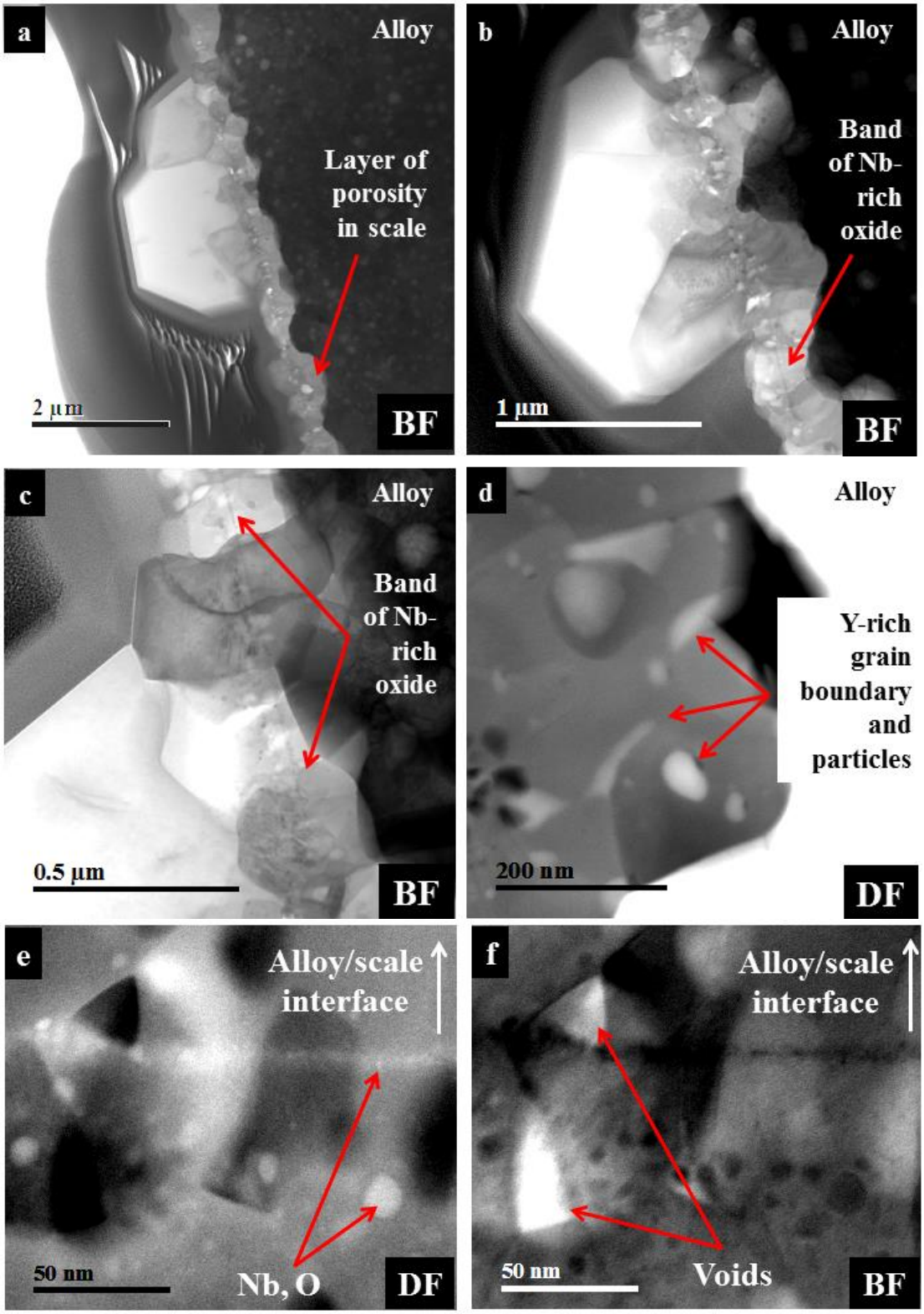

Figure 6.26: FIB section of scale on Alloy 625 ODS/SPS following 215 hours of isothermal oxidation in laboratory air at 900°C

6.3.4 Oxidation-induced changes in alloys

Analysis of Bulk Alloy

The bulk composition of each variant of the alloy is shown in Table 6.1, along with analyses provided by the suppliers. The analyses denoted ‘oxidised’ were obtained from the centre of each coupon following 1000 hours of oxidation, in order to provide terminal compositions for the depth profiles. Analyses were also obtained for the ODS alloys prior to oxidation, which are denoted ‘alloy’. The methodology used to obtain the compositions is the same as that used to analyse Alloy 718, which is described in section 5.3.5.

The analysis obtained from the SLM-consolidated alloy is in good agreement with that of the gas atomised powder. The analysis obtained from the wrought alloy is in very good agreement with that provided by the supplier. The analyses obtained from the ODS/SLM, ODS/SPS and SLM-consolidated alloy are well matched. However, it is also noticeable that the standard deviation of the ODS/SLM alloy is significantly larger than that of any other variant, which may be due to compositional variations arising from the formation of slag particles in the alloy. Y was not detected in any of the ODS alloys.

Table 6.1: Mean composition and standard deviation of bulk Alloy 625 determined for this work by SEM/EDS (Wt. %). Supplier analyses were obtained by XRF

Alloy	Ni	Fe	Cr	Nb	Mo	Ti	Al	Si	Mn
SLM oxidised (this work)	59.9 ±0.2	4.0 ±0.1	22.4 ±0.2	3.4 ±0.2	9.7 ±0.2	-	0.1 ±0.1	0.1 ±0.1	0.1 ±0.1
Gas atomised powder (supplier)	Bal.	3.60	20.83	3.64	9.10	0.02	0.04	0.10	-
Wrought oxidised (this work)	58.4 ±0.2	4.8 ±0.1	23.2 ±0.2	3.0 ±0.1	9.4 ±0.2	0.1 ±0.1	0.2 ±0.1	0.2 ±0.1	0.7 ±0.1
Wrought alloy (supplier)	60.08	4.68	22.02	3.44*	8.84	0.20	0.19	0.20	0.20
ODS/SLM oxidised (this work)	60.0 ±2.1	4.7 ±0.2	22.3 ±0.6	3.5 ±1.3	10.0 ±1.0	-	0.1 ±0.1	0.4 ±0.2	-
ODS/SLM alloy (this work)	61.4 ±1.1	5.1 ±0.4	21.2 ±0.6	2.9 ±0.9	9.1 ±1.0	-	0.1 ±0.1	0.4 ±0.2	-
ODS/SPS oxidised (this work)	59.9 ±0.3	4.6 ±0.1	21.8 ±0.3	3.7 ±0.2	9.9 ±0.2	-	-	0.2 ±0.1	-
ODS/SPS alloy (this work)	61.5 ±1.6	3.9 ±0.1	22.1 ±0.3	3.2 ±0.8	9.8 ±0.2	-	-	0.2 ±0.1	-

** Includes Ta*

Depth Profiles

Depth profiles obtained from the SLM-consolidated alloy and wrought alloy, obtained following 1000 hours of oxidation, are shown in Figures 6.27 and 6.28 respectively. Cr is depleted to ~80µm, but Fe, Ni and Mo are all enriched to approximately the same depth. Nb is enriched in both variants of the alloy to ~5µm, due to the presence of the layer of δ-phase at the scale/alloy interface, but only in the SLM-consolidated alloy is δ-phase obviously depleted in the bulk alloy. Mn, Ti and Al, which are present in the wrought alloy but not in the SLM-consolidated alloy, are all enriched at the surface of the wrought alloy, either in the scale or as internal oxide at the scale/alloy interface, but thereafter depleted to a depth of ~80µm i.e. the same

depth as the Cr depletion. The depth profiles obtained for the ODS alloys were essentially flat, with Nb and Mo enrichment of the surface present in both profiles. However, the correlation between Nb and Mo is not observed in the non-ODS depth profiles. A clear correlation is observed for Nb and Si in Alloy 625 ODS/SLM, which is also observed in Alloy 625 ODS/SPS and Alloy 625 SLM. It is reported that Si is partitioned to M_6C carbides Ni-base alloys, which increases the thermal stability of the carbides [259]. Partitioning of Si to M_6C carbides has been reported for Alloy 625 [105]. It should be noted that the depth profile shown for Alloy 625 ODS/SPS was collected over a depth of ~20μm, as opposed to ~120μm for the other variants of the alloy. This was done because it was thought the Cr diffusion profile would be shallow, but linescans of the oxidised alloy have confirmed the same flat depth profile to >50μm (not shown).

Chromium interdiffusion coefficient

The Cr interdiffusion coefficient was estimated for each variant of the alloy by fitting the Cr depth profiles using Equation 4, Figures 6.29 and 6.30. The profiles obtained from the SLM-consolidated and wrought alloys were successfully modelled, but the data obtained from Alloy 625 ODS/SLM alloy was noisy, and no depletion could be discerned in the profile obtained from Alloy 625 ODS/SPS. The D values obtained for the alloys are presented in Table 6.2, which show that $D_{SLM} \approx 1.2 D_{Wrought}$. The dendritic/cellular substructure of the SLM-consolidated alloy is probably responsible for fast diffusion of Cr in the alloy. The results also show that $D_{SLM} \approx 1.8 D_{SLM/ODS}$, which may indicate that the addition of the reactive element has modified the microstructure of the alloy, reducing the diffusion rate of Cr in the alloy. However, this seems unlikely as the ODS alloy had a very fine grain structure. It is much more likely that the diffusion rate was fast and the Cr concentration profile too shallow to be measured using EDS in a SEM.

Table 6.2: Chromium interdiffusion coefficients (D) estimated from fitting of the Cr depth profiles

	Chromium interdiffusion coefficients (m^2s^{-1})		
	This work	Chyrkin [151]	Chyrkin [151]
Alloy 625 SLM	2.3E-16 (900°C)	-	-
Alloy 625 (Wrought)	2.0E-16 (900°C)	2.5E-16 (900°C)	7.29E-16 (1000°C)
Alloy 625 ODS/SLM	1.3E-16 (900°C)	-	
Alloy 625 ODS/SPS	-	-	-

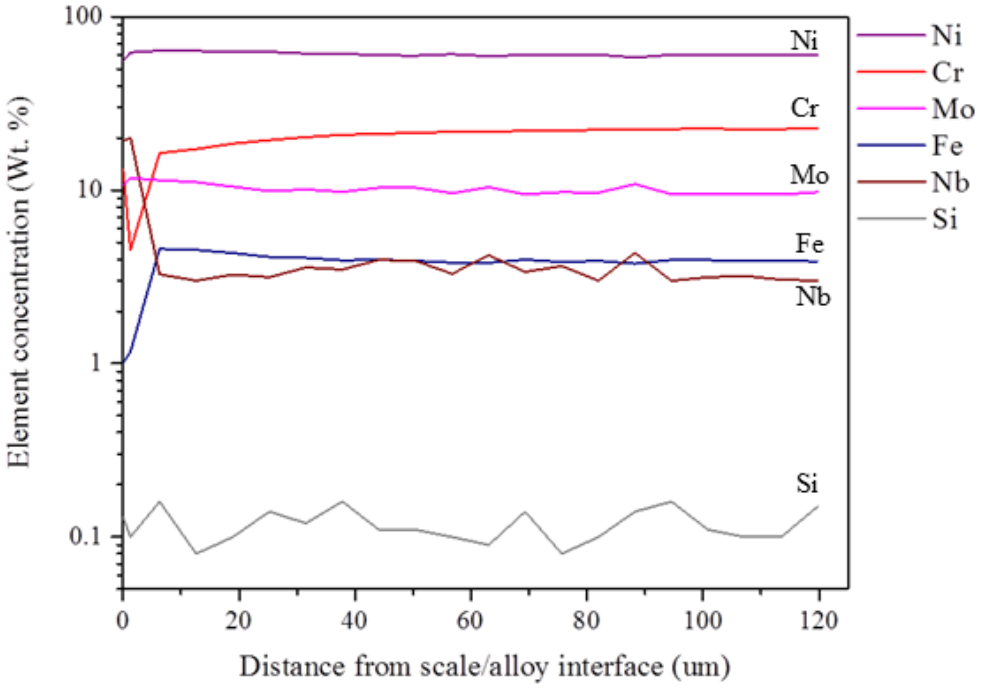

a

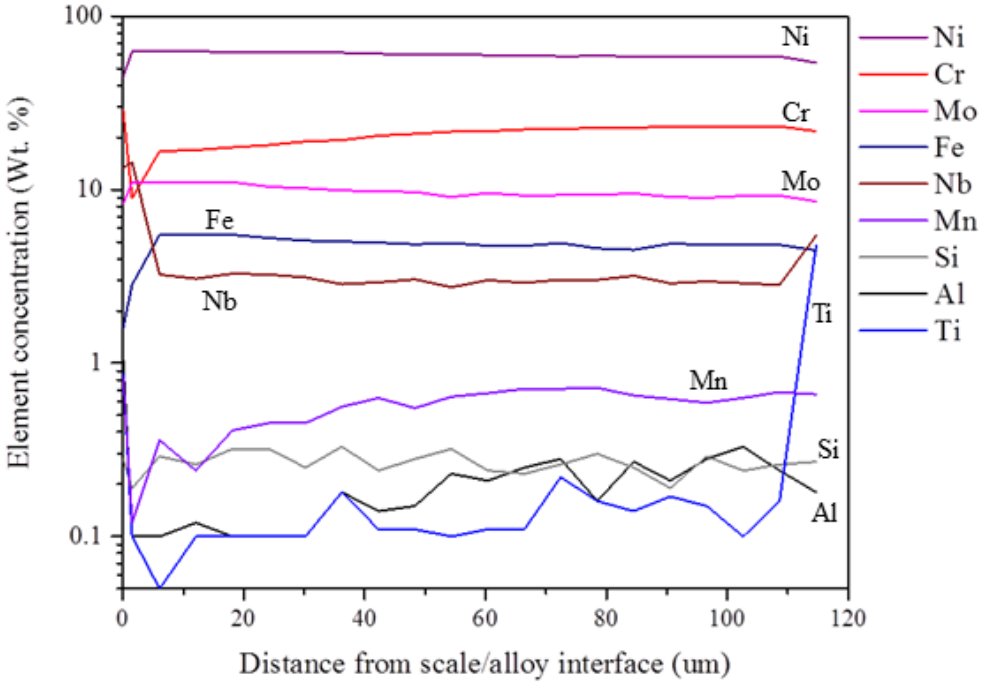

b

Figure 6.27: Plot of element concentration (Wt. %) against distance from scale/alloy interface (µm) following 1000 hours of isothermal oxidation in laboratory air at 900°C (a) SLM-consolidated Alloy 625, and (b) wrought Alloy 625

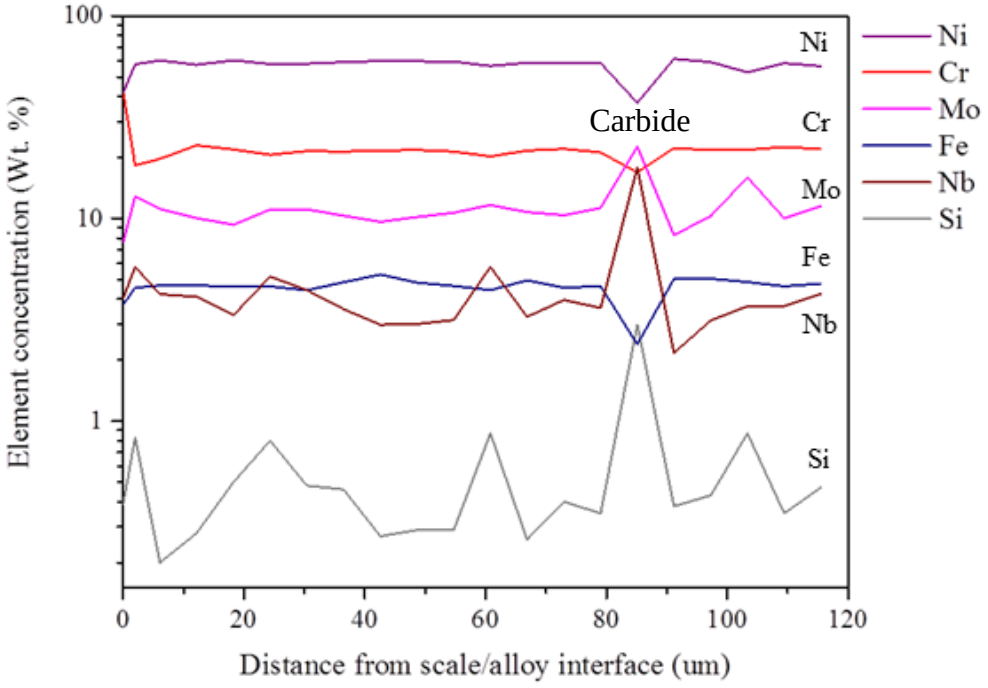

a

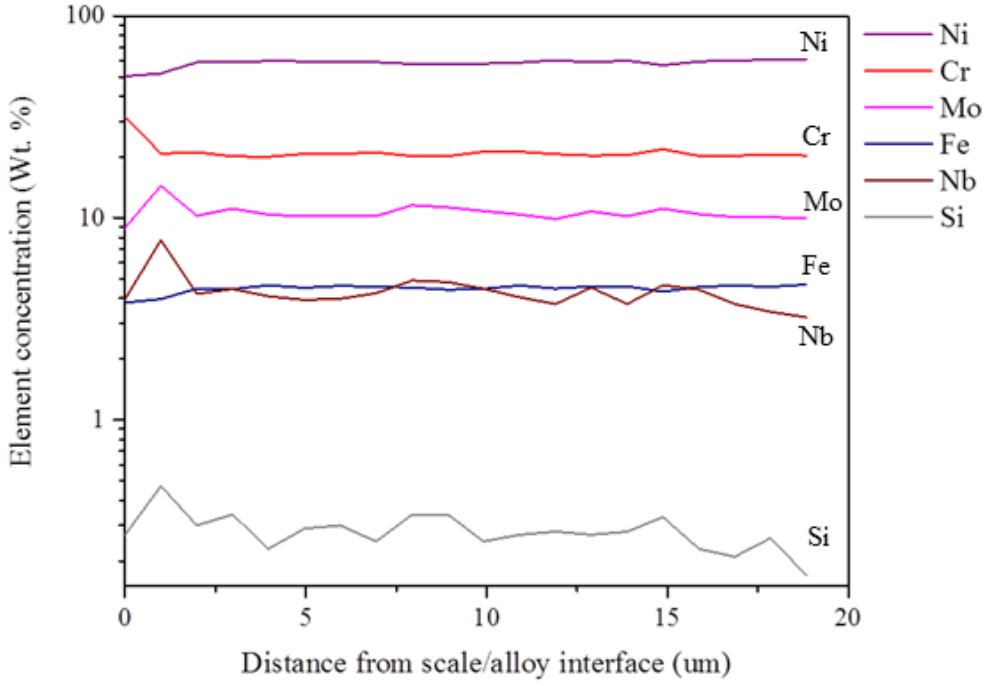

b

Figure 6.28: Plot of element concentration (Wt. %) against distance from scale/alloy interface (µm) following 1000 hours of isothermal oxidation in laboratory air at 900°C (a) Alloy 625 ODS/SLM, and (b) Alloy 625 ODS/SPS

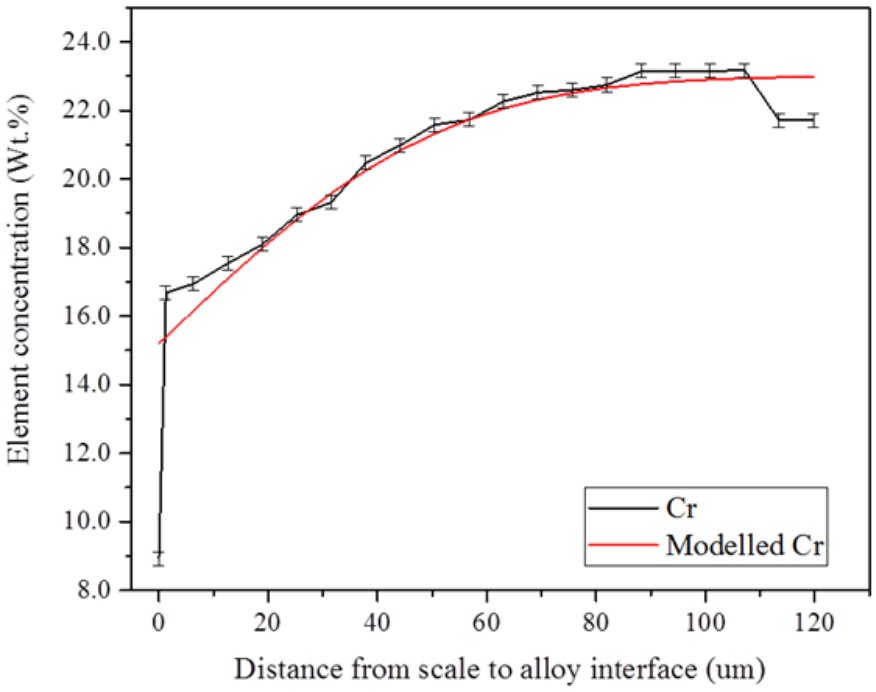

a

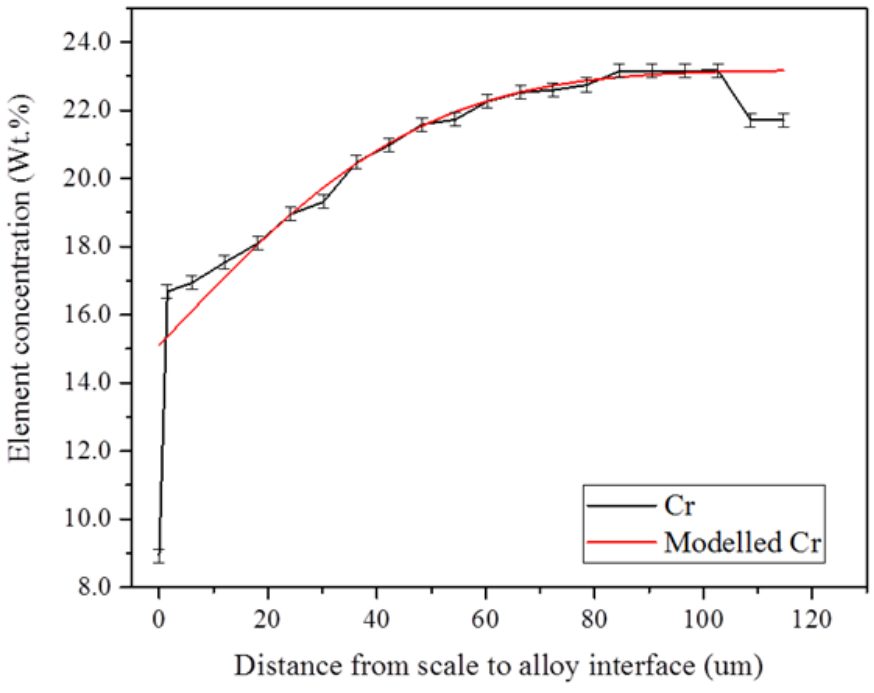

b

Figure 6.29: Modelled plot of Cr concentration (Wt. %) against distance from scale/alloy interface (µm) following 1000 hours of isothermal oxidation in laboratory air at 900°C (a) SLM-consolidated Alloy 625, and (b) Wrought Alloy 625

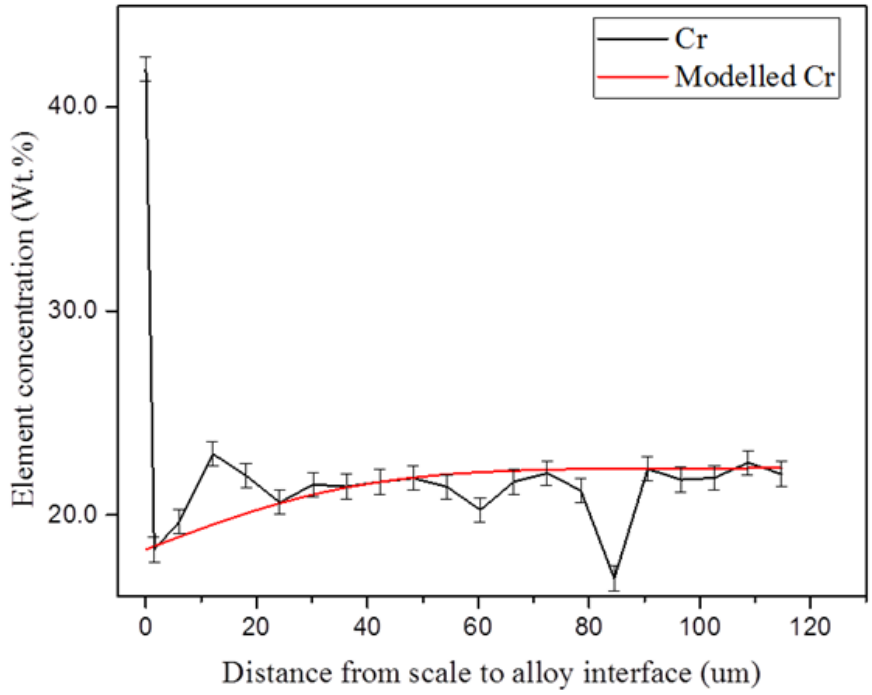

a

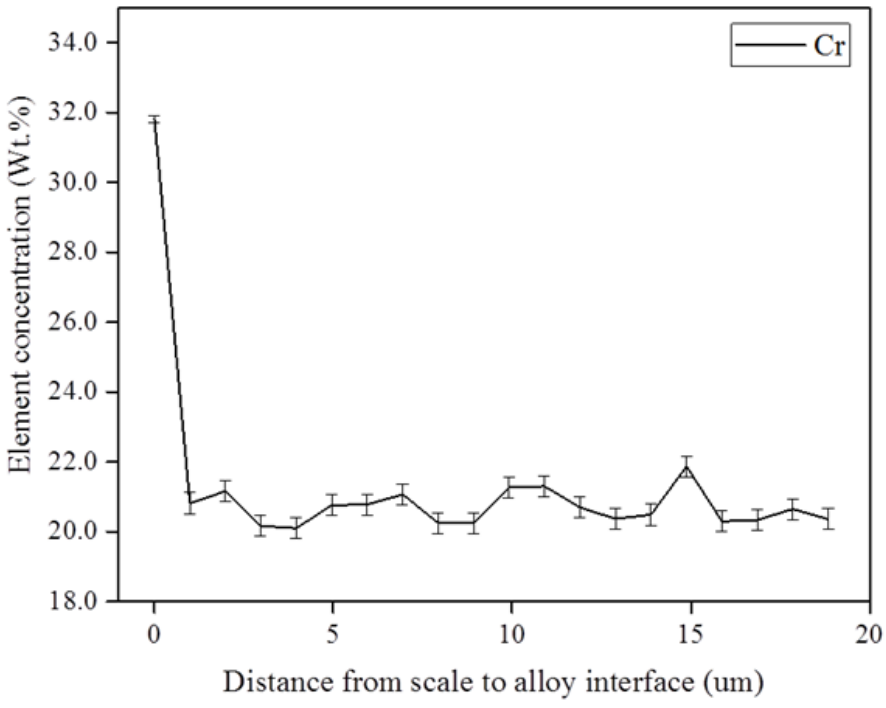

b

Figure 6.30: Plot of Cr concentration (Wt. %) against distance from scale/alloy interface (µm) following 1000 hours of isothermal oxidation in laboratory air at 900°C (a) Modelled Alloy 625 ODS/SLM, and (b) Alloy 625 ODS/SPS

6.4 Discussion

It is reported in the literature that Alloy 625 forms a chromia scale during high temperature oxidation, with a layer of δ-phase precipitated at the scale/alloy interface [105]. The same behaviour is observed in the present study for Alloy 625 SLM and the wrought Alloy 625. In addition, a semi-continuous layer of $Mn_xCr_{3-x}O_4$ spinel formed on the wrought alloy, at the scale/alloy interface, which has also been reported by others for Alloy 625 containing ~0.20 Wt. % Mn [183]. Spinel did not form on the SLM-consolidated alloy because the Mn content of the gas atomised powder from which it was built is <0.01 Wt. %. Both the SLM-consolidated alloy and the wrought alloy formed a wrinkled oxide scale.

The scale formed on the SLM-consolidated alloy was thin and comprised of relatively large grains of uniform size. Grain growth, rather than nucleation, appeared dominant. The scale mainly grew by the outward diffusion of Cr, except at sites separated by ~20-50μm where the scale appeared to undercut the layer of δ-phase at the scale/alloy interface. At these positions fine grain 'knots' developed in the scale. The grains in the 'knots' may have been pinned by particles of δ-phase, preventing their growth; it is also possible that the δ-phase particles promoted the nucleation of oxide grains in the 'knots'. The fine grain 'knots' may help to anchor the scale to the alloy.

The wrought alloy formed a relatively thick, wrinkled duplex scale comprising large grains at the base and fine grains at the scale/gas interface. At short oxidation times, the scale locally detached from the alloy above voids present at the scale/alloy interface. The voids appeared to be incorporated into the scale, delineating the regions where fine grains and large grains were dominant. The scale morphology is consistent with counter-current diffusion, which is reported to produce large growth stresses and lateral growth of the scale near to the scale/alloy interface [254-256]. Convex deformation of the scale, which obviously occurred on the wrought alloy, is indicative of oxide forming towards the sale/gas interface, rather than the scale/alloy

interface, as is clearly evident in the form of the fine grain region of the scale. Growth stresses can be relieved by plastic deformation of the scale, deformation of the alloy, detachment of the scale, or cracking of the scale [133]. In this case, there was no evidence of cracking or spalling of the scale, so it appears that the scale/alloy interface was strong, and growth stresses were accommodated by plastic deformation of the alloy, as clearly observed, and possibly by creep in the oxide scale. A large number of δ-phase particles were incorporated into the scale, but these did not appear to affect the morphology of the scale. It is not clear why fine grain 'knots' might form in the scale on the SLM-consolidated alloy as a result of the presence of δ-phase particles, but not in the scale present on the wrought alloy, nor in the scale present on Alloy 718.

Semi-continuous layers of δ-phase formed in both the SLM-consolidated and wrought alloy, as a result of depletion of δ-phase present in the alloy immediately under the growing scale. Grain growth in the SLM-consolidated alloy occurred where the δ-phase had dissolved as a result of Cr depletion, except in the top ~5μm of the alloy, where even at long oxidation times the dendritic/cellular structure was often evident. A dispersion of fine internal oxide particles had formed in this region of the alloy, and it may be possible that these pinned the small dendritic/cellular grains of the alloy. If correct, this postulation means that grain growth in the alloy immediately under the scale is subject to the competitive mechanisms of internal oxide precipitation and δ-phase dissolution. Grain growth also occurred in the wrought alloy under the scale, but this did not appear to be impeded by internal oxide particles. The wrought alloy appears to oxidise faster than the SLM-consolidated alloy because it grows as a result of strong counter-current diffusion, whereas the scale formed on the SLM-consolidated alloy grows by the outward diffusion of Cr. Grain growth appears dominant in the scale formed on the SLM-consolidated alloy, but in the scale formed on the wrought alloy grain growth appears dominant at the base of the scale and nucleation toward the scale/gas interface. These differences in the growth rate and morphology of the scales may be related to differences observed in the morphology of the scales following 25 hours of

oxidation, which showed that the scale formed on the SLM-consolidated alloy had a larger, more uniform grain size than the scale formed on the wrought alloy. The relationship between the Cr interdiffusion coefficients was determined to be $D^{SLM} \approx 1.2 D^{Wrought}$, which means that the SLM-consolidated alloy should selectively oxidise faster than the wrought alloy, as a consequence of faster Cr diffusion in the alloy. It should be noted, however, that once the Cr scale has formed it is the diffusion of Cr and O through the scale, rather than Cr diffusion in the alloy, that is rate-determining.

The rapid establishment of a slow growing Cr scale has been widely reported for small grain alloys and cold-worked alloys, and was demonstrated in the present work using coupons of silica-polished MA754 and ground coupons of MA754. It is therefore possible that the SLM-consolidated alloy oxidises more slowly, and with a better scale morphology, than the wrought alloy because of improved selective oxidation. In support of this theory are the results obtained from the examination of Alloy 625 ODS/SLM and Alloy 625 ODS/SPS by STEM, which show that a band of small Nb-rich oxide particles was present in both specimens. These were thought to be first-formed oxides, as Nb_2O_5 is thermodynamically more stable than Cr_2O_3, and is therefore expected to form in preference to Cr_2O_3 during transient oxidation but not at longer oxidation times [260]. However, Nb_2O_5 is a porous and non-protective scale [136], and as shown in the STEM images, may be expected to introduce voids into the scale. It may be expected that the scale formed on the wrought alloy during transient oxidation would, on account of slower selective oxidation because of the slower rate of diffusion in the alloy, contain more Nb oxides and voids than the scale formed on the SLM-consolidated alloy. Additions of Nb, at a concentration of ~1 Wt. %, have been found to reduce the oxidation resistance of ferritic steels in oxidation experiments conducted in air at temperatures of 800 and 900°C [261]. It was proposed that Nb-doping of the chromia scale by Nb^{4+} or Nb^{5+} may have introduced metal vacancies into the scale in a manner similar to that of Ti^{4+} doping. The authors reported that the oxidation resistance of the alloy was improved by the

addition of Si at a concentration of ~0.2 Wt. %, which resulted in the formation of Nb-Si. In the present work, the wrought alloy and the SLM-consolidated alloy contain Si at a concentration of ~0.1-0.2 Wt. %, but both also contain ~3.5 Wt. % Nb, which means that Nb/Si ratio is much higher in Alloy 625 than in the ferritic steel. However, Alloy 625 forms Nb-rich MC and M_6C carbides, which tie-up the Nb, and may be expected to reduce the negative effects of Nb on the oxidation resistance of the alloy. Carbides are much more common in the wrought alloy than in the SLM-consolidated alloy, probably as a result of fast cooling of the alloy during SLM-consolidation, which could imply that the carbides, rather than Nb in solution, may be the source of the Nb oxides that are proposed to be deleterious to the oxidation behaviour of the alloy. In the present work STEM was not used to characterise the scales formed on SLM-consolidated or wrought Alloy 625, but it could be used to investigate the validity of the proposed mechanism.

Alloy 625 ODS/SPS and Alloy 625 ODS/SLM formed very thin chromia scales during oxidation, which is consistent with the results of the kinetics experiments presented in Chapter 4, and shows that a dramatic improvement in oxidation behaviour was obtained by the addition of Y to Alloy 625. As discussed above, the scales present on both variants of the alloy contained a distinct band of Nb-rich oxide particles, which are thought to identify the location of the alloy surface prior to oxidation. If this is correct, it places the alloy surface toward the scale/gas interface, consistent with a scale growth mechanism dominated by the inward diffusion of O. This is consistent with the reactive element effect, which is widely believed to promote inward diffusion by blocking grain boundaries to the outward diffusion of cations [23, 162, 163]. Attempts to reproduce the results of other workers, who have demonstrated the segregation of reactive elements to the grain boundaries of oxide scales [169-171] proved largely unsuccessful despite the examination and analysis of many grain boundaries. Therefore, it was not possible to confirm that Y had segregated to the grain boundaries of the oxide scale formed on Alloy 625 ODS. Both Alloy 625 SLM and Alloy 625 ODS/SLM have a propensity for void formation, but this did not appear to be the case for wrought Alloy 625 and Alloy

625 ODS/SPS. It is believed that the voids were probably Kirkendall voids, which form during high temperature oxidation. Work has been done on rapidly solidified alloys, which in terms of consolidation rate may be considered analogous to SLM-consolidated alloys, which indicates that a large number of vacancies are trapped during rapid consolidation [250, 251, 262]. Following a study of rapidly solidified IN625 it was reported that the high vacancy concentration changes the precipitation kinetics of γ′′ and δ-phase [262]. If this is also true for SLM-consolidated alloys, it may mean that the concentration of injected vacancies needed to precipitate voids is lower in SLM-consolidated alloys than in conventional alloys i.e. SLM-consolidated alloys may be more likely to form voids during high temperature oxidation than, for example, wrought alloys. The ODS alloys did not form any internal oxide because of the very low concentrations of Al and Ti in the MA powder, and Nb, which as δ-phase dissolves in the Cr-depleted zone of Alloy 625 during oxidation, was stable in the alloy and did not solutionise and precipitate as δ-phase as might have been expected. A layer of δ-phase, which forms at the scale/alloy interface during the oxidation of Alloy 625, did not form in the ODS alloy. It is thought likely that this is because the grain boundary phases formed in the ODS alloys were more likely to be Nb carbide films than Laves phase. The interdiffusion coefficient D obtained for Alloy 625 ODS/SLM was ~0.5x that obtained for Alloy 625 SLM, but was obtained from noisy data. Cr was not obviously depleted in the depth profile obtained from Alloy 625 ODS/SPS. Cr diffusion is expected to be fast in both Alloy 625 ODS/SLM and Alloy 625 ODS/SPS because of their small grain size; it is possible that the alloys were depleted of Cr immediately under the scale, but that the depletion was too shallow to be measured using EDS in a SEM.

6.5 Chapter summary

Wrought Alloy 625 formed a duplex scale comprising large chromia oxide grains at the base of the scale, with fine grain chromia grains at the scale/gas interface. The morphology may be consistent with counter-current diffusion, which produces lateral

growth of the oxide grains near the scale/alloy interface. This produces compression in the scale, which is orientated parallel to the scale/alloy interface. Strong tensile stresses formed perpendicular to the scale/alloy interface, which were relieved by plastic deformation of the alloy, and possibly creep within the scale. The scale/alloy interface was strong with no evidence of decohesion apparent. The scale formed on Alloy 625 SLM was thinner as a result of slower cation diffusion through the scale, probably because of the larger size of the oxide grains. Fine grain 'knots' formed at intervals of ~20-30μm in the scale on the SLM-consolidated alloy; these appeared to have been pinned by spheroidal particles of δ-phase incorporated into the scale as a result of undercutting, by the scale, of the layer of δ-phase formed during oxidation at the scale/alloy interface. At longer oxidation times, a layer of spinel formed on the wrought alloy at the scale/gas interface, but not on the SLM-consolidated alloy. The relationship between the Cr interdiffusion coefficients is $D_{Cr}^{SLM} \approx 1.2 D_{Cr,}^{Wrought}$ which indicates that the dendritic/cellular substructure of the alloy increases Cr diffusion in the alloy. Alloy 625 ODS formed a very thin scale, consistent with the results of the kinetics experiments. The alloy appeared to oxidise, in both SLM-consolidated and SPS-consolidated forms, mainly by the inward diffusion of O, consistent with the reactive element effect. However, the segregation of Y to the grain boundaries of the scale was not observed. Alloy 625 ODS/SLM and Alloy 625 ODS/SPS contained a band of Nb-rich oxides, which are believed to be first formed oxides and indicate the location of the alloy surface prior to oxidation. Voids were associated with the Nb oxides. Nb oxides are porous and non-protective, and may promote oxidation by doping the scale [261]. It is possible that the morphology of the scale formed on the SLM-consolidated Alloy 625 is superior to that which forms on the wrought Alloy 625 because of faster selective oxidation, which suppresses the growth of Nb rich oxides during transient oxidation. However, the SLM-consolidated alloy contains fewer Nb-rich carbides than the wrought alloy, but a higher solution concentration of Nb. It is therefore possible that Nb-rich carbides are a source of Nb-rich oxides, possibly the primary source. Oxidation of NbC carbides to form porous scale was observed to occur in wrought Alloy 718.

CHAPTER 7

HAYNES 230

7.1 Introduction

SLM-consolidated Haynes 230 and SLM-consolidated Haynes 230 ODS were studied following high temperature isothermal oxidation at 900°C for durations of up to 1000 hours. Wrought Haynes 230 and SPS-consolidated Haynes 230 ODS were studied alongside the SLM-consolidated alloys for comparison. The results are reported in section 7.2, Characterisation of alloys, which includes subsections 7.2.1, SLM-consolidated Haynes 230, 7.2.2, Wrought Haynes 230, 7.2.3, Haynes 230 ODS/SLM and 7.2.4, Haynes 230 ODS/SPS. The results obtained from the study of the oxidised alloys are reported in section 7.3, Characterisation of oxidised alloys, and includes subsections 7.3.1, XRD analysis, 7.3.2, Haynes 230, 7.3.3, Haynes 230 ODS, 7.3.4, Oxidation-induced changes in alloys and 7.3.5, Oxidation of carbides in wrought Haynes 230. The results are discussed in section 7.4, and a chapter summary is provided in section 7.5.

7.2 Characterisation of alloys

7.2.1 SLM-consolidated Haynes 230

The as-consolidated alloy had a columnar microstructure orientated parallel to the build direction of the alloy, which was comprised of dendrites/cells of ~0.5µm in size, Figures 7.1 (a) and 7.1 (b). A W-rich phase was present on the boundaries of the dendrites/cells. Heat-treatment at 1200°C did not significantly alter the microstructure of the alloy, but it did precipitate a large volume fraction of W-rich carbides, Figures 7.1 (c) and 7.1 (d). It was assumed that these were M_6C carbides,

as expected for Haynes 230, but additional work was not carried-out to positively identify them. The intercellular carbides were typically <1µm in size, but adjacent to the grain boundaries of the alloy they were ~1-2µm in size, having grown at the expense of the smaller carbides, presumably as a result of Ostwald ripening.

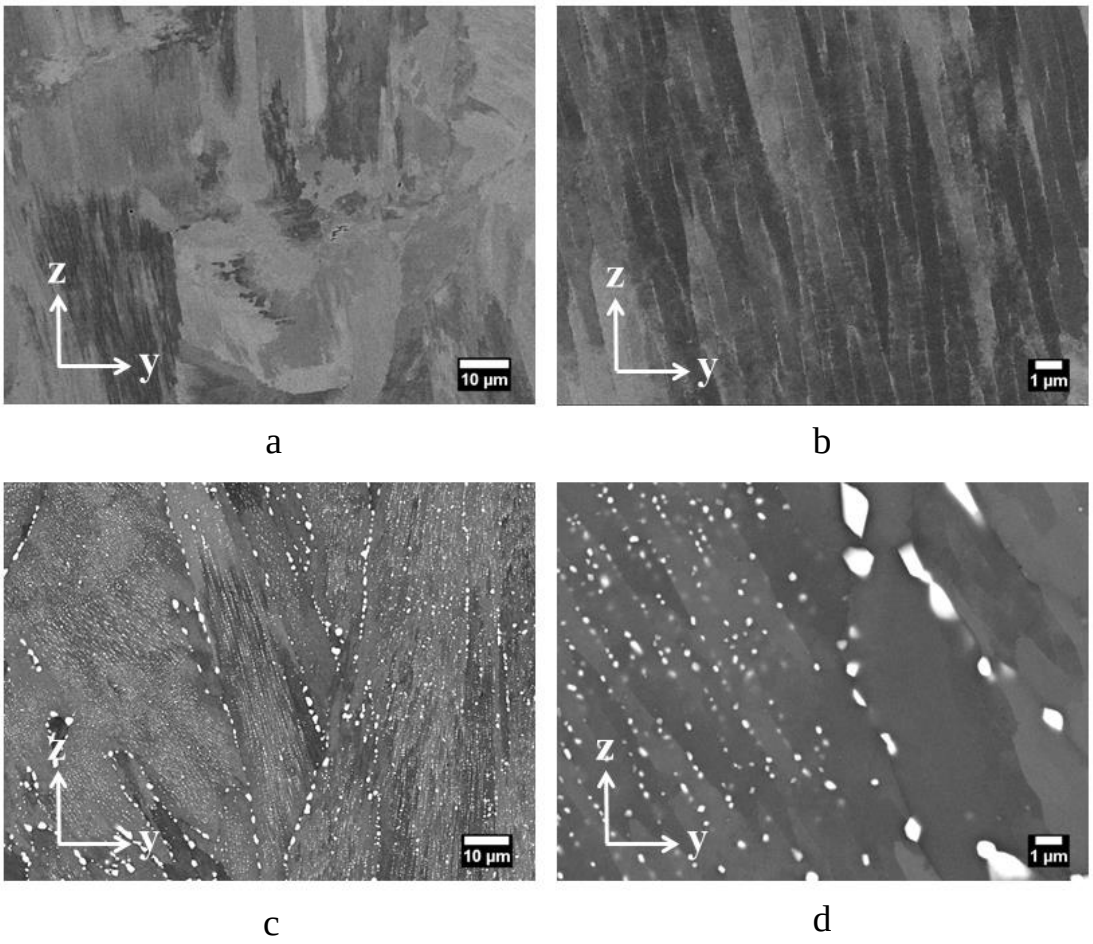

Figure 7.1: BSE micrographs of longitudinal sections of SLM-consolidated Haynes 230, (a), (b) as-consolidated, (c), (d) heat-treated

La-rich slag was present on the exterior surfaces of the consolidated blocks in the form of thin deposits, presumably oxide, Figure 7.2. The bulk alloy also contained slag, but as a eutectic formed approximately in lines perpendicular to the build direction of the alloy, Figure 7.3 (a). An area average spectrum, and a semi-quantitative analysis, acquired from the slag inclusion shown in Figures 7.3 (b) and

7.3 (c), are presented in Figure 7.3 (d). The inclusion contained the elements La, Ce, Al and O, and is typical of all those analysed. O was determined in the analysis by stoichiometry. Ce was unexpected, as it was not reported to be present in the alloy, and is likely to have been introduced as a contaminant from La doping of the ingot from which the gas atomised powder was produced, or as a result of deliberate doping of the ingot with La and mischmetal, a mixture of reactive elements typically containing 50% Ce, 25% La, 18% Nd, 5% Pr and other rare earths [263].

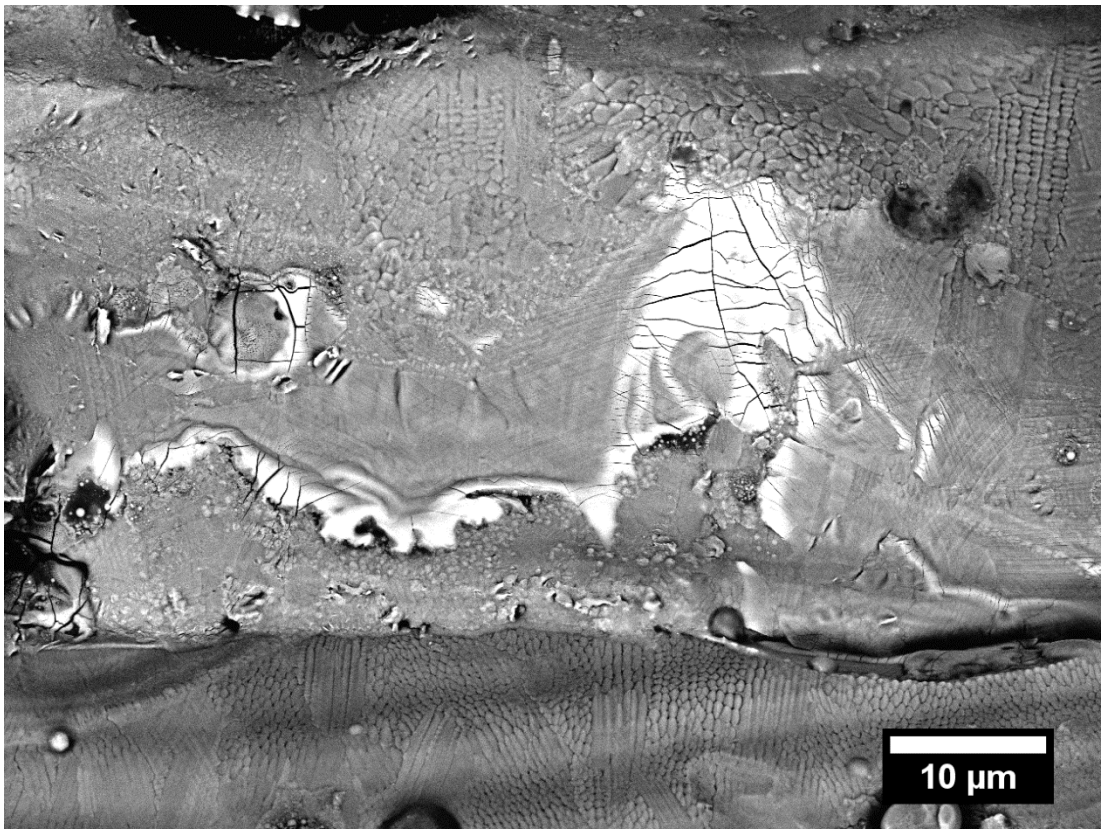

Figure 7.2: BSE micrograph of La-rich slag on exterior surface of a block of SLM-consolidated Haynes 230

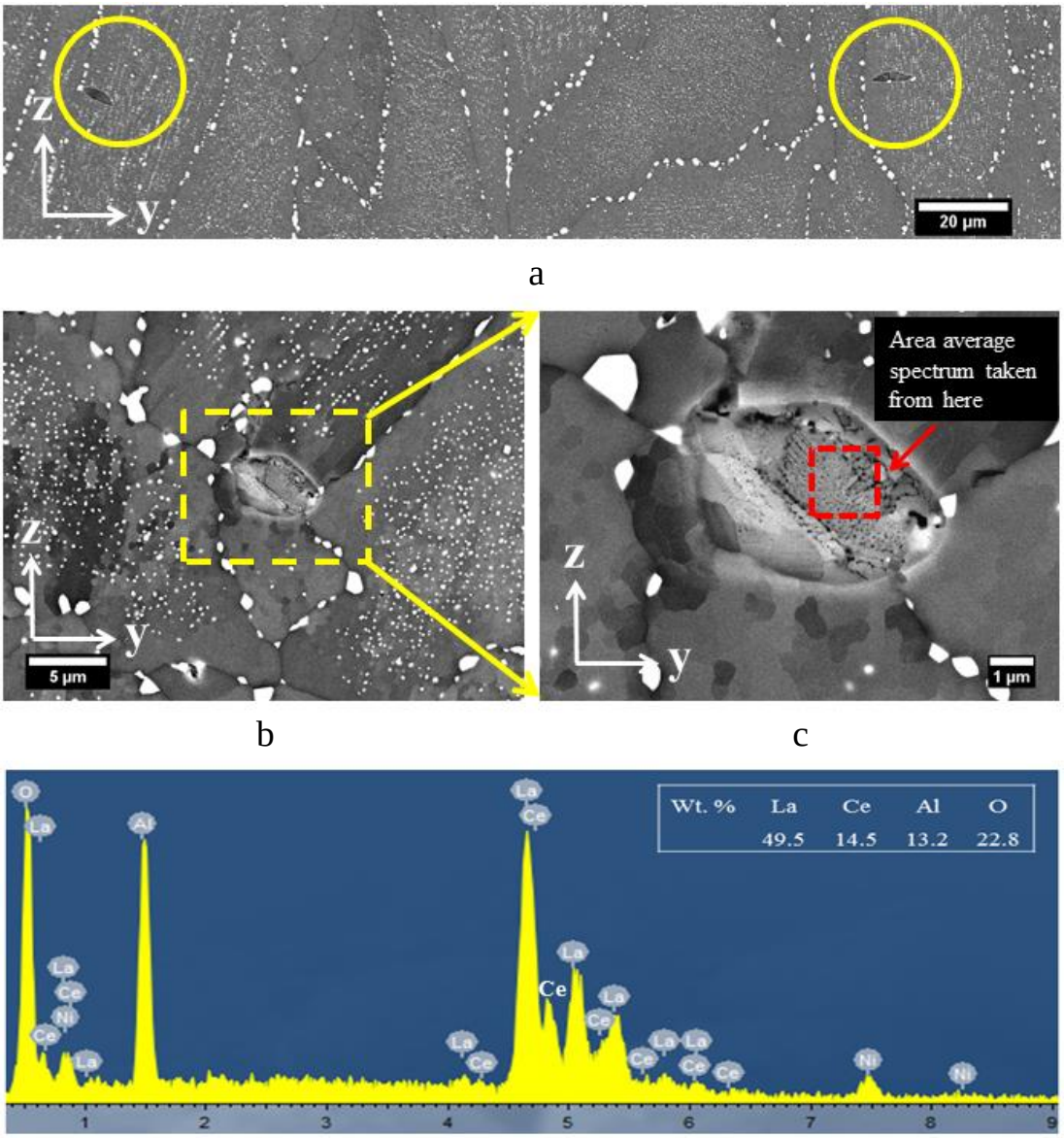

Figure 7.3: SLM-consolidated Haynes 230, (a)-(c) BSE micrographs of slag particles in alloy, (d) spectrum and semi-quantitative analysis obtained from the slag particle observed in (b) and (c)

7.2.2 Wrought Haynes 230

The alloy had an equiaxed grain structure, Figure 7.4 (a). Extensive twinning was evident in the alloy, as was a large population of inclusions, believed to be M_6C-type carbides, and whose composition is typically $(W_{2.1}Ni_{1.9}Cr_{1.8}Mo_{0.2})C$. The carbides were present at intragranular and intergranular sites, Figures 7.4 (b). Pinning of grain boundaries by carbides was evident, Figure 7.4 (c). La-rich particles were present in some of the carbides, which may act as nuclei for carbide precipitation, Figure 7.4 (d).

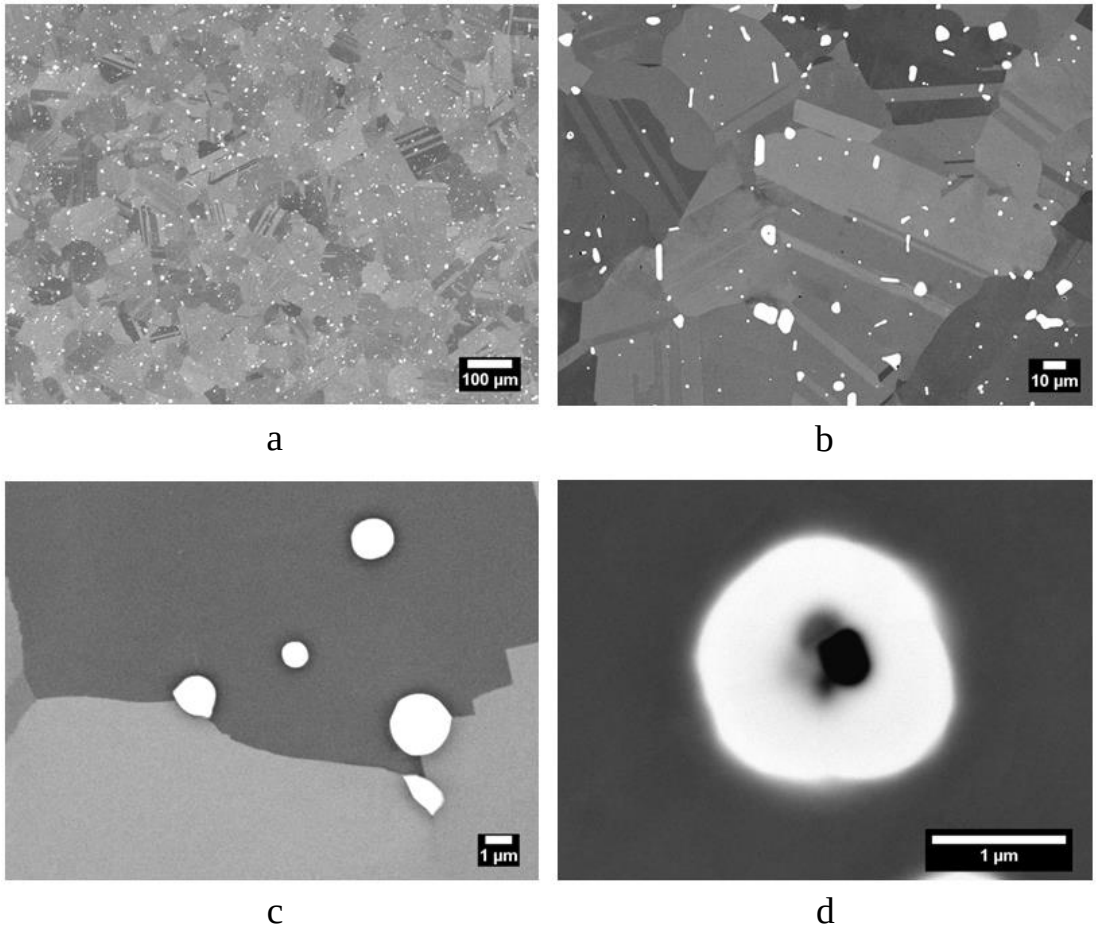

Figure 7.4: BSE micrographs of wrought Haynes 230 showing (a) equiaxed grain structure (b) large population of M_6C-type carbides, (c) small M_6C-type carbides on grain boundaries, and (d) La-rich particle in a M_6C-type carbide

7.2.3 Haynes 230 ODS/SLM

The alloy had a columnar grain structure orientated in the build direction, with cracks of 100-300µm in length present at the grain boundaries, Figure 7.5 (a). The grains were comprised of dendrites/cells of ~1µm in size, and present on the dendrite/cell boundaries was a film rich in W and Mo, probably carbide, Figure 7.5 (b). The alloy also contained voids, slag inclusions rich in Y and O, and a large population of submicron inclusions rich in Cr and O, probably Cr_2O_3. Cracks were also evident in transverse sections of the alloy, as were inclusions, voids and the W/Mo-rich film on the dendrite/cell boundaries, Figures 7.5 (c) and 7.5 (d).

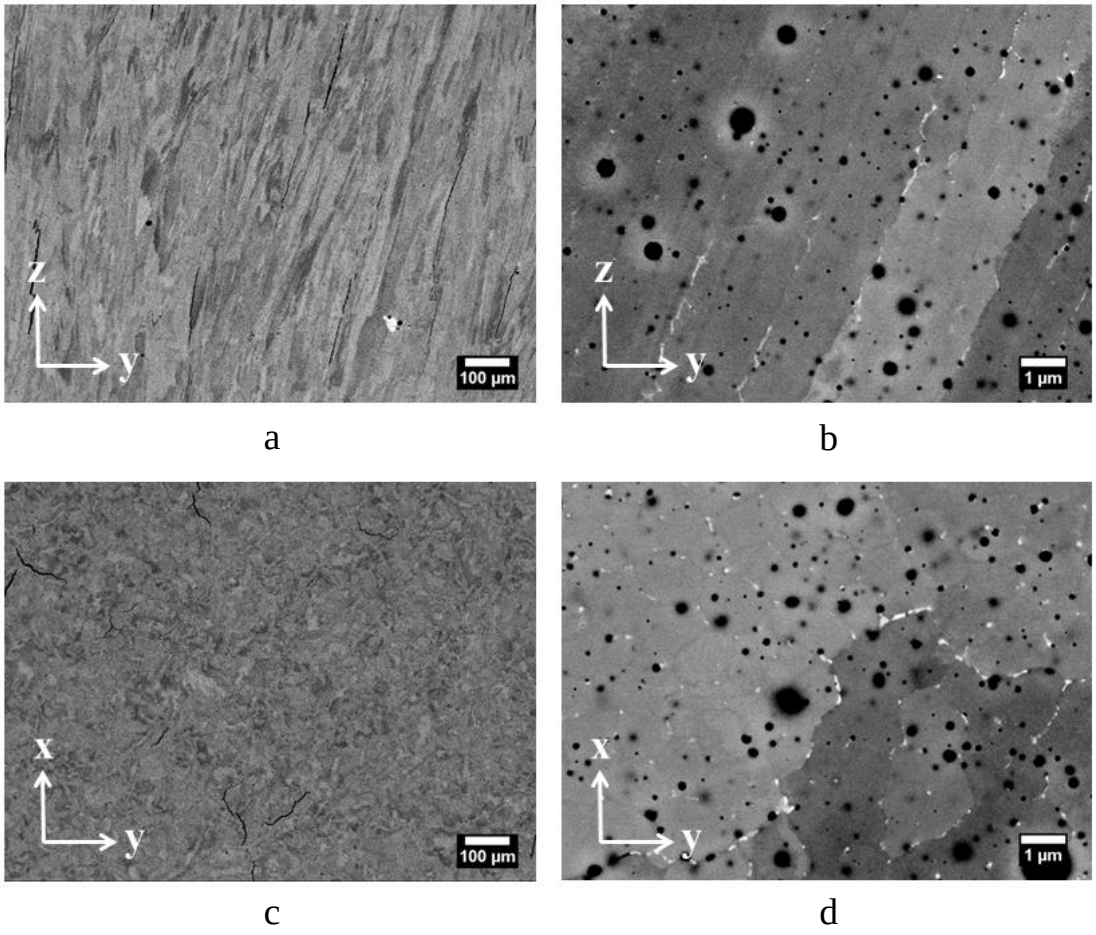

Figure 7.5: BSE micrographs of Haynes 230 ODS/SLM showing (a), (b) longitudinal section, and (c), (d) transverse section

7.2.4 Haynes 230 ODS/SPS

The alloy was porous, as a result of incomplete consolidation, Figure 7.6 (a). The alloy was comprised of regions of <1μm in grain size, which contained large numbers of inclusions of <0.2μm in size, and a few inclusion-free regions with a grain size of ~1μm, Figure 7.6 (b-d). This is consistent with Zener pinning of the grains. The inclusions were rich in W and Mo, and were assumed to be M_6C-type carbides, but they were not studied in detail.

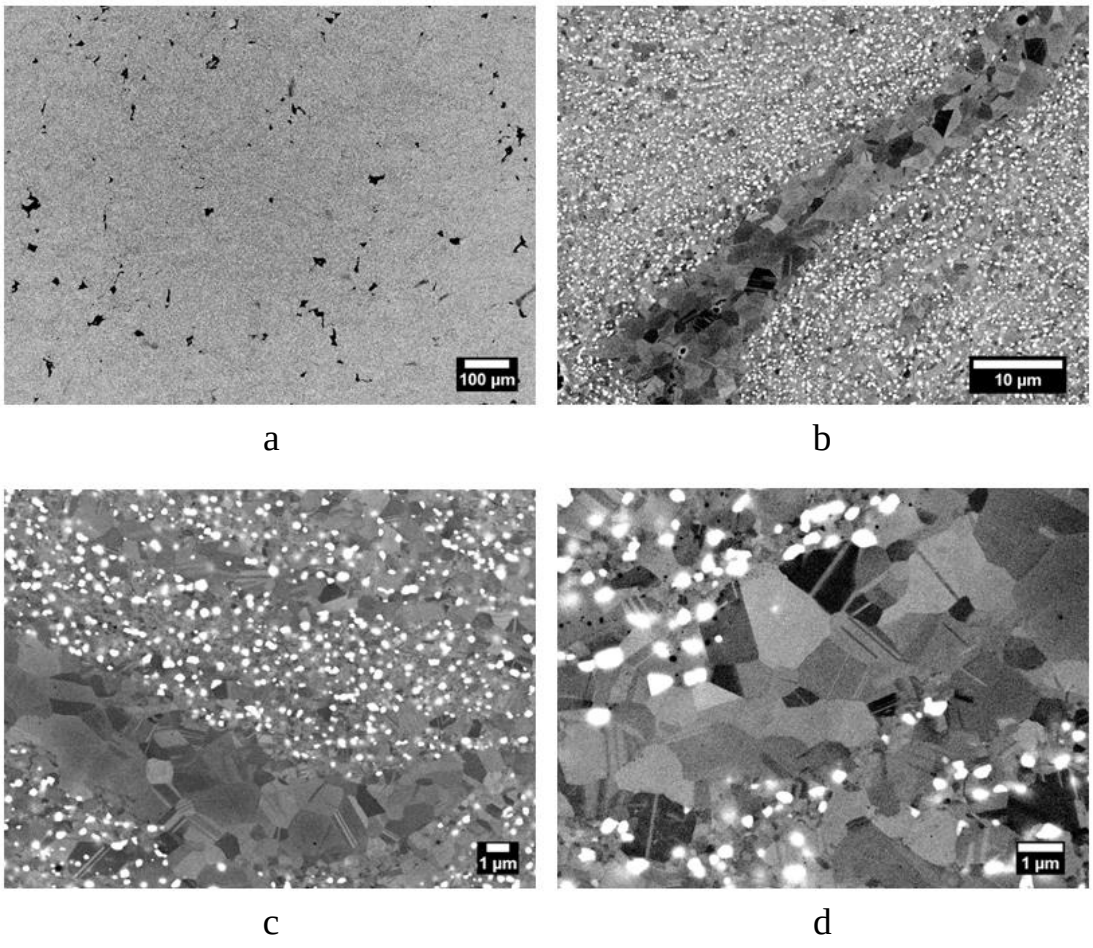

Figure 7.6: BSE micrographs of Haynes 230 ODS/SPS showing (a) porosity in alloy, (b) and (c) isolated bands of relatively large grains, (d) absence of inclusions from a band of large grains

7.3 Characterisation of oxidised alloys

7.3.1 XRD analysis

Diffractograms obtained from Haynes 230 SLM, wrought Haynes 230, Haynes 230 ODS/SLM and Haynes 230 ODS/SPS, following 25, 215 and 1000 hours of oxidation, are provided in Figures 7.7 and 7.8.

The scale formed on Haynes 230 SLM and wrought Haynes 230 was comprised of chromia and manganese spinel, Figures 7.7 (a) and 7.7 (b) respectively. The scale was chromia-rich at the shortest oxidation time, but became increasingly spinel-rich at longer oxidation times. The results obtained from Haynes 230 ODS/SLM are similar to those obtained from Haynes 230 SLM and wrought Haynes 230. The scale formed on Haynes 230 ODS/SPS was rich in spinel after 25 hours of oxidation, and chromia was essentially obscured following 1000 hours of oxidation. This is consistent with the formation of a thick spinel layer at the scale/gas interface.

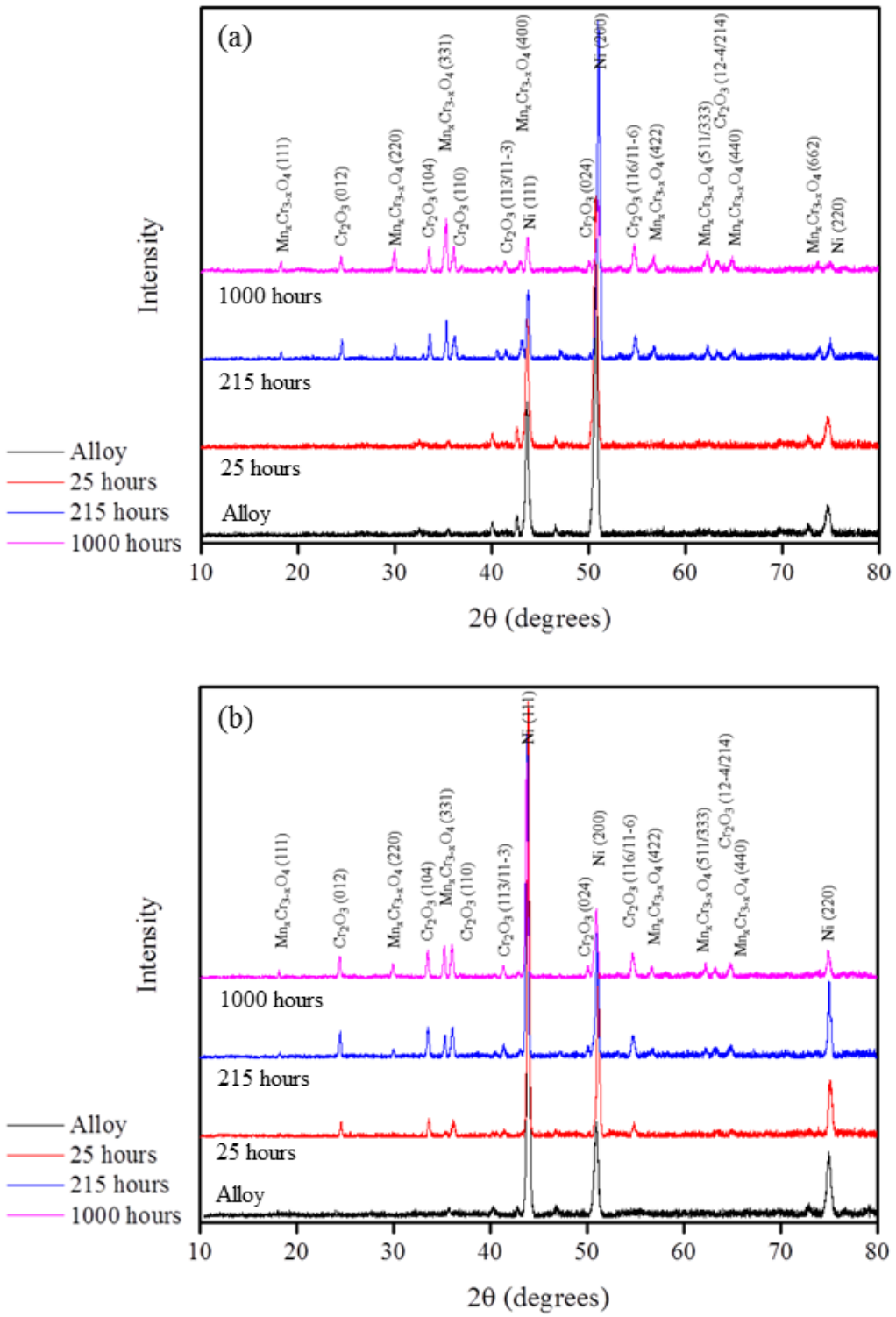

Figure 7.7: Diffractograms obtained from Haynes 230 following isothermal oxidation in laboratory air at 900°C (a) Haynes 230 SLM, (b) Wrought Haynes 230

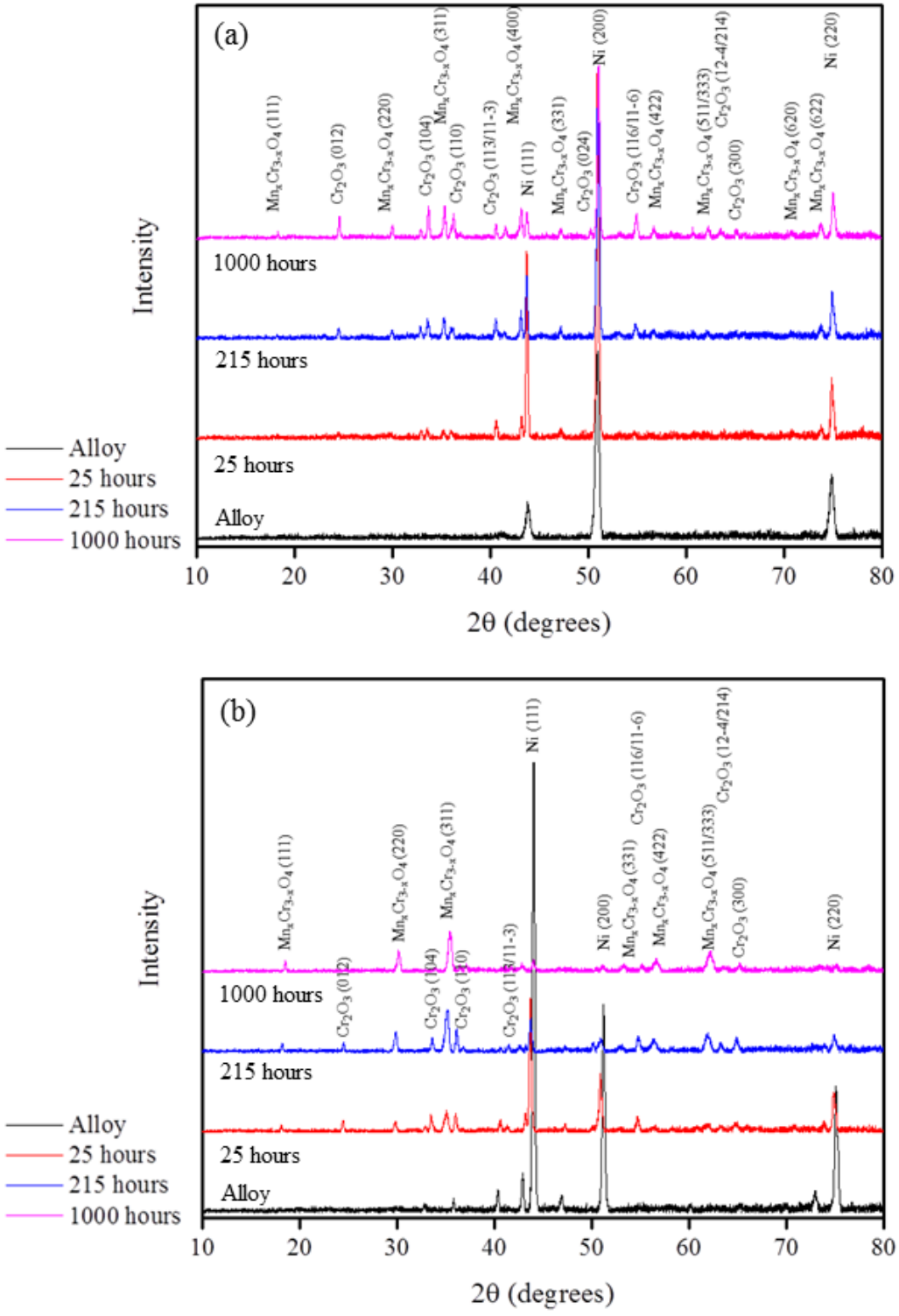

Figure 7.8: Diffractograms obtained from Haynes 230 ODS following isothermal oxidation in laboratory air at 900°C (a) Haynes 230 ODS/SLM, and (b) Haynes 230 ODS/SPS

7.3.2 Haynes 230

Initial Examination by Microscopy

The scale formed on the SLM-consolidated alloy was inhomogeneous, with regions orientated in the build direction that were either thicker or rougher, or thicker and rougher, than the rest of the surface, Figures 7.9 (a) and 7.9 (b). This appearance is probably related to the columnar microstructure of the underlying alloy. At oxidation times <215 hours La-rich particles were present in 'spots' in the scale on the wrought alloy where the scale was locally thin, Figures 7.9 (c) and (d).

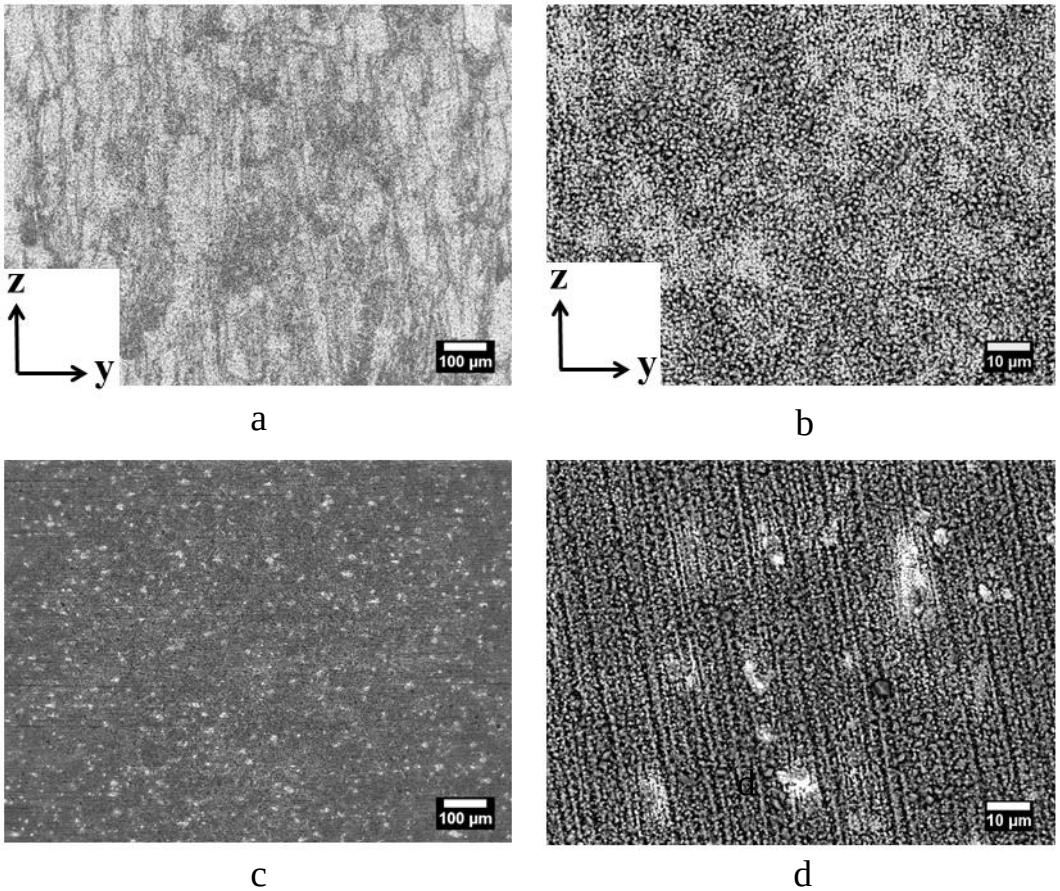

Figure 7.9: BSE micrographs Haynes 230 following isothermal oxidation in laboratory air at 900°C (a) SLM-consolidated, 25 hours, (b) SLM-consolidated, 1000 hours, (c) Wrought, 25 hours and (d) Wrought, 1000 hours

In cross-section, it can be seen that the scale formed on the SLM-consolidated alloy was initially of irregular thickness, but became uniformly thick at longer oxidation times, Figure 7.10. The scale was marginally thicker above the grain boundaries of the alloy. Grains rich in Cr, Mn and O, the spinel identified by XRD, formed preferentially above the grain boundaries at the scale/gas interface. This indicates that either the grain boundaries in the alloy, or the scale immediately above the grain boundaries in the alloy, were preferred pathways for Mn diffusion. The wrought alloy developed a scale that, at all oxidation times, was thinner, but less uniformly thick, than that which formed on the SLM-consolidated alloy, Figure 7.11. At all oxidation times many fragments of alloy, and a few carbide particles, were incorporated into the scales. Internal oxides penetrated the grain boundaries of the SLM-consolidated alloy, extending to a depth of ~15 µm after 1000 hours of oxidation. Internal oxide rarely formed at the grain boundaries of the wrought alloy, but was precipitated on the boundaries of small alloy grains formed during oxidation as a result of recovery and recrystallisation of cold work damage. The small alloy grains persisted to >215 hours of oxidation, which illustrates the slow rate of scale growth/alloy recession.

The M_6C-type carbides present in the SLM-consolidated alloy were angular in shape, and comprised grain boundary carbides of ~1µm in size and sub-micron intragranular carbides. The intragranular carbides dissolved in the oxidation affected zone to a depth of ~30µm, after 1000 hours of oxidation, while the intergranular carbides grew in size. However, after 1000 hours of oxidation, the intergranular carbides were absent to a depth of ~10um. The wrought alloy also contained M_6C-type carbides present at intergranular and intragranular sites within the alloy, and these ranged between spherical carbides of <1µm in size and angular carbides of ~10µm in size. During the early stages of oxidation a Cr-rich phase, probably $M_{23}C_6$, developed around the peripheries of the M_6C carbides and on the on the grain boundaries of the alloy. This behaviour is often reported for wrought Haynes 230 [111]. At longer oxidation times the effect was not obvious in the oxidation-affected zone of the SLM-consolidated alloy, probably as a result of dissolution of the phase

into the Cr-depleted alloy. In the wrought alloy changes were observed in the microstructure of M_6C carbides directly exposed to the atmosphere, or indirectly exposed to the atmosphere via grain boundaries. This behaviour is discussed in detail in section 7.3.5.

Element maps obtained from Haynes 230 SLM and wrought Haynes 230, following 215 hours of oxidation, are presented in Figures 7.12 and 7.13 respectively. A duplex scale formed on Haynes 230 SLM that is rich in Cr, Mn and O, with Mn locally concentrated where the scale has grown strongly by outward growth. Cr is depleted in the alloy to a depth of ~10µm, and possibly Mn, Fe and Ni are enriched at the surface in the Cr-depleted zone. Mo and W are strongly associated in the M_6C carbides. The wrought alloy also formed a duplex scale of chromia and $Mn_xCr_{3-x}O_4$ spinel at the scale/gas interface. Cr is depleted in the alloy to a depth of ~5µm, and Ni enriched to the same depth. Mn depletion of the alloy is not readily apparent. Al-rich internal oxides extend to a depth of ~10µm.

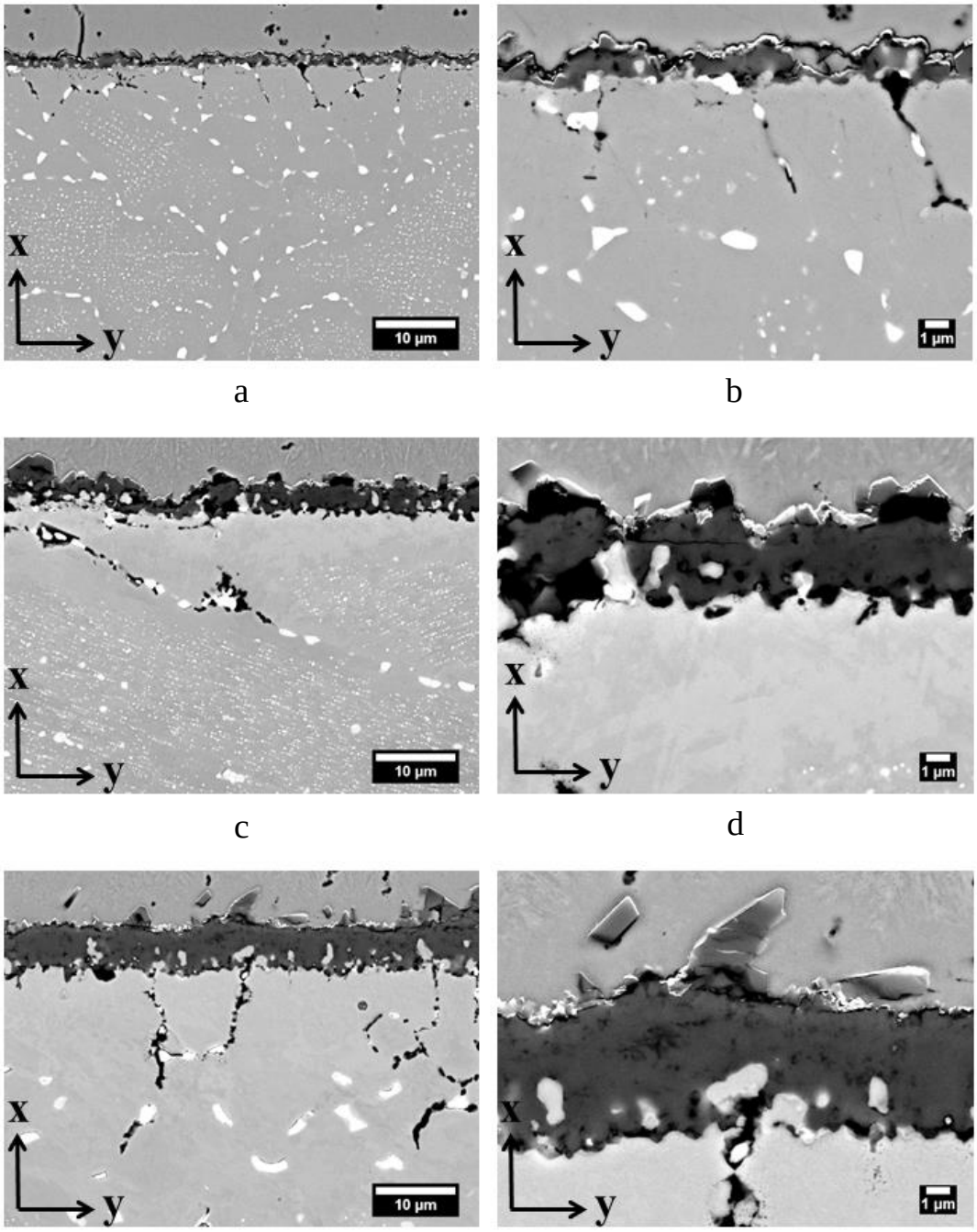

Figure 7.10: BSE micrographs of cross-sections of SLM-consolidated Haynes 230 following isothermal oxidation in laboratory air at 900°C (a), (b) 25 hours, (c), (d) 215 hours and (e), (f) 1000 hours

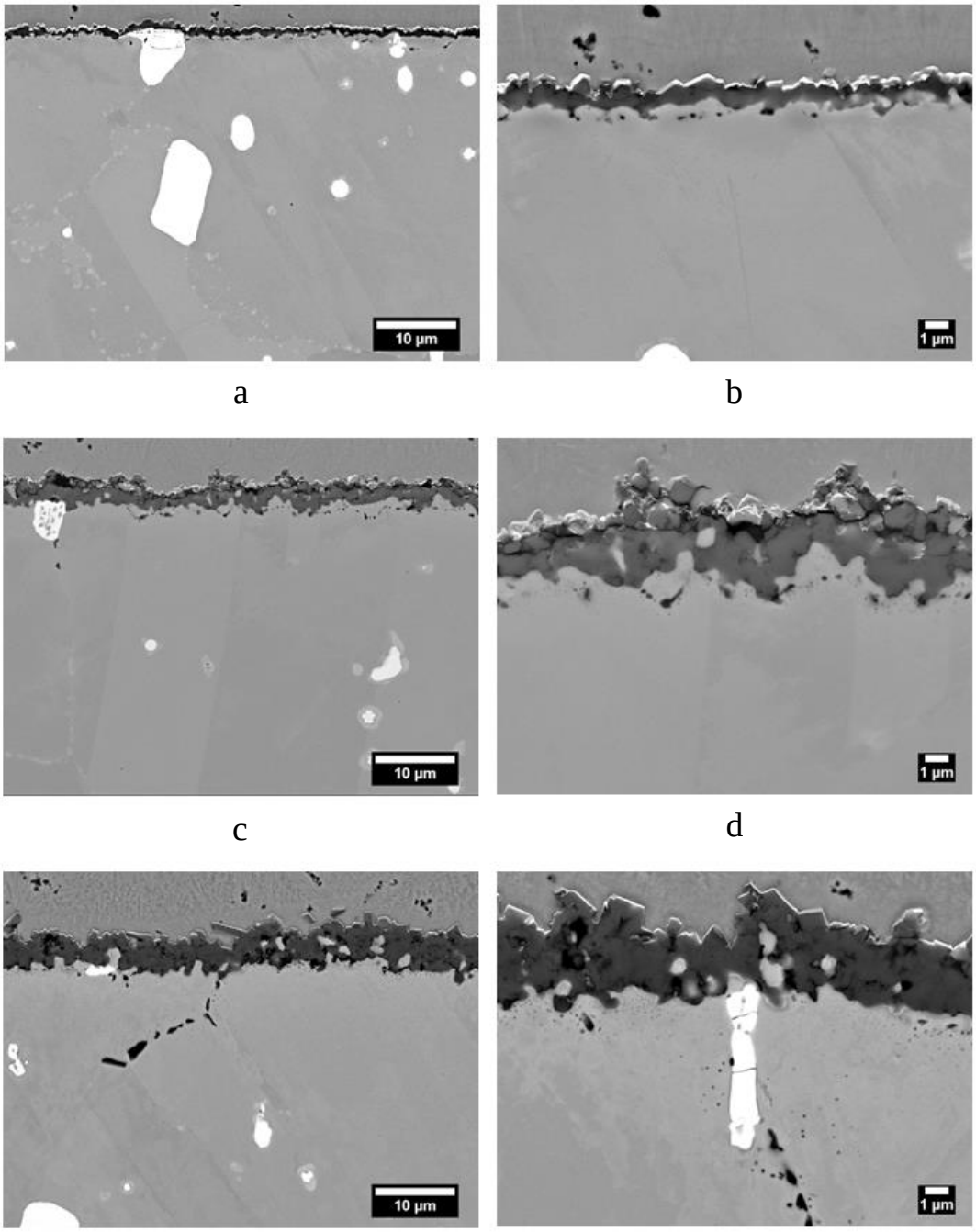

Figure 7.11: BSE micrographs of cross-sections of wrought Haynes 230 following isothermal oxidation in laboratory air at 900°C (a), (b) 25 hours, (c), (d) 215 hours and (e), (f) 1000 hours

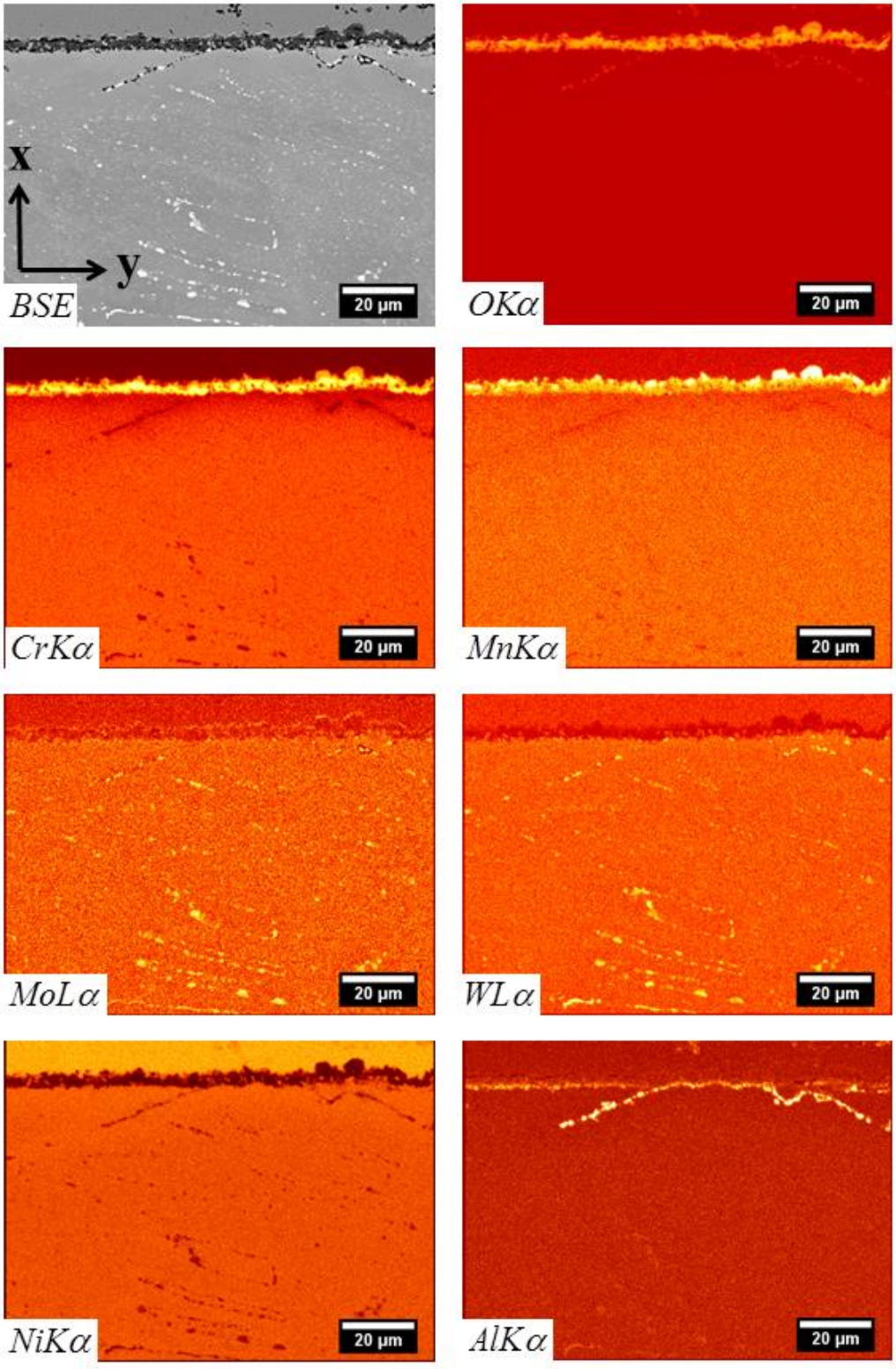

Figure 7.12: Element maps obtained from a cross-section of SLM-consolidated Haynes 230 following 215 hours of isothermal oxidation in laboratory air at 900°C

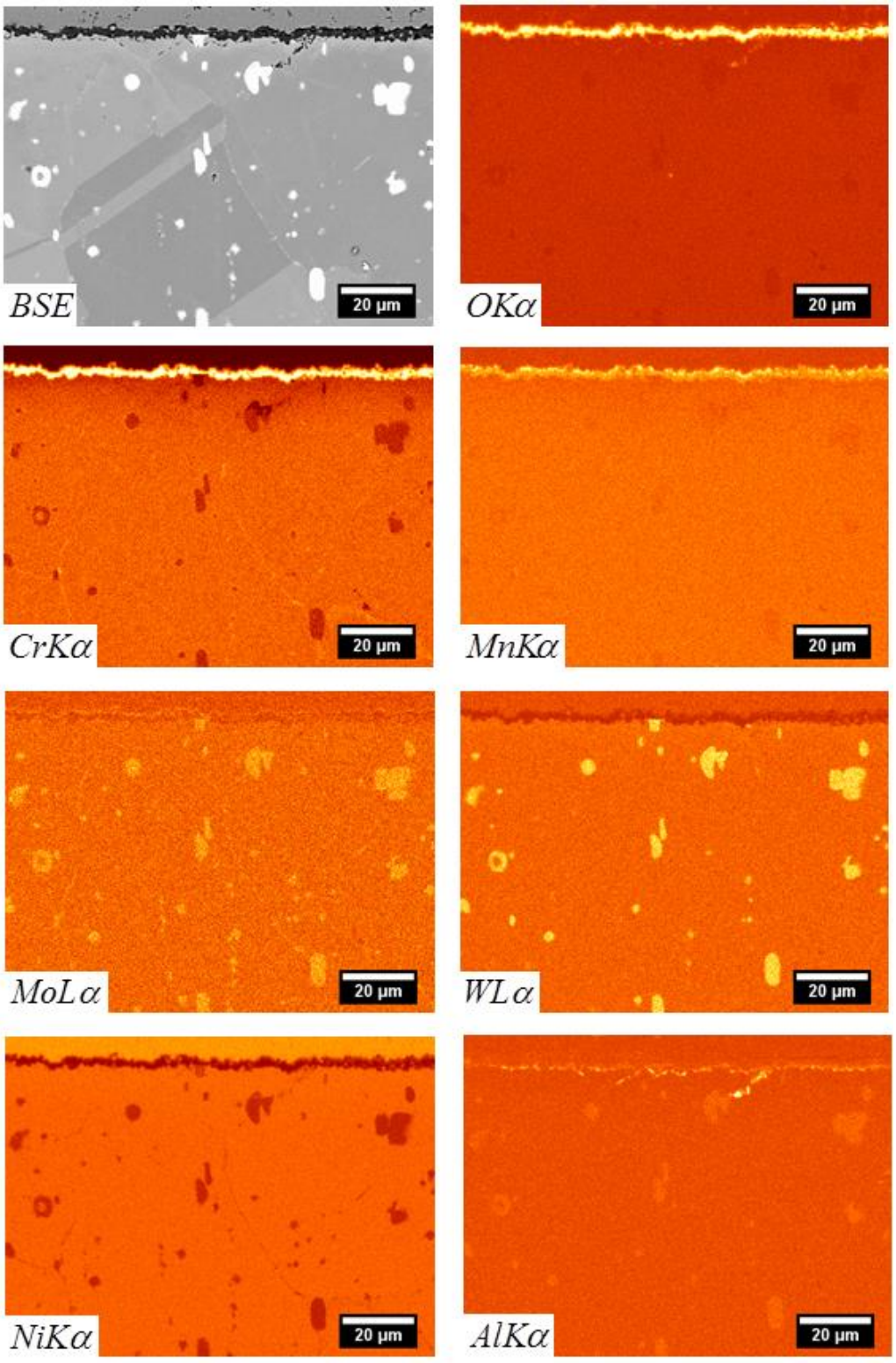

Figure 7.13: Element maps obtained from a cross-section of wrought Haynes 230 following 215 hours of isothermal oxidation in laboratory air at 900°C

Detailed Examination of Scale Morphology

The scale formed on the SLM-consolidated alloy was, after 1000 hours of oxidation, dominated by 2-3µm size clusters of chromia grains, Figure 7.14 (a). Spinel grains of ~1-2µm in size were also evident at the scale/gas interface, some of which appeared to have been partially overgrown by chromia. The wrought alloy was, after the same oxidation time, largely covered by spinel grains. However, chromia grains of ~0.1-0.2µm in size were clearly present below the spinel, Figure 7.14 (b).

Cross-sections of the scales formed on the SLM-consolidated alloy and the wrought alloy, following 25 hours and 1000 hours of oxidation, are shown in Figures 7.15 and 7.16 respectively. The micrographs show that the chromia scales were equiaxed, with a grain size of ~0.2µm in size. Therefore the faster oxidation rate of the SLM-consolidated alloy is probably not due to a smaller oxide grain size.

A significant volume fraction of alloy was incorporated into both chromia scales, which appears to occur as a result of inward growth of the scale. This is expected to be the dominant scale growth mechanism for Haynes 230 because of the reactive element addition. Some of the smaller fragments of alloy may have floated up through the scale, but large 'protrusions' of alloy into the scale, still connected to the bulk, or only just disconnected from it, can be used to estimate the thickness of the inward growth. This, measured as the separation of the two red lines overlaid on Figures 7.15 and 7.16, is ~5-6µm and ~4-5µm for the SLM-consolidated alloy and wrought alloy respectively. The additional chromia scale present on the SLM-consolidated alloy, which is believed to be grown by the outward diffusion of Cr, is ~2µm.

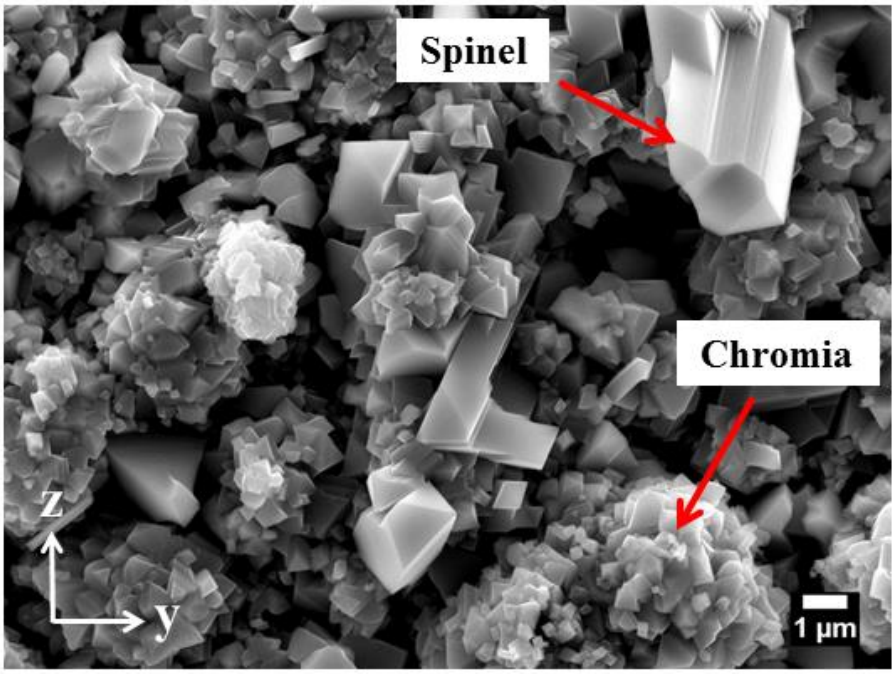

a

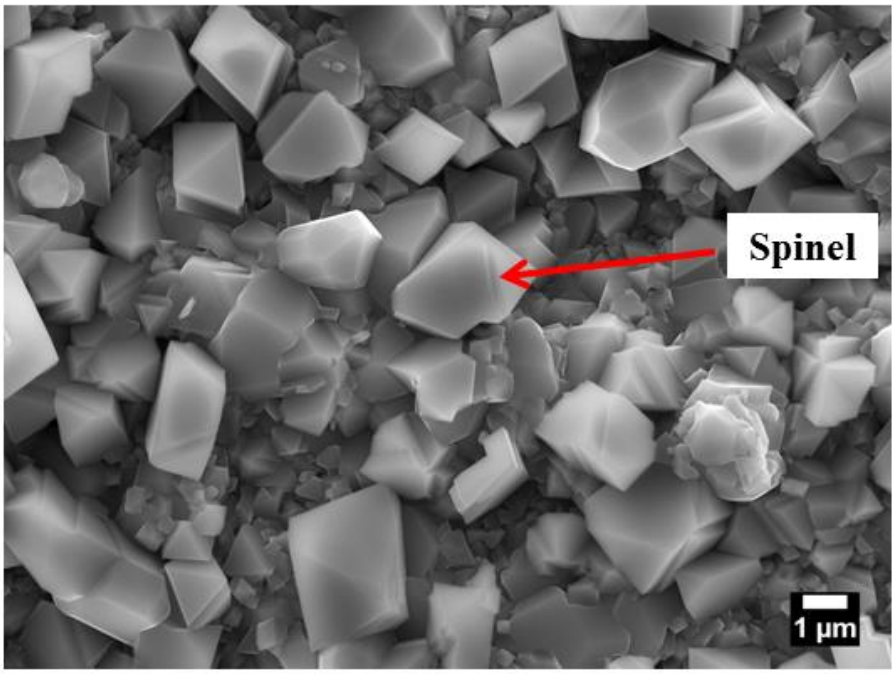

b

Figure 7.14: SE micrographs of Haynes 230 following 1000 hours of isothermal oxidation in laboratory air at 900°C (a) SLM-consolidated alloy, (b) Wrought alloy

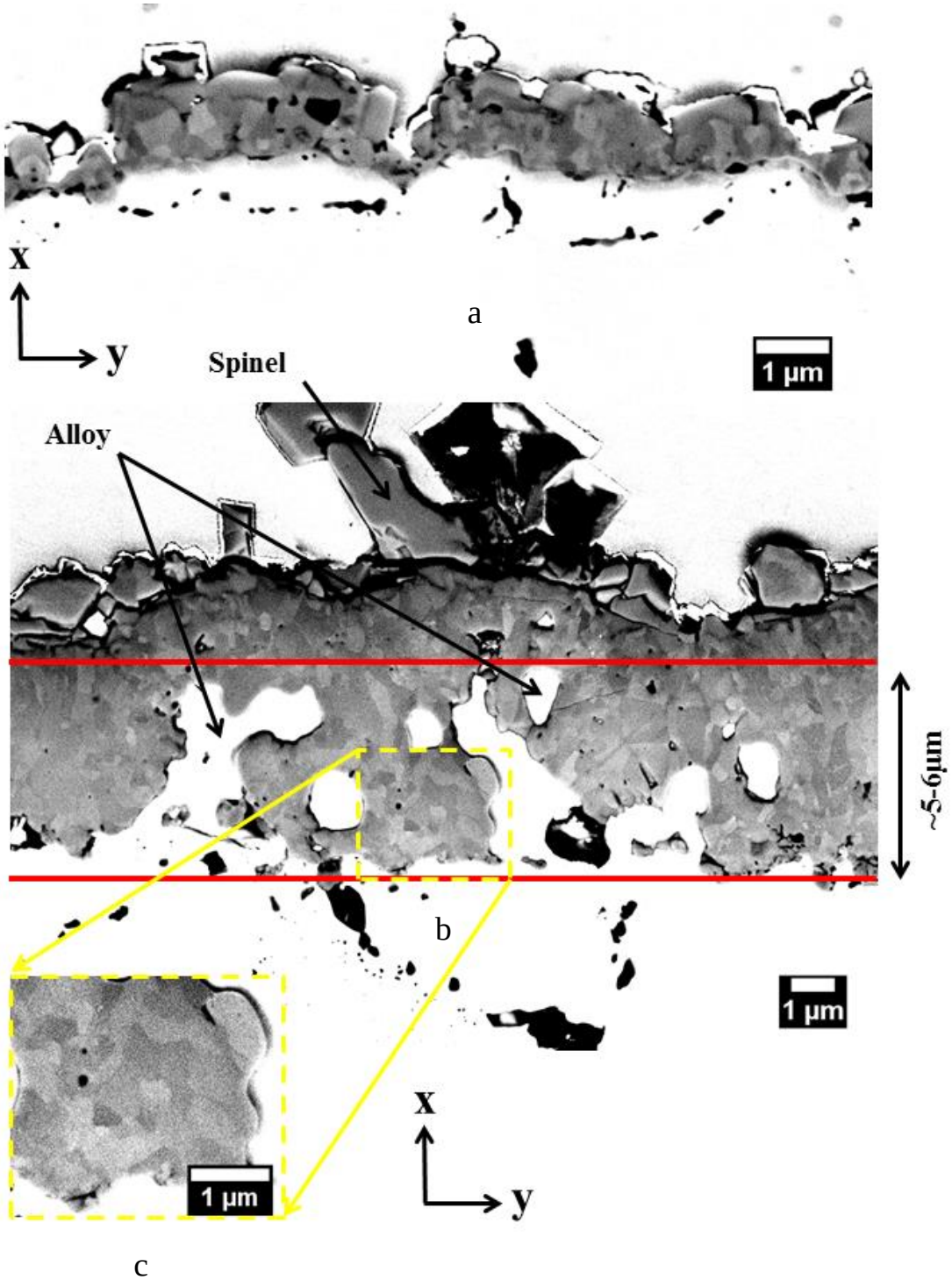

Figure 7.15: BSE micrographs of cross-sections of SLM-consolidated Haynes 230 following isothermal oxidation in laboratory air at 900°C (a) 25 hours, (b) and (c) 1000 hours

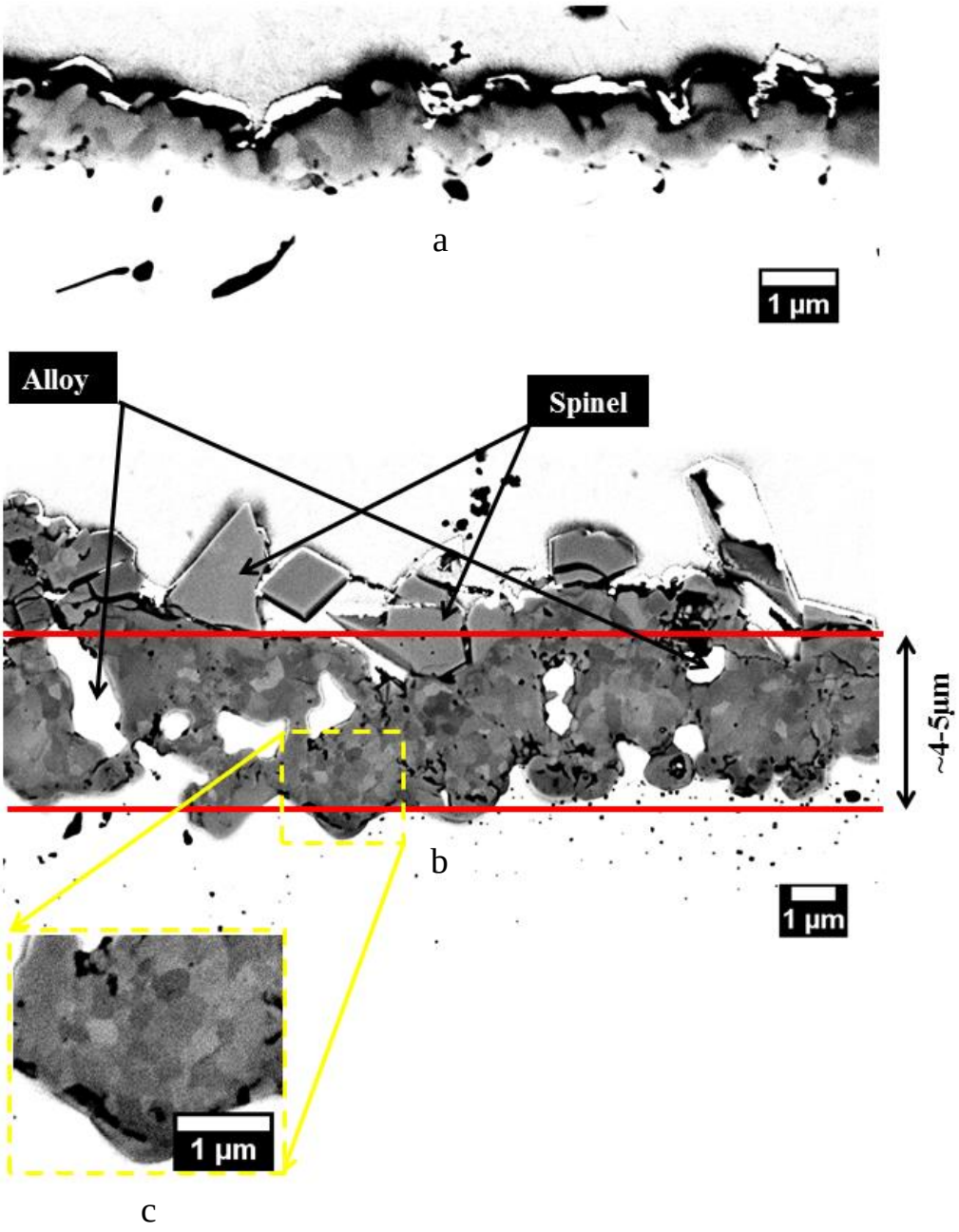

Figure 7.16: BSE micrographs of cross-sections of wrought Haynes 230 following isothermal oxidation in laboratory air at 900°C (a) 25 hours, (b) and (c) 1000 hours

7.3.3 Haynes 230 ODS

Initial Examination by Microscopy

The scale formed on the SLM-consolidated alloy was reasonably uniformly thin, except for long, narrow patches of thick scale orientated parallel to the build direction of the alloy, Figure 7.17 (a). The thick patches of scale were observed to spall after ≥215 hours of oxidation, revealing cracks in the underlying alloy, Figure 7.17 (b). These are assumed to be the same cracks observed at the grain boundaries of the as-consolidated alloy. The scale spalled during cooling to ambient temperature, as evidenced by the metallic appearance of the alloy exposed by spalling.

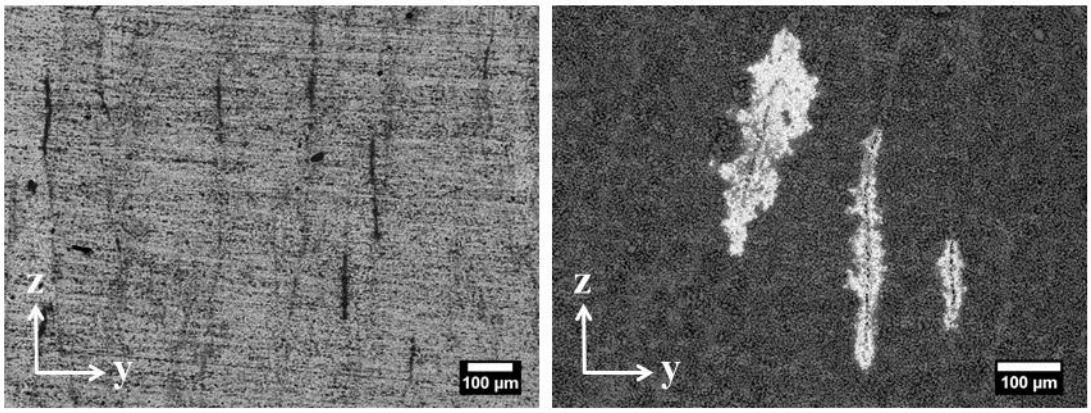

a b

Figure 7.17: BSE micrographs of Haynes 230 ODS/SLM following isothermal oxidation in laboratory air at 900°C (a) 25 hours, and (b) 1000 hours

The scale formed on the SPS-consolidated alloy was, at short oxidation times, featureless, but at longer oxidation times it became very ‘lumpy’, Figures 7.18 (a) and 7.18 (b). This is indicative of widespread detachment of the scale from the underlying alloy. One or two loose fragments of scale, present on the surface of the coupon oxidised for 1000 hours, showed that the scale had begun to spall, though none was found in the crucible in which the alloy was oxidised.

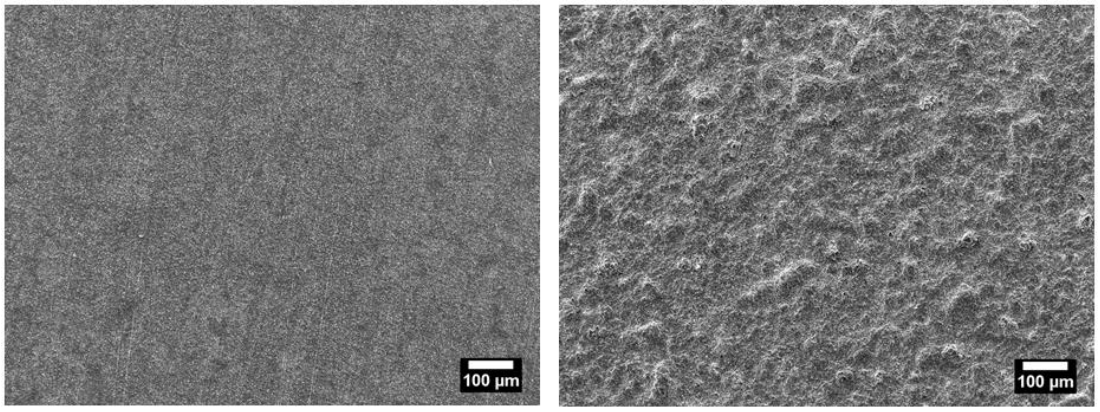

a b

Figure 7.18: SE micrographs of Haynes 230 ODS/SPS following isothermal oxidation in laboratory air at 900°C (a), 25 hours, and (b), 1000 hours

In cross-section, the scale formed on the SLM-consolidated alloy was irregular in thickness, particularly at oxidation times <1000 hours, Figure 7.19. The alloy contained submicron M_6C carbides, which were either blocky or acicular/plate-like in form. The carbides dissolved in response to the oxidation of the alloy, to a depth of ~10µm after 1000 hours of oxidation, and were precipitated in the form of blocky carbides of ~1µm in size at the scale to alloy interface. Large numbers of voids, believed to be Kirkendall voids, condensed in the alloy at all oxidation times >25 hours, at depths of ~10-15µm from the scale/alloy interface. The voids may have formed as a result of the injection of vacancies into an alloy that already contained a large concentration of vacancies. Internal oxides did not obviously form in the alloy, but their presence would be difficult to discern because of the large number of Cr-rich oxide inclusions and voids present in the alloy.

The oxidation behaviour of the SPS-consolidated alloy was very different to that of the SLM-consolidated alloy. A uniform, but thick oxide scale developed within the first 25 hours of oxidation, which grew strongly by the inward diffusion of O, causing large numbers of alloy particles to be incorporated into the scale, Figure 7.20. The scale had a duplex structure with small Cr-rich oxide grains present at the scale/alloy interface and large $Mn_xCr_{3-x}O_4$ spinel grains present at the scale/gas

interface. At longer oxidation times the ratio of $Mn_xCr_{3-x}O_4$ spinel to Cr-rich scale increased significantly. Extensive internal oxidation also occurred within the first 25 hours of oxidation, and during this time voids of 1-5µm in size developed at the scale/alloy interface and within the internally oxidised zone. With increasing oxidation time, the internal oxide grew and coalesced to form interconnected masses, which caused the scale to bulge upwards. This caused the scale to crack at positions where the tensile stresses were greatest, meaning that the protective properties of the scale were compromised. Decohesion of the scale occurred at numerous positions along the examined cross-section, probably on cooling to ambient temperature, giving the oxidised alloy the rumpled appearance observed in plan-view.

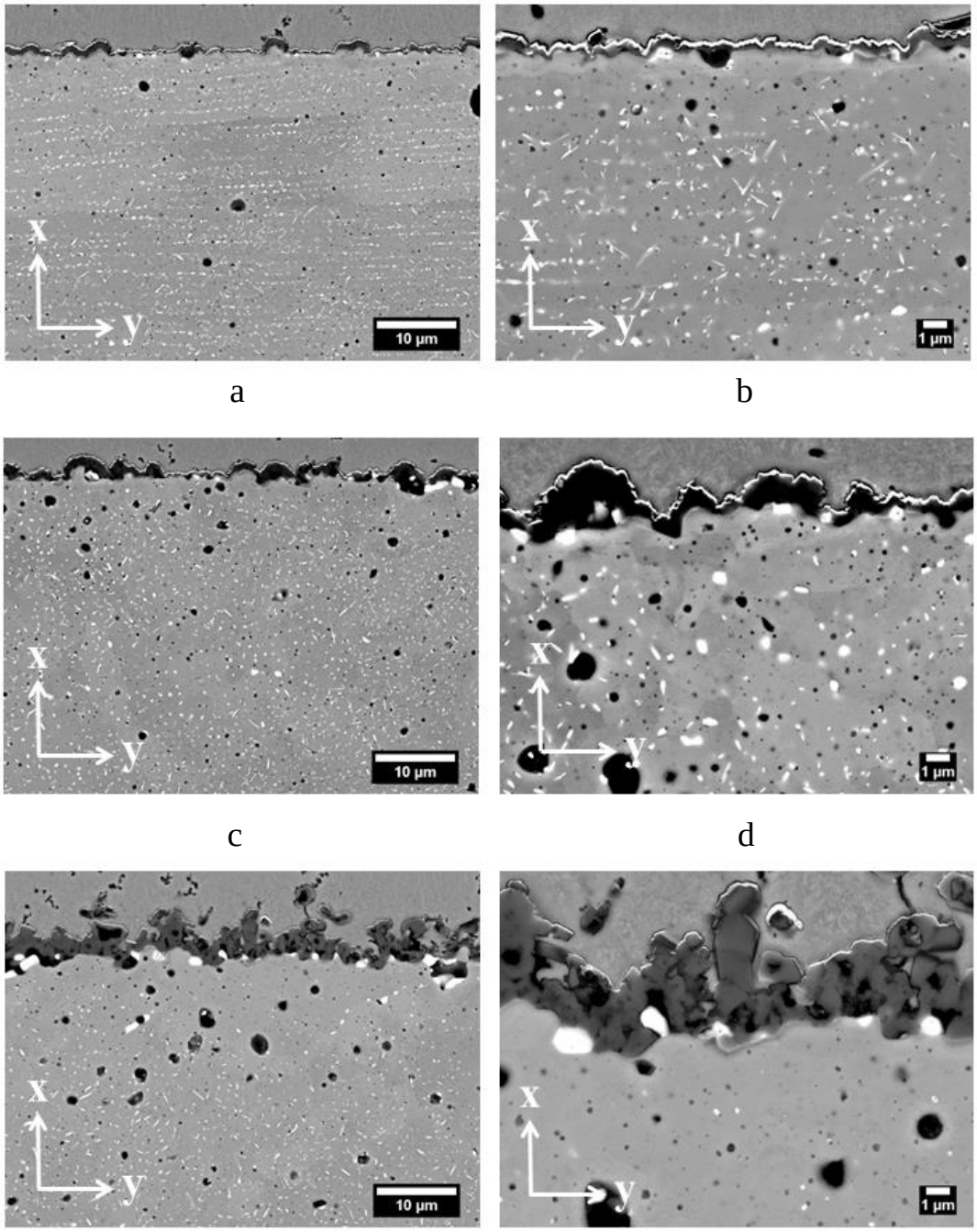

Figure 7.19: BSE micrographs of cross-sections of Haynes 230 ODS/SLM following isothermal oxidation in laboratory air at 900°C (a), (b) 25 hours, (c), (d) 215 hours and (e), (f) 1000 hours

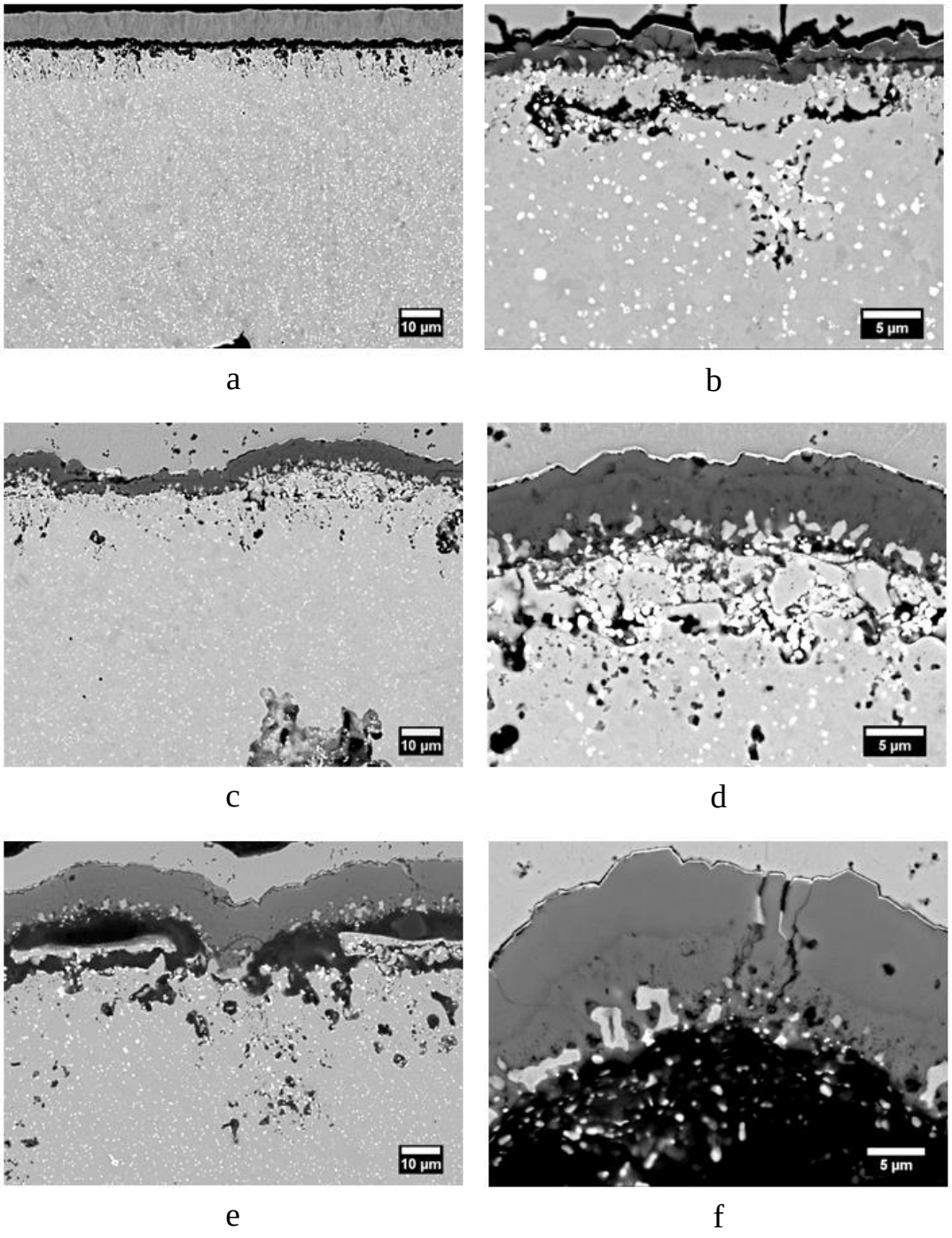

Figure 7.20: BSE micrographs of cross-sections of Haynes 230 ODS/SPS following isothermal oxidation in laboratory air at 900°C (a), (b) 25 hours, (c), (d) 215 hours and (e), (f) 1000 hours

Element maps obtained from Haynes 230 ODS/SLM and Haynes 230 ODS/SPS, after 215 hours of oxidation, are shown in Figures 7.21 and 7.22 respectively. The scale formed on the SLM-consolidated alloy was rich in Cr, Mn and O, indicative of chromia and $Mn_xCr_{3-x}O_4$ spinel. The spinel was concentrated where the scale was thickest. The alloy was depleted in Cr to a depth of ~10-15µm, but a Cr-rich phase, probably $M_{23}C_6$, was present on the grain boundaries at greater depths. W-rich inclusions, some of which contained Mo, were depleted to a depth of ~5µm but were otherwise uniformly distributed throughout the bulk alloy. Al-rich oxides were generally present on the surface of the specimen, and particularly in the voids. It is thought that the specimen had retained some alumina from the preparation of the specimen. The SPS-consolidated alloy formed a duplex oxide scale, which at its base was Cr-rich and at the scale/gas interface was rich in Mn and Cr. This is consistent with chromia and spinel, as determined by XRD. However, the total thickness of the scale, and the ratio of spinel to chromia, are unusual and may indicate that the addition of Y has promoted scale growth, most particularly spinel. Depletion of Cr in the matrix is not obvious, but there is the depletion of a population of inclusions rich in Cr and Mn to a depth of ~50µm. The inclusions may have formed as a result of O contamination of the gas atomised powder during mechanical alloying. The internal oxide is Al-rich, and this forms a semi-continuous layer at the scale/alloy interface, which extends along the full length of the mapped region of the alloy. At its deepest the Al-rich oxide layer extends to a depth of ~20µm from the scale/alloy interface.

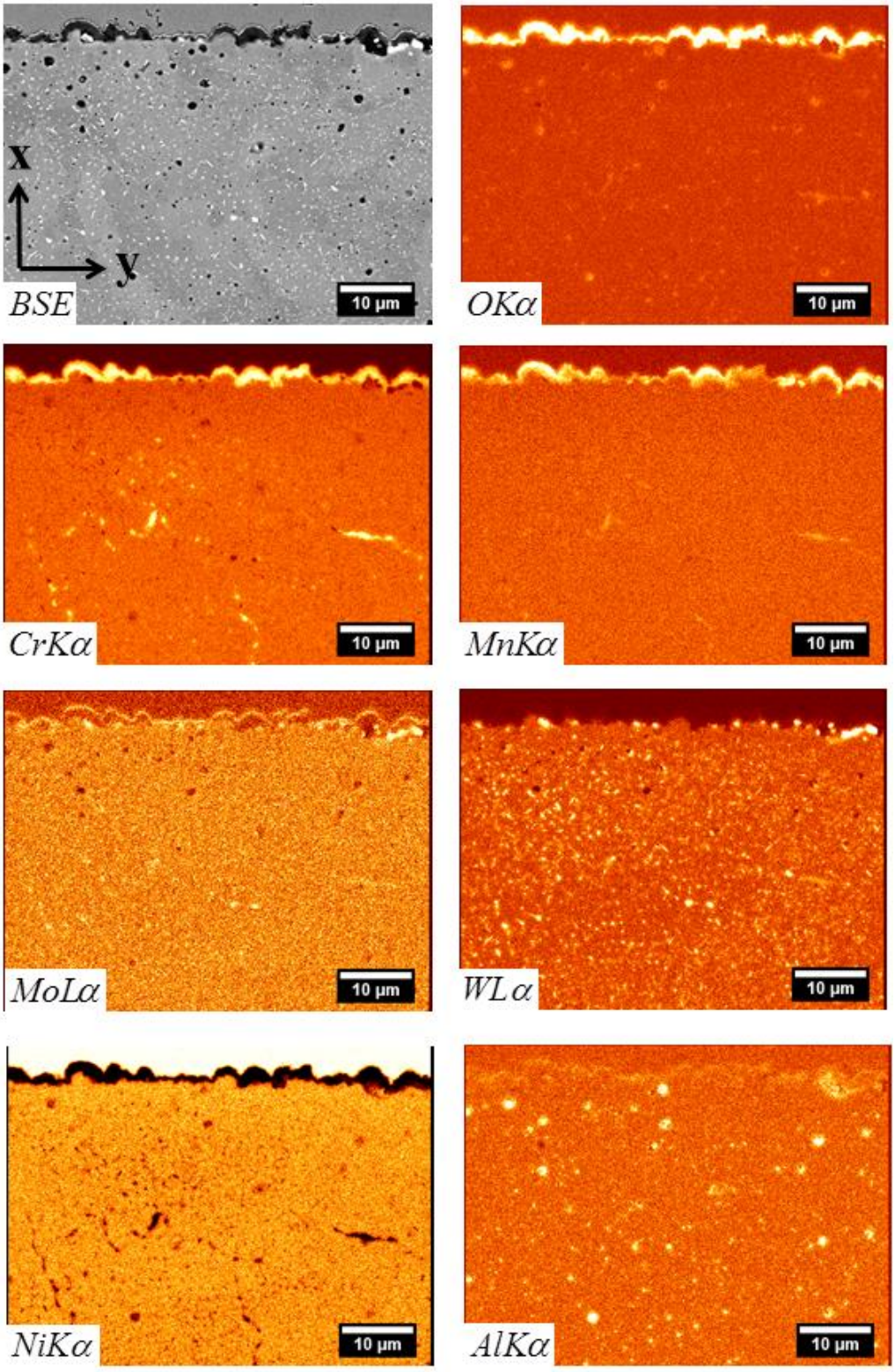

Figure 7.21: Element maps obtained from a cross-section of Haynes 230 ODS/SLM following 215 hours of isothermal oxidation in laboratory air at 900°C

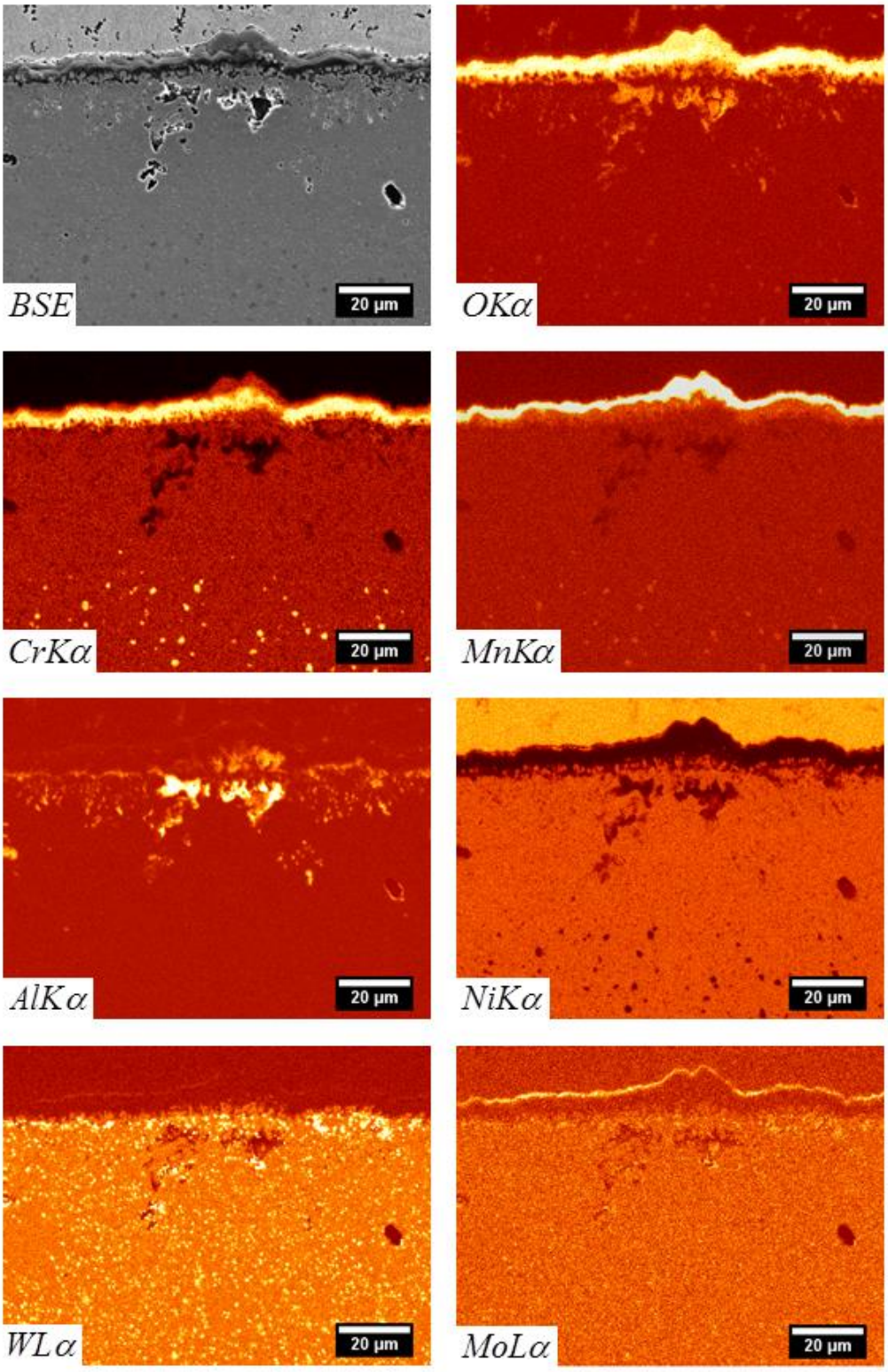

Figure 7.22: Element maps obtained from a cross-section of Haynes 230 ODS/SPS following 215 hours of isothermal oxidation in laboratory air at 900°C

Detailed Examination of Scale Morphology

The scale formed on Haynes 230 ODS/SLM was, at short oxidation times, mainly comprised of small Cr-rich oxide grains, but at longer oxidation times spinel grains came to dominate the surface of the scale, Figure 7.23 (a). The surface of Haynes 230 ODS/SPS was completely covered by spinel after 1000 hours of oxidation, Figure 7.23 (b). The spinel grains formed on Haynes 230 ODS/SLM were rhombohedral in shape, whereas the spinel grains formed on Haynes 230 ODS/SPS were blocky in shape and, as highlighted on Figure 7.23 (b), exhibited terracing.

A cross-section of the scale formed on Haynes 230 ODS/SLM, following 215 hours of oxidation, was examined in a STEM following preparation using the FIB. The scale was ~0.5-1µm thick, and had a grain size of ~0.5µm, Figure 7.24. The micrographs also show spinel grains at the scale/gas interface, which contain dislocations. These are known to act as fast transport paths during the high temperature oxidation of alloys [264]. A line of voids, orientated parallel to the scale/alloy interface, is present within the Cr-rich scale, may indicate the position of the surface of the alloy prior to oxidation. If correct, this indicates that the Cr-rich scale has grown mainly by the inward diffusion of O, as expected for an alloy doped with reactive elements.

Haynes 230 ODS/SPS oxidised rapidly to form a scale ~2µm thick after 25 hours of oxidation, and ~12µm thick after 1000 hours of oxidation, Figure 7.25. The bulk of the scale was, at the shorter oxidation time, composed of fine grain chromia, which had grown by inward diffusion, as evidenced by the large volume of alloy that had been incorporated into it. The chromia was overgrown by a thin but continuous layer of columnar spinel, which shows that outward diffusion had also occurred through the scale. After 1000 hours of oxidation the ratio of spinel to chromia thickness had increased to ~1:1, which indicates that, with increasing oxidation time, the rate of spinel formation increased relative to that of chromia. The columnar structure of the spinel was maintained during the course of the experiment, but the chromia scale

appeared more columnar after 1000 hours of oxidation than it did after 25 hours of oxidation, which may be because of creep in the scale arising from tensile stresses acting perpendicular to the scale/alloy interface. Terracing of the spinel is readily apparent, which is indicated by the yellow dashed line in Figure 7.25. The boundary between spinel and chromia is seen in more detail in Figure 7.26 (a), which shows that the spinel grains are pinned at spinel/chromia triple points and that growth of the spinel causes the spinel/chromia interface to bulge inward toward the scale/alloy interface. It can be seen in Figure 7.26 (b) that spinel has grown around the chromia grain adjacent to it, suggesting different rates of spinel formation. It is reported that spinel grows as a consequence of the reaction between MnO and Cr_2O_3 scale to form $Mn_xCr_{3-x}O_4$. Evidence of terracing of the spinel, observed in Figures 7.23 (b) and 7.25 (b) is shown in detail in Figure 7.26 (b).Very small chromia grains formed at the base of the scale, where it protruded into the alloy. These grains were full of porosity, particularly in the upper half of the chromia layer i.e. adjacent to the spinel, Figure 7.26 (c). The porosity may arise from deformation of the scale as a result of growth stresses, or perhaps more likely vacancy condensation. This may be related to strong cation transport by lattice diffusion, with vacancies condensing in the scale rather than the alloy because of poor contact between the scale and the alloy.

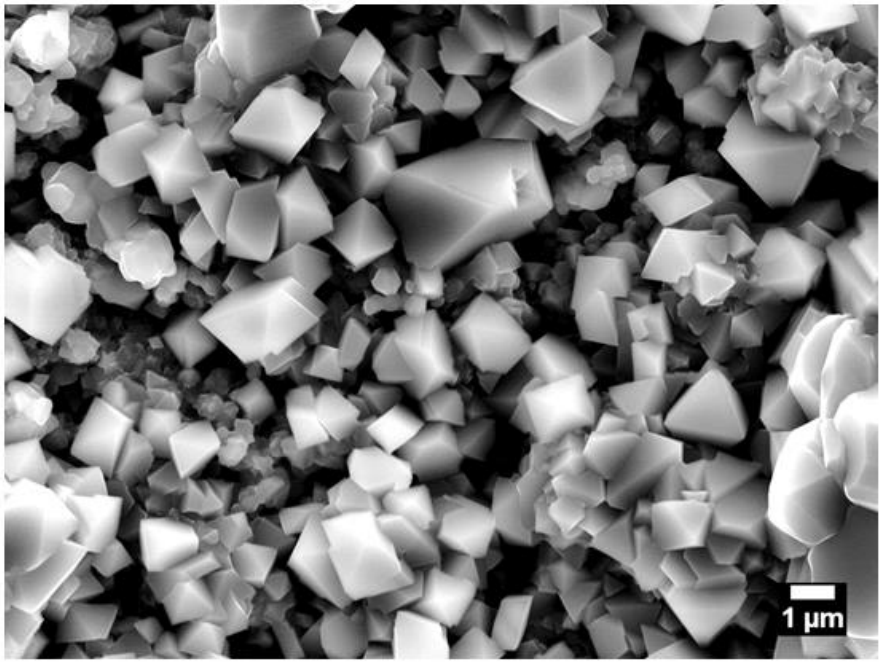

a

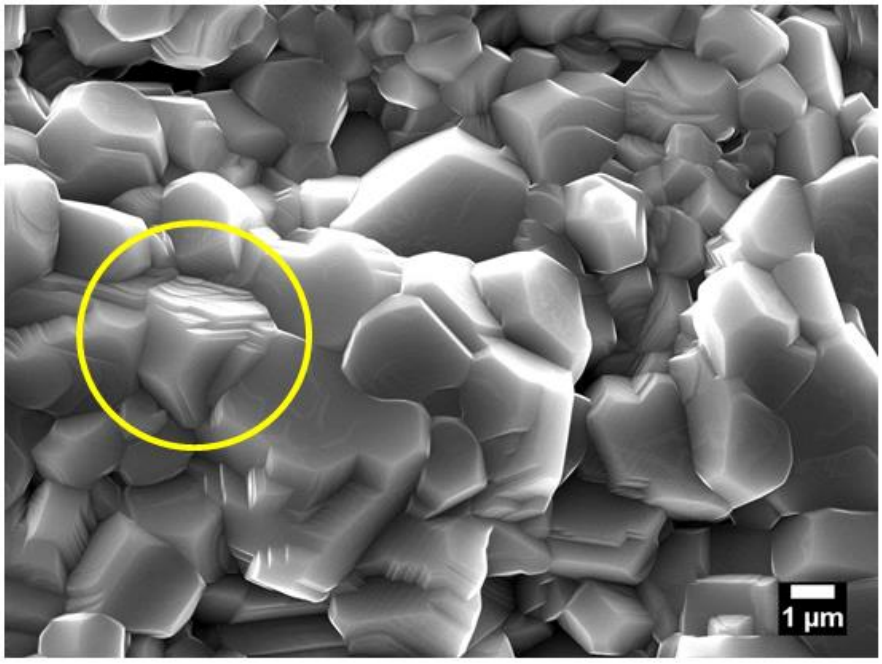

b

Figure 7.23: SE micrographs of Haynes 230 ODS following 1000 hours of isothermal oxidation in laboratory air at 900°C (a) SLM-consolidated alloy, (b) SPS-consolidated alloy

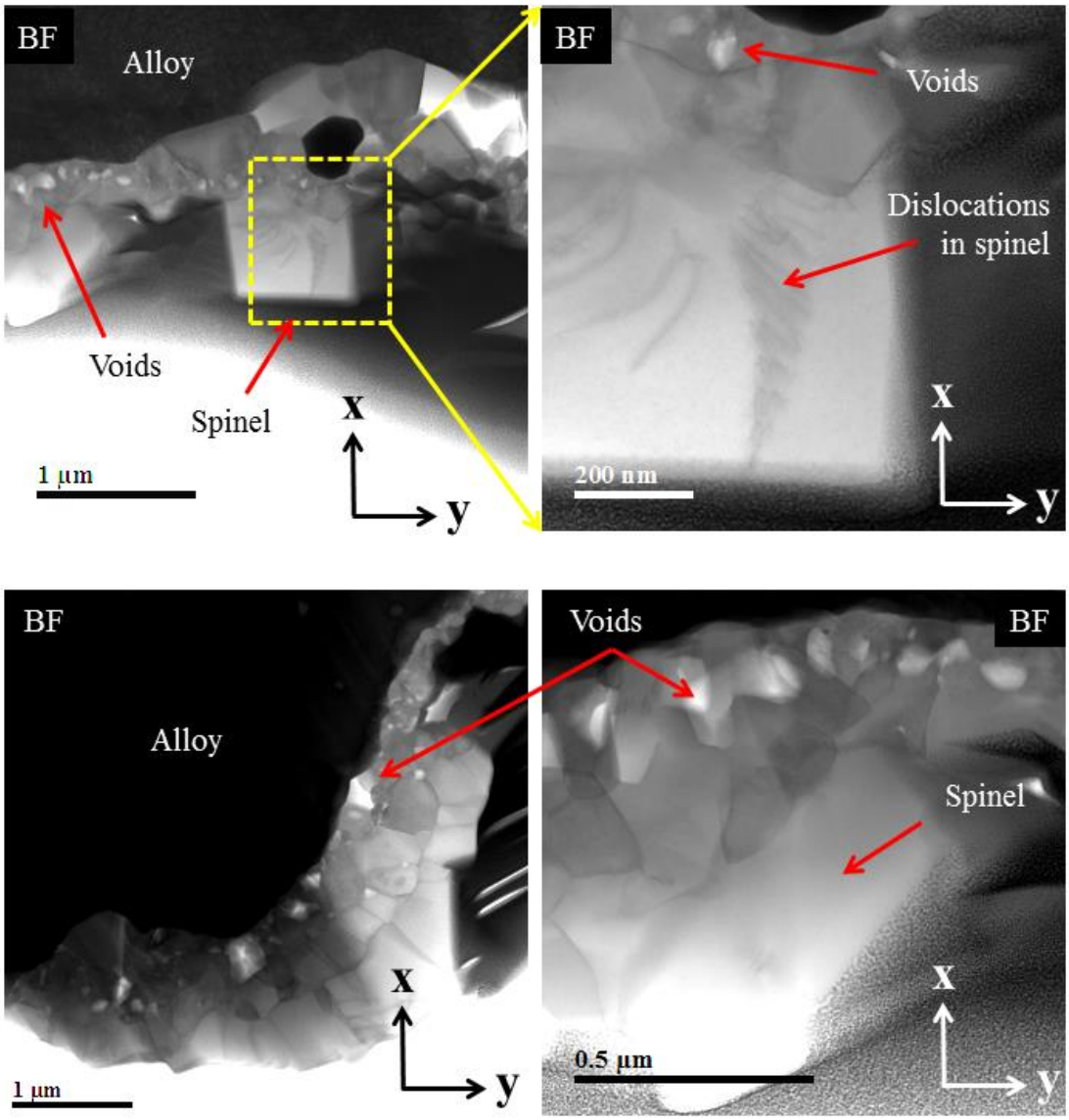

Figure 7.24: STEM micrographs of a cross-section of Haynes 230 ODS/SLM following 215 hours of isothermal oxidation in laboratory air at 900°C

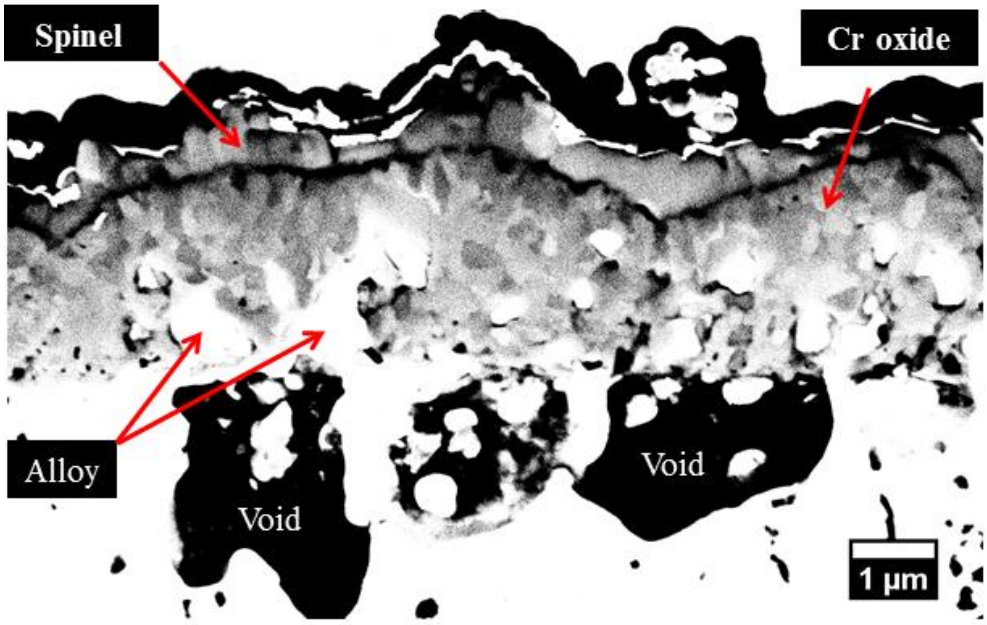

a

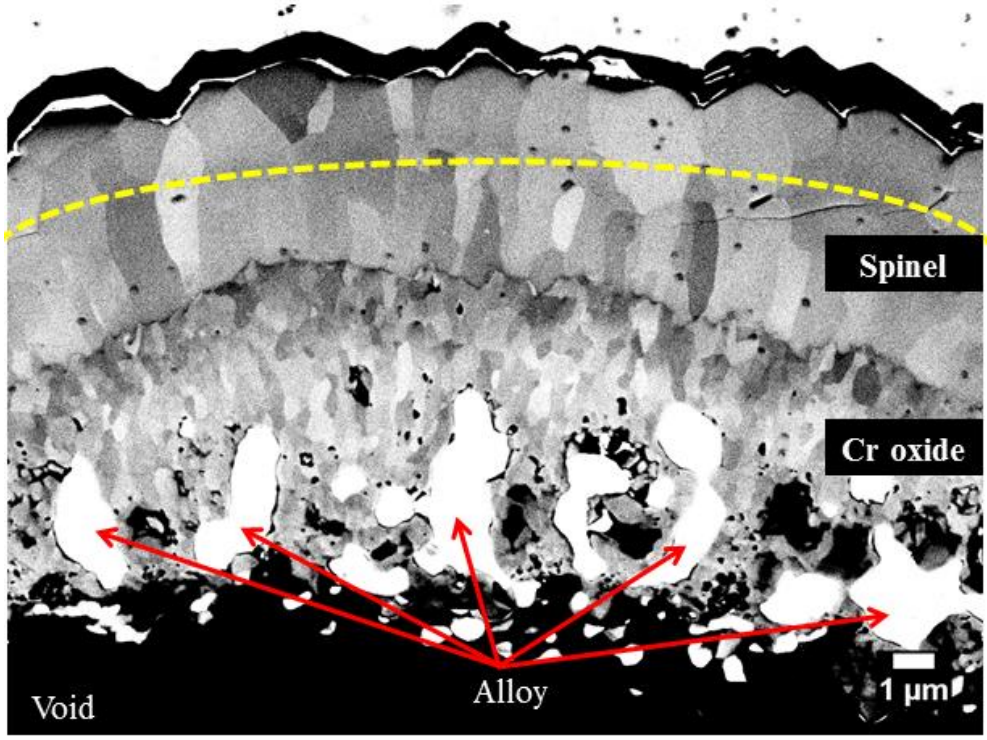

b

Figure 7.25: BSE micrographs of cross-sections of SPS-consolidated Haynes 230 following isothermal oxidation in laboratory air at 900°C (a) 25 hours, (b) 1000 hours

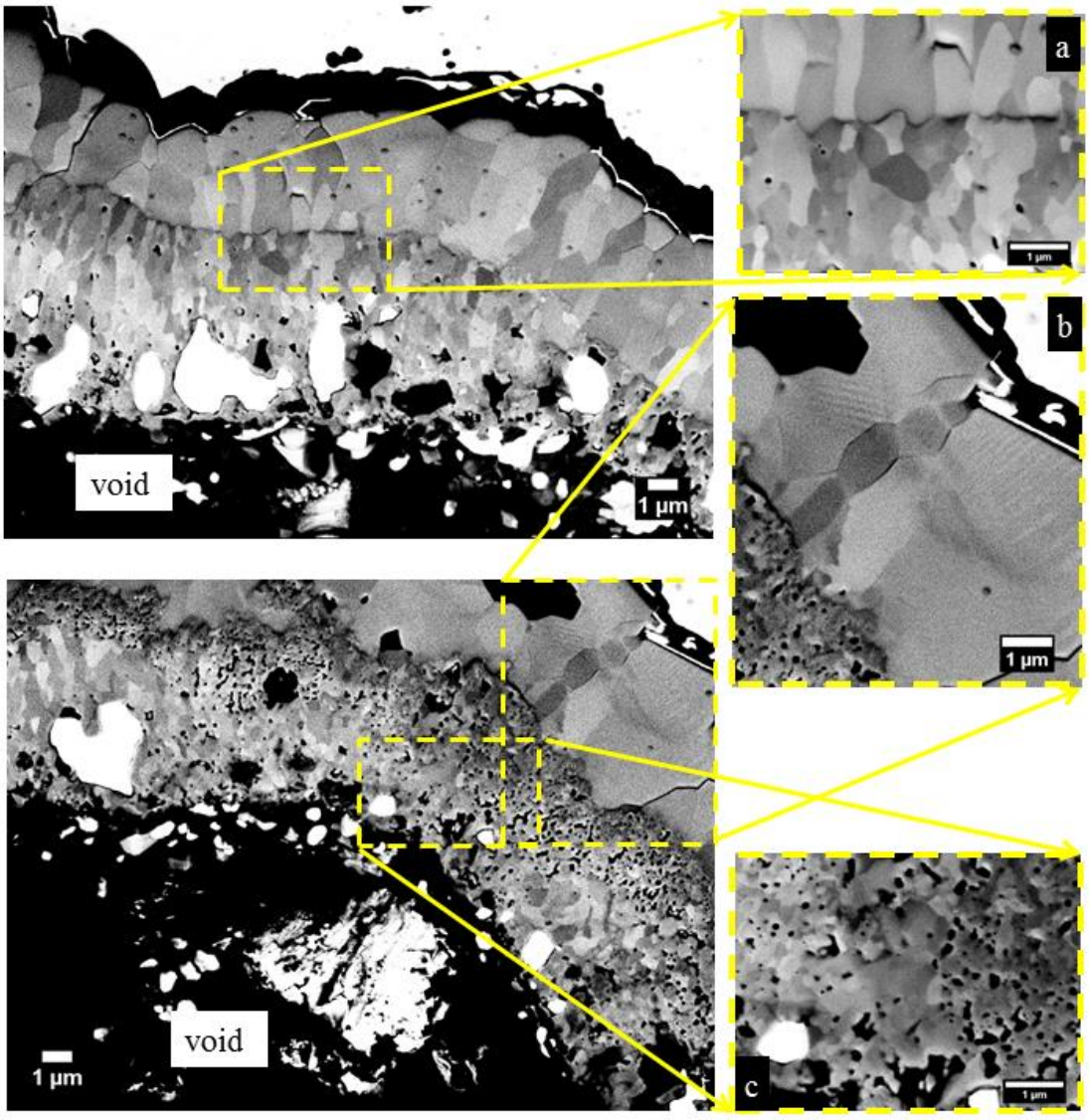

Figure 7.26: BSE micrographs of cross-section of SPS-consolidated Haynes 230 following 1000 hours of isothermal oxidation in laboratory air at 900°C

7.3.4 Oxidation-induced changes in alloys

Analysis of Bulk Alloys

Analyses obtained for the alloys and powders are provided in Table 7.1, along with the analyses provided by the suppliers. The methodology used to obtain the results is the same as described in section 5.3.5. The analyses denoted ‘oxidised’ were

obtained from the centre of each coupon following 1000 hours of oxidation, in order to provide terminal compositions for the depth profiles. Analyses were also obtained for the ODS alloys prior to oxidation, which are denoted ‘alloy’ in Table 7.1.

The analyses obtained from the SLM-consolidated and wrought alloys are in good agreement with the supplier analyses for the gas atomised powder and wrought alloy, except for Mn, which is significantly too high in the results obtained for the present work. The analysis obtained from the centre of the oxidised coupon of Haynes 230 ODS/SLM is well matched to that of the as-consolidated alloy, however the analysis obtained from the centre of the oxidised coupon of Haynes 230 ODS/SPS is depleted in Cr with respect to the alloy. This may indicate fast diffusion of Cr to the surface of the alloy.

Table 7.1: Mean composition and standard deviation of bulk Haynes 230 determined for this work by SEM/EDS (Wt. %). Supplier analyses were obtained by XRF

Alloy	Ni	Fe	Cr	W	Mo	Al	Si	Mn	Co
SLM oxidised (this work)	55.9 ±0.6	1.70 ±0.1	21.9 ±0.2	15.9 ±0.8	2.3 ±0.1	0.5 ±0.1	0.3 ±0.1	1.3 ±0.1	0.2 ±0.1
Gas atomised powder (supplier)	Bal.	1.53	21.88	14.06	1.92	0.39	0.48	0.68	0.13
Wrought oxidised (this work)	58.9 ±0.2	1.4 ±0.1	22.0 ±0.1	14.5 ±0.1	1.3 ±0.1	0.4 ±0.1	0.2 ±0.1	1.0 ±0.1	0.3 ±0.1
Wrought alloy (supplier)	Bal.	1.53	22.12	14.63	1.20	0.26	0.40	0.20	0.18
ODS/SLM oxidised (this work)	58.2 ±0.5	2.2 ±0.1	23.2 ±0.3	12.1 ±0.3	2.4 ±0.1	0.2 ±0.1	0.3 ±0.2	1.2 ±0.1	0.3 ±0.1
ODS/SLM alloy (this work)	55.1 ±1.0	1.7 ±0.2	23.4 ±0.6	15.2 ±0.8	2.6 ±0.5	0.3 ±0.2	0.2 ±0.2	1.2 ±0.3	- -
ODS/SPS oxidised (this work)	58.0 ±1.5	1.8 ±0.1	22.3 ±0.3	13.3 ±1.5	2.2 ±0.1	0.3 ±0.1	0.4 ±0.1	0.8 ±0.1	0.2 ±0.1
ODS/SPS alloy (this work)	56.5 ±1.4	1.7 ±0.4	23.4 ±0.4	15.0 ±1.0	2.4 ±0.6	0.5 ±0.2	- -	0.7 ±0.1	- -

Depth Profiles

The depth profiles are shown for Haynes 230 SLM and wrought Haynes 230 in Figure 7.27, and for Haynes 230 ODS/SLM and Haynes 230 ODS/SPS in Figure 7.28.

Haynes 230 SLM and wrought Haynes 230 were both depleted in Cr, Mn and Al, and enriched in Fe and Ni, to a depth of ~60µm from the scale/alloy interface. Al was enriched at the scale/alloy interface, probably as internal oxide. Haynes 230 ODS/SLM was depleted in Cr and Mn to ~15µm, and enriched in Ni and Fe to the

same depth. Al varied markedly within the profile, fluctuating between ~0.1-1.0 Wt. %, presumably as a result of the analysis of particles of internal oxide. The only element that obviously changed in the Haynes 230 ODS/SPS depth profile was Al, which was enriched to depth of ~20-30μm as a result of extensive internal oxidation. However, there is no depletion of Al in the depth profile, which probably means that it was depleted to a depth beyond that of the profile. The analyses provided in Table 7.1 possibly show Al depletion at the centre of the oxidised coupon.

Chromium interdiffusion coefficients

The profiles were fitted using Equation 4 in order to estimate the Cr interdiffusion coefficients (D) for the different variants of the alloy, Figures 7.29 and 7.30. Haynes 230 ODS/SPS could not be fitted because there was no measurable depletion of Cr in the depth profile. The results show that $D^{SLM} \approx 2D^{Wrought}$, which is consistent with the results obtained from Alloy 718 and Alloy 625, and indicates that the dendritic/cellular microstructure contributes significantly to the diffusion of Cr in the alloy. The results also show that $D^{SLM} \approx 5D^{SLM/ODS}$, which is difficult to explain. It is possible that the depth profile was terminated too early because the maximum Cr concentration in the profile is ~22.0 Wt. %, which is ~1.0 Wt. % below the bulk concentration of the alloy.

Table 7.2: Chromium interdiffusion coefficients (D) estimated from fitting of the Cr depth profiles

	Chromium interdiffusion coefficients (m^2s^{-1})		
	This work	Chyrkin [151]	Chyrkin [151]
Haynes 230 SLM	1.4E-16 (900°C)	-	-
Wrought Haynes 230	0.7E-16 (900°C)	-	-
Haynes 230 ODS/SLM	0.3E-16 (900°C)	-	-
Haynes 230 ODS/SPS	Not Determined	-	-
Alloy 625	2.0E-16 (900°C)	2.5E-16 (900°C)	7.29E-16 (1000°C)

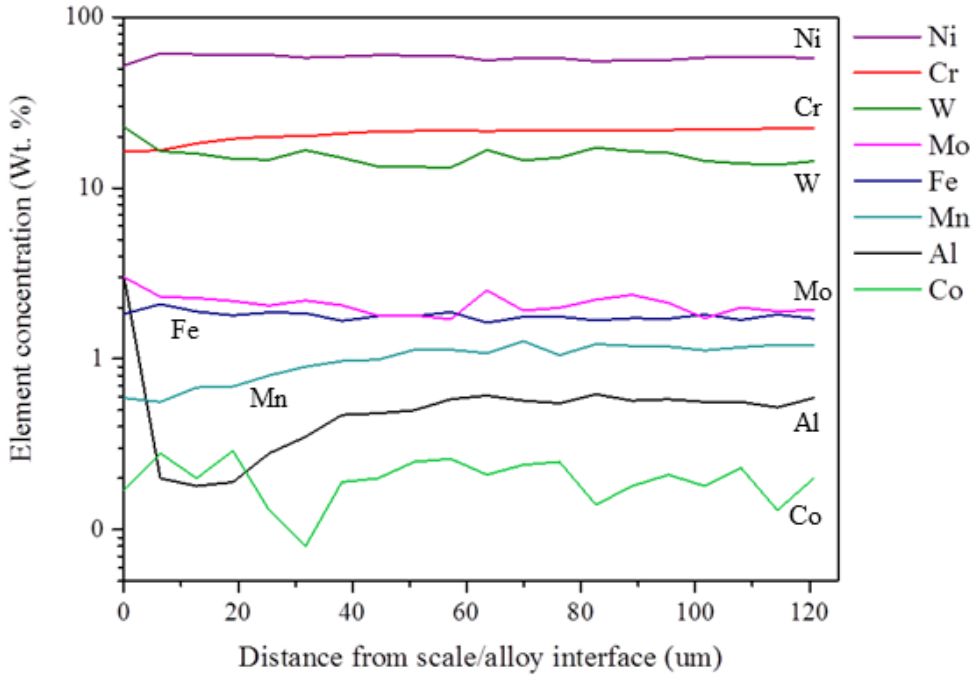

a

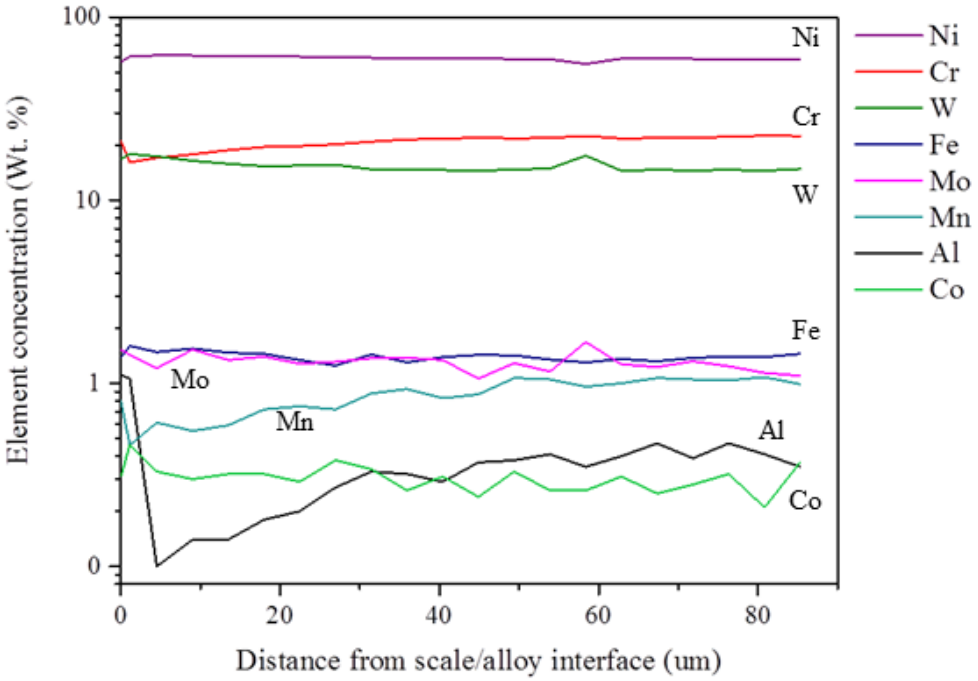

b

Figure 7.27: Plot of element concentration (Wt. %) against distance from scale/alloy interface (μm) following 1000 hours of isothermal oxidation in laboratory air at 900°C (a) Haynes 230 SLM, and (b) Wrought Haynes 230

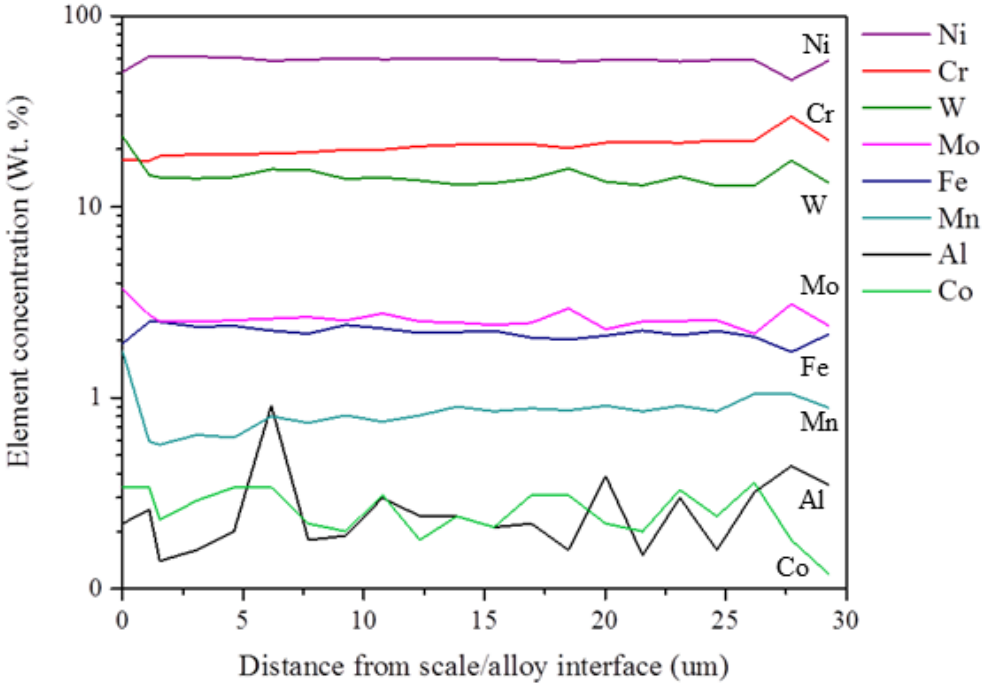

a

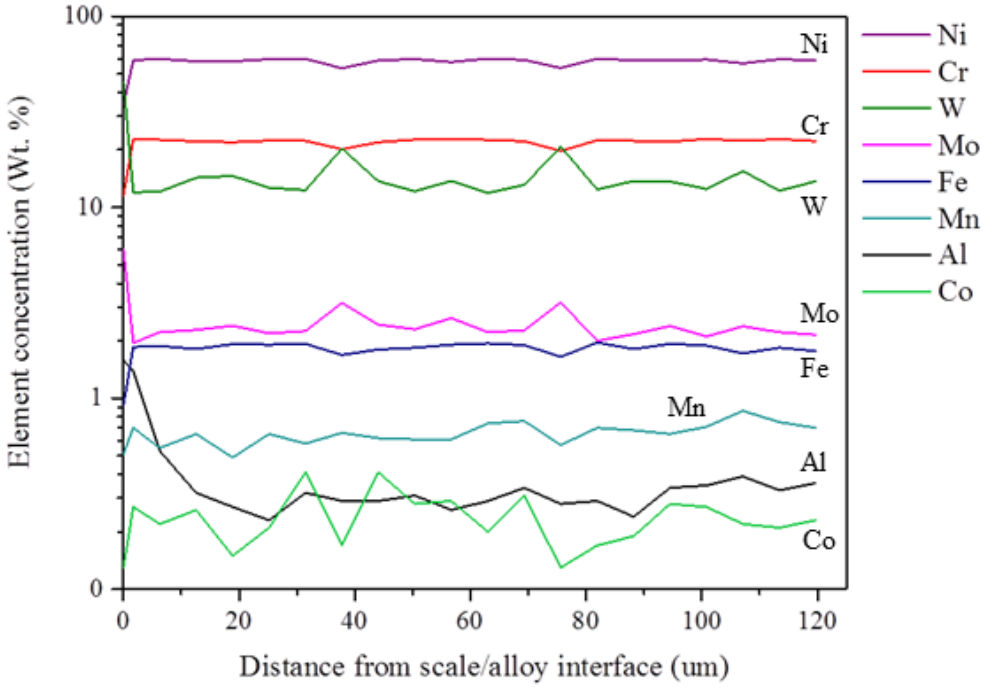

b

Figure 7.28: Plot of element concentration (Wt. %) against distance from scale/alloy interface (µm) following 1000 hours of isothermal oxidation in laboratory air at 900°C (a) Haynes 230 ODS/SLM, and (b) Haynes 230 ODS/SPS

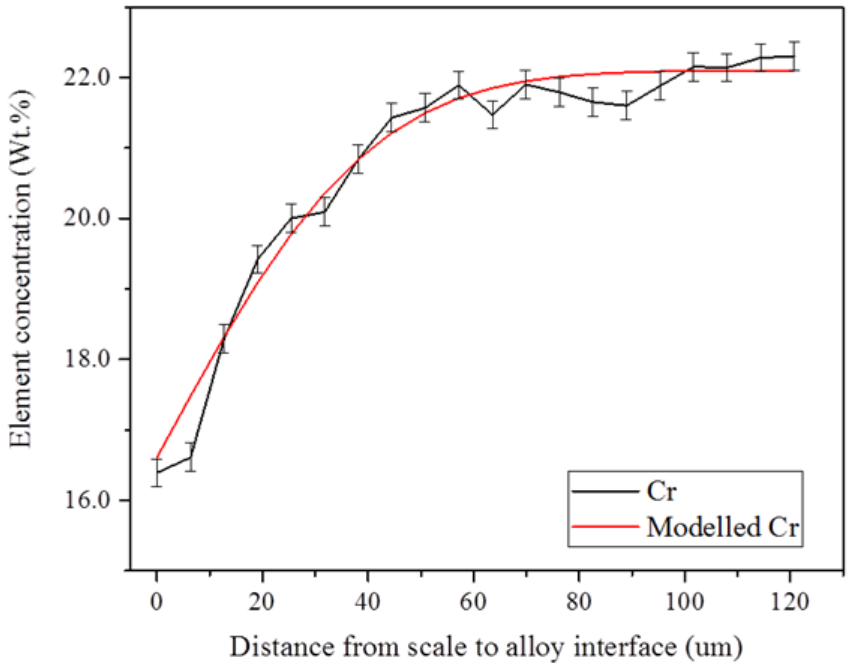

a

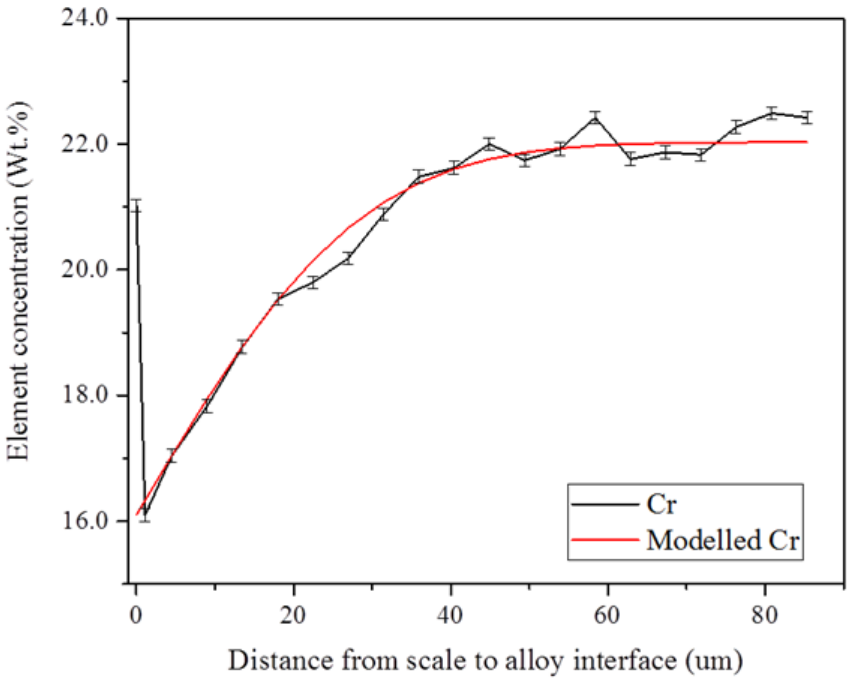

b

Figure 7.29: Modelled plot of Cr concentration (Wt. %) against distance from scale/alloy interface (µm) following 1000 hours of isothermal oxidation in laboratory air at 900°C (a) SLM-consolidated Haynes 230, and (b) Wrought Haynes 230

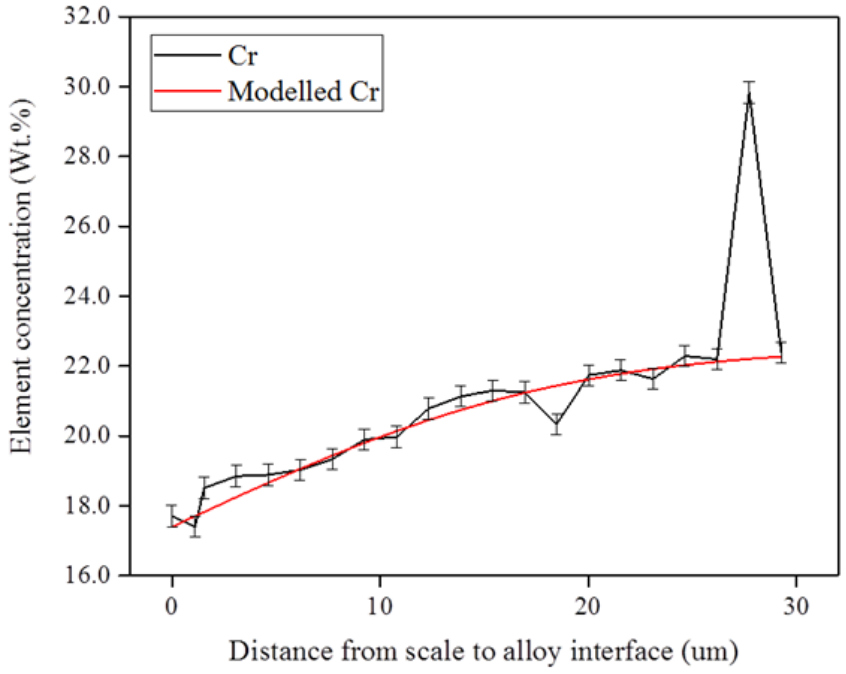

a

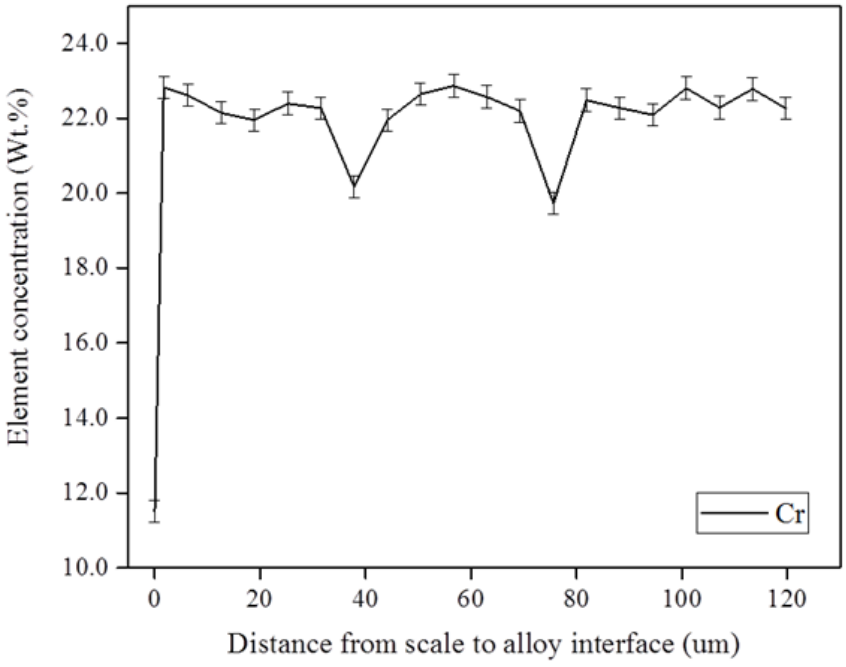

b

Figure 7.30: Plot of Cr concentration (Wt. %) against distance from scale/alloy interface (µm) following 1000 hours of isothermal oxidation in laboratory air at 900°C (a) Modelled Haynes 230 ODS/SLM, and (b) Haynes 230 ODS/SPS

7.3.5 Oxidation of carbides in wrought Haynes 230

During the oxidation of the wrought alloy, Cr-rich $M_{23}C_6$ developed around the M_6C carbides present in the bulk alloy, arrowed in Figures 7.31 (a) and 7.31 (b). Cr-rich $M_{23}C_6$ also developed along the grain boundaries of the alloy, an effect known as sensitisation, and which has been reported to occur in wrought Haynes 230 [265].

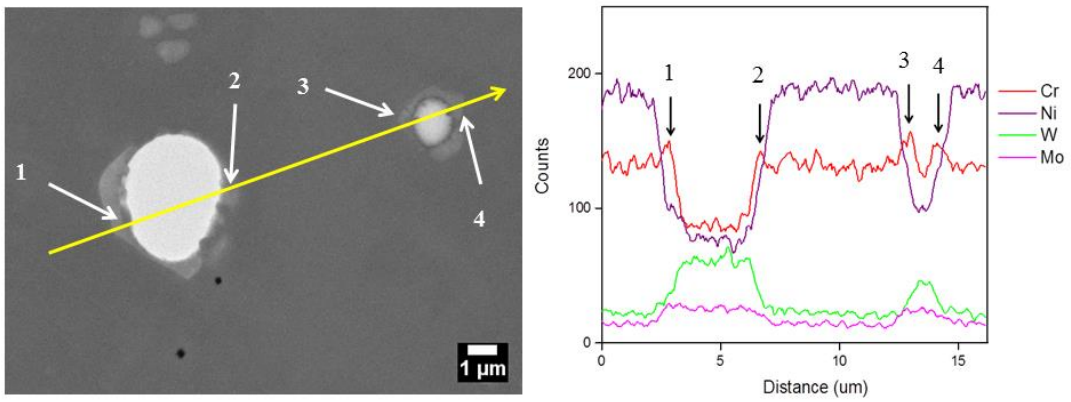

Figure 7.31: Bulk wrought Haynes 230 following 215 hours of isothermal oxidation in laboratory air at 900°C (a) Cr-rich $M_{23}C_6$ formed around M_6C carbides, and (b) linescan for principal elements obtained by traversing the yellow line shown in the micrograph

Where exposed to the atmosphere, either directly, or connected to the atmosphere via grain boundaries of the alloy, segregation occurred within the M_6C carbides in the form of a low average atomic number phase that formed on the grain boundaries. For carbides of similar size there was, with increasing oxidation time, a general increase in the ratio of the 'reacted' microstructure to the 'original' microstructure, Figure 7.32. Where not connected to the atmosphere, the M_6C carbides did not form any internal reaction product. Cr-rich $M_{23}C_6$, which was present around the M_6C carbides in the bulk alloy, appeared to be absent, or largely absent, from around the 'reacted' M_6C carbides at the surface of the alloy.

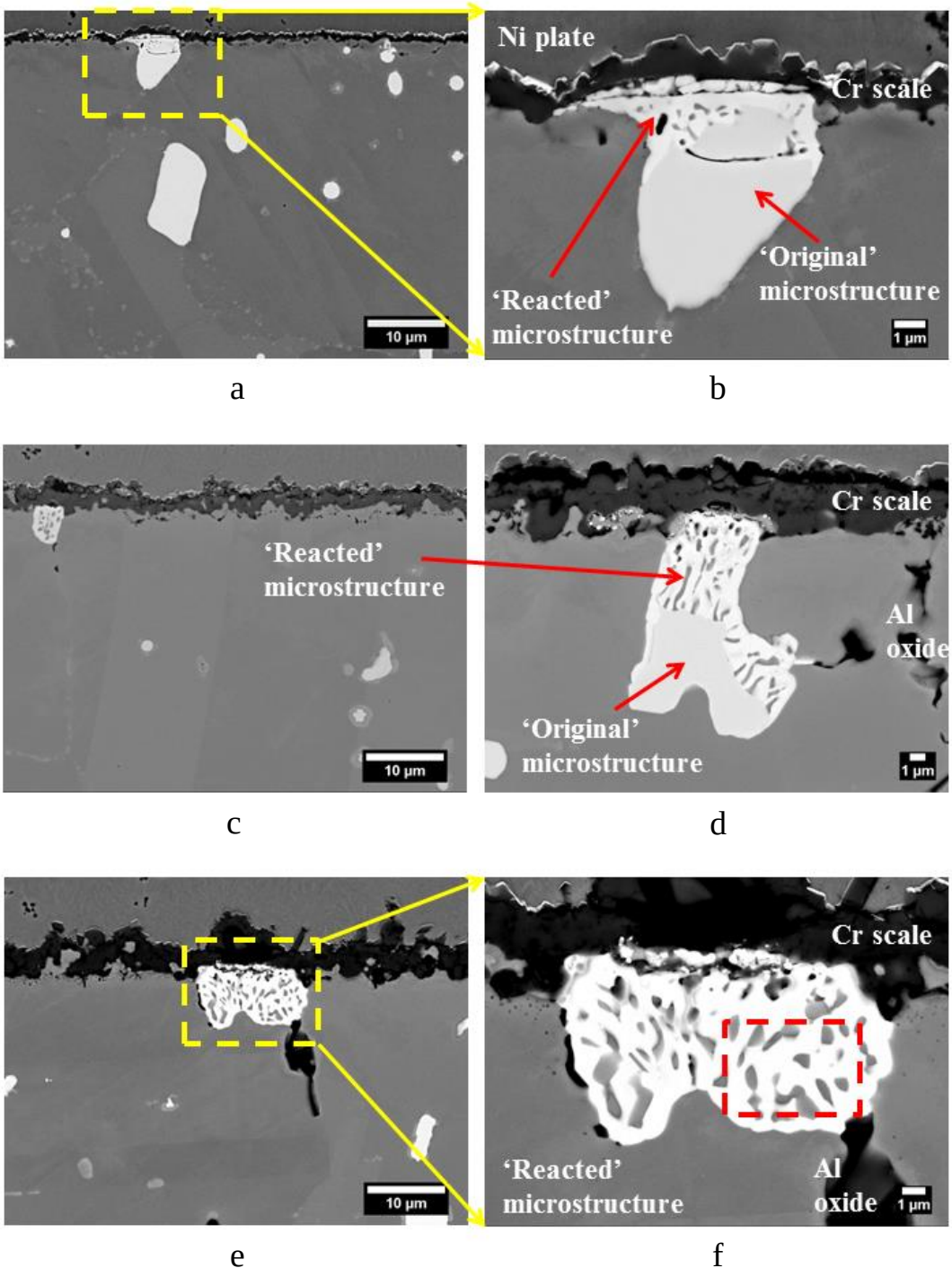

Figure 7.32: BSE micrographs of M_6C carbides at the surface of wrought Haynes 230 following of isothermal oxidation in laboratory air at 900°C (a), (b) 25 hours, (c), (d) 215 hours, and (e), (f) 1000 hours

The region highlighted in red in Figure 7.32 (f) is shown in more detail in Figure 7.33. Topographical relief is evident in Figure 7.33 (a), as a result of differential polishing, and reveals ridges corresponding to the grain boundaries of the inclusion. The low average atomic number phase appears to nucleate and grow at triple points. Variations in the intensity of the phase may indicate subtle differences in its composition, though the effect appears more likely to be due to charging, Figure 7.33 (b).

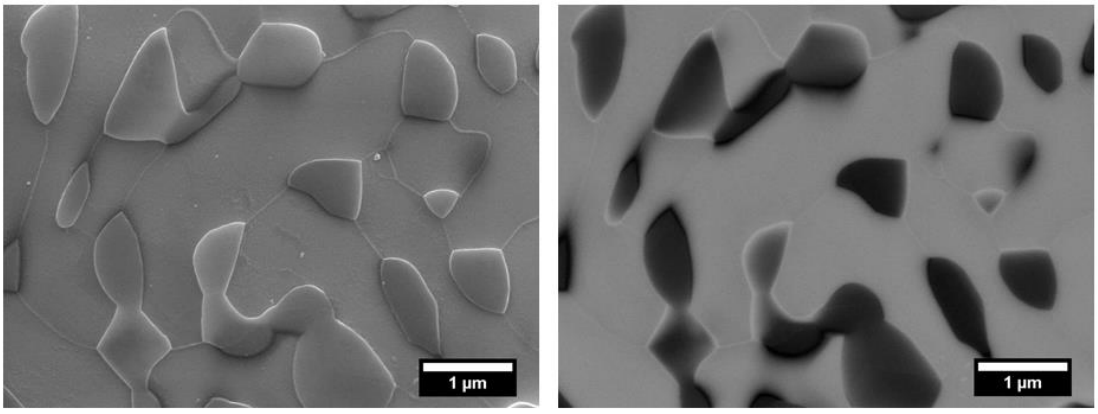

a b

Figure 7.33: SE and BSE micrographs of structure in M_6C inclusion at the surface of wrought Haynes 230 following 1000 hours of isothermal oxidation in laboratory air at 900°C

The inclusion shown in Figure 7.32 (d) is shown in more detail in Figure 7.34, and in elemental maps in Figure 7.35. The inclusion contains the elements W, Mo, Cr and Ni. The phase formed on the grain boundaries of the inclusion is rich in Cr and Ni. O is detected in the grain boundary phase where it is located near to the oxidised surface of the alloy, but not in the bulk inclusion. The region denoted 'original microstructure' in Figure 7.34 has a composition that approximates to $(W_{2.0}Ni_{2.3}Cr_{1.4}Mo_{0.2})C$, which is consistent with the composition of the carbides present in the alloy prior to oxidation. The region denoted 'original microstructure' is also of a lower average atomic number than the region denoted 'reacted microstructure' because it is, by comparison, Cr-rich but depleted in Ni and W. With

respect to the alloy, Cr is slightly depleted in the ‘original microstructure’ region but strongly depleted in the region denoted ‘reacted microstructure’, and Ni is strongly depleted in the region denoted ‘original microstructure’, but only slightly depleted in the region denoted ‘reacted microstructure’.

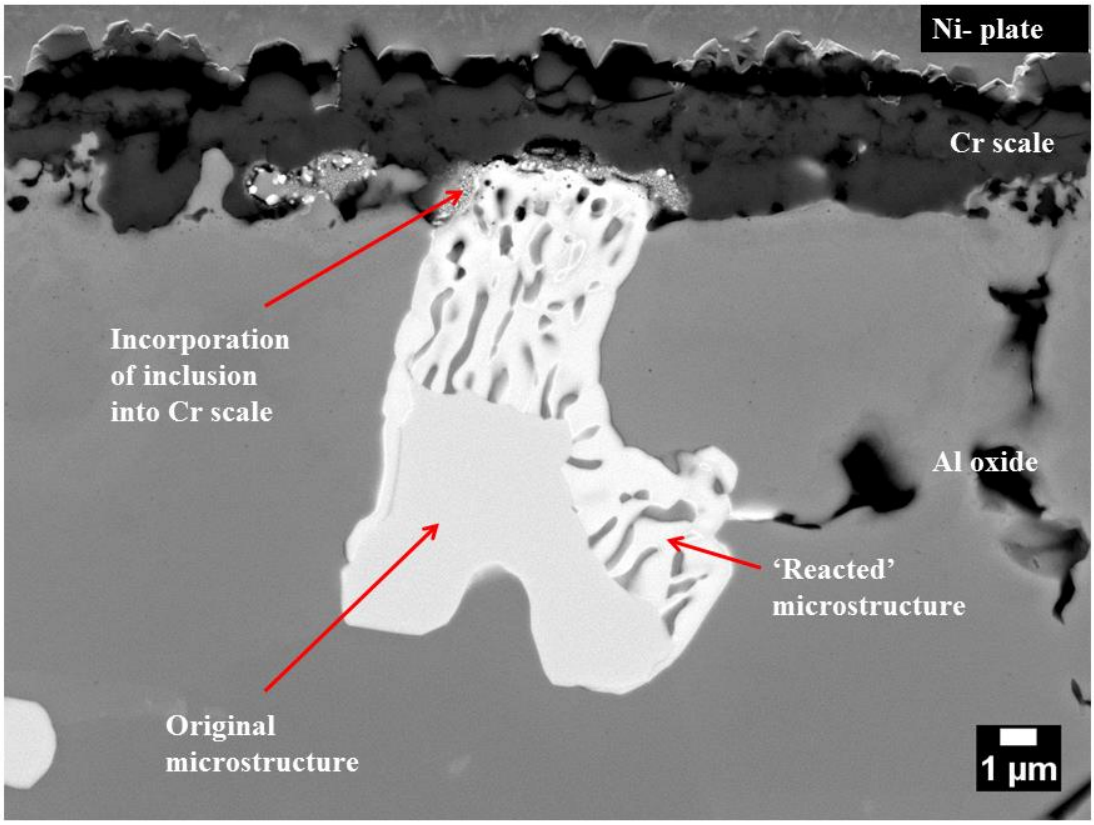

Figure 7.34: BSE micrograph of structure in M_6C inclusion at the surface of wrought Haynes 230 following 215 hours of isothermal oxidation in laboratory air at 900°C

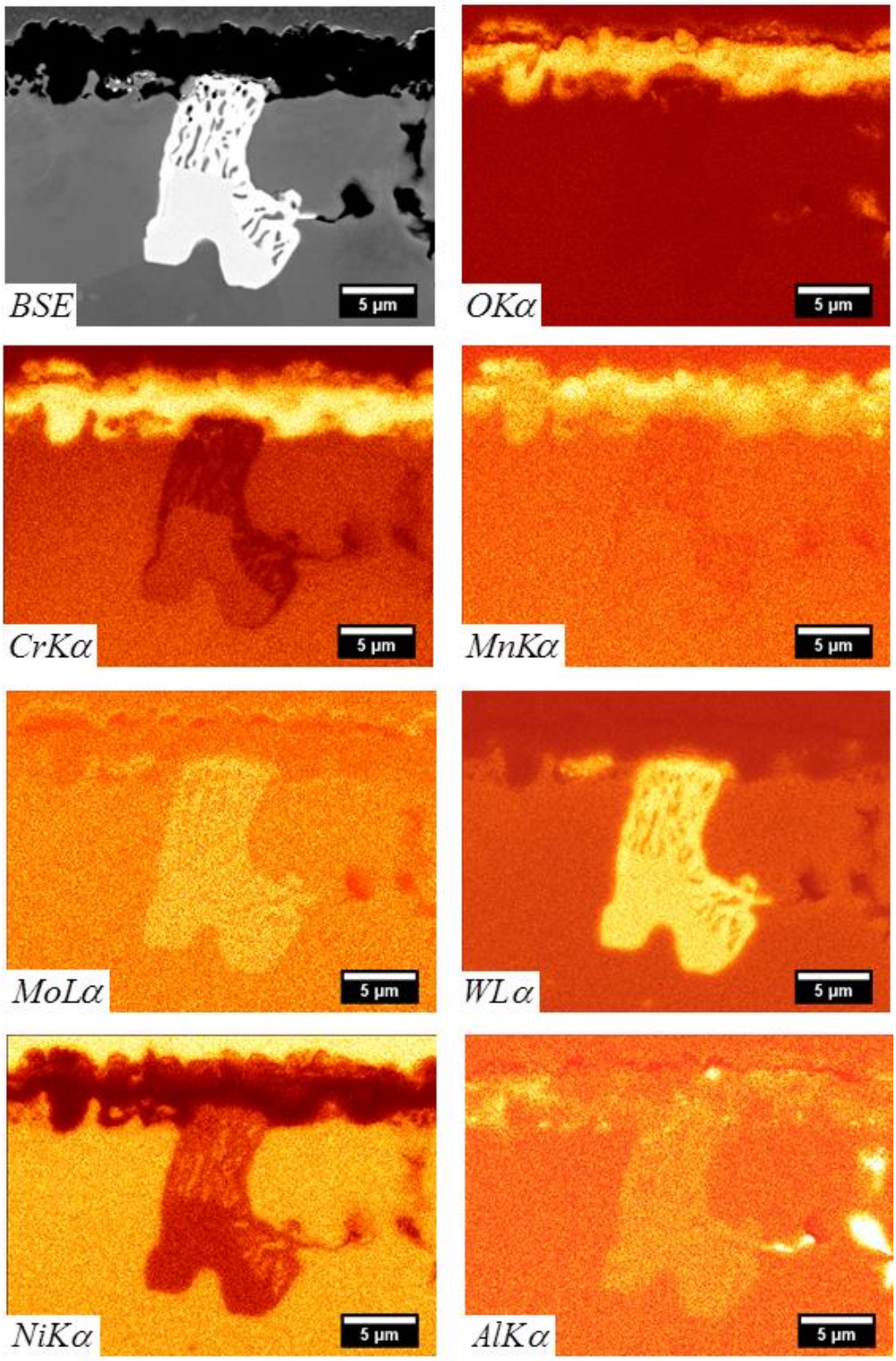

Figure 7.35: Element maps obtained from a cross-section of wrought Haynes 230 following 215 hours of isothermal oxidation in laboratory air at 900°C

7.4 Discussion

The results presented in this chapter have shown that Haynes 230, in both SLM-consolidated and wrought forms, oxidises to form a duplex scale comprising a chromia basal layer, and $Mn_xCr_{3-x}O_4$ spinel at the scale/gas interface. This has been reported in the open literature for Haynes 230 [180, 192-198]. Chromia scale is mainly expected to grow on Haynes 230 by the inward diffusion of O because of the reactive element effect, which largely blocks the outward diffusion of cations in the scale by interrupting grain boundary transport [23]. The appearance of the chromia scale formed on wrought Haynes 230 is consistent with inward growth, as expected, but the chromia scale grown on SLM-consolidated Haynes 230 appears to be consistent with inward and outward growth. This led to the formation of a thicker scale on SLM-consolidated Haynes 230, which is consistent with the faster oxidation kinetics reported in Chapter 4. It is probable that the difference in the oxidation behaviour of SLM-consolidated Haynes 230 and wrought Haynes 230 alloy is attributable to the lower initial concentration of La in the gas atomised powder i.e. 0.01 Wt. % as opposed to 0.016 Wt. % in the wrought alloy, and depletion of the reactive element addition during SLM-consolidation, which is observed in the form of surface slag and internal eutectic slag inclusions. Therefore, the loss of reactive elements from the alloy during consolidation by SLM is probably, at least in part, why the SLM-consolidated alloy oxidises faster than the wrought alloy.

Chromium interdiffusion coefficients were determined for SLM-consolidated Haynes 230 and wrought Haynes 230. The relationship was $D_{SLM} \approx 2D_{Wrought}$, which indicates that the dendritic/cellular microstructure of the SLM-consolidated alloy contributes to diffusion of Cr in the alloy. A Cr diffusion rate could not be determined for Haynes 230 ODS/SPS because it produced a flat depth profile. Analysis of the alloy at the centre of the oxidised coupon showed that the Cr concentration was slightly depleted with respect to that of the as-consolidated alloy, which is indicative of very fast rate diffusion in the alloy. This has been observed by

others for doped austenitic alloys [151]. The shape of the Al profile obtained for the alloy, Figure 7.28, is consistent with this observation, as it does not show a minimum c.f. the shape of the Al profiles in Figure 7.27. Fast diffusion in the alloy is consistent with the small grain size of the alloy, as observed in the present work, and which is often reported for SPS-consolidated alloys [75-79].

It was reported in Chapter 4 that Haynes 230 ODS/SPS oxidised rapidly. In this chapter it has been shown that a thick duplex scale comprising chromia at the scale/alloy interface and $Mn_xCr_{3-x}O_4$ spinel at the scale/gas interface forms during the oxidation of Haynes 230 ODS/SPS. Extensive internal oxidation occurred in the alloy, forming a semi-continuous layer of Al-rich oxide immediately under the scale, indicative of a large flux of O into the alloy. This is consistent with overdoping of the alloy [173, 174]. Haynes 230 ODS/SLM oxidised much more slowly than Haynes 230 ODS/SPS, even though they were consolidated from the same mechanically alloyed powder. The much improved oxidation rate, and scale morphology, is attributed to the 'slagging off' of excess reactive elements during consolidation by SLM. Voids, which formed at the scale/alloy interface during oxidation, may be Kirkendall voids, and caused decohesion of the scale at the scale/alloy interface, probably during cooling of the oxidised coupons to ambient temperature. Cavitation has been reported to occur in Ni as a result of the reaction between carbides and O [266, 267]. Carbides are numerous in Haynes 230 and may be responsible for void formation in Haynes 230 ODS/SPS, but Dyson reported that the effect is impossible in Ni-base superalloys when the O activity is controlled by the formation of Cr_2O_3 [268]. Kuenzly and Douglas reported significant void formation in a Ni_3Al alloy, and proposed that it occurred because the back diffusion of Ni, enriched at the surface of the alloy as a result of Al depletion, was faster than the outward diffusion of Al in the alloy [269]. However, it seems unlikely that the mechanism proposed by Kuenzly and Douglas is applicable to Haynes 230 ODS/SPS because of fast diffusion of Cr in the alloy, which means that the Cr depletion necessary for the creation of a driving force for the back diffusion of Ni probably never occurred.

An estimate of the weld pool temperature can be made by reference to the composition of the slag formed in SLM-consolidated Haynes 230. The slag present on the exterior surfaces of the SLM-consolidated blocks appeared to be La oxide, but eutectic inclusions rich in La, Ce, Al and O formed in the alloy. It should be noted that Ce was not reported in the data sheet that accompanied the gas atomised powder, but its presence suggests that the alloy from which the gas atomised powder was made had been doped with mischmetal [263]. Phase diagrams have been reported by several workers for the La_2O_3:$LaAlO_3$ system, either from experimental data, such as that reported by Bondar and Vinogradova [270], or from thermodynamic calculations [271]. While accepting that the SLM-consolidation process is a non-equilibrium system, and that the effect of Ce is not accounted for, it is considered reasonable that the phase diagram reported by Bondar and Vinogradova, Figure 7.36 (a), can be used as a guide to the likely solidification behaviour of the inclusions. At an Al concentration equivalent to that determined for the inclusions, which was typically ~10-15 Wt. %, a eutectic comprising La_2O_3 and $LaAlO_3$ (perovskite) is formed, which has a solidification temperature of ~1875°C. A continuous range of solid solutions are formed in the $LaAlO_3$-$CeAlO_3$ system, which solidify at a temperature of ~2100°C, Figure 7.36 (b) [272]. It is therefore possible that the inclusions may be a ternary eutectic comprising (La,Ce)AlO_3, $LaAlO_3$ and La_2O_3, but structural analysis using a STEM or TEM would be needed to confirm this. This indicates that the gas atomised powder may have been subjected to a temperature of ~2000°C during consolidation, which is ~600°C hotter than the melting point of Ni. Weld pool temperatures >2000°C have been estimated for the consolidation of 316L by SLM, using a laser power of 200W and a scan speed of $100mms^{-1}$ [273]. Boegelein modelled the temperature to be >2000°C for the interaction of a moving laser spot with a low carbon steel [245].

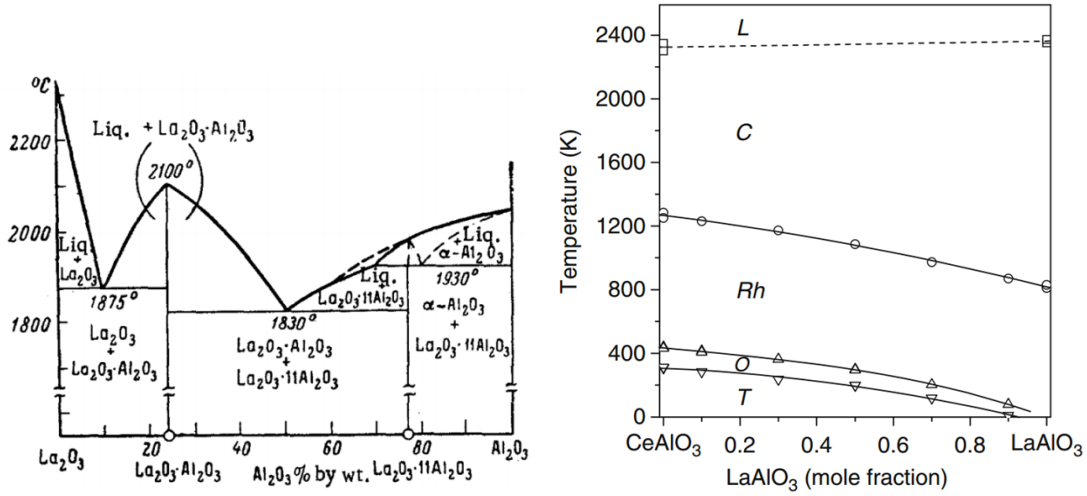

Figure 7.36: Phase equilibria for La_2O_3-Al_2O_3 [270], and $CeAlO_3$-$LaAlO_3$ systems [272]

Where connected to the atmosphere, either directly, or indirectly via the grain boundaries of the alloy, the M_6C carbides in the wrought alloy 'reacted' to form a low average atomic number phase on their grain boundaries, which was rich in Cr and Ni, Figures 7.32-7.35. The ratio of 'reacted' to 'original' regions, in carbides of similar size and present at the scale/alloy interface appeared to increase with oxidation time, which suggests that the 'reaction' process was under diffusion control. The behaviour reported here was also observed by Veverkova [115] during long term high-temperature ageing of bulk Haynes 230, but a mechanism for the effect was not proposed, Figure 7.37. A mechanism is proposed in Chapter 8 for the formation of the 'reacted' carbides.

The M_6C carbides in Haynes 230 SLM appeared stable, and did not 'react' even when directly exposed to the atmosphere. The inclusions in Haynes 230 ODS/SLM were observed to precipitate as acicular inclusions in the alloy, then dissolve in the Cr-depleted zone immediately under the scale and re-precipitate as blocky inclusions at the scale/alloy interface. Similar behaviour has been reported in the cobalt base alloy Haynes 25, which has been reported to form a layer of Co_3W at the scale/alloy interface during oxidation at temperatures between 700°C and 800°C. The

mechanism for M_6C dissolution is believed to be increased C activity in the Cr-depleted region of the alloy, which results in the back-diffusion of C [116, 183, 274]. Precipitation may occur at the scale/alloy interface because the chemical potential is minimised at the scale/alloy interface [105].

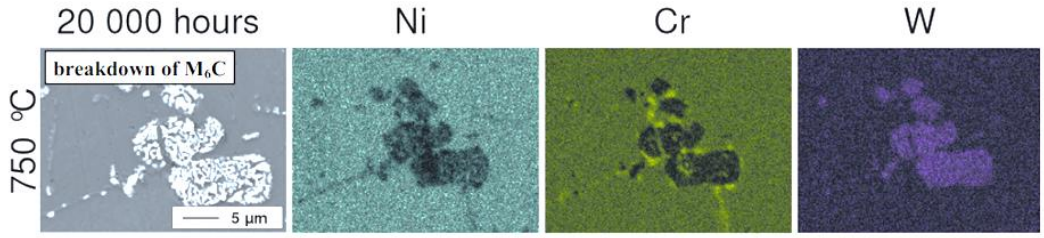

Figure 7.37: 'Breakdown' of M_6C carbides in bulk Haynes 230 following 20000 hours of exposure to 750°C [115]

7.5 Chapter summary

The present work has shown that SLM-consolidated Haynes 230 oxidises more quickly than wrought Haynes 230 because of 'slagging off' of the reactive elements during consolidation, which changes the chromia formation mechanism from one almost completely dominated by the inward diffusion of O, to one that, though still dominated by the inward diffusion of O, oxidises also by the outward diffusion of Cr. Analysis of the slag formed in the SLM-consolidated alloy indicates that the gas atomised powder may have been heated to ~2000°C during consolidation, which is ~600°C above the melting point of Ni, and means that the build parameters probably need modification to improve the retention of reactive elements in SLM-consolidated builds.

Haynes 230 ODS/SPS formed a thick duplex scale, comprising a basal layer of chromia and a layer of $Mn_xCr_{3-x}O_4$ spinel at the scale/gas interface. Extensive internal oxidation, indicative of a large O flux, possibly transported by O vacancies in the scale, led to the formation of a semi-continuous layer of Al-rich oxide in the oxidation-affected zone of the alloy. Void formation also occurred in the oxidation-

affected zone of the alloy, including at the scale/alloy interface. These may be Kirkendall voids, or possibly the result of cavitation caused by a reaction between O from the atmosphere and carbides in the alloy, which has been observed to occur in Ni. The scale locally detached from the alloy, giving it a rumpled appearance. It is probable that Haynes 230 ODS/SPS was consolidated from a mechanically alloyed powder that was overdoped with reactive elements, which led to the observed fast rate of oxidation and poor scale morphology. Haynes 230 ODS/SLM, which was consolidated from the same mechanically alloyed powder as Haynes 230 ODS/SPS, produced an alloy that oxidised much more slowly, and formed a more protective scale. This is attributed to a greater concentration of reactive elements in the sintered alloy, which occurs because of 'slagging off' of the excess reactive elements during SLM-consolidation of the mechanically alloyed powder. Far less spinel formed on Haynes 230 ODS/SLM than formed on Haynes 230 ODS/SPS, which may be consistent with enhanced cation diffusion in Haynes 230 ODS/SPS, as interstitials, as a result of overdoping. M_6C-type carbides, rich in W and Mo, and present in the wrought alloy, and connected to the gas atmosphere, formed low average atomic number 'particles' on the grain boundaries. The carbides present in the SLM-consolidated and SPS-consolidated alloy did not 'react', even when directly exposed to the atmosphere, which is probably due to differences in the composition of the carbides, though this was not investigated in the present work. This subject is discussed in more detail in Chapter 8.

In summary, the work has shown that Haynes 230 ODS/SPS was probably overdoped with reactive elements, which increased the rate of oxidation of the alloy, as shown in Chapter 4, and caused the alloy to form a thick duplex scale, with extensive internal oxide formation and void formation. The oxidation behaviour of Haynes 230 ODS/SLM, consolidated from the same MA powder, was much improved as a result of 'slagging off' of excess reactive elements from the alloy. However, in the case of SLM-consolidated Haynes 230, which is appropriately doped with reactive elements, 'slagging off' reduced the oxidation resistance of the alloy.

CHAPTER 8

DISCUSSION AND CONCLUSIONS

8.1 Introduction

The results obtained during the course of the present work are discussed in sections 8.2, base alloys, and 8.3, ODS alloys. Conclusions are provided in section 8.4.

8.2 Base alloys

Alloys

The SLM-consolidated alloys, Alloy 718, Alloy 625 and Haynes 230, had a columnar grain structure orientated in the build direction of the alloy comprised of dendritic/cellular substructures of <1μm in size. These observations have been widely reported for SLM-consolidated Alloy 718 and SLM-consolidated Alloy 625 [97-101, 107, 108], but there are no results in the open literature for SLM-consolidated Haynes 230. As-consolidated Haynes 230 was free of inclusions, but many submicron carbides were precipitated in the alloy during heat-treatment at 1200°C. Slightly larger carbides formed at the grain boundaries of the alloy as a result of ripening. The carbides were rich in W and Mo, and are thought to be M_6C type carbides, as expected for Haynes 230 [110-114]. The microstructure of SLM-consolidated Haynes 230 was not modified during the heat-treatment and the hardness values were 215±10HVN0.5 for the annealed wrought alloy, 300±10HVN0.5 for the SLM-consolidated alloy in the as-consolidated condition, and 275±7HVN0.5 for the SLM-consolidated alloy in the heat-treated condition. Alloy 718 and Alloy 625 were also harder in the SLM-consolidated form than in the wrought form, and their microstructures could only be partially modified during heat-treatments at temperatures of 954°C and 1038°C respectively. The greater

hardness of the SLM-consolidated alloys is probably due to greater grain refinement [11, 107]. A number of workers have found that the microstructure of SLM-consolidated Alloy 718 can only be modified at temperatures of ~1100°C [97-101], which is consistent with the present work.

Absence of inclusions from SLM-consolidated Alloy 718 and Alloy 625

SLM-consolidated Alloy 718 and SLM-consolidated Alloy 625 were essentially free of inclusions, an effect that has been reported by other workers [107, 108]. The wrought alloys contained numerous NbC carbides in stringers aligned parallel to the extrusion direction of the alloys. The solidification sequence for Alloy 718 and Alloy 625 is very similar, and is in the order $L \rightarrow \gamma$, $L \rightarrow (\gamma + NbC)$ eutectic, $L \rightarrow (\gamma + Laves)$ eutectic [89, 90]. High C/Nb compositions promote the formation of NbC at the expense of Laves phase [91, 96]. The C/Nb ratio for SLM-consolidated Alloy 718 was ~2x that of wrought Alloy 718, while the C/Nb ratio for SLM-consolidated Alloy 625 was ~0.5x that of wrought Alloy 625. Therefore, more NbC carbides might be expected in SLM-consolidated Alloy 718 than in wrought Alloy 718, and less carbides in SLM-consolidated Alloy 625 than in wrought Alloy 625. However, both of the SLM-consolidated alloys formed significant amounts of Laves phase, but very few carbides. While it seems likely that the fast cooling rates associated with SLM-consolidation inhibits the formation of carbides, possibly by preventing growth, the observation that carbides do not develop during post-build heat-treatment suggests that nucleation of the carbides had not occurred during SLM-consolidation. It is possible that C was lost, or partially lost, from the alloys during SLM-consolidation, promoting Laves phase formation. SLM-consolidated Haynes 230 was, in the as-consolidated condition, also free of carbides, but during annealing at 1200°C a large number of submicron inclusions, containing W and Mo, and probably M_6C type carbides, formed in the alloy. This shows that the carbides had nucleated during SLM-consolidation, but had not grown, which may be due to the slow diffusivity of W in Ni-base alloys [111].

Oxidation of Alloy 718

SLM-consolidated Alloy 718 oxidised approximately 20% faster than wrought Alloy 718, Table 8.1. The scale formed on the SLM-consolidated alloy appeared slightly finer grained and more columnar than that which formed on the wrought alloy, which may explain the difference in oxidation rate. The relationship between the chromium interdiffusion coefficients (D), determined for the two variants of the alloy from Cr depletion profiles obtained following 1000 hours of oxidation, was $D_{SLM} \approx 2D_{Wrought}$. This may be expected because of the dendritic/cellular substructure of the SLM-consolidated alloy. However, it was noted that scale formed thickly over the grain boundaries of the SLM-consolidated alloy, but not over the grain boundaries of the wrought alloy prepared in the same way prior to oxidation i.e. Cr diffusion is probably less homogeneous in the SLM-consolidated alloy than it is in the wrought alloy, possibly because the SLM-consolidated alloy contains more high angle boundaries than in the wrought alloy [246].

Oxidation of Alloy 625

The scale formed on SLM-consolidated alloy was wrinkled, and comprised of a thin scale comprised of relatively large grains and fine grain 'knots' located every 20-50μm along the length of the scale/alloy interface. The fine grain 'knots' may have developed as the result of an increase in the nucleation rate of the grains, or due to pinning of the grain boundaries, by 10-20nm size spheroidal particles of δ-phase that were incorporated into the scale from the layer of δ-phase present at the scale/alloy interface. The wrought alloy formed a duplex scale, comprising large basal grains and fine grains at the scale/gas interface, which may be consistent with counter-current diffusion, which is reported to generate large growth stresses and produce wrinkling [254-256]. The growth stresses were accommodated by plastic deformation of the alloy, and possibly by creep with in the oxide scale. There was no

evidence of cracking in the scale. Particles of δ-phase were incorporated into the sale, but did not appear to alter the scale morphology.

The SLM-consolidated alloy oxidised at ~0.5x the rate of the wrought alloy, Table 8.1, which is consistent with the microscopy results. A relationship of $D_{SLM} \approx 1.2 D_{Wrought}$ was determined for Cr interdiffusion, which means that the SLM-consolidated alloy may selectively oxidise more quickly than the wrought alloy. Examination of 625 ODS/SLM and Alloy 625 ODS/SPS, by STEM, has shown that Nb-rich oxide particles were present in the scales, which are thought to be first-formed oxides. Nb-rich oxides can be porous and poorly protective, and Nb has been found to increase the oxidation rate of ferritic steels in oxidation experiments conducted in air at temperatures of 800 and 900°C, which was thought to be due to doping of the scale [261]. It is possible that faster selective oxidation in SLM-consolidated Alloy 625, compared to wrought Alloy 625, is better able suppress Nb oxide formation and its incorporation into the chromia scale during transient oxidation.

SLM-consolidated Alloy 625 has a propensity for void formation, may be Kirkendall voids. It is reported that alloys consolidated by rapid solidification contain more vacancies than alloys consolidated by conventional means [250, 251, 262], which may mean that SLM-consolidated alloys form Kirkendall voids more quickly than wrought alloys because of the higher initial vacancy concentration in the alloy. However, one might reasonably expect the same behaviour in Alloy 718 and Haynes 230, which was not observed.

Oxidation of Haynes 230

The scale formed on Haynes 230 was mainly comprised of Cr_2O_3, with $Mn_xCr_{3-x}O_4$ spinel present at the scale/gas interface. The spinel became increasingly prominent during the course of the oxidation of the alloy, indicating that its relative rate of formation increases with time. The SLM-consolidated alloy oxidised ~3x faster than

the wrought alloy, Table 8.1. The mechanism for scale formation is shown in the schematic, Figure 8.1, which shows that the SLM-consolidated alloy forms scale as a result of inward (I) and outward (O) growth of chromia, whereas the wrought alloy forms chromia scale by inward (I) growth, as expected for an alloy doped with reactive elements [23, 162, 163].

The results obtained from SLM-consolidated Haynes 230 are probably best explained as a reduction in the reactive element effect, which arises from a lower initial La concentration in the alloy, and losses due to 'slagging off' during consolidation. This resulted in La-rich oxide forming on the surface of the alloy blocks, and in the blocks at the interface between the layers of the build. This implies that La had floated to the top of the weld pools during consolidation, as observed to occur for Y during TIG welding [44]. Interestingly, the particles of perovskite slag in the alloy also contained Ce, which suggests that the ingot from which the gas atomised powder was produced had been doped using mischmetal. By reference to the La_2O_3-Al_2O_3 phase diagram it is estimated that the alloy was probably exposed to a temperature ≥1900°C, as the perovskite eutectic solidifies at ~1875 °C [270], which is ~600°C hotter than the melting point of Ni. The estimation of the temperature reached in the melt pool during SLM-consolidation is consistent with the literature, which reports that temperatures >2000°C can be reached during the SLM-consolidation of 316L steel [273]. The results obtained from SLM-consolidated Haynes 230 therefore show that there is scope to optimise SLM-consolidation parameters in order to reduce the weld pool temperature. Haynes 230 typically has a composition that contains ~0.02 Wt. La [110], but the 'preferred' range for the La addition is 0.005-0.05 [206].

The gas atomised powder studied for the present work contained 0.01 Wt. % La, which is at the lower end of the preferred concentration range. Given that La will be lost, or otherwise tied-up, during consolidation by SLM, gas atomised powders at the top end of the permissible concentration range should be used for SLM-consolidation.

There is little information to be had in the open literature regarding the minimum concentration of La necessary for improved oxidation resistance. Some papers do discuss the effect of low level La additions, usually in combination with Y additions, on the oxidation resistance of single crystal superalloys for turbine blade applications, but the findings are unclear. In one paper, by Ford et al, it was found that the addition of 10-30ppm La improved the oxidation resistance of CMSX-4 by ~15x [275]. However, in a separate piece of work, low ppm Y and La additions appeared to have no measureable effect on the oxidation behaviour of CMSX-4 [276, 277], while an improvement in oxidation behaviour was reported for CMSX-4 following co-doping with low concentrations of La, Y and Hf [278]. Pang et al found that 65 and 300ppm additions of La + Y led to the formation of Ni-Y and Ni-La eutectics [279].

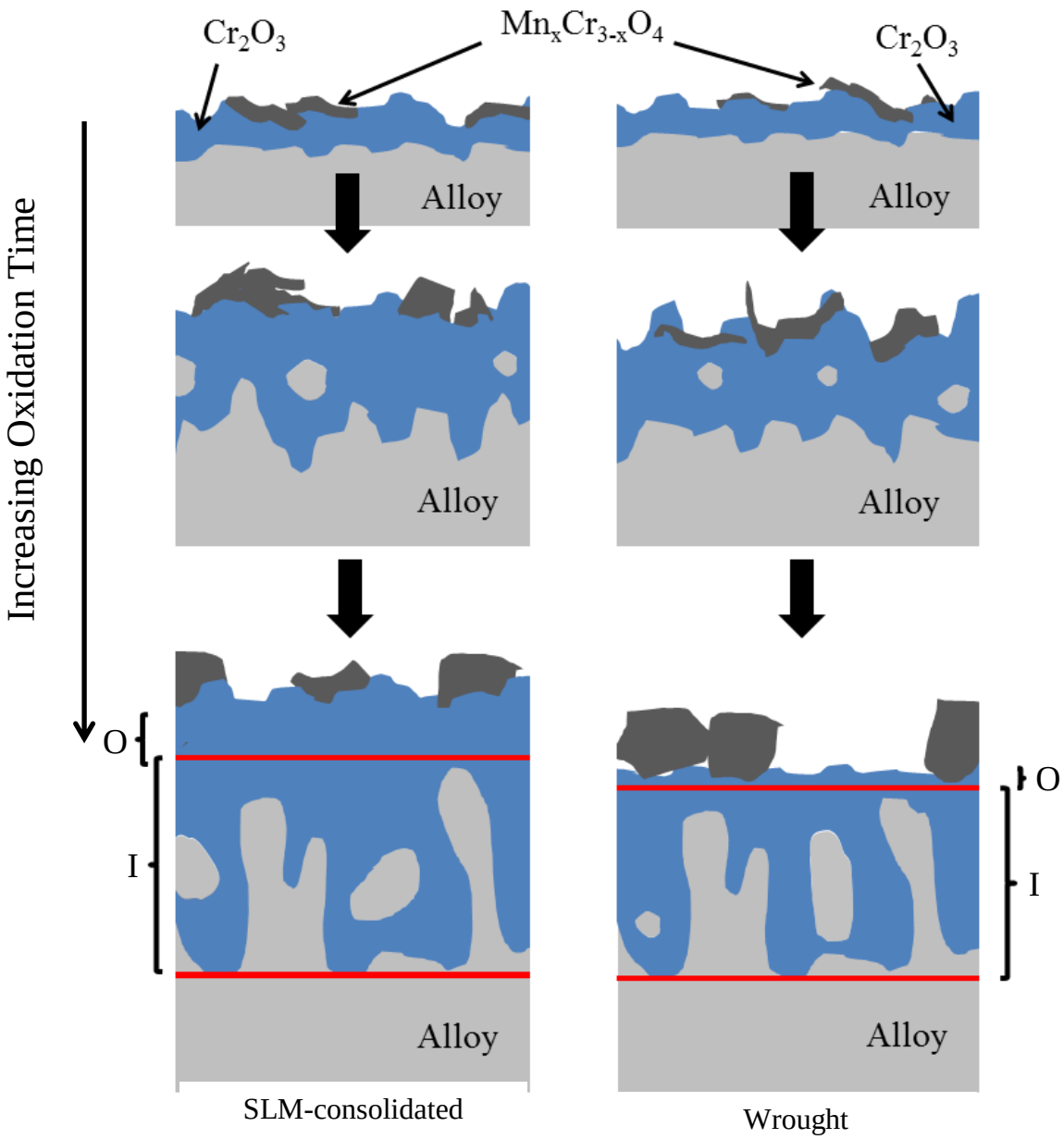

Figure 8.1: Schematic showing scale formation on SLM-consolidated and wrought Haynes 230 following 25, 215 and 1000 hours of isothermal oxidation in laboratory air at 900°C

Isotropic oxidation behaviour of SLM-consolidated base alloys

The oxidation rate constants were determined for the SLM-consolidated alloys from sections cut parallel to their build direction, but a single specimen of each alloy type, cut perpendicular to the build direction, was also oxidised for 215 hours in laboratory air at 900°C. Scale thickness measurements obtained from these specimens, using a FIB, and which are not presented in the thesis, indicated that the alloys had oxidised approximately isotropically, despite the anisotropic grain structure. More work is needed to validate this initial observation.

Oxidation of carbides in wrought Alloy 718

SLM-consolidated Alloy 718 was essentially inclusion-free, but wrought Alloy 718 contained a large number of carbides, which had a composition rich in Nb and Ti, and are believed to be Ti-substituted NbC carbides. It was observed that the carbides are readily oxidised, with some oxidised carbides appearing to grow significantly above the plane of the surface of the alloy, while others remained largely in the plane of the surface of the alloy. The oxidation of NbC carbides in Ni-base alloys has been studied by a number of workers, including Connolley, who reported that cracks were initiated directly at oxidised NbC carbides during LCF testing of forged Alloy 718 at 600°C [240], while crack growth in Ni-base superalloys that contain Nb has been attributed to the formation of brittle Nb_2O_5 ahead of the crack tip as a result of the thermal decomposition of NbC carbides on the grain boundaries of the alloy [280, 281]. Litz et al presented results obtained from the oxidation of MC carbides in IN 738LC and IN 939, in which they described how shear strain caused by the volume expansion of MC carbides can lead to cracking in the scale around the carbides allowing aggressive components to enter the alloy and cause internal corrosion [239]. The process was also studied by Hong et al [282].

As a result of the present work, a more detailed description of the mechanism can be provided for an oxidised inclusion that remains essentially in the plane of the surface

of the alloy. This is shown schematically in Figure 8.2. The inclusion initially oxidises to form Nb-rich oxides, probably mainly Nb_2O_5 [253]. This results in a significant increase in the volume of the inclusion; Connolley estimated that the volume of crystalline Nb_2O_5 was ~1.96x that of NbC [240]. The increase in the volume of the inclusion arising from its oxidation causes it to expand upwards and also laterally, Figure 8.2 (a). This exerts compressive stresses on the adjacent alloy and scale, resulting in plastic deformation of the alloy and spalling of the scale, Figure 8.2 (b). Spalling of the scale produces a loosely adhered, porous scale, Figure 8.2 (c). The scale subsequently re-grows on the exposed alloy, Figure 8.2 (d). The alloy may locally go into 'breakaway' during the oxidation of the carbides, as evidenced by the presence of Fe oxides in the scale that formed over the examined oxidised carbide. The re-formed scale is Cr-rich oxide, but Nb-rich oxides may enter it. The oxidised carbides act as conduits for O ingress into the alloy and may allow internal oxides to form at greater depths than would otherwise be the case.

Porous scale was not observed in any specimen at oxidation times >25 hours, presumably because it was replaced by re-grown, compact scale. This also means that spalling of the scale probably did not occur at oxidation times >25 hours. It can therefore be inferred that the carbides are fully oxidised during the first 25 hours of oxidation, and that at longer oxidation times they are stable and do not generate strain in the scale adjacent to them.

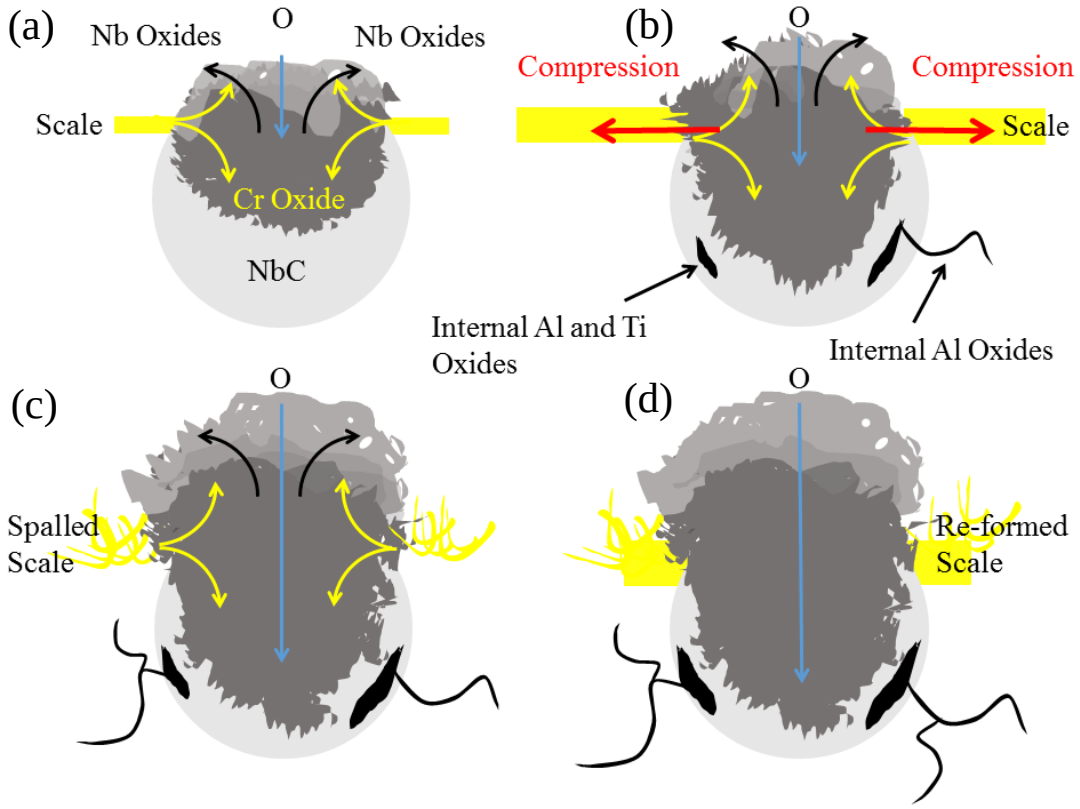

Figure 8.2: Oxidation of a NbC carbide exposed at the surface of wrought Alloy 718 during the first 25 hours of isothermal oxidation in laboratory air at 900°C

Oxidation of carbides in Haynes 230

During oxidation, Cr-rich $M_{23}C_6$ was observed to form around the M_6C carbides present in the wrought alloy. This is reported to occur in Haynes 230 at 800-900°C, forming $M_{23}C_6$ [283]. The reaction is usually expressed in the form [284]:

$$M_6C + M^1 \rightarrow M_{23}C_6 + M^2$$

where M^1 is typically Cr, and M^2 is alloy-dependent, but may include W, Ni, Cr and Mo

M_6C carbides were located near to the surface of the alloy, which when exposed to the gas atmosphere formed sinuous ‘particles’ of low average atomic number on their grain boundaries. The mechanism proposed for the formation of the reacted carbides is shown in the schematic, Figure 8.3. It should be noted that the direction z in the schematic is the extrusion direction of the round bar from which the specimens were cut. The process begins with oxidation at the exposed surface of the carbide, which precipitates Cr oxides on the grain boundaries of the carbide. At the same time, Cr-rich $M_{23}C_6$ forms all around the surface of the carbide at the carbide/alloy interface by the reaction shown above, but dissolves in the alloy in the oxidation-affected zone of the alloy, which is Cr depleted, but not below the oxidation-affected zone of the alloy. Cr and C diffuse out of the oxidised region of the carbide and into the alloy, and are probably replaced by Ni, which diffuses in from the Ni-rich alloy in the oxidation-affected zone of the alloy. Diffusion of the reacting species occurs by transport along the grain boundaries of the carbide, and in the oxidised region of the alloy the surfaces of the carbides assume a scalloped appearance. The process is one of decarburisation of the carbides, which increases with time as O penetrates deeper into the carbides. Al-rich oxides may form in the decarburised regions of the carbides, but only near to the gas atmosphere. The grain boundary ‘particles’, except for the Cr-rich oxides near to the atmosphere, may be remnants of stable carbide, possibly $M_{23}C_6$. The proposed mechanism is consistent with work done on the Ni-base alloys IN738 and GTD-111, which showed that the thermal decomposition of MC-type carbides, present in the bulk alloy, occurred as a result of outward diffusion of C, forming Cr-rich $M_{23}C_6$, which was accompanied by the inward diffusion of Ni [285]. Haynes 230 has been studied at high temperatures in impure He environments [286-289], with micrographs presented in one paper showing that M_6C carbides located at <5µm from the scale/alloy interface did not contain, after 813 hours at 950°C, the low average atomic number ‘particles’ observed in the present work [288]. This confirms the observation that O is required to form the ‘particles’ on the grain boundaries of the decarburized carbides. The behaviour reported here was observed by Veverkova during long term high temperature ageing of bulk Haynes

230, Figure 7.37 [115]. It is probable that the carbides observed in Veverkova's study were also decarburised as a result of trace levels of O present in the bulk alloy, demonstrating that the process can occur at low O activities.

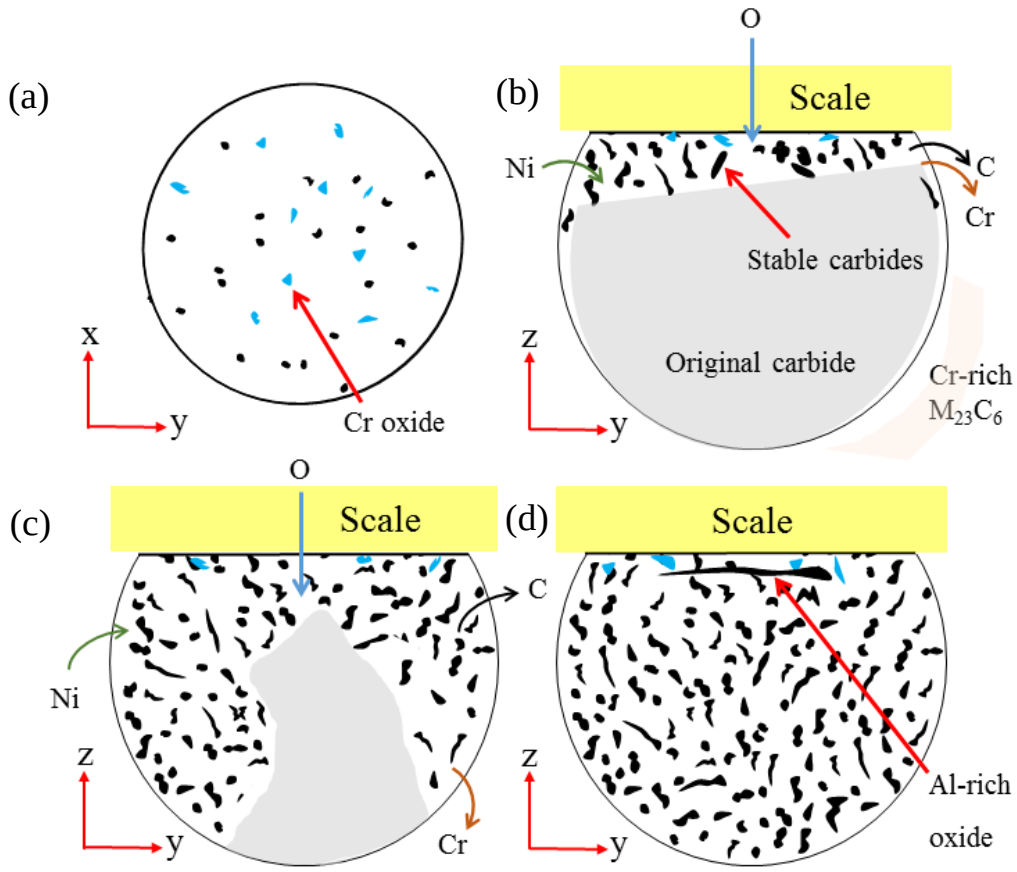

Figure 8.3: Schematic showing decarburisation of a M_6C carbide exposed at the surface of wrought Haynes 230 during isothermal oxidation in laboratory air at 900°C

8.3 ODS alloys

Alloys

Slag, pores and cracks were evident in Alloy 625 ODS/SLM and, to a lesser extent, Haynes 230 ODS/SLM. The microstructure of the alloys is consistent with literature

results for SLM-consolidated ODS alloys [66-69] and with the appearance of the SLM-consolidated base alloys, being comprised of columnar grains orientated in the build direction and dendritic/cellular substructures of <1µm in size. A high average atomic number phase was present on the grain and dendrite/cell boundaries of the alloys, which was Nb-rich in Alloy 625 ODS/SLM, but rich in W and Mo in Haynes 230 ODS/SLM. These were probably carbide phases, as they proved more stable than Laves phase/δ-phase during oxidation.

Alloy 625 ODS/SPS and Haynes 230 ODS/SPS had a bimodal distribution of submicron grains, with the regions of smaller grains populated by a mixture of inclusions of <0.2µm in size. The inclusions appeared to have restricted grain growth. Similar microstructures are widely reported for ODS alloys consolidated by SPS [75-79]. The inclusions present in Alloy 625 ODS/SPS appeared to be a mixture of Cr-rich oxides and Nb-rich carbides, while those in Haynes 230 ODS/SPS were rich in W and Mo, and were assumed to be M_6C-type carbides. The alloys were porous, especially Alloy 625 ODS/SPS, but not obviously cracked. The porosity may be related to the fast heating rate used to consolidate the specimens, which has been reported to cause porosity in SPS-consolidated alloys [83-85].

The cracking observed to occur in Alloy 625 ODS/SLM and Haynes 230 ODS/SLM may be related to solidification cracking, caused by a combination of SLM-consolidation and the reactive element addition. This can be inferred by an absence of cracking in Alloy 625 SLM, Alloy 625 ODS/SPS, Haynes 230 SLM and Haynes 230 ODS/SPS. The cracks are likely to arise as a result of stresses generated during rapid cooling of the SLM-consolidated alloys, possibly combined with carbide films present on the grain boundaries of the alloys. These probably arise as a result of C contamination of the powders during MA, meaning that cracking is probably not caused per se by the reactive element addition.

Oxidation of Alloy 625ODS

Alloy 625 ODS/SLM and Alloy 625 ODS/SPS formed very thin chromia scales, which appeared to grow mainly by the inward diffusion of O. This is consistent with the reactive element effect, which is generally believed to occur as a result of 'blocking' of the outward diffusion of cations due to the segregation of reactive elements to the grain boundaries of the scale [23, 163]. This has been observed experimentally [169-171]. However, attempts to confirm this behaviour in Alloy 625 ODS proved unsuccessful, with the only evidence of Y in the scales being restricted to a few particles found at the scale/alloy interface of Alloy 625 ODS/SPS. A band of oxidised Nb-rich oxide particles, which are believed to be some of the first formed oxides, was present, with voids, in the scales formed on both the SLM-consolidated alloy and the SPS-consolidated alloy. The band appeared to indicate the position of the surface of the coupons prior to oxidation. Voids, thought to be Kirkendall voids, formed in Alloy 625 ODS/SLM.

The oxidation rate constants determined for Alloy 625 ODS/SLM and Alloy 625 ODS/SPS are produced in Table 8.1. The results show that Alloy 625 ODS oxidised >10x slower than Alloy 625, which is attributed to the beneficial effect of the reactive element addition. Alloy 625 ODS oxidised even more slowly than MA754, a legacy commercial Ni-base ODS alloy. This is slightly surprising given the complexity of Alloy 625 and the possibility of interplay between the different elements in the alloy. The results also appear to show that the Alloy 625 ODS/SLM oxidised more slowly than Alloy 625 ODS/SPS, but caution is needed with respect to k_p values because of the very small size over which scale thickness measurements are taken. It is probably prudent to assume that Alloy 625 ODS/SLM and Alloy 625 ODS/SPS oxidised at approximately the same rate. This appears to show that the alloy is tolerant of reactive elements additions, perhaps because Nb reacts to form stable oxides with Y, as shown in the elemental maps obtained from Alloy 625 ODS/SLM. Alloy 625 Hf-ODS/SPS oxidised at the same rate as Alloy 625 ODS

despite being doped with a 1.0 Wt. % reactive element addition, as opposed to a 0.5 Wt. % reactive element addition for Alloy 625 ODS. It is possible that Hf was tied up as carbides, possibly as a result of carbon contamination from the MA process or during SPS-consolidation.

It is worth noting that the Cr depletion profiles could not be fitted for Alloy 625 ODS/SLM, which produced a noisy profile, or Alloy 625 ODS/SPS, which displayed a completely flat depth profile. This can be explained by fast Cr diffusion in the SPS-consolidated alloy, which has a very small grain size, so that Cr was able to rapidly diffuse from the centre to the surface of the coupon during oxidation. This type of behaviour has been reported in the literature [290]. The same logic may also be applied to Alloy 625 ODS/SLM, which also has a fine grain microstructure, but Alloy 625 SLM, which has a similar microstructure to Alloy 625 ODS/SLM, was obviously Cr depleted under the scale. Therefore the absence of significant Cr depletion in Alloy 625 ODS/SLM is probably due to fast diffusion in the alloy, combined with a very slow rate of chromia scale formation.

Oxidation of Haynes 230 ODS

A thick duplex scale formed on the Haynes 230 ODS/SPS, which was comprised of chromia at the scale/alloy interface, grown mainly by the inward diffusion of O, and $Mn_xCr_{3-x}O_4$ at the scale/gas interface. At longer oxidation times the ratio of $Mn_xCr_{3-x}O_4$ spinel to Cr_2O_3 increased significantly, consistent with strong growth by the outward diffusion of cations, particularly Mn. Lobnig has shown that lattice diffusion is faster for Mn in chromia than for Cr in chromia [291]. This, and the strong inward flux of O, possibly indicates that lattice diffusion occurred via O vacancies and metal interstitials. Extensive internal oxidation occurred in the alloy, as did the formation of voids at the scale/alloy interface. Decohesion of the scale was observed at regular intervals along the scale/alloy interface, probably occurring on cooling to ambient temperature. This gave the oxidised alloy a rumpled appearance. The voids may be Kirkendall voids, but cavitation has been reported to occur in Ni

as a result of the reaction between carbides and O on grain boundaries [266, 267]. However, Dyson reported that the effect is impossible in Ni-base superalloys when the O activity is controlled by the formation of Cr_2O_3 [268]. Kuenzly and Douglas reported significant void formation in a Ni_3Al alloy, and proposed that it occurred because of the back diffusion of Ni, enriched at the surface of the alloy as a result of Al depletion due to scale formation, was faster than the outward diffusion of Al in the alloy [269]. However, it seems unlikely that the mechanism proposed by Kuenzly and Douglas is applicable to Haynes 230 ODS/SPS because of fast diffusion of Cr in the alloy, which means that the Cr depletion necessary for the creation of a driving force for the back diffusion of Ni probably never occurred. The cause of the voids is therefore uncertain; they could be attributable to Kirkendall voids on account of the large cation flux from the alloy to the scale, but cavitation may be possible, based on the circumstantial evidence of a high carbon-content alloy and a large O flux into the alloy, as indicated by extensive internal oxide formation. It was mentioned above that Cr diffusion was fast in Haynes 230 ODS/SPS, which is inferred from the fact that the Cr depletion profile was too shallow to be determined for the alloy. It is also worth noting that a satisfactory Cr interdiffusion coefficient could not be determined for Cr in Haynes 230 ODS/SLM, though Cr depletion was apparent.

A parabolic oxidation rate constant was determined for Haynes 230 ODS/SPS from the scale thickness measurements, but the TGA data could not be fitted using a single parabolic oxidation rate constant. However, two limiting values, of 5.24E-13$g^2cm^{-4}s^{-1}$ and 9.5E-13$g^2cm^{-4}s^{-1}$, were calculated using two parabolic oxidation rate constants i.e. 10-215 hours, and 215-1000 hours. This indicates that the rate of oxidation is ~10-20x faster than that of wrought Haynes 230. The TGA data could be fitted using a paralinear oxidation rate constant of the form usually used to determine the kinetics for the simultaneous growth and vaporisation of chromia [227, 228]. Using this method, the parabolic oxidation rate constant was determined to be 5.20E-13 $g^2cm^{-4}s^{-1}$, which is consistent with the smaller of the two limiting values determined using two parabolic oxidation rate constants, and the linear rate constant 2.57E-10 $gcm^{-2}s^{-1}$. The value obtained for the linear rate constant is approximately

consistent with literature values for chromia vaporisation at temperatures ~900°C [231, 232], but the mechanism is thought unlikely because it is at odds with the scale thickness results, the absence of similar results for any of the other alloys, which were oxidised under the same conditions, and the presence of a spinel layer at the scale/gas interface, which is reported to limit chromia vaporisation [204]. In addition, examination of the data showed that the difference between the TGA data and scale thickness data is likely to be due to additional mass gain at oxidation times <215 hours. The combination of fast oxidation kinetics and extensive internal oxidation is a characteristic of over-doping [172-174, 177], and it is therefore proposed that the alloy was over-doped with reactive elements. Several explanations were considered for the slowing of the oxidation rate at oxidation times >215 hours, including the loss of contact between the scale and the alloy in the detached regions, the formation of a protective layer of alumina in the alloy under the scale, which has been observed during the oxidation of Stal-15 [292], and mass increase due to the oxidation of Al in the alloy, which was estimated to range between ~1.8E-5gcm^2 and ~9.0E-4gcm^2, assuming 0.2 Wt. % of the Al in the alloy is oxidised to a depth of between ~100um and the full thickness of the coupon. The assumption that ~0.2 Wt. % of the Al is oxidised is made by reference to the depth profile obtained from the oxidised alloy. The discrepancy in the TGA and scale thickness data was thought to be ~5.0E-4gcm^{-2}, which is in the expected range. The most likely explanation for the difference in the TGA and scale thickness data is considered to be mass increase associated with formation of internal alumina in the alloy.

Haynes 230 ODS/SLM formed a relatively thin scale, comprising chromia, with $Mn_xCr_{3-x}O_4$ spinel at the scale/gas interface, formed during oxidation. The scale appeared to grow by a combination of inward and outward diffusion. Some voids, possibly Kirkendall voids, formed in the alloy at oxidation times >25 hours. Haynes 230 ODS/SLM also oxidised >10x slower than Haynes 230 ODS/SPS, based on k_p values, which is probably due to the slagging off of excess reactive elements from the alloy during SLM-consolidation. However, the oxidation resistance was not

significantly better than wrought Haynes 230, but it was significantly better than SLM-consolidated Haynes 230.

Table 8.1: Isothermal oxidation rate constants k_w ($g^2cm^{-4}s^{-1}$) and k_p (cm^2s^{-1}), and chromium interdiffusion coefficients D (cm^2s^{-1}) for the different variants of the alloys studied in the present work. MA754 is included for reference

Ranking	Alloy	k_w	k_p	D
1	625 ODS/SLM	NA	1.29E-15	1.3E-12
2	625 Hf-ODS/SPS	7.43E-15	ND	ND
2	*625 ODS/SPS	8.73E-15	1.37E-14	-
4	Haynes 230 ODS/SLM	NA	3.92E-14	0.3E-12
5	MA754	2.19E-14	ND	ND
6	Wrought Haynes 230	5.32E-14	5.18E-14	0.7E-12
7	625 SLM	7.34E-14	8.16E-14	2.3E-12
8	Haynes 230 SLM	1.72E-13	1.34E-13	1.4E-12
9	Wrought Alloy 625	3.19E-13	1.80E-13	2.0E-12
10	Wrought Alloy 718 (P4000)	3.56E-13	2.29E-13	ND
10	Wrought Alloy 718 (P600)	3.55E-13	2.38E-13	0.8E-12
12	718 SLM	4.75E-13	2.89E-13	1.5E-12
13	*Haynes 230 ODS/SPS	5.24E-13 - 9.50E-13	5.36E-13	-

* D could not be determined because there was no discernible depletion of Cr in the depth profiles; ND - Not determined; NA - Insufficient alloy to carry out TGA experiments

Effect of reactive element additions on alloys

A plot of the oxidation rate constant k_p against reactive element addition is produced in Figure 8.4, which shows the trends obtained for Alloy 625 and Haynes

230. The plot also includes data obtained from the base alloys. Reactive element concentration is only one of the factors involved in determining k_p, and others, such as differences in grain size, Cr concentration, consolidation method etc., will also affect k_p, but are not accounted for in Figure 8.4. Therefore, Figure 8.4 is only a guide to the effect of reactive element additions on the alloys. In addition, it should be noted that the concentration of reactive elements in SLM-consolidated Haynes 230, Haynes 230 ODS/SLM and Alloy 625 ODS/SLM are unknown, having been reduced from the initial concentration by losses due to slag formation. For convenience, these points are plotted at the mid-point of the possible concentration range, which is 0.25 Wt. % for Haynes 230 ODS/SLM and Alloy 625 ODS/SLM. Also, k_p was not determined for Alloy 625 Hf-ODS/SPS, but it is assumed to be the same as that determined for Alloy 625 ODS/SPS because k_w was essentially the same for the two alloys.

Figure 8.4 shows that the addition of 0.5 Wt. % Y_2O_3, or 0.5 Wt. % Y_2O_3 + 0.5 Wt. % HfO_2, produces a significant improvement in the oxidation resistance of Alloy 625, but the addition of 0.5 Wt. % Y_2O_3 to Haynes 230 produces a significant reduction in the oxidation resistance of Haynes 230. This shows that reactive element additions are alloy dependent, as a result of the interplay between the different elements in the alloys. Alloy 625 ODS is ~2.5x more oxidation resistant than MA754, a legacy commercial ODS Ni superalloy, which demonstrates how successful the addition of Y_2O_3 to the base alloy has been. The mechanism for the improvement in oxidation behaviour of Alloy 625 is believed to be the reactive element effect. It is not clear why Alloy 625 is so tolerant of reactive element additions, even when doped with 0.5 Wt. % Y_2O_3 and 0.5 Wt. % HfO_2, but Haynes 230 is intolerant of reactive element additions. One possible reason is the presence of Nb in Alloy 625, which may serve to 'buffer' the alloy against overdoping by forming stable inclusions rich Nb and Y, as observed for Alloy 625 ODS/SLM. Synergistic effects may also be operative in Haynes 230 ODS as a result of the

presence of Y, La and Ce in the alloy. It is also noted that the presence of Al in Haynes 230 led to extensive internal oxidation in Haynes 230, but this appears to be an effect of overdoping rather than the cause. However, examination of patents relevant to the development of Haynes 230 states that La and Al act synergistically to improve the oxidation resistance of the alloy, and that Al must be present in the alloy at a concentration >0.02 Wt. % [208]. This raises the possibility that if the gas atomised Alloy 625 powder had contained Al, Alloy 625 ODS may also have formed internal oxides, or possibly even exhibited poor oxidation resistance, following a 0.5 Wt. % addition of Y_2O_3 (the Al content of the gas atomised Alloy 625 powder was <0.04 Wt. %). It is proposed that an addition of 0.5 Wt. % Y_2O_3 to a series of Alloy 625 alloys, ranging in Al content from 0-0.4 Wt. %, would make for an interesting oxidation experiment.

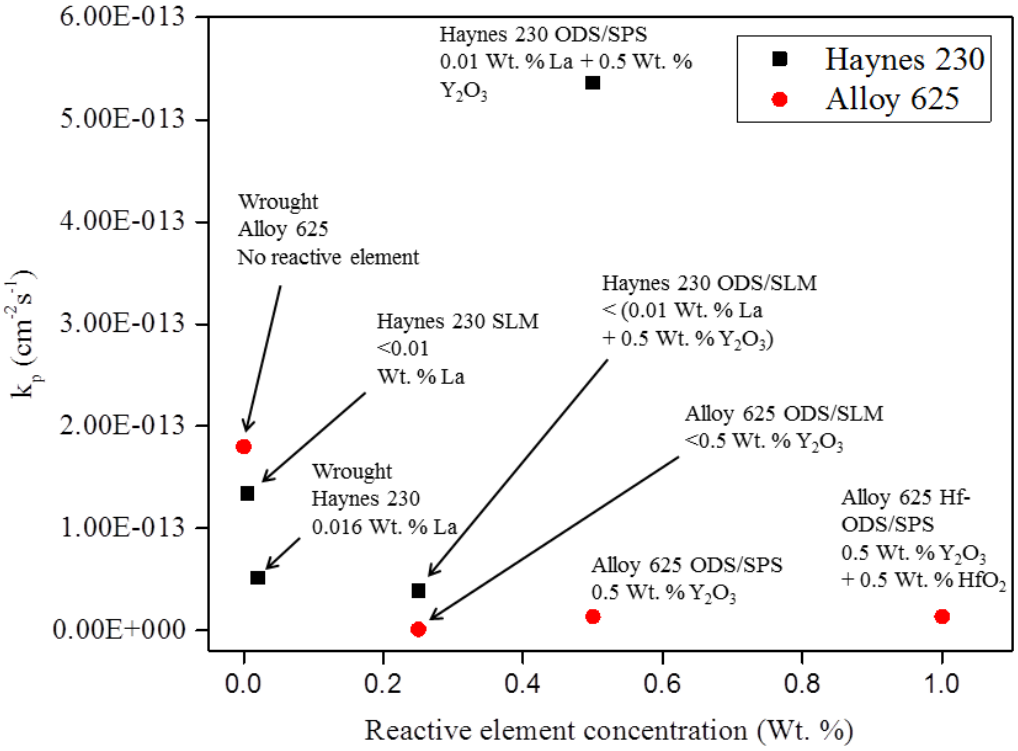

Figure 8.4: Effect of reactive element additions on the parabolic oxidation rate constant (k_p) ($cm^2 s^{-1}$) determined for the different variants of Alloy 625 and Haynes 230 following isothermal oxidation in laboratory air at 900°C

8.4 Conclusions

SLM-consolidated Haynes 230 was significantly less oxidation resistant than wrought Haynes 230, due to a difference in the scale growth mechanism. Scale growth on wrought Haynes 230 was dominated by inward growth, as expected for an alloy doped with a reactive element, but the scale significantly grew more quickly on the SLM-consolidated alloy by a combination of inward and outward growth. This is attributed to the lower La content of the gas atomised powder from which the SLM-consolidated alloy was fabricated, and the loss of La from the alloy during consolidation as slag. The oxidation behaviour of SLM-consolidated Alloy 718 was marginally inferior to that of wrought Alloy 718, but SLM-consolidated Alloy 625 oxidised more slowly, and with a better scale morphology, than wrought Alloy 625. The improvement in the oxidation behaviour of SLM-consolidated Alloy 625 may be due to suppression of the growth of non-protective Nb-rich oxides during transient oxidation, which may result from faster selective oxidation of Cr, due to the dendritic/cellular substructure of the SLM-consolidated alloy, or as a result of fewer Nb-rich carbides in the alloy, which appears to occur because of faster cooling of the alloy during SLM-consolidation.

The ODS variant of Alloy 625, made following the addition of 0.5 Wt. % Y_2O_3 to the alloy, has potential as a high temperature alloy. In SLM-consolidated and in SPS-consolidated forms it developed a protective chromia scale that grew 10-40x slower than the scale on wrought Alloy 625. The improvement in oxidation behaviour is consistent with the beneficial effects of reactive element additions. In SPS-consolidated form, the ODS variant of Haynes 230 oxidised rapidly, forming a thick duplex scale comprising a basal layer of Cr_2O_3 and $Mn_xCr_{3-x}O_4$ spinel at the scale/gas interface. Large voids and extensive internal oxidation of Al occurred in the oxidation-affected zone of the alloy. Haynes 230 ODS/SPS was believed to be over-doped with reactive elements following a 0.5 Wt. % addition of Y_2O_3 to the alloy. It is not clear why Alloy 625 is more tolerant of reactive element additions than Haynes 230. Haynes 230 ODS/SLM, which was consolidated from the same

mechanically alloyed powder as Haynes 230 ODS/SPS, oxidised more slowly than Haynes 230 ODS/SPS, with a better scale morphology and without the extensive internal oxidation and voids that accompanied the oxidation of the SPS-consolidated alloy. The improvement in the oxidation behaviour of the alloy is attributed to the 'slagging off' of reactive elements, which was observed to have occurred during SLM-consolidation.

CHAPTER 9

FUTURE WORK

Alloy 625 ODS appears to be a useful candidate alloy for conventional consolidation, such as extrusion or HIPping, but additional work is needed to optimise the reactive element addition, and to test the alloy under cyclic oxidation conditions and at different temperatures. Haynes 230 ODS does not appear to be a good base alloy for development of ODS superalloys.

It was not possible to consolidate crack-free Ni-base ODS superalloys by SLM. Until this problem is overcome, it is recommended that any future work to study the high temperature oxidation behaviour of SLM-consolidated Ni-base superalloys is restricted to non-ODS alloys. The high temperature oxidation behaviour of SLM-consolidated Alloy 625 and SLM-consolidated Haynes 230 should be investigated further, as the results of the present study show that SLM-consolidated Alloy 625 oxidises more slowly than SLM-consolidated Haynes 230. This is a reversal in the order of the wrought alloys. Alloy 625 is primarily used in aqueous environments, but Haynes 230 was designed for high temperature applications and so the finding that its oxidation resistance may be degraded as a result of consolidation by SLM represents useful additional knowledge. SLM-consolidated alloys should also be tested under cyclic oxidation conditions, which are more realistic than isothermal experiments, and will establish how resistant SLM-consolidated alloys are to spalling.

The effect that build parameters have on the oxidation behaviour of SLM-consolidated alloys also needs to be investigated, as the results of the present study may not necessarily indicate how the same alloys will oxidise following consolidation using a different set of SLM build parameters.

References

1. **Gardan, J., *Additive manufacturing technologies: state of the art and trends.* International Journal of Production Research, 2016. 54(10): p. 3118-3132.**

2. **Chen, L., et al., *The research status and development trend of additive manufacturing technology.* The International Journal of Advanced Manufacturing Technology, 2016: p. 1-10.**

3. **Huynh, L., J. Rotella, and M.D. Sangid, *Fatigue behavior of IN718 microtrusses produced via additive manufacturing.* Materials & Design, 2016. 105: p. 278-289.**

4. **Lin, J.J., et al., *Microstructural evolution and mechanical properties of Ti-6Al-4V wall deposited by pulsed plasma arc additive manufacturing.* Materials & Design, 2016. 102: p. 30-40.**

5. **Moon, S.K., et al., *Application of 3D printing technology for designing light-weight unmanned aerial vehicle wing structures.* International Journal of Precision Engineering and Manufacturing-Green Technology, 2014. 1(3): p. 223-228.**

6. **Murr, L.E., *Frontiers of 3D Printing/Additive Manufacturing: from Human Organs to Aircraft Fabrication†.* Journal of Materials Science & Technology.**

7. **Waller, J., et al., *NASA OSMA NDE Program Additive Manufacturing Foundational Effort.* 2016.**

8. **Shafiee, A. and A. Atala, *Printing Technologies for Medical Applications.* Trends in Molecular Medicine, 2016. 22(3): p. 254-265.**

9. **Chen, J., L. Xue, and S.H. Wang, *Experimental studies on process-induced morphological characteristics of macro-and microstructures in laser consolidated alloys.* Journal of Materials Science. 46(17): p. 5859-5875.**

10. **Chen, J. and L. Xue, *Process-induced microstructural characteristics of laser consolidated IN-738 superalloy.* Materials Science and Engineering: A. 527(27): p. 7318-7328.**

11. **Wang, Z., et al., *The microstructure and mechanical properties of deposited-IN718 by selective laser melting.* Journal of Alloys and Compounds. 513: p. 518-523.**

12. **Basak, A., R. Acharya, and S. Das, *Additive Manufacturing of Single-Crystal Superalloy CMSX-4 Through Scanning Laser Epitaxy: Computational Modeling, Experimental Process Development, and Process Parameter Optimization.* Metallurgical and Materials Transactions A, 2016. 47(8): p. 3845-3859.**

13. **List, F.A., et al.,** ***Properties of Inconel 625 mesh structures grown by electron beam additive manufacturing.*** **Materials Science and Engineering: A, 2014. 615: p. 191-197.**

14. **Sateesh, N.H., et al.,** ***Microstructure and Mechanical Characterization of Laser Sintered Inconel-625 Superalloy.*** **Procedia Materials Science, 2014. 5: p. 772-779.**

15. **Jia, Q. and D. Gu,** ***Selective laser melting additive manufacturing of Inconel 718 superalloy parts: Densification, microstructure and properties.*** **Journal of Alloys and Compounds. 585: p. 713-721.**

16. **Jia, Q. and D. Gu,** ***Selective laser melting additive manufactured Inconel 718 superalloy parts: high-temperature oxidation property and its mechanisms.*** **Optics & Laser Technology, 2014. 62: p. 161-171.**

17. **Hong, C., et al.,** ***High-temperature oxidation performance and its mechanism of TiC/Inconel 625 composites prepared by laser metal deposition additive manufacturing.*** **Journal of Laser Applications, 2015. 27(S1): p. S17005.**

18. **Pint, B.A., J.R. DiStefano, and I.G. Wright,** ***Oxidation resistance: One barrier to moving beyond Ni-base superalloys.*** **Materials Science and Engineering: A, 2006. 415(1–2): p. 255-263.**

19. **Häussler, D., et al.,** ***Interaction processes between dislocations and particles in the ODS nickel-base superalloy INCONEL MA 754 studied by means of in situ straining in an HVEM.*** **Materials Science and Engineering: A, 2001. 309: p. 500-504.**

20. **Jang, J.S.C. and C.C. Koch,** ***The hall-petch relationships in mechanically alloyed Ni_3Al with oxide dispersoids.*** **Scripta metallurgica, 1988. 22(5): p. 677-682.**

21. **Vlasenko, S., et al.,** ***Evaluation of microstructural parameters of oxide dispersion strengthened steels from X-ray diffraction profiles.*** **Journal of Nuclear Materials, 2016. 470: p. 139-146.**

22. **Whittle, D.P. and J. Stringer,** ***Improvements in High Temperature Oxidation Resistance by Additions of Reactive Elements or Oxide Dispersions.*** **Philosophical Transactions. Series A, Mathematical, Physical and Engineering Sciences / The Royal Society, 1980. 295(1413): p. 309.**

23. **Pint, B.A.,** ***Experimental observations in support of the dynamic-segregation theory to explain the reactive-element effect.*** **Oxidation of Metals, 1996. 45(1-2): p. 1-37.**

24. **Sims, C.T.,** ***Superalloys: Genesis and Character, Superalloys II, Sims, C.T., Stoloff, N.S. and Hagel, W.C. (Eds.)*****. (1987), Page 3.: John Wiley & Sons.**

25. **Reed, R.C.,** ***Superalloys - Fundamentals and Applications*****. Cambridge University Press.**

26. **Geddes, B., H. Leon, and X. Huang,** ***Superalloys - Alloying and Performance*****. ASM International.**

27. **Sims, C.T.,** ***A history of superalloy metallurgy for superalloy metallurgists.*** **Superalloys 1984, 1984: p. 399-419.**

28. **Ikeda, Y., K.Nii, and K.Yoshihara,** ***Prec. 3rdJIMlnt. Symp. on High TemperatureCorrosionof Metals and Alloys, supplement to Trans. Jpn. Inst. Met., 24 (1983) 207.***

29. **Donachie, M.J. and S.J. Donachie,** ***Superalloys - A Technical Guide (2nd Edition)*****. ASM International.**

30. **Meyers, M.A. and K.K. Chawla,** ***Mechanical behavior of materials. [electronic book]*****. Online access with JISC subscription agreeent: Knovel. Cambridge ; Cambridge University Press, 2009.**

31. **Forde, M.,** ***39. The Nature and Behaviour of Alloys*****, in** ***ICE Manual of Construction Materials, Volume 2 - Metals and Alloys; Polymers; Polymer Fibre Composites in Civil Engineering; Timber; Glass; Non-Conventional Materials; Appendices*****. ICE Publishing.**

32. **Durand-Charre, M.,** ***The microstructure of superalloys*****. 1998: CRC press.**

33. **Pineau, A. and S.D. Antolovich,** ***High temperature fatigue of nickel-base superalloys–a review with special emphasis on deformation modes and oxidation.*** **Engineering Failure Analysis, 2009. 16(8): p. 2668-2697.**

34. **Huda, Z.,** ***Development of design principles for a creep-limited alloy for turbine blades.*** **Journal of materials engineering and performance, 1995. 4(1): p. 48-53.**

35. **Benjamin, J.S. and M.J. Bomford,** ***Effect of yttrium oxide volume fraction and particle size on elevated temperature strength of a dispersic strengthened superalloy.*** **Metallurgical and Materials Transactions B, 1974. 5(3): p. 615-621.**

36. **Heilmaier, M. and B. Reppich,** ***Creep lifetime prediction of oxide-dispersion-strengthened nickel-base superalloys: A micromechanically based approach.*** **Metallurgical and Materials Transactions A, 1996. 27(12): p. 3861-3870.**

37. **Mujahid, M. and J.W. Martin,** ***The effect of oxide particle coherency on Zener pinning in ODS superalloys.*** **Journal of Materials Science Letters, 1994. 13(3): p. 153-155.**

38. **Stubbins, J., et al.,** ***Development of Austenitic ODS Strengthened Alloys for Very High Temperature Applications*****. 2015, Battelle Energy Alliance, LLC, Idaho Falls, ID (United States).**

39. **Capdevila, C. and H.K.D.H. Bhadeshia, *Manufacturing and microstructural evolution of mechanuically alloyed oxide dispersion strengthened superalloys.* Advanced Engineering Materials, 2001. 3(9): p. 647-656.**

40. **Wilcox, B.A. and A.H. Clauer, *The role of grain size and shape in strengthening of dispersion hardened nickel alloys.* Acta Metallurgica, 1972. 20(5): p. 743-757.**

41. **Bhadeshia, H.K.D.H., *Seminars on the Modelling of Atomic and Microstructures in Metals and AlloysRecrystallisation of practical mechanically alloyed iron-base and nickel-base superalloys.* Materials Science and Engineering: A, 1997. 223(1): p. 64-77.**

42. **Bhadeshia, H., *Recrystallisation of practical mechanically alloyed iron-base and nickel-base superalloys.* Materials Science and Engineering: A, 1997. 223(1): p. 64-77.**

43. **Baloch, M.M. and H.K.D.H. Bhadeshia, *Directional recrystallisation in Inconel MA 6000 nickel base oxide dispersion strengthened superalloy.* Materials Science and Technology (United Kingdom), 1990. 6(12): p. 1236-1246.**

44. **Molian, P.A., Y.M. Yang, and P.C. Patnaik, *Laser welding of oxide dispersion-strengthened alloy MA754.* Journal of Materials Science, 1992. 27(10): p. 2687-2694.**

45. **Braski, D.N., et al., *Effect of Y2O3 dispersoids in 80Ni-20Cr alloy on the early stages of oxidation at low-oxygen potential.* Oxidation of Metals, 1986. 25(1-2): p. 29-50.**

46. **Hilger, I., et al., *Fabrication and characterization of oxide dispersion strengthened (ODS) 14Cr steels consolidated by means of hot isostatic pressing, hot extrusion and spark plasma sintering.* Journal of Nuclear Materials, 2016. 472: p. 206-214.**

47. **Oono, N., et al., *Irradiation effects in oxide dispersion strengthened (ODS) Ni-base alloys for Gen. IV nuclear reactors.* Journal of Nuclear Materials, 2015. 465: p. 835-839.**

48. **Benjamin, J.S., *Dispersion strengthened superalloys by mechanical alloying.* Metallurgical and Materials Transactions B, 1970. 1(10): p. 2943-2951.**

49. **Benjamin, J.S., *Mechanical alloying.* Scientific American, 1976. 234(5): p. 40-48.**

50. **Benjamin, J.S., *Mechanical alloying - A perspective.* Metal powder report, 1990. 45(2): p. 122-127.**

51. **Suryanarayana, C. and F.H. Froes, *Nanocrystalline titanium-magnesium alloys through mechanical alloying.* Journal of Materials Research, 1990. 5(09): p. 1880-1886.**

52. **Suryanarayana, C. and N. Al-Aqeeli, *Mechanically alloyed nanocomposites.* Progress in materials science.**

53. **Suryanarayana, C., E. Ivanov, and V.V. Boldyrev, *The science and technology of mechanical alloying.* Materials Science and Engineering: A, 2001. 304: p. 151-158.**

54. **Gilman, P.S. and J.S. Benjamin, *Mechanical alloying.* Annual Review of Materials Science, 1983. 13(1): p. 279-300.**

55. **Suryanarayana, C., *Recent developments in mechanical alloying.* Rev.Adv.Mater.Sci, 2008. 18: p. 203-211.**

56. **Koch, C.C., *Materials synthesis by mechanical alloying.* Annual review of materials science, 1989. 19(1): p. 121-143.**

57. **Murr, L.E., et al., *Metal Fabrication by Additive Manufacturing Using Laser and Electron Beam Melting Technologies.* Journal of Materials Science & Technology, 2012. 28(1): p. 1-14.**

58. **Vandenbroucke, B. and J.P. Kruth, *Selective laser melting of biocompatible metals for rapid manufacturing of medical parts.* Rapid Prototyping Journal, 2007. 13(4): p. 196-203.**

59. **Kumar, S. and S. Pityana, *Laser-Based Additive Manufacturing of Metals.* Advanced Materials Research. 227: p. 92-95.**

60. **Chang, I. and Y. Zhao, *18.3.4 Selective Laser Melting/Electron Beam Melting*. 2014, Woodhead Publishing.**

61. **Coleman, A. and M. Kearns, *ADVANCES IN APPLICATIONS OF GAS ATOMISED METAL POWDERS IN NEAR NET SHAPE MANUFACTURING.* http://smt.sandvik.com/en/.**

62. **Kurz, W., *Solidification microstructure-processing maps: theory and application.* Advanced Engineering Materials, 2001. 3(7): p. 443-452.**

63. **Thijs, L., et al., *A study of the microstructural evolution during selective laser melting of Ti–6Al–4V.* Acta Materialia, 2010. 58(9): p. 3303-3312.**

64. **Nelson, T., J. Lippold, and M. Mills, *Nature and evolution of the fusion boundary in ferritic-austenitic dissimilar weld metals, Part 1-Nucleation and growth.* WELDING JOURNAL-NEW YORK-, 1999. 78: p. 329-s.**

65. **Thijs, L., et al., *Fine-structured aluminium products with controllable texture by selective laser melting of pre-alloyed AlSi10Mg powder.* Acta Materialia, 2013. 61(5): p. 1809-1819.**

66. **Walker, J.C., et al., *Fabrication of Fe-Cr-Al oxide dispersion strengthened pm2000 alloy using selective laser melting.* Advanced Engineering Materials, 2009. 11(7): p. 541-546.**

67. **Boegelein, T., et al. *Selective Laser Melting of Oxide Dispersion Strengthened Steels*. in *ASME 2011 Pressure Vessels and Piping Conference*. 2011. American Society of Mechanical Engineers.**

68. **Boegelein, T., et al.,** ***Characterisation of a complex thin walled structure fabricated by selective laser melting using a ferritic oxide dispersion strengthened steel.*** **Materials Characterization, 2016. 112: p. 30-40.**

69. **Boegelein, T., et al.,** ***Mechanical response and deformation mechanisms of ferritic oxide dispersion strengthened steel structures produced by selective laser melting.*** **Acta Materialia, 2015. 87: p. 201-215.**

70. **Munir, Z., U. Anselmi-Tamburini, and M. Ohyanagi,** ***The effect of electric field and pressure on the synthesis and consolidation of materials: a review of the spark plasma sintering method.*** **Journal of Materials Science, 2006. 41(3): p. 763-777.**

71. **Somiya, S.,** ***Handbook of advanced ceramics: materials, applications, processing, and properties*****. 2013: Academic Press.**

72. **Suárez, M., et al.,** ***Challenges and opportunities for spark plasma sintering: a key technology for a new generation of materials*****. 2013: INTECH Open Access Publisher.**

73. **Munir, Z.A., U. Anselmi-Tamburini, and M. Ohyanagi,** ***The effect of electric field and pressure on the synthesis and consolidation of materials: A review of the spark plasma sintering method.*** **Journal of Materials Science, 2006. 41(3): p. 763-777.**

74. **Somiya, S.,** ***Principles of the SPS Process,*** **in** ***Handbook of Advanced Ceramics - Materials, Applications, Processing, and Properties (2nd Edition)*****. Elsevier.**

75. **Ji, G., et al.,** ***The mechanisms of microstructure formation in a nanostructured oxide dispersion strengthened FeAl alloy obtained by spark plasma sintering.*** **Intermetallics, 2007. 15(2): p. 108-118.**

76. **Deog, K.Y., B.S. Man, and B.D. Wirth,** ***Formation of Nano-sized ODS Clusters in Mechanically Alloyed NiAl-(Y, Ti, O) Alloys.***

77. **Yu, H., et al.,** ***Microstructure characterization of Co–20Cr–(5, 10) Al oxide dispersion strengthened superalloys.*** **Materials Characterization, 2016. 112: p. 188-196.**

78. **Pasebani, S., et al.,** ***Oxide dispersion strengthened nickel based alloys via spark plasma sintering.*** **Materials Science and Engineering: A, 2015. 630: p. 155-169.**

79. **Sasaki, T., et al.,** ***Effect of heat treatment on the hardness and microstructure in Co–3Al–1.5Y2O3–1.2Hf ODS alloy.*** **Materials Science and Engineering: A, 2014. 601: p. 139-144.**

80. **Chen, C.-L. and Y. Zeng,** ***Effect of consolidation and oxide dispersoid addition on phase formation and mechanical properties of WTi ODS alloy.*** **International Journal of Refractory Metals and Hard Materials, 2016. 60: p. 11-16.**

81. **Kaplin, C. and M. Brochu,** ***The effect of grain size on the oxidation of NiCoCrAlY.*** **Applied Surface Science, 2014. 301: p. 258-263.**

82. **Pint, B.A., J. Leibowitz, and J.H. Devan,** ***The Effect of an Oxide Dispersion on the Critical Al Content in Fe-Al Alloys.*** **Oxidation of Metals, 1999. 51(1): p. 181-197.**

83. **Auger, M.A., et al.,** ***Microstructure and mechanical behavior of ODS and non-ODS Fe-14Cr model alloys produced by spark plasma sintering.*** **Journal of Nuclear Materials. 436(1): p. 68-75.**

84. **Zhang, Z., et al.,** ***Mechanical behavior of cryomilled Ni superalloy by spark plasma sintering.*** **Metallurgical and Materials Transactions A, 2009. 40(9): p. 2023-2029.**

85. **Chen, D.J. and M.J. Mayo,** ***Rapid Rate Sintering of Nanocrystalline ZrO2− 3 mol% Y2O3.*** **Journal of the American Ceramic Society, 1996. 79(4): p. 906-912.**

86. **Eiselstein, H.L. and D.J. Tillack.** ***The invention and definition of alloy 625*****. in** ***International Symposium on Metallurgy and Applications of Superalloys*****.**

87. **Brooks, J.W. and P.J. Bridges,** ***Metallurgical stability of inconel alloy 718.*** **Superalloys, 1988. 88: p. 33-42.**

88. ***Special Metals, Inc. INCONEL® Alloy 718 - Technical Bulletin*** ***http://www.specialmetals.com/*****.**

89. **Cieslak, M., et al.,** ***The solidification metallurgy of alloy 718 and other Nb-containing superalloys.*** **Superalloy, 1989. 718: p. 59-68.**

90. **Knorovsky, G.A., et al.,** ***INCONEL 718: A solidification diagram.*** **Metallurgical Transactions A, 1989. 20(10): p. 2149-2158.**

91. **DuPont, J.N., et al.,** ***Solidification of Nb-bearing superalloys: Part I. Reaction sequences.*** **Metallurgical and Materials Transactions A, 1998. 29(11): p. 2785-2796.**

92. **Patel, S.J. and G.D. Smith.** ***The role of Niobium in wrought superalloys*****. in** ***International symposium niobium*****. 2001.**

93. **Wlodek, S. and R. Field,** ***THE EFFECTS OF LONG TIME EXPOSURE ON ALLOY 718.***

94. **Radavich, J.F.** ***The physical metallurgy of cast and wrought alloy 718*****. in** ***Conference Proceedings on Superalloy*****. 1989.**

95. **Rowe, M., V. Ishwar, and D. Klarstrom,** ***Properties, weldability, and applications of modern wrought heat-resistant alloys for aerospace and power generation industries.*** **Journal of engineering for gas turbines and power, 2006. 128(2): p. 354-361.**

96. **DuPont, J., C. Robino, and A. Marder,** ***Solidification and weldability of Nb-bearing superalloys.*** **Welding Journal, 1998.**

97. **Zhang, D., et al.,** ***Effect of standard heat treatment on the microstructure and mechanical properties of selective laser melting manufactured Inconel 718 superalloy.*** **Materials Science & Engineering A. 644: p. 32-40.**

98. **Aydinoz, M.E., et al.,** ***On the microstructural and mechanical properties of post-treated additively manufactured Inconel 718 superalloy under quasi-static and cyclic loading.*** **Materials Science & Engineering A. 669: p. 246-258.**

99. **Chlebus, E., et al.,** ***Effect of heat treatment on the microstructure and mechanical properties of Inconel 718 processed by selective laser melting.*** **Materials Science & Engineering A. 639: p. 647-655.**

100. **Strößner, J., Michael Terock, and Uwe Glatzel,** ***"Mechanical and Microstructural Investigation of Nickel-Based Superalloy IN718 Manufactured by Selective Laser Melting (SLM)." Advanced Engineering Materials 17.8 (2015): 1099-1105.***

101. **Amato, K., et al.,** ***Microstructures and mechanical behavior of Inconel 718 fabricated by selective laser melting.*** **Acta Materialia, 2012. 60(5): p. 2229-2239.**

102. **Trosch, T., et al.,** ***Microstructure and mechanical properties of selective laser melted Inconel 718 compared to forging and casting.*** **Materials Letters. 164: p. 428-431.**

103. ***Special Metals, Inc. INCONEL® Alloy 625 - Technical Bulletin*** ***http://www.specialmetals.com/.***

104. **Floreen, S., G.E. Fuchs, and W.J. Yang,** ***The metallurgy of alloy 625.*** **Superalloys, 1994. 718(625): p. 13-37.**

105. **Chyrkin, A., et al.,** ***Sub-scale depletion and enrichment processes during high temperature oxidation of the nickel base alloy 625 in the temperature range 900–1000 C.*** **Oxidation of Metals, 2011. 75(3-4): p. 143-166.**

106. **DuPont, J.N.,** ***Solidification of an alloy 625 weld overlay.*** **Metallurgical and Materials Transactions A, 1996. 27(11): p. 3612-3620.**

107. **Li, S., et al.,** ***Microstructure Characteristics of Selective Laser Melting Formed Commercial Inconel625 Superalloy.***

108. **Amato, K., et al.,** ***Comparison of Microstructures and Properties for a Ni-Base Superalloy (Alloy 625) Fabricated by Electron Beam Melting.*** **Journal of Materials Science Research. 1(2): p. p3.**

109. **Criales, L.E., Y.M. Arısoy, and T. Özel,** ***Sensitivity analysis of material and process parameters in finite element modeling of selective laser melting of Inconel 625.*** **The International Journal of Advanced Manufacturing Technology, 2016: p. 1-14.**

110. ***Haynes International, Inc. Haynes 230 Alloy Product brochure - http://www.haynesintl.com/.***

111. **Klarstrom, D., L. Pike, and V. Ishwar,** ***Nickel-base alloy solutions for ultrasupercritical steam power plants.*** **Procedia Engineering, 2013. 55: p. 221-225.**

112. **Lu, Y.L., et al.,** ***Effects of temperature and hold time on creep-fatigue crack-growth behavior of HAYNES 230 alloy.*** **Materials Science and Engineering: A, 2006. 429(1): p. 1-10.**

113. **Klarstrom, D.** ***The development of HAYNES 230 alloy*****. in** ***Materials Design Approaches and Experiences as held during the TMS Fall Meeting*****. 2001.**

114. **Klarstrom, D., et al.** ***A new gas turbine combustor alloy*****. in** ***ASME 1984 International Gas Turbine Conference and Exhibit*****. 1984. American Society of Mechanical Engineers.**

115. **Veverkova, J., et al.,** ***High temperature microstructural degradation of Haynes Alloy 230.*** **2008.**

116. **Jalowicka, A., et al.,** ***Effect of Specimen Thickness on Microstructural Changes During Oxidation of the NiCrW Alloy 230 at 950–1050° C.*** **JOM, 2015. 67(11): p. 2573-2588.**

117. **Ernst, S.,** ***Weldability studies of Haynes® 230 alloy.*** **Weld. J.(Miami, FL, US), 1994. 73(4): p. 80s-89s.**

118. **Borland, J.,** ***Generalized theory of super-solidus cracking in welds (and castings).*** **British Welding Journal, 1960. 7(8): p. 508-512.**

119. **Kou, S.,** ***Weld Metal Solidification Cracking*****, in** ***Welding Metallurgy*****. 2003, John Wiley & Sons, Inc. p. 263-300.**

120. **Young, J.,** ***Chapter 3 Oxidation of Pure Metals*****, in** ***Corrosion Series*****, Y. David John, Editor. 2008, Elsevier Science. p. 81-137.**

121. **Birks, N., G.H. Meier, and F.S. Pettit,** ***Introduction to High Temperature Oxidation of Metals, 2nd Edition, Cambridge University Press, Cambridge, 2006.***

122. **Birks, N., G.H. Meier, and F.S. Pettit,** ***Introduction to High Temperature Oxidation of Metals, 2nd Edition, Cambridge University Press, Cambridge, 2006.*** **Pages 49-73.**

123. **Halvarsson, M., et al.,** ***Microstructural investigation of the breakdown of the protective oxide scale on a 304 steel in the presence of oxygen and water vapour at 600 C.*** **Corrosion Science, 2006. 48(8): p. 2014-2035.**

124. **Birks, N., G.H. Meier, and F.S. Pettit,** ***Introduction to High Temperature Oxidation of Metals, 2nd Edition, Cambridge University Press, Cambridge, 2006.*** **Page xii.**

125. Pint, B., L. Walker, and I. Wright, *Characterization of the breakaway al content in alumina-forming alloys.* Materials at High Temperatures, 2004. 21(3): p. 175-185.

126. Hindam, H. and D.P. Whittle, *Microstructure, adhesion and growth kinetics of protective scales on metals and alloys.* Oxidation of Metals, 1982. 18(5-6): p. 245.

127. Wood, G.C., *High-temperature oxidation of alloys.* Oxidation of Metals, 1970. 2(1): p. 11-57.

128. Stott, F.H., *Developments in understanding the mechanisms of growth of protective scales on high-temperature alloys.* Materials Characterization, 1992. 28(3): p. 311-325.

129. Kutz, M., *5. High Temperature Oxidation*, in *Handbook of Environmental Degradation of Materials (2nd Edition)*. Elsevier.

130. Lai, G.Y., *High-Temperature Corrosion and Materials Applications*. ASM International.

131. Young, J., *Chapter 2 Enabling Theory*, in *Corrosion Series*, Y. David John, Editor. 2008, Elsevier Science. p. 29-79.

132. Saunders, S., et al., *Oxidation, hot corrosion and protection of metallic materials.* Physical Metallurgy, 1996: p. 1292-1361.

133. Kofstad, P., *High temperature corrosion. Elsevier Applied Science Publishers Ltd., London – New York.* 1988: p. 252.

134. Wagner, C., *Beitrag zur theorie des anlaufvorgangs.* Z. Phys. Chem. B, 1933. 21: p. 25-41.

135. Kofstad, P., *High temperature corrosion.* Elsevier Applied Science Publishers, Crown House, Linton Road, Barking, Essex IG 11 8 JU, UK, 1988., 1988: p. 372.

136. Kofstad, P., *High temperature corrosion. Elsevier Applied Science Publishers Ltd., London – New York.* 1988: p. 315-319.

137. Atkinson, H.V., *A review of the role of short-circuit diffusion in the oxidation of nickel, chromium, and nickel-chromium alloys.* Oxidation of Metals, 1985. 24(3-4): p. 177-197.

138. Evans, H., A. Donaldson, and T. Gilmour, *Mechanisms of breakaway oxidation and application to a chromia-forming steel.* Oxidation of Metals, 1999. 52(5-6): p. 379-402.

139. Wood, G., et al., *A Comparison of the Oxidation of Fe-Cr, Ni-Cr and Co-Cr alloys in oxygen and water vapour.* Materials and Corrosion, 1970. 21(11): p. 900-910.

140. Giggins, C.S. and F.S. Pettit, *Oxidation of Ni-Cr alloys between 800 and 1200 C.* Trans Met Soc AIME, 1969. 245(12): p. 2495-2507.

141. **Geng, L., Y.-S. Na, and N.-K. Park,** ***Oxidation behavior of Alloy 718 at a high temperature.*** **Materials & Design, 2007. 28(3): p. 978-981.**

142. **Giggins, C.S. and F.S. Pettit,** ***The effect of alloy grain-size and surface deformation on the selective oxidation of chromium in Ni-Cr alloys at temperatures of 900 and 1100 deg C(Ni-Cr alloys effects of grain size and surface deformation on oxidation properties at high temperature).*** **METALLURGICAL SOCIETY OF AIME, TRANSACTIONS, 1969. 245: p. 2509-2514.**

143. **Grabke, H.J., et al.,** ***Effects of Grain Size, Cold Working, and Surface Finish on the Metal-Dusting Resistance of Steels.*** **Oxidation of Metals, 1998. 50(3-4): p. 241-254.**

144. **Trindade, V.B., et al.,** ***Effect of alloy grain size on the high-temperature oxidation behavior of the austenitic steel TP 347.*** **Materials Research, 2005. 8(4): p. 371-375.**

145. **Trindade, V., et al.,** ***Oxidation mechanisms of Cr-containing steels and Ni-base alloys at high-temperatures–. Part I: The different role of alloy grain boundaries.*** **Materials and Corrosion, 2005. 56(11): p. 785-790.**

146. **Caplan, D., M. Graham, and M. Cohen,** ***Effect of cold work on the oxidation of nickel at high temperature.*** **Journal of the Electrochemical Society, 1972. 119(9): p. 1205-1215.**

147. **Calvarin, G., R. Molins, and A. Huntz,** ***Oxidation mechanism of Ni—20Cr foils and its relation to the oxide-scale microstructure.*** **Oxidation of Metals, 2000. 53(1-2): p. 25-48.**

148. **Evans, H. and A. Donaldson,** ***Silicon and chromium depletion during the long-term oxidation of thin-sectioned austenitic steel.*** **Oxidation of metals, 1998. 50(5-6): p. 457-475.**

149. **Dayananda, M. and D. Behnke,** ***Effective interdiffusion coefficients and penetration depths.*** **Scripta metallurgica et materialia, 1991. 25(9): p. 2187-2191.**

150. **Campbell, C., J. Zhao, and M. Henry,** ***Comparison of experimental and simulated multicomponent Ni-base superalloy diffusion couples.*** **Journal of Phase Equilibria and Diffusion, 2004. 25(1): p. 6-15.**

151. **Chyrkin, A.,** ***Oxidation induced phase transformations and lifetime limits of chromia forming nickel base alloy 625.*** **2011, Fachgruppe für Metallurgie und Werkstofftechnik.**

152. **Pfeil, L.B. and W.T. Griffiths,** ***Improvements in heat resistant alloys, GB Patent 459848A (1937).***

153. **Pfeil, L.B.,** ***Improvements relating to Heat Resisting Alloys containing Chromium, GB Patent 574088 (1945).***

154. **Antill, J.E. and K.A. Peakall,** ***J. Iron Steel Inst., 205 1136-1142.*** **1967.**

155. Felten, E.J., *J. Electmchem Soc., 108, 490*. 1961.

156. Golightly, F.A., F.H. Stott, and G.C. Wood, *The influence of yttrium additions on the oxide-scale adhesion to an iron-chromium-aluminum alloy.* Oxidation of Metals. 10(3): p. 163-187.

157. H, P., *Werkst. Korros., 8, 574*. 1957.

158. Stringer, J., *Met.Rev., 11 ,113*. 1966.

159. Quadakkers, W.J., et al., *Differences in growth mechanisms of oxide scales formed on ODS and conventional wrought alloys.* Oxidation of Metals, 1989. 32(1-2): p. 67-88.

160. Pieraggi, B. and R.A. Rapp, *Chromia scale growth in alloy oxidation and the reactive element effect.* Journal of the Electrochemical Society, 1993. 140(10): p. 2844-2850.

161. Stringer, J., B.A. Wilcox, and R.I. Jaffee, *The high-temperature oxidation of nickel-20 wt. % chromium alloys containing dispersed oxide phases.* Oxidation of Metals, 1972. 5(1): p. 11-47.

162. Pint, B.A. *Progress in understanding the reactive element effect since the Whittle and Stringer literature review*. in *Proceedings of the John Stringer Symposium. Edited by PF Tortorelli and PY Hou. ASM, Materials Park, OH*. 2003. Citeseer.

163. Naumenko, D., B.A. Pint, and W.J. Quadakkers, *Current Thoughts on Reactive Element Effects in Alumina-Forming Systems: In Memory of John Stringer.* Oxidation of Metals, 2016. 86(1): p. 1-43.

164. Smeggil, J.G. and G.G. Peterson, *Nature of indigenous sulfur segregated to the free metal surface and to the scale-metal interface.* Oxidation of Metals. 29(1): p. 103-119.

165. Smeggil, J.G., N.S. Bornstein, and M.A. DeCrescente, *The importance of interfacial chemistry in protective oxide scale adherence.* Oxidation of Metals. 30(3): p. 259-266.

166. Melas, I. and D.G. Lees, *Factors affecting adhesion of chromia scale on chromium.* Materials Science and Technology, 1988. 4(5): p. 455.

167. Lees, D.G., *On the reasons for the effects of dispersions of stable oxides and additions of reactive elements on the adhesion and growth-mechanisms of chromia and alumina scales-the "sulfur effect".* Oxidation of Metals, 1987. 27(1): p. 75-81.

168. Smialek, J., et al., *Effects of hydrogen annealing, sulfur segregation and diffusion on the cyclic oxidation resistance of superalloys: a review.* Thin solid films, 1994. 253(1): p. 285-292.

169. Pint, B.A. and K.A. Unocic, *Ionic segregation on grain boundaries in thermally grown alumina scales.* Materials at High Temperatures, 2012. 29(3): p. 257-263.

170. **Tawancy, H., N. Abbas, and A. Bennett, *Role of Y during high temperature oxidation of an M-Cr-Al-Y coating on an Ni-base superalloy.* Surface and Coatings Technology, 1994. 68: p. 10-16.**

171. **Yurek, G.J., K. Przybylski, and A. Garratt-Reed, *Segregation of Y to Grain Boundaries in Cr2 O 3 and NiO Scales Formed on an ODS Alloy.* Journal of the Electrochemical Society, 1987. 134(10): p. 2643-2644.**

172. **Pint, B.A., *Grain Boundary Segregation of Cation Dopants in α-Al[sub 2]O[sub 3] Scales.* Journal of the Electrochemical Society (JES), 1998. 145(6): p. 1819.**

173. **Klöwer, J., *High temperature Corrosion behaviour of iron aluminides and iron-aluminium-chromium alloys.* Materials and Corrosion, 1996. 47(12): p. 685-694.**

174. **Klower, J., *Factors affecting the oxidation behaviour of thin Fe-Cr-Al foils. Part II: The effect of alloying elements: Overdoping.* Materials and Corrosion/Werkstoffe und Korrosion, 2000. 51(5): p. 373.**

175. **Pint, B., P. Tortorelli, and I. Wright, *Effect of cycle frequency on high-temperature oxidation behavior of alumina-forming alloys.* Oxidation of Metals, 2002. 58(1-2): p. 73-101.**

176. **Pint, B.A. *Study of the reactive element effect in ODS iron-base alumina formers*. in *Materials science forum*. 1997. Trans Tech Publ.**

177. **Chevalier, S., et al., *The combined effect of refractory coatings containing reactive elements on high temperature oxidation behavior of chromia-forming alloys.* Corrosion science, 2003. 45(8): p. 1661-1673.**

178. **Chevalier, S., *What did we learn on the reactive element effect in chromia scale since Pfeil's patent?*. . Materials and Corrosion, 65: 109–115. doi: 10.1002/maco.201307310, 2014.**

179. **Pint, B., *The Oxidation Behavior of Oxide-Dispersed β-NiAl.* Oxidation of Metals, 1998. 49(5): p. 531-559.**

180. **England, D.M. and A.V. Virkar, *Oxidation Kinetics of Some Nickel-Based Superalloy Foils and Electronic Resistance of the Oxide Scale Formed in Air Part I.* Journal of the Electrochemical Society, 1999. 146(9): p. 3196-3202.**

181. **DelaunayRID, F., et al., *SEM-EDS and XPS studies of the high temperature oxidation behaviour of Inconel 718.* Microchimica Acta, 2000. 132(2-4): p. 337-343.**

182. **Greene, G.A. and C.C. Finfrock, *Oxidation of Inconel 718 in air at high temperatures.* Oxidation of Metals, 2001. 55(5-6): p. 505-521.**

183. **Garcia-Fresnillo, L., et al.,** ***Oxidation behaviour and microstructural stability of alloy 625 during long-term exposure in steam.*** **Journal of materials science, 2014. 49(17): p. 6127-6142.**

184. **Buscail, H., et al.,** ***Effects of water vapour on the oxidation of a nickel-base 625 alloy between 900 and 1,100 °C.*** **Journal of Materials Science. 46(18): p. 5903-5915.**

185. **Kumar, L., et al.,** ***Studies on the oxidation behavior of Inconel 625 between 873 and 1523 K.*** **Oxidation of Metals, 1996. 45(1-2): p. 221-244.**

186. **Chyrkin, A., et al.,** ***Oxidation Limited Lifetime of Ni-Base Metal Foams in the Temperature Range 700–900° C.*** **Advanced Engineering Materials, 2010. 12(9): p. 873-883.**

187. **Alman, D.E., et al.,** ***Influence of a Cerium Surface Treatment on the Oxidation Behavior of Cr2O3-Forming Alloys (title on slides varies: Oxidation Behavior of Cerium Surface Treated Chromia Forming Alloys)*****. 2007. Medium: ED.**

188. **Sugama, T.,** ***Y 2 O 3-sealed Ni–Al protective coatings for Inconel 625.*** **Surface and Coatings Technology, 1998. 106(2): p. 106-116.**

189. **Kim, I.H. and S.I. Kwun.** ***Oxide Growth Mechanism and Oxidation Resistance in Mechanically Alloyed Ni-20Cr-20Fe-5Nb-1Y2O3 Alloy*****. in** ***Materials Science Forum*****. 2005. Trans Tech Publ.**

190. **Samanta, S., S. Mitra, and T. Pal,** ***Effect of rare earth elements on microstructure and oxidation behaviour in TIG weldments of AISI 316L stainless steel.*** **Materials Science and Engineering: A, 2006. 430(1): p. 242-247.**

191. **Antill, J.E., et al.,** ***The effect of surface implantation of yttrium and cerium upon the oxidation behaviour of stainless steels and aluminized coatings at high temperatures.*** **Corrosion Science, 1976. 16(10): p. 729-745.**

192. **Magdefrau, N.J., et al.,** ***The effect of Mn1.5Co1.5O4 coatings on the development of near surface microstructure for Haynes 230 oxidized at 800 °C in air.*** **Surface and Coatings Technology, 2014. 242: p. 109-117.**

193. **Tawancy, H.,** ***High-temperature oxidation behavior of a wrought Ni-Cr-W-Mn-Si-La alloy.*** **Oxidation of Metals, 1996. 45(3-4): p. 323-348.**

194. **Kim, D., C. Jang, and W.S. Ryu,** ***Oxidation characteristics and oxide layer evolution of Alloy 617 and Haynes 230 at 900 °C and 1100 °C.*** **Oxidation of Metals, 2009. 71(5-6): p. 271-293.**

195. **Jang, C., et al.,** ***Oxidation behaviors of wrought nickel-based superalloys in various high temperature environments.*** **Transactions of Nonferrous Metals Society of China, 2011. 21: p. 1524-1531.**

196. **Jian, L., et al.,** ***Oxidation kinetics of Haynes 230 alloy in air at temperatures between 650 and 850 C.*** **Journal of Power Sources, 2006. 159(1): p. 641-645.**

197. **Olivares, R.I., W. Stein, and P. Marvig,** ***Thermogravimetric Study of Oxidation-Resistant Alloys for High-Temperature Solar Receivers.*** **JOM: The Journal of The Minerals, Metals & Materials Society (TMS), 2013. 65(12): p. 1660-1669.**

198. **Tung, H.-M. and J.F. Stubbins,** ***Incipient oxidation kinetics and residual stress of the oxide scale grown on Haynes 230 at high temperatures.*** **Materials Science and Engineering: A, 2012. 538: p. 1-6.**

199. **Dongmei, L., et al.,** ***Isothermal oxidation behavior of Haynes 230 alloy in air at 1100 C.*** **Rare Metal Materials and Engineering, 2008. 37(9): p. 1545-1548.**

200. **Marasco, A. and D. Young,** ***The oxidation of iron-chromium-manganese alloys at 900 C.*** **Oxidation of Metals, 1991. 36(1-2): p. 157-174.**

201. **Holcomb, G.R. and D.E. Alman,** ***The effect of manganese additions on the reactive evaporation of chromium in Ni–Cr alloys.*** **Scripta Materialia, 2006. 54(10): p. 1821-1825.**

202. **Stanislowski, M., et al.,** ***Reduction of chromium vaporization from SOFC interconnectors by highly effective coatings.*** **Journal of Power Sources, 2007. 164(2): p. 578-589.**

203. **Kim, T.-H., et al.,** ***Analysis of oxidation behavior of Ni-base superalloys by laser-induced breakdown spectroscopy.*** **Journal of Analytical Atomic Spectrometry, 2012. 27(9): p. 1525-1531.**

204. **Pop, D. and K. Wolski,** ***Surface segregation in HAYNES 230 alloy.*** **Applied Surface Science, 2006. 253(4): p. 2244-2250.**

205. **Wild, R.K.,** ***High temperature oxidation of austenitic stainless steel in low oxygen pressure.*** **Corrosion Science, 1977. 17(2): p. 87-104.**

206. **Klarstrom, D.L.,** ***Oxidation-resistant nickel alloy*****. 1984.**

207. **Kondo, T., et al.,** ***Nickel-base alloy excellent in corrosion resistance at high temperatures*****. 1978, Google Patents.**

208. **Klein; Howard Joseph (Kokomo, I., Herchenroeder; Robert B. H. (Kokomo, IN) 1972.**

209. **Kofstad, P.,** ***High temperature corrosion. Elsevier Applied Science Publishers Ltd., London – New York.*** **1988: p. 11.**

210. **Pint, B.A. and I.G. Wright,** ***Oxidation behavior of ODS Fe-Cr alloys.*** **Oxidation of Metals, 2005. 63(3-4): p. 193-213.**

211. **Schneider, C.A., W.S. Rasband, and K.W. Eliceiri, *NIH Image to ImageJ: 25 years of image analysis.* Nat Meth, 2012. 9(7): p. 671-675.**

212. ***ASTM E384-16, Standard Test Method for Microindentation Hardness of Materials, ASTM International, West Conshohocken, PA, 2016, www.astm.org*.**

213. **Scott, V.D., G. Love, and S.J.B. Reed, *Quantitative Electron-probe Microanalysis*. 1995: Ellis Horwood.**

214. **Reed, S., in *Electron Microprobe Analysis and Scanning Electron Microscopy in Geology:*. 2005, Cambridge University Press. p. 107-132.**

215. **Sands, D.E., *5.6 Bragg's Law*, in *Introduction to Crystallography*. Dover Publications.**

216. ***ICSD database - https://icsd.fiz-karlsruhe.de/search/index.xhtml*.**

217. **Pennycook, S., et al., *Scanning transmission electron microscopy for nanostructure characterization*, in *Scanning Microscopy for Nanotechnology*. 2006, Springer. p. 152-191.**

218. **Gitanjaly, et al., *Role of CeO2 coating in enhancing high temperature corrosion resistance of Ni-base superalloys as an inhibitor.* Materials at High Temperatures, 2010. 27(2): p. 109-116.**

219. ***Metallographic and Materialographic Specimen Preparation, Light Microscopy, Image Analysis, and Hardness Testing*.**

220. **H. Brown and B.B. Knapp, *Nickel. In: Modern Electroplating, 3rd edition, ed. F.A. Lowenheim, John Wiley & Sons, New York (USA) et al. ISBN 0-471-54968-12, 87-341. _592*. 1974.**

221. **Tomus, D. and H.P. Ng, *In situ lift-out dedicated techniques using FIB–SEM system for TEM specimen preparation.* Micron, 2013. 44: p. 115-119.**

222. **Giannuzzi, L.A. and F.A. Stevie, *A review of focused ion beam milling techniques for TEM specimen preparation.* Micron, 1999. 30(3): p. 197-204.**

223. **Mayer, J., et al., *TEM Sample Preparation and FIB-Induced Damage.* MRS Bulletin, 2007. 32(5): p. 400.**

224. **Yadollahi, A., et al., *Effects of building orientation and heat treatment on fatigue behavior of selective laser melted 17-4 PH stainless steel.* International Journal of Fatigue.**

225. **Tang, Q., et al., *Oxide Particle Refinement in 4.5 mass% Al Ni-Based ODS Superalloys.* Materials Transactions, 2012. 53(4): p. 645-651.**

226. **Chen, C.-L. and Y. Zeng,** ***Effect of consolidation and oxide dispersoid addition on phase formation and mechanical properties of W< img border=.*** **International Journal of Refractory Metals and Hard Materials, 2016. 60: p. 11-16.**

227. **Wajszel, D.,** ***A method for calculating paralinear constants for the formation of volatile scale.*** **Journal of The Electrochemical Society, 1963. 110(6): p. 504-507.**

228. **Tedmon, C.,** ***The effect of oxide volatilization on the oxidation kinetics of Cr and Fe-Cr alloys.*** **Journal of the Electrochemical Society, 1966. 113(8): p. 766-768.**

229. **Webb, W.W., J.T. Norton, and C. Wagner,** ***Oxidation of tungsten.*** **Journal of The Electrochemical Society, 1956. 103(2): p. 107-111.**

230. **Haycock, E.,** ***Transitions from parabolic to linear kinetics in scaling of metals.*** **Journal of The Electrochemical Society, 1959. 106(9): p. 771-775.**

231. **Berthod, P.,** ***Kinetics of High Temperature Oxidation and Chromia Volatilization for a Binary Ni–Cr Alloy.*** **Oxidation of Metals, 2005. 64(3): p. 235-252.**

232. **Gindorf, C., et al.,** ***CHROMIUM VAPORISATION FROM METALLIC INTERCONNECT AND RETENTION BY PEROVSKITE LAYERS.*** **Vol. 99-19, 1999: p. 774-782.**

233. **Liu, F., et al.,** ***Microstructure and residual stress of laser rapid formed Inconel 718 nickel-base superalloy.*** **Optics & Laser Technology. 43(1): p. 208-213.**

234. **Dinda, G.P., A.K. Dasgupta, and J. Mazumder,** ***Texture control during laser deposition of nickel-based superalloy.*** **Scripta Materialia.**

235. **Carter, L.N., et al.,** ***The influence of the laser scan strategy on grain structure and cracking behaviour in SLM powder-bed fabricated nickel superalloy.*** **Journal of Alloys and Compounds, 2014. 615: p. 338-347.**

236. **Herchl, R., et al.,** ***Short-circuit diffusion in the growth of nickel oxide scales on nickel crystal faces.*** **Oxidation of Metals, 1972. 4(1): p. 35-49.**

237. **Stott, F., et al.,** ***Factors affecting the high-temperature oxidation behavior of some dilute nickel-and cobalt-base alloys.*** **Oxidation of Metals, 1977. 11(3): p. 141-150.**

238. **Connolley, T., M. Starink, and P. Reed,** ***EFFECT OF OXIDATION ON HIGH TEMPERATURE FATIGUE CRACK INITIATION AND SHORT CRACK GROWTH IN INCONEL 7 18.*** **Superalloys. TMS, 2000: p. 435-444.**

239. **Litz, J., A. Rahmel, and M. Schorr,** ***Selective carbide oxidation and internal nitridation of the Ni-base superalloys IN 738 LC and IN 939 in air.*** **Oxidation of Metals, 1988. 30(1-2): p. 95-105.**

240. Connolley, T., P. Reed, and M. Starink, *Short crack initiation and growth at 600 C in notched specimens of Inconel718.* Materials Science and Engineering: A, 2003. 340(1): p. 139-154.

241. Cruchley, S., et al., *Chromia layer growth on a Ni-based superalloy: Sub-parabolic kinetics and the role of titanium.* Corrosion Science. 75: p. 58-66.

242. Pérez-González, F., N. Garza-Montes-de Oca, and R. Colás, *High temperature oxidation of the Haynes 282© nickel-based superalloy.* Oxidation of Metals, 2014. 82(3-4): p. 145-161.

243. Geels, K., et al., *Metallographic and materialographic specimen preparation, light microscopy, image analysis, and hardness testing*. 2007: ASTM International West Conshohocken, PA.

244. Atkinson, A., *Wagner theory and short circuit diffusion.* Materials science and technology, 1988. 4(12): p. 1046-1051.

245. Boegelein, T., *Selective laser melting of a ferritic oxide dispersion strengthened steel*. 2014, University of Liverpool.

246. Deffley, R.J., *Development of processing strategies for the additive layer manufacture of aerospace components in Inconel 718*. 2012, University of Sheffield.

247. Zakrzewska, K., M. Radecka, and M. Rekas, *Effect of Nb, Cr, Sn additions on gas sensing properties of TiO 2 thin films.* Thin Solid Films, 1997. 310(1): p. 161-166.

248. Ruiz, A.M., et al., *Insights into the structural and chemical modifications of Nb additive on TiO2 nanoparticles.* Chemistry of materials, 2004. 16(5): p. 862-871.

249. Al-hatab, K., et al., *Cyclic Oxidation Behavior of IN 718 Superalloy in Air at High Temperatures.* Oxidation of Metals. 75(3-4): p. 209.

250. Agarwal, S. and H. Herman. *Phase decomposition in aluminum alloys quenched from the liquid state*. in *Phase Transitions-1973: Proceedings of the Conference on Phase Transitions and Their Applications in Materials Science, University Park, Pennsylvania, May 23-25, 1973*. 2013. Elsevier.

251. Wood, J.V., et al., *Rapidly solidified nickel-base superalloys.* Journal of Materials Science, 1980. 15(11): p. 2709-2719.

252. Jackman, L., M. Boldy, and A. Coffey, *The influence of reduced carbon on alloy 718.* Superalloys, 1991. 718(625): p. 261-270.

253. Miller, C.F., G.W. Simmons, and R.P. Wei, *High temperature oxidation of Nb, NbC and Ni3Nb and oxygen enhanced crack growth.* Scripta materialia, 2000. 42(3): p. 227-232.

254. Rhines, F.N. and J.S. Wolf, *The role of oxide microstructure and growth stresses in the high-temperature scaling of nickel.* Metallurgical Transactions, 1970. 1(6): p. 1701-1710.

255. Caplan, D., A. Harvey, and M. Cohen, *Oxidation of chromium at 890-1200°C.* Corrosion Science, 1963. 3(3): p. 161-IN8.

256. Caplan, D. and G.I. Sproule, *Effect of oxide grain structure on the high-temperature oxidation of Cr.* Oxidation of Metals, 1975. 9(5): p. 459.

257. Douglass, D. and J. Armijo, *The effect of silicon and manganese on the oxidation mechanism of Ni-20 Cr.* Oxidation of Metals, 1970. 2(2): p. 207-231.

258. Wallwork, G., *The oxidation of alloys.* Reports on Progress in Physics, 1976. 39(5): p. 401.

259. Xu, Z., et al., *The effect of silicon on precipitation and decomposition behaviors of M6C carbide in a Ni–Mo–Cr superalloy.* Journal of Alloys and Compounds, 2015. 620: p. 197-203.

260. Miller, C., G. Simmons, and R. Wei, *Mechanism for oxygen enhanced crack growth in inconel 718.* Scripta materialia, 2001. 44(10): p. 2405-2410.

261. Froitzheim, J., et al., *Development of high strength ferritic steel for interconnect application in SOFCs.* Journal of Power Sources, 2008. 178(1): p. 163-173.

262. Dey, G.K., et al., *Microstructural studies on rapidly solidified inconel 625.* Materials Science and Engineering: A, 1989. 119: p. 175-184.

263. Daintith, J., *Dictionary of Chemistry (6th Edition)*. Oxford University Press. p. 356.

264. Atkinson, A., R. Taylor, and P. Goode, *Transport processes in the oxidation of Ni studied using tracers in growing NiO scales.* Oxidation of metals, 1979. 13(6): p. 519-543.

265. Chien, F.-R. and R. Brown, *Cyclic oxidation of Haynes 230 alloy.* Journal of materials science, 1992. 27(6): p. 1514-1520.

266. Bricknell, R. and D. Woodford, *The mechanism of cavity formation during high temperature oxidation of nickel.* Acta Metallurgica, 1982. 30(1): p. 257-264.

267. Caplan, D., et al., *Effect of carbon on cavity formation during the high-temperature oxidation of Ni.* Oxidation of Metals, 1980. 14(4): p. 279-299.

268. Dyson, B., *An analysis of carbon/oxygen gas bubble formation in some nickel alloys.* Acta Metallurgica, 1982. 30(8): p. 1639-1646.

269. **Kuenzly, J.D. and D. Douglass,** ***The oxidation mechanism of Ni3Al containing yttrium.*** **Oxidation of Metals, 1974. 8(3): p. 139-178.**

270. **Bondar', I. and N. Vinogradova,** ***Phase equilibria in the lanthanum oxide—Alumina system.*** **Russian Chemical Bulletin, 1964. 13(5): p. 737-741.**

271. **Wu, P. and A.D. Pelton,** ***Coupled thermodynamic-phase diagram assessment of the rare earth oxide-aluminium oxide binary systems.*** **Journal of alloys and compounds, 1992. 179(1): p. 259-287.**

272. **Vasylechko, L., A. Senyshyn, and U. Bismayer,** ***Chapter 242 Perovskite-Type Aluminates and Gallates,*** **in** ***Handbook on the Physics and Chemistry of Rare Earths*****. 2009, Elsevier. p. 113-295.**

273. **Chivel, Y.,** ***Optical In-Process Temperature Monitoring of Selective Laser Melting.*** **Physics Procedia, 2013. 41: p. 904-910.**

274. **García Fresnillo, L., et al.,** ***Oxide scale formation and subsurface phase transformations during long-term steam exposure of the cobalt base alloy 25.*** **Materials and Corrosion, 2012. 63(10): p. 878-888.**

275. **Ford, D.A., et al.,** ***Improved performance rhenium containing single crystal alloy turbine blades utilizing PPM levels of the highly reactive elements lanthanum and yttrium.*** **Journal of engineering for gas turbines and power, 1999. 121(1): p. 138-143.**

276. **Pint, B.A., M.A. Bestor, and J.A. Haynes,** ***Cyclic oxidation behavior of HVOF bond coatings deposited on La- and Y-doped superalloys.*** **Surface and Coatings Technology, 2011. 206(7): p. 1600-1604.**

277. **Haynes, J.A., K.A. Unocic, and B.A. Pint,** ***Effect of water vapor on the 1100 °C oxidation behavior of plasma-sprayed TBCs with HVOF NiCoCrAlX bond coatings.*** **Surface and Coatings Technology, 2013. 215: p. 39-45.**

278. **Unocic, K.A., C.M. Parish, and B.A. Pint,** ***Characterization of the alumina scale formed on coated and uncoated doped superalloys.*** **Surface and Coatings Technology. 206(7): p. 1522-1528.**

279. ***Superalloys 2012 (1)*****. 2012, Somerset, US: Wiley-TMS.**

280. **Huang, Z., et al.,** ***Environmentally assisted, sustained-load crack growth in powder metallurgy nickel-based superalloys.*** **Metallurgical and Materials Transactions A, 2002. 33(6): p. 1681-1687.**

281. **Gao, M. and R.P. Wei,** ***GRAIN BOUNDARY NIOBIUM CARBIDES IN INCONEL 718.*** **Scripta Materialia, 1997. 37(12): p. 1843-1849.**

282. **Hong, J.K., et al.** ***Microstructures of oxidized primary carbides on superalloy Inconel 718*****. in** ***Materials Science Forum*****. 2005. Trans Tech Publ.**

283. **Bai, G., et al.,** ***Effect of thermal exposure on the stability of carbides in Ni–Cr–W based superalloy.*** **Materials Science and Engineering: A, 2011. 528(6): p. 2339-2344.**

284. ***Sims, C.T.S., Norman S.;Hagel, William C., Superalloys II: high-temperature materials for aerospace and industrial power. 1987, New York: Wiley & sons.***

285. **Lvov, G., V.I. Levit, and M.J. Kaufman,** ***Mechanism of primary MC carbide decomposition in Ni-base superalloys.*** **Metallurgical and Materials Transactions A, 2004. 35(6): p. 1669-1679.**

286. **Cabet, C., et al.,** ***High temperature reactivity of two chromium-containing alloys in impure helium.*** **Journal of Nuclear Materials, 2008. 375(2): p. 173-184.**

287. **Graham, L.W.,** ***Corrosion of metallic materials in HTR-helium environments.*** **Journal of Nuclear Materials, 1990. 171(1): p. 76-83.**

288. **Cabet, C., et al.,** ***High temperature corrosion of structural materials under gas-cooled reactor helium.*** **Materials and Corrosion, 2006. 57(2): p. 147-153.**

289. **Adharapurapu, R.R., et al.,** ***Chromia-Assisted Decarburization of W-Rich Ni-Based Alloys in Impure Helium at 1273 K (1000° C).*** **Metallurgical and Materials Transactions A, 2011. 42(5): p. 1229-1244.**

290. **Chyrkin, A., et al.,** ***Modelling compositional changes in nickel base alloy 602 CA during high temperature oxidation.*** **Materials at high temperatures, 2015. 32(1-2): p. 102-112.**

291. **Lobnig, R., et al.,** ***Diffusion of cations in chromia layers grown on iron-base alloys.*** **Oxidation of Metals, 1992. 37(1-2): p. 81-93.**

292. **Moverareu, R.R., et al.,** ***A new single crystal superalloy for power generation applications.*** **Superalloys 2012, 2012: p. 197.**